



HAL
open science

Methods for Monostatic and Bistatic Polarimetric SAR Image Analysis

Ileana-Madalina Ciuca

► **To cite this version:**

Ileana-Madalina Ciuca. Methods for Monostatic and Bistatic Polarimetric SAR Image Analysis. Signal and Image processing. Université Grenoble Alpes [2020-..]; Universitatea politehnica (Bucarest), 2023. English. NNT : 2023GRALT043 . tel-04220608

HAL Id: tel-04220608

<https://theses.hal.science/tel-04220608>

Submitted on 28 Sep 2023

HAL is a multi-disciplinary open access archive for the deposit and dissemination of scientific research documents, whether they are published or not. The documents may come from teaching and research institutions in France or abroad, or from public or private research centers.

L'archive ouverte pluridisciplinaire **HAL**, est destinée au dépôt et à la diffusion de documents scientifiques de niveau recherche, publiés ou non, émanant des établissements d'enseignement et de recherche français ou étrangers, des laboratoires publics ou privés.

THÈSE

Pour obtenir le grade de

DOCTEUR DE L'UNIVERSITÉ GRENOBLE ALPES ET DE L'UNIVERSITÉ POLITEHNICA DE BUCAREST



École doctorale : EEATS – Électronique, Électrotechnique, Automatique, Traitement du Signal
Spécialité : SIPT – Signal Image Parole Télécoms
Unité de recherche : Grenoble Images Parole Signal Automatique (GIPSA-Lab.)
Département des Télécommunications (ETTI, UPB)

Méthodes de Traitement des Images RSO Polarimétriques, Monostatiques et Bistatiques

Methods for Monostatic and Bistatic Polarimetric SAR Image Analysis

Présentée par :

Madalina CIUCA

Direction de thèse :

Michel GAY

Ingénieur de Recherche (HDR), CNRS, UGA

Silviu CIOCHINA

Professeur des Universités, UPB

Gabriel VASILE

Chercheur, CNRS, UGA

Andrei ANGHEL

Professeur des Universités, UPB

Directeur de thèse

Co-Directeur de thèse

Encadrant

Co-Encadrant

Rapporteurs :

Jean-Philippe OVARLEZ

Directeur de recherche, ONERA, Centrale Supélec

Antoine ROUEFF

Professeur des Universités, Université de Toulon

Thèse soutenue publiquement le **21/06/2023** devant le jury composé de :

Olivier MICHEL

Professeur des Universités, Université Grenoble Alpes

Président, Examineur

Jean-Philippe OVARLEZ

Directeur de recherche, ONERA, CentraleSupélec

Rapporteur

Antoine ROUEFF

Professeur des Universités, Université de Toulon

Rapporteur

Emanuel TROUVE

Professeur des Universités, Université Savoie Mont-Blanc

Examineur

Michel GAY

Ingénieur de Recherche, Université Grenoble Alpes

Directeur de thèse

Silviu CIOCHINA

Professeur des Universités, Université Politehnica de Bucarest

Co-Directeur de thèse

Invités :

Gabriel VASILE

Chercheur, CNRS, Université Grenoble Alpes

Andrei ANGHEL

Professeur des Universités, Université Politehnica de Bucarest



UNIVERSITÉ DE GRENOBLE ALPES

THESIS

for jointly obtaining the

DOCTORATE DEGREE

of University of Grenoble Alpes

Doctoral School of Electronics, Electrical Engineering, Automation, Signal Processing
and

of University Politehnica of Bucharest

Doctoral School of Electronics, Telecommunications and Information Technology

Presented and defended by

Ileana Mădălina CIUCĂ

Methods for Monostatic and Bistatic Polarimetric SAR Image Analysis

Thesis directed by Michel GAY and Silviu CIOCHINA

and supervised by Gabriel VASILE and Andrei ANGHEL

Prepared in the Grenoble Image Parole Signal Automatique Laboratory (GIPSA-lab) and the
Faculty of Electronics, Telecommunications and Information Technology

defended on 21/06/2023, in front of the jury:

<i>Reviewers:</i>	Jean-Philippe OVARLEZ	-	Research Director, ONERA & Centrale Supélec
	Antoine ROUEFF	-	Professor, University of Toulon
<i>Examiner:</i>	Emanuel TROUVÉ	-	Professor, University of Savoie Mont-Blanc
<i>President:</i>	Olivier MICHEL	-	Professor, University of Grenoble Alpes
<i>Directors:</i>	Michel GAY	-	CNRS Research Engineer, GIPSA-lab
	Silviu CIOCHINĂ	-	Professor, University Politehnica of Bucharest
<i>Supervisors:</i>	Gabriel VASILE	-	CNRS Researcher, GIPSA-lab
	Andrei ANGHEL	-	Professor, University Politehnica of Bucharest

Acknowledgement

Completing this thesis would not have been possible without the support and influence of many people. Throughout its beautiful times, its difficulties and setbacks, this journey will remain, in so many ways, an incredibly valuable experience, professionally and personally. For this, I will always be grateful.

The first round of warm thanks are for the members of the jury. Thank you to Prof. Antoine Roueff and Research Director Jean-Philippe Ovarlez for accepting to review my thesis manuscript, for your insightful suggestions and valuable remarks. Thank you to Prof. Emanuel Trouvé for participating in the thesis committee, for your kindness and relevant questions. My sincere appreciation goes towards Prof. Olivier Michel for presiding the thesis jury, for useful advice and professionalism shown not only with this occasion but also as part of my CSI committee.

I would like to express my sincere gratitude to my thesis direction from the two establishments, UGA and UPB. Special thanks goes also to both doctoral schools and the human resource departments for support and patience.

To my thesis directors, HDR Dr. Michel Gay and Prof. Silviu Ciochina, thank you for accepting to supervise my thesis, for allowing me this opportunity and for your guidance in both scientific and more administrative tasks.

To my thesis supervisors, Prof. Gabriel Vasile and Prof. Andrei Anghel, words are too incomplete to describe your countless advice, patience and your active participation throughout this scientific endeavors. You have taught me what a true mentor looks like.

There are several other academics I have had the chance to meet at different stages of this journey, which have motivated, challenged or provided counsel. Among them, I would like to acknowledge Prof. Marco Congedo, Prof. Fabien Ndagijimana, Prof. Steeve Zozor, Prof. Remus Cacoveanu and Prof. Mihai Datcu.

I recall the numerous online activities being held in the early mists of the pandemic, at both establishments, throughout the doctoral schools, or independently. In particular, I owe a great deal of gratitude to one of those endeavors, for keeping my motivation afloat.

A heartfelt thanks goes to all the PhD students, colleagues and friends I have had the chance to meet and get inspired by during these years.

A tender thought goes, as always, to my family.

Abstract

Titre: Méthodes de Traitement des Images RSO Polarimétriques, Monostatiques et Bistatiques

Mots clés: polarimétrie radar, PolSAR, monostatique, bistatique, consimilarité, similarité, décomposition polaire, variété, regroupement non supervisé.

Résumé:

Les données polarimétriques radar à synthèse d'ouverture (RSO, ou SAR en anglais) enregistrent la diversité de retrodiffusion en mesurant la réponse électromagnétique dans deux bases orthogonales de polarisation. L'interaction des micro-ondes avec les milieux anthropiques et naturels peut modifier l'état polarimétrique incident. Les applications PolSAR exploitent cette dépendance des ondes incidentes et de retrodiffusion, qui s'est avérée être un atout important, en particulier pour la détection et la classification.

L'objectif principal de cette thèse est de contribuer à l'analyse des données SAR polarimétriques. Conformément aux développements technologiques attendus dans le domaine des instruments radar, le cas de la géométrie bistatique est aussi discuté. Pour la représentation et le traitement des données, le formalisme matriciel a été utilisé. Comme en PolSAR les matrices de diffusion ont des propriétés qui dépendent de la géométrie de diffusion, les méthodes proposées dans la thèse sont applicables au cas le plus général, c'est-à-dire avec des données non réciproques (monostatiques ou bistatiques).

La thèse propose deux modèles pour la matrice de diffusion à partir de la Représentation Réelle et de la Décomposition Polaire. Les deux sections sont complémentaires, avec des modèles basés sur : un traitement algébrique vs. géométrique, une factorisation en utilisant la similarité conjuguée vs. la similarité ou un contexte cohérent vs. incohérent. La première contribution discute la similarité conjuguée en PolSAR. Cela oriente l'étude vers la représentation réelle, sa décomposition propre et l'extraction de paramètres non accessibles par les méthodes précédentes. La deuxième contribution est basée sur les propriétés de la décomposition polaire et de la géométrie Riemannienne des matrices semi-définies positives. Un algorithme de clustering géométrique, combinant les k-means et une distance géodésique Riemannienne est introduit.

Des ensembles de données aéroportées, monostatiques PolSAR (en bande L, C, et X) ainsi que des données polarimétriques monostatiques et bistatiques simulées sont utilisés pour tester les méthodes proposées dans cette thèse.

Title: Methods for Monostatic and Bistatic Polarimetric SAR Image Analysis

Keywords: radar polarimetry, PolSAR, monostatic, bistatic, consimilarity, similarity, polar decomposition, manifold, clustering.

Abstract:

Polarimetric Synthetic Aperture Radar (PolSAR) data records the scattering diversity by measuring the electromagnetic response in two orthogonal polarization bases. The interaction of the microwaves with both anthropogenic and natural media can modify the incident polarimetric state. PolSAR applications exploit the incident-scattering polarization dependence, which was proven as an important asset, especially for detection and classification.

The main aim of this thesis is to contribute to the analysis of full-polarimetric PolSAR data. In line with expected technological developments in the area of radar instruments, the case of bistatic geometry is discussed. Throughout the work, the matrix formalism has been assumed for data representation and processing. Because PolSAR scattering matrices have properties which depend on the scattering geometry, the methods proposed in the thesis are applicable to the most general case, i.e., with non-reciprocal data (monostatic or bistatic).

The thesis proposes two frameworks for the scattering matrix based on the Real Representation and the Polar Decomposition. The two parts are complementary, with models based on an algebraic vs. geometric processing, on a conjugate similarity vs. similarity factorization or on a coherent vs. incoherent application context. The first contribution is oriented towards the study of the conjugate similarity in PolSAR by the use of the Real Representation. The second contribution is based on the properties of the polar decomposition and the Riemannian geometry of positive semidefinite matrices. A geometric clustering algorithm, combining the k-means and a Riemannian geodesic distance is introduced.

Airborne, monostatic PolSAR datasets (L-, C-, X-Band) and simulated monostatic and bistatic polarimetric data are used for testing the proposed methods.

Contents

Notations and symbols	xvii
Abbreviations and acronyms	xix
Introduction	1
1 Polarimetric Radar Diversity	5
1.1 Polarization of electromagnetic waves	6
1.1.1 Plane wave model	6
1.1.2 Jones vector and polarization ellipse	7
1.1.3 Radar polarization imaging modes	10
1.2 Imaging radar	10
1.2.1 Monostatic geometry - Synthetic Aperture Radar	11
1.2.2 Bistatic geometry	13
1.2.3 Bistatic polarimetric diversity	16
1.3 Scattering matrix	17
1.3.1 Forward Scattering Alignment (FSA) and Backscattering (BSA)	18
1.3.2 The monostatic simplification	19
1.3.3 Similarity and conjugate similarity transformations	20
1.4 Coherent decompositions	25
1.4.1 Summation decompositions	26
1.4.2 Multiplicative decompositions	27
1.4.3 Target scattering vector	29
1.5 Incoherent decompositions	30
1.5.1 Entropy-alpha decomposition (monostatic/bistatic, quad-pol/dual-pol)	33

1.5.2	Application: Dual-polarimetric bistatic and monostatic VV-HV H-alpha classification	35
1.6	Conclusions	43
2	Real Representation Scattering Matrix (RRSM)	45
2.1	A state-of-art investigation on general conjugate similarity	46
2.1.1	On mathematical solutions for the consimilarity transformation	46
2.1.2	On properties of conjugate eigenvectors/eigenvalues	49
2.1.3	On homogeneous/inhomogeneous scattering matrices	49
2.1.4	Solution through the Real Representation Scattering Matrix . .	51
2.2	Properties of the Real Representation Scattering Matrix	53
2.2.1	Real canonical form and eigenvalues of RRSM	53
2.2.2	Real concanonical form and con-eigenvalues/eigenvectors . . .	54
2.3	PolSAR monostatic data and the Real Representation	56
2.3.1	Graves method vs. RRSM method - Coneigenvalues comparison	57
2.3.2	On monostatic and bistatic SM nonreciprocity	60
2.4	Computational Electromagnetic simulations	64
2.4.1	Bistatic scattering - Coordinate system definition	64
2.4.2	Simulation software	65
2.4.3	Radar cross-section and monostatic evaluations	70
2.5	RRSM Eigen-classification with simulated data	78
2.5.1	Monostatic simulations	78
2.5.2	Bistatic simulations	79
2.6	Conclusions	85
3	Polar Decomposition Geometrical Clustering	87
3.1	Unsupervised classification and clustering in PolSAR	88
3.1.1	Metrics, distances and similarity measures for PolSAR applications	88
3.1.2	PolSAR clustering	90

3.2	PolSAR polar factors	92
3.2.1	State of art on PolSAR Polar Decomposition	93
3.2.2	Algebraic and geometric properties of polar factors	94
3.3	Manifold of Hermitian/unitary factors	97
3.3.1	On manifolds and Riemannian geometry	97
3.3.2	Manifold embedding for Hermitian positive definite matrices . .	98
3.3.3	Manifold embedding for Unitary matrices	101
3.4	Geometric clustering with Hermitian factors	104
3.4.1	Evaluating the contribution of the unitary factor	104
3.4.2	Method description	106
3.5	Geometric clustering: Implementation and testing	108
3.5.1	Simulated datasets	108
3.5.2	Real datasets	111
3.6	Conclusions	113
	Conclusion	117
A	Polarimetric datasets used in the thesis	121
A.1	Quad-pol Data	121
A.2	Monostatic-Bistatic VV-HV Dual-pol Data	126
B	Scattering and Coherency matrices for elementary scatterers	127
C	Jordan canonical form	129
D	Real representation of 4 particular scattering matrices	131
E	Solving the conjugate similarity equivalence for SM via RR	133
F	PolSAR data simulation model and Sobel kernel gradient	139

G	Matrix logarithm and matrix exponential	143
H	Riemannian barycenter computation	145
I	Publications and communications	147
	Résumé étendu	149
	Bibliography	189

List of Figures

1.1	Elliptical polarization.	8
1.2	Linear and circular polarization.	10
1.3	Monostatic, bistatic and multistatic radar systems.	11
1.4	Spaceborne monostatic imaging radar.	12
1.5	Spaceborne to ground-based bistatic radar.	13
1.6	Full-polarimetric radar observations.	17
1.7	Scattering alignment conventions.	18
1.8	Conjugate similarity and SVD operations for reciprocal and nonreciprocal scattering matrices.	24
1.9	Classification of coherent decompositions.	26
1.10	Shape of feature space (bistatic/monostatic/dual-pol) depending on dimensions of target vector.	36
1.11	Monostatic quad-pol vs. VV-HV dual-pol. Translation in position [(a) to (b)] inside the $H - \alpha$ plane for 8 scatterer from each of the zones in the original monostatic Plane Space.	37
1.12	Monostatic quad-pol vs. VV-HV dual-pol. Changes in the α angle interpretation for the oriented and orientation-free, zero-entropy, elementary scatterer in Table B.1.	38
1.13	Brétigny monostatic dataset. Simple $H - \alpha$ classifier: (a) Quad-polarimetric. (b) VV-HV Dual-polarimetric. Plane space representations: (c) Quad-polarimetric. (d) VV-HV Dual-polarimetric. (e) Legend and zones description for the quad-pol $H - \alpha$ plane space.	40
1.14	Monostatic-bistatic VV-HV dual-pol data. Simple $H - \alpha$ classifier: (a) Monostatic dual-pol, Sentinel-1. (b) Bistatic dual-pol, ground-based receiver. Dual-pol plane space: (c) Scatterers with common scattering mechanism in both monostatic and bistatic results.	42
2.1	Mapping the consimilarity operation between two complex matrices (S, S_{cst}) to that of ordinary similarity between two real matrices ($S_{\text{RR}}, S_{\text{RR}_{\text{st}}}$).	53

2.2	Comparison of absolute difference (Δd) between values obtained by the Graves method and values obtained using the RR method - Largest coneigenvalue (ξ_1).	58
2.3	Comparison of absolute difference (Δd) between values obtained by the Graves method and values obtained using the RR method - Largest coneigenvalue (ξ_1).	59
2.4	Absolute value and phase of nonreciprocity factor for monostatic datasets.	63
2.5	Bistatic scattering geometry (spherical coordinates)	65
2.6	Distribution of bistatic angles in scattering range.	66
2.7	Processing workflow integrating the CEM software.	66
2.8	Scatterers in spherical coordinate system geometry	67
2.9	Incidence and scattering directions.	68
2.10	Monostatic Dihedral (V Polarization). (a) RCS comparison: CST simulated vs. analytic formula (1D, [dBm ²]). CST Simulated: Absolute value for normalized Electric Field E_s [dB(V/m)]: (b) 3D. (c) 2D.	72
2.11	Monostatic Plate (V Polarization). (a) RCS comparison: CST simulated vs. 2 analytic formulas (1D, [dBm ²]). CST Simulated: Absolute value for normalized Electric Field E_s [dB(V/m)]: (b) 3D. (c) 2D.	73
2.12	Monostatic 90° Dihedral . (a) Estimation of α_{Cloude} parameter for the dihedral's response for all observation directions. (b) Estimation of α_{TSVM} parameter for the dihedral's response for all observation directions. (c) Difference between results from (a) and (b).	77
2.13	Monostatic Square Plate . (a) Estimation of α_{Cloude} parameter for the plate's response for a selection of observation directions. (b) Estimation of α_{TSVM} parameter for the plate's response for a selection of observation directions. (c) Difference between results from (a) and (b).	77
2.14	Monostatic Dihedral .(a) Absolute value of nonreciprocity factor. (b) RRSM eigen-classification color image.	79
2.15	Monostatic Plate .(a) Absolute value of nonreciprocity factor. (b) RRSM eigen-classification color image.	79

2.16	90° Dihedral (Bistatic Results, Time Domain Solver). Incidence directions at $\varphi_i = 0^\circ$ and $\theta_i = 0^\circ$ (first column), $\theta_i = 25^\circ$ (second column), $\theta_i = 40^\circ$ (third column) and scattering directions $\theta_s, \varphi_s \in [-45^\circ, 45^\circ]$. (a)-(c) Normalized absolute value of bistatic E_s ([dB(V/m)], V Polarization). (Following results are after selecting scattering directions at which $ E_s \geq -30$ dB) (d)-(f) Absolute values of nonreciprocity factor. (g)-(i) RRSM eigen-classification type (color-coded image). (j)-(l) RRSM eigen-classification as bargraphs for bistatic angle intervals between $[0^\circ, 90^\circ]$.	81
2.17	Square Plate (Bistatic Results, Time Domain Solver). Incidence directions at $\varphi_i = 0^\circ$ and $\theta_i = 0^\circ$ (first column), $\theta_i = 25^\circ$ (second column), $\theta_i = 40^\circ$ (third column) and scattering directions $\theta_s, \varphi_s \in [-45^\circ, 45^\circ]$. (a)-(c) Normalized absolute value of scattered bistatic E_{field} ([dB(V/m)], V Polarization). (Following results are after selecting scattering directions at which $ E_s \geq -30$ dB). (d)-(f) Absolute values of nonreciprocity factor. (g)-(i) RRSM eigen-classification type (color-coded image). (j)-(l) RRSM eigen-classification type as bargraphs for bistatic angle intervals between $[0^\circ, 90^\circ]$.	82
2.18	Bistatic targets. Combined representations with: the modulus of RRSM complex eigenvalues, the bistatic angle and the NRF parameter. (a-c) 90° Dihedral. (d-f) Plate.	85
3.1	Generic scheme of a centroid-based clustering algorithm for PolSAR data.	92
3.2	Brétigny Dataset. (a) Representation in \mathbb{R}^3 of $\mathcal{F}(\mathbf{H})$ coordinates for all \mathbf{H} factors in the dataset. (b) Zoomed view in red rectangle area from (a) and random selection of only 800 points.	95
3.3	Brétigny Dataset. (a) Representation in \mathbb{R}^3 of $ \mathcal{F}(\mathbf{U}) $ for all \mathbf{U} factors in the dataset. (b) Representation in \mathbb{R}^3 based on $\mathcal{L}(\mathbf{U})$ for all \mathbf{U} factors in the dataset.	97
3.4	Example of a manifold (\mathbb{M}) and its tangent space at point X ($T_X\mathbb{M}$).	98
3.5	Brétigny Dataset - Geometric vs. algebraic averaging.	103
3.6	Brétigny Dataset. (a) Angles obtained from the normalized unitary barycenter matrices [deg]. (b) Phase values obtained from the normalized unitary barycenter matrices [deg]. Following statistics are computed excluding white-masked values: (c) Histogram of angles from (a). (d) Histogram of absolute phases from (b). (e) Notches boxplot with mean and median values for angular parameter in (a). (f) Notches boxplot with mean and median values for (absolute) phase parameter in (b).	105
3.7	Simulated dataset 1.	108
3.8	Simulated dataset 1 with intra-class cut.	108
3.9	Simulated dataset 2.	110

3.10	Real Dataset 1 - Proposed method vs. Wishart clustering	112
3.11	Real Dataset 2 - Proposed method vs. Wishart clustering	114
3.12	Real Dataset 2 - Close-ups of clustering results in Fig. 3.11.	115
3.13	Key topics in radar polarimetry discussed throughout the thesis.	117
A.1	(a) Google Maps optical image, Brétigny (France), May 2004. (b) Pauli color composite Ramses Brétigny data.	121
A.2	Géoportail complementary information https://www.geoportail.gouv.fr (a) IGN Topographical map layer - Acquisition area view (2018). (b) IGN Topographical map - Close-up from (a) of the imaged zone. (c) CORINE Land Cover – Prairies (2015). (d) Forest (v.2, 2018) and Hydrologic (2021) Map Layers. (e) Example of Parcels Division (RPG) for 2007 (! NOT from the year of acquisition). For (c), (d), (e) an Aerial Photograph Layer (2000-2005) serves as basemap, similar to Fig. A.1a.	123
A.3	(a) Google Maps optical image, Foulum (Denmark), July 2005. (b) Pauli color composite Emisar Foulum data. (c) Incomplete ground truth (Legend: blue - water; green - forest; cyan - peas; magenta - winter rape; red - winter wheat; yellow - beet, as in [234]).	124
A.4	(a) Pauli color composite Convair Ice data. (b) Pauli color composite Convair Ottawa data.	125
A.5	RGB Color composite dual-pol VV-HV images. (a) Monostatic Sentinel-1. (b) Bistatic ground-based (superimposed on OpenStreetMap image of the area).	125
E.1	Flowchart for RRSM eigenvalues testing, with tolerance parameters. . .	135
E.2	Convair Ottawa results (left); Convair Ice results (right); (a)(c)(e) <i>Convair Ottawa dataset</i> : Changes in the distribution of NRF absolute values for the RRSMs returning complex eigenvalues (yellow color), introduced by varying δ_{imag} . (b)(d)(f) Same as with (a)(c)(e), but for Convair Ice data. (g) <i>Convair Ottawa dataset</i> : Distribution of NRF absolute values for RRSMs returning real eigenvalues (blue color), when $\delta_{imag} = 5\%$. (h) Same as (g), for Convair Ice data.	137
E.3	Bargraphs for RRSM eigenvalues classification. (a) Ramses Brétigny. (b) Convair Ottawa. (c) Convair Ice. (d) Emisar Foulum.	138
F.1	Magnitude of geodesic Sobel gradient - Example with Brétigny dataset .	141

G.1	Matrix logarithm and exponentiation as operations which allow to commute between the manifold (\mathbb{M}) and the tangent space ($T_X\mathbb{M}$) at point $X, \forall X \in \mathbb{M}$	144
G.2	Geodesics and tangent vectors passing through the set of points $\{X_i\}, 1 \leq i \leq 5$, and their barycenter.	144
I.1	Observation radar polarimétrique.	151
I.2	Similarité conjuguée et opérations SVD pour les matrices de diffusion réciproques et non réciproques.	154
I.3	Classification des décompositions cohérentes.	154
I.4	Données mono- et bi-statique en double polarisation VV-HV et classification dans l'espace $H-\alpha$	157
I.5	Opération de similarité conjuguée entre deux matrices complexes ($\mathbf{S}, \mathbf{S}_{cst}$) et de similarité entre deux matrices réelles ($\mathbf{S}_{RR}, \mathbf{S}_{RR,est}$). La transformation d'équivalence par consimilarité est $\mathbf{X} \in \mathbb{C}^{2 \times 2}$ et la transformation d'équivalence par similarité dans l'espace réel des matrices blocs est $\mathbf{Y} \in \mathbb{R}^{4 \times 4}$	158
I.6	Comparaison de la différence absolue (Δd) entre les valeurs obtenues par la méthode de Graves et les valeurs obtenues par la méthode RR - Plus grande convaleur (ξ_1).	160
I.7	Dièdre monostatique (V Polarisation). (a) Comparaison RCS : Valeurs simulées par logiciel et par formule analytique (1D, [dBm ²]). (b) Valeurs absolues du champ électrique normalisé E_s (3D, [dB(V/m)]), simulées par logiciel.	161
I.8	Dièdre - Résultat bistatique Directions de l'incidence : col. 1 : $\{\theta_i = 0^\circ, \varphi_i = 0^\circ\}$, col. 2 : $\{\theta_i = 25^\circ, \varphi_i = 0^\circ\}$, col. 3 : $\{\theta_i = 40^\circ, \varphi_i = 0^\circ\}$. (a)-(c) Classification des valeurs propres RRSM. (d)-(f) Classification des valeurs propres RRSM par rapport à l'angle bistatique, $\beta \in [0^\circ, 90^\circ]$	162
I.9	Schéma générique d'un algorithme de clustering pour les données PolSAR.	163
I.10	Variété, espace tangent, géodésique	165
I.11	Ensemble de données réelles - Méthode proposée vs. regroupement de Wishart	166

List of Tables

1.1	Extensive list of full-polarimetric bistatic missions, platforms and experiments. Acronyms: spaceb = spaceborne, airb = airborne, groundb = ground-based, acq. = acquisition.	15
1.2	Future spaceborne-spaceborne missions to combine bistatic and polarimetric diversities.	16
1.3	General equations of similarity and consimilarity.	20
1.4	Eigenvalues/Eigenvectors and conjugate counterparts.	21
1.5	Target scattering vector models lexicographic and Pauli basis.	27
1.6	Other PolSAR full-polarimetric target scattering vector models.	30
1.7	$H-\alpha$ Plane Space limits.	36
1.8	Transition percentages inside feasible zones of the plane space.	42
2.1	The homogeneous-inhomogeneous classification of Jones [123] / Sinclair [125] matrices under similarity/consimilarity.	50
2.2	Eigenvalues of RRSM and con-eigenvalues/eigenvectors of the SM.	56
2.3	Non-exhaustive assessment of existing nonreciprocity parameters.	61
2.4	Four particular scattering matrices (Annex D): Expressions for Pauli vectors and the nonreciprocity factor.	64
2.5	Parameters used for monostatic and bistatic CST simulations.	68
2.6	Monostatic dihedral and plate results. Evaluation based on angular polarimetric descriptors. Percentage distribution of estimated values in 10° intervals between $[0^\circ, 90^\circ]$ (for all observation directions in the investigated range).	75
2.7	Bistatic dihedral/plate/sphere simulation results. RRSM eigenclassification percentage distribution. Three incidence directions are considered: $(\theta_i, \varphi_i) \in \{(0^\circ, 0^\circ), (25^\circ, 0^\circ), (40^\circ, 0^\circ)\}$	80
2.8	Bistatic dihedral and plate simulation results. RRSM eigenclassification vs. intervals of bistatic angles, $\beta \in [0^\circ, 90^\circ]$, with 5° increment. Three incidence directions are considered: $(\theta_i, \varphi_i) \in \{(0^\circ, 0^\circ), (25^\circ, 0^\circ), (40^\circ, 0^\circ)\}$	83

3.1	Partitional clustering PolSAR examples	92
3.2	Example of PolSAR applications using the AIRM metric.	100
3.3	Simulated dataset 2 - Per class accuracy for Wishart method.	110
3.4	Simulated dataset 2 - Per class accuracy for proposed method.	110
A.1	Monostatic full-polarimetric datasets used in the paper.	121
B.1	Elementary scatterers in HV basis.	127
B.2	Coherency matrices corresponding to distinct scatterers in the $H - \alpha$ plane space.	127
D.1	Four particular scattering matrices. General form (S) and Real Representation (S_{RR}).	131
E.1	Coneigenvalues and coneigenvectors of elementary scatterers in Table B.1, Annex B.	135
E.2	Convair Ottawa and Convair Ice: Variations in the distribution of RRSM eigenvalues type for changes in tolerance parameter δ_{imag}	137
F.1	Vertical Sobel kernel.	141
F.2	Horizontal Sobel kernel.	141
I.1	Équations de similarité et de similarité conjuguée:	152
I.2	Valeurs/vecteurs propres et homologues conjugués.	152
I.3	Valeurs propres de la RRSM et valeurs/vecteurs propres de la consimilarité pour SM.	159
I.4	Dièdre monostatique. Évaluation basée sur des descripteurs polarimétriques angulaires (α_{Cloude} et α_{TSVM}). Pourcentage des valeurs estimées en intervalles de 10° entre $[0^\circ, 90^\circ]$	161

Notations and symbols

$\mathbf{E}_{\mathcal{R}}(\mathbf{r},t)$	Electric Field (real phasor component)
$\mathbf{E}_{\mathbb{J}}$	Jones vector
\otimes	Kronecker product
$\det(\cdot)$	Determinant of matrix
$\text{diag}(\cdot)$	Diagonal matrix of elements inside parenthesis
\oplus	Direct sum
$\hat{(\cdot)}$	Estimated value
$\mathbb{E}\{\cdot\}$	Expectation operator
$\exp\{\cdot\}$	Exponential
$\ \cdot\ _F$	Frobenius Norm
$\Gamma(\cdot)$	Gamma function
$\mathcal{I}\{\cdot\}$	Imaginary part operator
$(\cdot)^*$	Matrix/vector conjugate operator
$(\cdot)^{-1}$	Matrix/vector inverse
$(\cdot)^{\text{H}}$	Matrix/vector Hermitian operator
$(\cdot)^{\text{T}}$	Matrix/vector transposition operator
$\text{Exp}(\cdot)$	Matrix exponential
$\text{Log}(\cdot)$	Matrix logarithm
$ \cdot $	Modulus
$\mathcal{R}\{\cdot\}$	Real part operator
$\text{Tr}\{\cdot\}$	Trace of matrix
$\hat{(\cdot)}$	Versor (i.e., unit vector)

\mathbb{C}	Set of complex numbers
\mathbb{R}	Set of real numbers
$\mathbb{C}^{m \times n}$	Euclidean space of $(m \times n)$ complex matrices
$\mathbb{R}^{m \times n}$	Euclidean space of $(m \times n)$ real matrices
$\text{Vect}\{\cdot\}$	Vectorization operator

Notation: The boldface lower case letters are used for vectors, e.g. \mathbf{z} , and the bold face upper case letters are used for matrices, e.g. \mathbf{Z} .

Abbreviations and acronyms

AIRM	Affine Invariant Riemannian Metric
AR	Axial Ratio
BiTSVM	Bistatic Target Scattering Vector Model
BiRCS	Bistatic Radar Cross Section
BSA	Backscatter Alignment
CEM	Computational Electromagnetic
CP	Circular Polarization
dB	Decibel
CSA	Chinese Space Agency
CTD	Coherent Target Decomposition
DCT	Density Clustering Technique
DLR	German Aerospace Center (DE: Deutsches Zentrum für Luft-und Raumfahrt)
dual-pol	Dual Polarimetric
EM	Electromagnetic
EMAC	European Multi-sensor Airborne Campaign
EMISAR	ElectroMagnetic Institute Synthetic Aperture Radar
ESA	European Space Agency
full-pol	Full polarimetric / Quad polarimetric
FF	Form Factor
FIT	Finite Integration Technique
FSA	Forward Scattering Alignment
GLRT	Generalized Likelihood Ratio Test
H	(Linear) Horizontal Polarization Height of geometric object (evident from context, only in Chapter 2)
IES	Integral Equation Solver
ICA	Independent Component Analysis

ICTD	Incoherent Target Decomposition
IW	Interferometric Wide
HRWS	High Resolution Wide Swath
HPD	Hermitian Positive Definite
K-L	Kullback-Leibler
LH	Left-Handed
LHCP	Left-Handed Circular Polarization
LOS	Line of Sight
LP	Linear Polarization
MBET	Monostatic-to-Bistatic Equivalence Theorem
MIMO	Multiple Input Multiple Output
ML	Maximum Likelihood
MLFMM	Multilevel Fast Multipole Method
MLC	Multi-look Complex
MoM	Method of Moments
NNED	Nonnegative Eigenvalue Decomposition
NRF	Nonreciprocity factor
ONERA	The French Aerospace Lab (FR: Office National d'Etudes et de Recherches Aérospatiales)
PEC	Perfect Electrical Conductor
PM	Pursuit Monostatic
PDF	Probability Density Function
PO	Physical Optics
PolInSAR	Polarimetric Interferometric Synthetic Aperture Radar
PolSAR	Polarimetric Synthetic Aperture Radar
PRI	Pulse Repetition Interval
RCS	Radar Cross Section
RGB	Red-Green-Blue
RH	Right-Handed
RHCP	Right-Handed Circular Polarization

RR	Real Representation
RRSM	Real Representation Scattering Matrix
RS	Remote Sensing
RSO	Radar à Synthèse d'Ouverture
Rx	Receiver
SAR	Synthetic Aperture Radar
SCS	Scattering Cross Section
SIRV	Spherically Invariant Random Vector
SLC	Single-look Complex
SM	Scattering Matrix
SPD	Symmetric Positive Definite
SSVD	Symmetric Singular Value Decomposition
SVD	Singular Value Decomposition
TDS	Time Domain Solver (TDS)
TDX	TanDEM-X
TEM	Transverse Electromagnetic
Tg	Target
TomoSAR	Tomographic SAR
TSVM	Target Scattering Vector Model
TSX	TerraSAR-X
TUD	Technical University of Denmark
Tx	Transmitter
V	(Linear) Vertical Polarization
W	Width of geometric element
ψ-Ω-Φ-LS	ψ - Ω - Φ Lossless and Sufficient Target Vector Model

Introduction

Introduction and motivations

Remote sensing allows the detection and monitoring of an object's physical characteristics, at a distance. Microwave remote sensing is the branch which uses for this study electromagnetic signals belonging to the radar (or, microwave) frequency domain. It is further divided into active and passive sub-branches, depending whether the sensor carries, or not, its own signal source.

Active microwave remote sensing is nowadays a conventional technology in Earth observation applications, seen as a complement to the optical technology, e.g., due to its unrestricted imaging ability (day or night, all weather). The most popular radar remote sensing implementation is through the Synthetic Aperture Radar (SAR) technique. By combining several, adjacent, multi-angle observations, SAR has the ability to provide high-resolution (nowadays, even around tens of cm) image-like visualizations of an area's complex radar backscattering return.

SAR images have been collected on a global scale for several decades now. By combining sets of multiple observations of the same area, the primary form of diversity for all remote sensing applications is multi-temporal. With satellite instruments, the revisit time is periodic and the acquisitions are often termed multi-pass. Other forms of diversity are possible in microwave remote sensing: frequency, polarization and spatial (or, multi-platform) can be accessible when the radar sensor is equipped with specialized instrumentation.

The last decade has shown an increased interest towards multi-platform radar systems. Instrumental steps in this direction have been the launch in 2010 of the "twin" satellite to TerraSAR-X, TanDEM-X, along with the preparatory and in-orbit scientific studies it demanded. This has made a statement on the technological maturity and the possible advantages the multi-platform diversity can bring (e.g., the possibility of having multiple single-pass acquisitions from distinct spatial positions).

The polarization is a wave property defined in a plane transverse to the propagation direction. It is a research subject studied across disciplines and especially in domains involving electromagnetic radiation. The polarization may carry the signature of an absorption/scattering process, quantified through measurable changes in perpendicular directions of the transverse plane.

In radar polarimetry, the active instrument is the one fixing the polarization at emission, which will usually be modified by the interaction of the radiation with the Earth surface, measured at one or more frequencies. Polarimetric SAR (hereafter, PolSAR) offers access to a multidimensional, simultaneous set of measurements of the radiation reaching the sensor. Crop monitoring, land use/land cover classification, persistent scatterers detection in urban environment, or the study of glaciers and Arctic

ice are among its principal applications.

This thesis focuses on the study of polarimetric radar diversity with datasets obtained by acquisition in monostatic or bistatic geometry. New methods and algorithms for PolSAR processing (linear polarization) are proposed. These are developed around two working hypotheses, aiming to address current challenges in radar polarimetry, as follows.

- **Context:** Between the end of the 20th century and the beginning of the 21st century, polarimetric diversity was most often combined with multi-temporal or multi-frequency diversity to obtain composite data sets. Most of the PolSAR methods are based on the algebraic model of reciprocal data, meaning they have been developed and tested mainly using monostatic data.

Challenge: Due to the growing interest in bistatic/ multistatic radar platforms, it is expected that such PolSAR data will become accessible in the future (both as single acquisitions and in composite sets that will exploit the spatial diversity offered by multi-platform geometries).

Within the thesis: The polarimetric data should no longer be constrained by the monostatic reciprocity property.

- **Context:** The progressive decrease of the size of resolution cells in radar images has been achieved through technological and data processing developments. This steady improvement of the spatial resolution has made SAR images attractive in various practical applications and competitive with optical sensors.

Challenge: However, it has been shown that statistical model-based methods used in SAR/PolSAR need to be modified when working with high spatial resolution data and many models have been eventually proposed to accurately represent these statistics [1].

Within the thesis: The difficulty of choosing an optimal model could be solved by proposing techniques that do not rely solely on the statistical distribution of the data.

Thesis outline

This thesis focuses on developing new tools and methods for the understanding and the analysis of (linear polarization) full-polarimetric radar images. This subsection briefly outlines the composition of the thesis and presents the key topics covered in each of the following chapters. The contributions are intended to address some of the identified challenges.

Chapter 1 sets the main theoretical framework. For this, it introduces the elementary descriptors of wave polarization, compares the radar versus optical scattering alignment conventions and the matrix versus vector PolSAR formalism, which are at the core of most analysis methods for coherent and incoherent decompositions.

Chapter 2 develops from the following question: Which processing is adequate if one operates under the radar convention, i.e., Backscattering Alignment (BSA), adopts a matrix formalism computation and deals with radar observations which are not reciprocal (inherent property, not the result of measurement errors)?

A purely mathematical perspective is necessary at first. We introduce the conjugate similarity transformation (hereafter, consimilarity) and propose a solution based on the real representation. The results returned by this method are proven to match the ones from the non-negative factorization of the squared scattering matrix, only in the case when the matrix is reciprocal. The method revealed complex-valued solutions for the case of some non-reciprocal scattering matrices. The chapter then explores practical applications for the real representation, particularly through its eigen-decomposition. Monostatic and bistatic wide-angle polarimetric simulations of two coherent targets are obtained and investigated on the premise of pursuing a concrete link between scattering geometry, nonreciprocity and the complex eigenvalues.

Chapter 3 continues to explore applications under the PolSAR matrix formalism, but considers now an operation based on similarity, i.e., the polar decomposition. A geometric perspective is adopted in the chapter. The polar decomposition factors are seen not only as algebraic products, but using well-known results in information geometry, as matrix terms embedded into a manifold. Eventually, the method proposed in the chapter uses exclusively the Hermitian positive definite factor and operations onto its associated Riemannian manifold. When assuming the PolSAR vector formalism, the classical incoherent target decompositions (ICTDs) operate with the sample covariance matrix, which is generally estimated as a weighted sum of vector inner products. Differently, we propose to use the intrinsic geometric mean of Hermitian positive definite matrices, followed by a partitional clustering algorithm having a geodesic distance for intra/inter-cluster attribution.

Two particularly appealing properties are that the algorithm does not assume a statistical distribution of the data and does not modify, at any step, the algebraic and the geometric matrix structure. Qualitative and quantitative tests are performed using real and simulated monostatic datasets. Despite this choice, the technique could be applied to the most general type of polarimetric diversity, i.e., bistatic full-polarimetric.

The **last chapter** provides an overall focus on the thesis' contributions and proposes an outlook on future work.

To improve readability, retain the focus of the main chapters on personal contributions, but still provide extensive clarifications where needed, proofs and other extra material are transferred to **Annexes B-H**. The real datasets used by the thesis are airborne, with medium-high (as of current technological level) spatial resolution (i.e., $\sim 1\text{m}$). All details are provided in Annex A.

Contributions into peer-reviewed publications and conferences during the time-frame of this thesis are listed in **Section I**.

Polarimetric Radar Diversity

All the diversity, all the charm, and all the beauty of life are made up of light and shade.

Lev Tolstoy

Contents

1.1 Polarization of electromagnetic waves	6
1.1.1 Plane wave model	6
1.1.2 Jones vector and polarization ellipse	7
1.1.3 Radar polarization imaging modes	10
1.2 Imaging radar	10
1.2.1 Monostatic geometry - Synthetic Aperture Radar	11
1.2.2 Bistatic geometry	13
1.2.3 Bistatic polarimetric diversity	16
1.3 Scattering matrix	17
1.3.1 Forward Scattering Alignment (FSA) and Backscattering (BSA)	18
1.3.2 The monostatic simplification	19
1.3.3 Similarity and conjugate similarity transformations	20
1.4 Coherent decompositions	25
1.4.1 Summation decompositions	26
1.4.2 Multiplicative decompositions	27
1.4.3 Target scattering vector	29
1.5 Incoherent decompositions	30
1.5.1 Entropy-alpha decomposition (monostatic/bistatic, quad-pol/dual-pol)	33
1.5.2 Application: Dual-polarimetric bistatic and monostatic VV-HV H-alpha classification	35
1.6 Conclusions	43

From simple scattering mechanism extraction and throughout more complex applications (e.g., land classification, disaster monitoring, height estimation), polarimetry has become a key element for remote sensing. It allows to obtain new and improved characteristics of a scattering object under investigation.

This chapter provides a short theoretical background to the domain of radar polarimetry, with a selection of thesis-relevant elements. The presentation is more general in Section 1.1 and Section 1.2, which focus on introductory notions of wave polarization, the imaging radar and the latest technological advancements in bistatic imaging radars.

Following up, Section 1.3 discusses the algebra of polarimetric radar transformations and its particularities when analyzing both monostatic and bistatic data. Sections 1.4 and 1.5 describe decomposition methods for Polarimetric SAR PolSAR data analysis for both deterministic (e.g., man-made targets with a stable scattering mechanism) and nondeterministic targets. The thesis concentrates on techniques which can be applied to both monostatic and bistatic data. We generally assume complete polarimetric diversity (i.e., full-polarimetric data). Nonetheless, the end of the current chapter provides a comparative analysis on a set of dual-polarimetric monostatic-bistatic measurements.

1.1 Polarization of electromagnetic waves

A radar (acronym: Radio Detection and Ranging) is an active instrument which allow coherent transmission and reception of electromagnetic (EM) signals. Radar instruments operate with signals in the electromagnetic spectrum which typically belong to the Microwave Band (300 MHz - 300 GHz).

The polarimetric radar recovers the simultaneous projections on orthogonal polarimetric bases, while a non-polarimetric system measures only one of the possible projections. The IEEE Standard Definitions for Antennas (Nr. 145, 2013) [2] distinguishes between the polarization of a vector field/wave and that of an antenna.

1.1.1 Plane wave model

Throughout the thesis, one or multiple assumptions fixing the theoretical context are introduced in each chapter. Generic or specific, they are the axioms on which the models and experiments adopted in the manuscript are build. The gain in providing this concise indexing is double-folded: limitations imposed alongside the assumptions are easily uncovered and the reader can gain a rapid overview of the models. For a generic plane wave, these are as follows:

Assumptions Set - 1.1.

- I. The plane wave solution of the electromagnetic waves equations is sufficient in describing the propagation of the radar signals.
- II. The signal is monochromatic and has a small bandwidth relative to the working frequency, f .
- III. The electric and magnetic field components are transverse to the direction of propagation (i.e., Transverse Electromagnetic (TEM) propagation mode). In far field, at any (time/space) instant, the two lie inside the 2D plane perpendicular to the wave vector's direction.

Hypothesis 1.1.I. is a reliable approximation for far-field observations of radar instruments, which is the broad case of operation for imaging radars. Due to the duality of electric and magnetic fields, describing the solution for only one of the fields is sufficient. The connection between the two fields is complete considering the impedance of the propagating medium.

The polarization of a wave is generally defined by the oscillation direction of the electric field components in the transverse plane. It is often understood as the figure "that the extremity of a (specified) vector field draws as a function of time". Otherwise, the polarization of an antenna is "that of the plane wave it radiates at large distances in a given direction" [3, 2].

The plane wave solution for the electric field is [4]:

$$\mathbf{E}_{\mathcal{R}}(\mathbf{r}, t) = \mathbf{E}_0 \cos(\mathbf{k} \cdot \mathbf{r} - \omega \cdot t + \phi_0), \quad (1.1)$$

where \mathbf{E}_0 and ϕ_0 are the initial constant amplitude and phase vectors, respectively. Further, $\omega = 2\pi f$ denotes the angular frequency while \mathbf{k} is the wave vector (modulus, $|\mathbf{k}| = 2\pi/\lambda$, dependent on the wavelength, λ).

Eq. (1.1) is alternatively written [4]:

$$\mathbf{E}_{\mathcal{R}}(\mathbf{r}, t) = \mathcal{R}\{\mathbf{E}(\mathbf{r}) \cdot e^{j\omega t}\}, \quad (1.2)$$

with $j = \sqrt{-1}$ as the imaginary unit and $\mathbf{E}(\mathbf{r})$ the complex, time-independent, electric field phasor.

In the Cartesian plane (x, y, z), the propagation direction of the wave is generally chosen to coincide with the z-axis. In an observation plane z_0 , considered at the origin O of the coordinate system, the time-varying projections of the complex electric field in orthogonal basis aligned with the axes of the coordinate system is:

$$\mathbf{E}(z_0, t) = \begin{bmatrix} E_x(z_0, t) \\ E_y(z_0, t) \\ E_z(z_0, t) \end{bmatrix} = \begin{bmatrix} E_{0x} \cdot e^{-j(kz_0 - \omega t - \phi_x)} \\ E_{0y} \cdot e^{-j(kz_0 - \omega t - \phi_y)} \\ 0 \end{bmatrix}. \quad (1.3)$$

Given the transverse nature of the propagating wave, the electric field component in the z direction is zero. Parameters ϕ_x and ϕ_y represent the absolute phase values of the electric field's x and y projections.

1.1.2 Jones vector and polarization ellipse

For characterizing the complex amplitudes of the electric field components in the transverse plane, the formalism of the Jones vector is used. This is described as:

$$\mathbf{E}_{\mathbb{J}} = \begin{bmatrix} E_x \\ E_y \end{bmatrix} = \begin{bmatrix} E_{0x} \cdot e^{j\phi_x} \\ E_{0y} \cdot e^{j\phi_y} \end{bmatrix}. \quad (1.4)$$

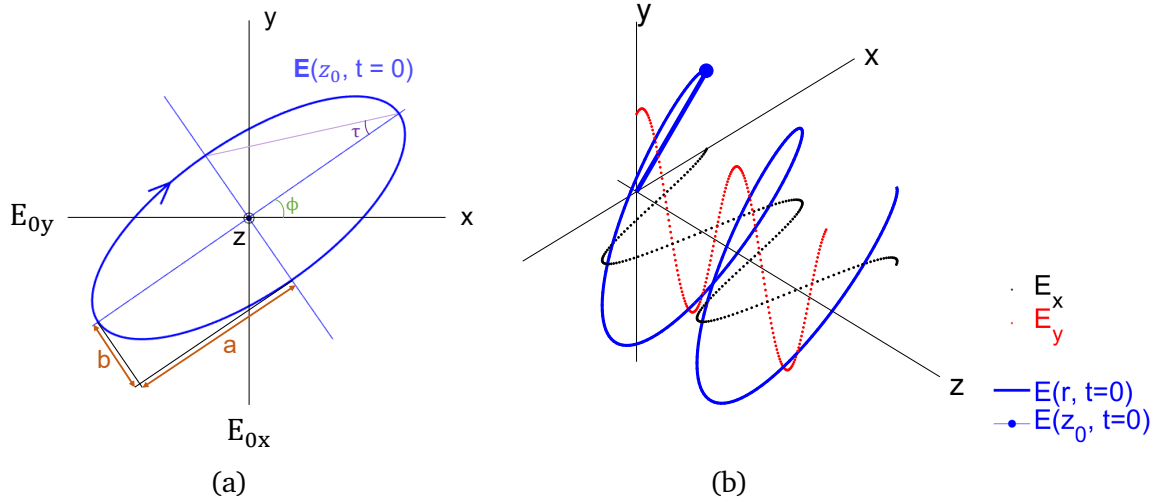


Figure 1.1: Elliptical polarization. (a) Polarization ellipse with descriptive parameters. (b) Electric field evolution for Jones vector $\mathbf{E}_J = [2.7-1j; 2+1j]$ (obtained using the Matlab Phased Array System Toolbox.)

The complex polarization wave ratio is the fraction between the two elements from the Jones vector:

$$\rho_E = \frac{E_y}{E_x} = \frac{E_{0y}}{E_{0x}} \cdot e^{j\delta_{\phi_{yx}}} = \tan\alpha_{\rho_E} \cdot e^{j\delta_{\phi_{yx}}} \quad (1.5)$$

We consider the Jones vector to completely characterize the polarization state of the electric field in the transverse plane, for a fixed position in time (t) and space (z). For situations in which TEM is no longer a correct approximation of the propagation mode, the formalism is extended to a 3×1 generalized Jones vector [5]. However, in the current thesis, the case of 2×1 dimensional Jones vector is considered, exclusively.

The curve drawn by the tip of the electric field vector in all transverse planes aligned on the propagation direction describes the polarization of the plane wave. When the oscillation is random from one transverse plane to the other, the electric field may be partially polarized or unpolarized [6]. In the most general case of polarized waves, the locus of points takes the form of an ellipse (Fig. 1.1). Proposing such a shape is not aleatory, as it can be shown that the amplitudes of the electric field components in the transverse plane and their relative phase difference ($\delta_{\phi_{yx}} = \phi_y - \phi_x$) verify the equation of a (rotated) ellipse [7]:

$$\frac{1}{\sin^2(\delta_{\phi_{yx}})} \left[\frac{E_x^2}{E_{0x}^2} - 2 \cdot \frac{E_x}{E_{0x}} \frac{E_y}{E_{0y}} \cos(\delta_{\phi_{yx}}) + \frac{E_y^2}{E_{0y}^2} \right] = 1. \quad (1.6)$$

A change in the locus of points depends on both amplitude of components from the two orthogonal directions (here, E_{0x} and E_{0y}), and relative phase difference, $\delta_{\phi_{yx}}$. As a result, the standards quantitatively define the polarization by the shape (i.e., axial ratio), orientation and sense of the polarization ellipse [2]. Each of these characteristics is individually analysed hereafter:

- **orientation:** We consider an unoriented ellipse (a —semi-major axis, b —semi-minor axis), in reference coordinates X-Y: $\frac{X^2}{a^2} + \frac{Y^2}{b^2} = 1$. The transformation to rotated coordinates U-V via an angle ϕ is equivalent to the algebraic multiplication:

$$\begin{bmatrix} U \\ V \end{bmatrix} = [X \quad Y] \begin{bmatrix} \cos\phi & \sin\phi \\ -\sin\phi & \cos\phi \end{bmatrix} = [X\cos\phi - Y\sin\phi \quad X\sin\phi + Y\cos\phi] \quad (1.7)$$

The rotated ellipse is now described by [8]:

$$\frac{(X\cos\phi - Y\sin\phi)^2}{a^2} + \frac{(X\sin\phi + Y\cos\phi)^2}{b^2} = 1 \quad (1.8)$$

Using equivalence of terms from (1.6) and (1.8), the rotation angle is determined as:

$$\tan\phi = 2 \frac{E_{0x}E_{0y}}{E_{0x}^2 - E_{0y}^2} \cos(\delta\phi_{yx}) \quad \xrightarrow{(1.5)} \quad \tan\phi = \tan(2\alpha_{\rho_{\mathbf{E}}}) \cos(\delta\phi_{yx}). \quad (1.9)$$

- **axial ratio (AR):** It is a real number, obtained as the ratio between the semi-major and semi-minor axes of the ellipse. This quantity is directly related to the ellipticity (or tilt) angle, $\tau \in [-\pi/4, \pi/4]$, as:

$$\tau = \arctan\left(\frac{b}{a}\right). \quad (1.10)$$

Then,

$$\sin 2\tau = \sin(2\alpha_{\rho_{\mathbf{E}}}) \sin\delta\phi_{yx}. \quad (1.11)$$

- **sense:** The sense of the rotating ellipse can be either right-handed (RH) or left-handed (LH) as the wave is observed to progress clockwise or counter-clockwise, in the propagation direction. The sign of the ellipticity parameter describes this "handedness" property of the ellipse: negative sign for the clockwise rotation and positive sign for the counter-clockwise.

For the general case, of elliptical polarization, no constraints are imposed on the set of parameters (E_{0x} , E_{0y} , $\delta\phi_{yx}$). Alternatively, oscillations under the shape of a circle or line are (constrained/degenerate) cases which are preferred in practical applications [9]:

- **circular polarization (CP):** The two components are of equal amplitude $E_0 = E_{0x} = E_{0y}$ and have a phase difference $\delta\phi_{yx} = m\frac{\pi}{2}$, $m \in \{\pm 1, \pm 3, \pm 5, \dots\}$. Depending on the sign of the phase difference, it is possible to separate between right-handed RHCP and left-handed LHCP circular polarization.
- **linear polarization (LP):** The two components are in phase or opposition of phase, $\delta\phi_{yx} = m\pi$, $m \in \{0, \pm 1, \pm 2, \dots\}$.

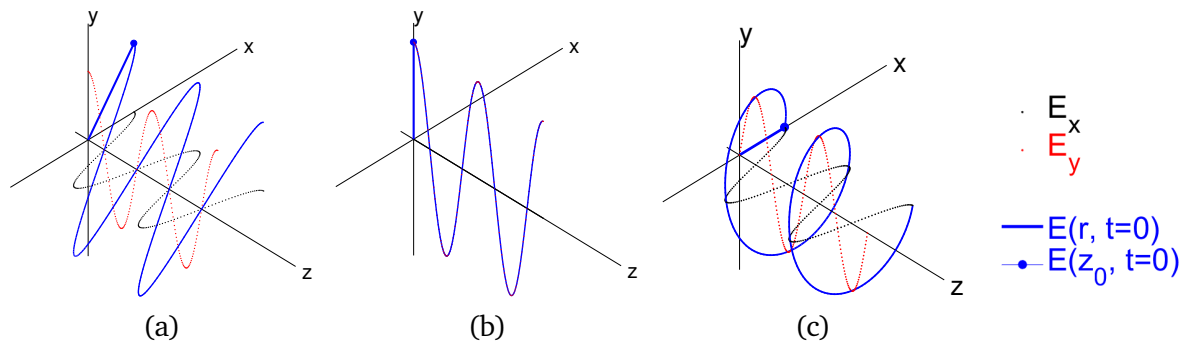


Figure 1.2: Linear and circular polarization. (a) 45° Linear Polarization. (b) Vertical Polarization (V). (c) Circular Polarization. (obtained using Matlab Phased Array System Toolbox™).

1.1.3 Radar polarization imaging modes

The basic imaging radar transmits and receives electromagnetic radiation in only one polarization. Whichever the acquisition geometry, a polarimetric imaging radar is equipped to allow partial or full polarimetric diversity. Obtaining a minimum configuration (i.e., partial diversity) requires that the receiving unit of the instrument is capable to coherently measure the electric field components in two orthogonal bases. This is the case of dual-polarimetric (dual-pol) acquisitions. With fully polarimetric (full-pol or quad-pol) instruments, the transmission is itself possible in two polarimetric bases. The classification of imaging modes can be performed under these main categories, considering: a) the polarimetric coherence and b) the polarimetric transmitter (Tx) - receiver (Rx) basis combinations:

- **Basis combinations:** When the polarimetric basis used with the transmitter and receiver are not identical, the configuration is called hybrid [10]. This has been tested in applications having partial diversity. One such example is the use of CP for transmitting and orthogonal LPs for receiving. With full-pol instruments, the Tx and Rx polarimetric basis is usually the same.
- **Coherence:** When the coherence of the receiving channels is not preserved, a significant part of the polarimetric information is lost. This has been reported only as a distinct subgroup of dual-polarimetry [9].

1.2 Imaging radar

This subsection introduces elementary definitions related to the synthetic aperture radar, the monostatic and bistatic geometries, spatial azimuth and range resolutions, etc. The concepts will be used throughout the entire manuscript.

The conventional *imaging radar* assumes a monostatic geometry in which the transmitting and receiving units are co-located (Fig. 1.3, blue dotted box). Imaging radars operate in mainly three configurations: spaceborne, airborne, and ground-based.

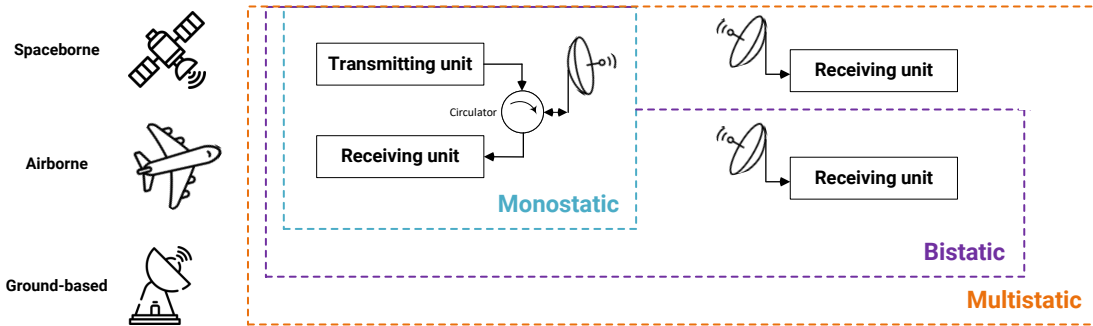


Figure 1.3: Monostatic, bistatic and multistatic radar systems.

The main remote sensing radar imaging technology in use is that of Synthetic Aperture Radar (SAR) [11]. The two directions of a radar image are the *slant-range* (i.e., the radar Line of Sight (LOS) direction, connecting instrument and target, also known as cross-track) and the *azimuth* (or along-track). SAR is a type of pulsed, side-looking radar, in which the instrument is located on a platform moving in the azimuth direction. One land area is observed from multiple adjacent positions in azimuth and the stack of backscattered responses is used into constructing the SAR image. Elementary parameters of a SAR system are: the imaging frequency, the signal's bandwidth and pulse width, the Pulse Repetition Interval (PRI), etc.

The *resolution* of a radar image is an important performance indicator in both spatial and radiometric domains. The minimum amount of separation (measured in units of distance) which can exist between two targets along each imaging direction, so that they are completely separated, is known as (range/azimuth) *spatial resolution*. On the other hand, the *radiometric resolution* is the minimum brightness contrast for which two equally reflective targets are discriminated.

The discussion on monostatic SAR systems shortly follows in Subsection 1.2.1. The bistatic/multistatic systems propose more complex imaging geometries, which integrate physically-separated, synchronized-operating transmitter(s) and receiver(s). Subsection 1.2.2 covers this type of diversity.

1.2.1 Monostatic geometry - Synthetic Aperture Radar

Fig. 1.4 shows the example of a spaceborne, monostatic SAR system imaging an area on the surface of the Earth (swath). At one time instant, R_1 and R_2 are the extreme slant ranges (i.e., the near and far-range) and delimit the extremities of a swath (yellow ellipse). The look angle varies across the swath in an interval $[\theta_{iNR}, \theta_{iFR}]$. This imaging mode is known as Stripmap [12] and is the general model used in textbooks for derivation of resolution formulas. More advanced beam-modes, which have the advantage of enhanced azimuth resolution, are Spotlight and ScanSAR.

Complementary to the radar slant-range, the radar image may be projected into a

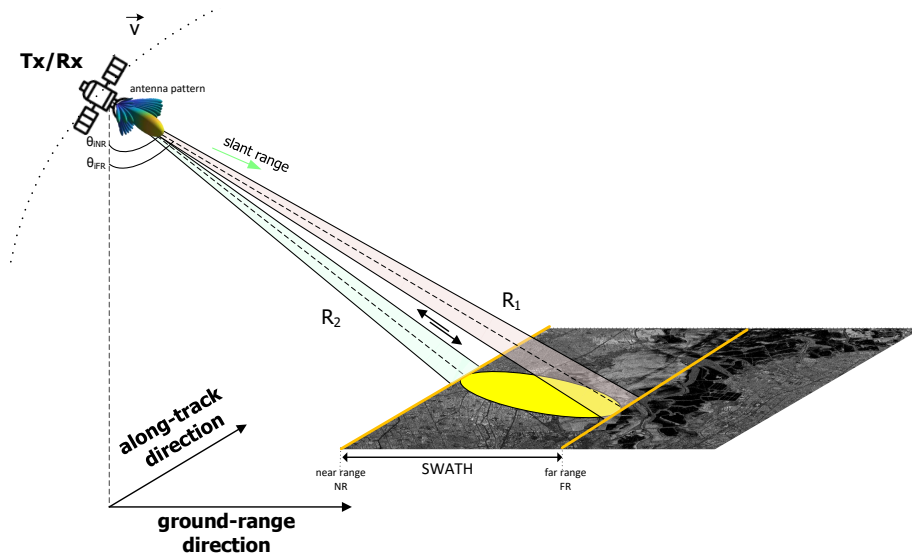


Figure 1.4: Spaceborne monostatic imaging radar.

reference surface (horizontally flat or in accordance to the Earth ellipsoid irregularities). This is now called the *ground-range* and it offers the advantage of having a common, georeferenced coordinate system between multiple acquisitions.

The emitted SAR electromagnetic chirps use a pulse compression technique, a type of signal modulation which allows an optimum counterbalance between peak transmitted power and enhancement of slant range resolution. For a real aperture radar, the azimuth resolution depends on frequency, incidence angle and the exact dimensions of the system's antenna. The SAR technology allows to improve the resolution in azimuth by using coherent signal processing of the backscattered echoes across the integration time of the synthetic aperture. In both range and azimuth, the final SAR resolution is independent on the distance between the monostatic radar instrument and the target.

Combining such performance characteristics with the ability to image the Earth's surface day and night, even under fog and clouds, has greatly increased the popularity of SAR. Nowadays, among the world's Space Agencies there are over 30 years of almost continuous spaceborne SAR remote sensing monitoring expertise [11].

When speaking of SAR image processing, both image formation and image analysis chains come to mind. The image formation comprises the range and azimuth compression [12] as well as geometric (i.e., layover, foreshortening) and radiometric distortions compensation. A 2D grid of range-azimuth cells (i.e., pixels) renders a SAR image. It is usually distributed in the form of a complex image (Single-look complex - SLC or Multi-look complex - MLC) which preserves both amplitude and phase at each pixel. Alternatively, only the amplitude or intensity (i.e., power) values are sometimes available. The value associated to a pixel is dimensionless and a function of the radar reflectivity, referred to as the backscattering coefficient. The pixel's intensity is known to be proportional to the equivalent radar cross section [13]. This measurement information is transformed by image analysis into qualitative and quantitative

observables. In the current thesis, the focus is exclusively on image analysis, performed from a polarimetric diversity perspective. SAR images are essentially scattering maps obtained for the radar's operative microwave frequency band and full-polarimetric measurements allow the complete backscattering description for the transverse electric field. Moreover, the aim of the thesis is towards developing and testing methods adapted also in bistatic polarimetry and capable to characterize its scattering information.

1.2.2 Bistatic geometry

In a *bistatic system*, the Tx and Rx units are at different locations and have a considerable separation (i.e., a large baseline). If the emitter and receiver are only separate hardware equipment, but placed in near proximity, the geometry is known as *quasi-monostatic* (i.e., nearly monostatic). As long as the synchronization between the two units is maintained, they can be carried out on the same or different platforms. However, assuring a proper (phase/frequency) synchronization of local oscillators between separate units has long been an important setback for the actual development of bistatic systems. In [14], a comprehensive review of the history and developments of bistatic radar systems from their beginning in the XX century and until around the first decade of the XXI century is offered. In depth analysis of the more latter period and some additional bistatic experiments are covered in [15].

Multistatic systems are an extension of the bistatic ones, possessing an increased transmitting/receiving diversity (at least two transmitting/receiving units, placed at different positions).

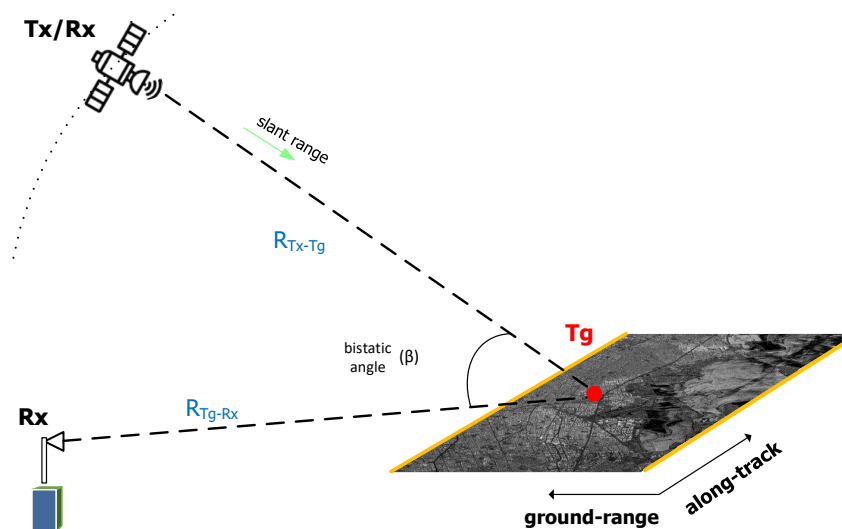


Figure 1.5: Spaceborne to ground-based bistatic radar.

The bistatic geometry most similar to monostatic is one in which the transmitter and receiver are placed in the same plane at a similar height and if in movement, their velocities are comparable. A bistatic geometry presents a higher number of degrees of liberty, compared to monostatic. Apart from geometry, the technological choices contribute to

the complete description of the system. For example, two possible alternatives are the use of passive or active receiving unit(s). An active receiver may act as an individual monostatic system, alternating between transmission and reception. Another type of active receiver can operate as a transponder, broadcasting the acquired signals to another node of the bistatic/multistatic architecture [16]. When it comes to ease of deployment, however, the passive receiver is the far more preferred type. Fig. 1.5 presents, as example, a space-surface bistatic geometry with an opportunistic satellite transmitter and a ground-based passive receiver. The bistatic range is the sum of two slant-ranges, $R_{Tx-Tg} + R_{Tg-Rx}$. The baseline is the direct LOS between transmitter of opportunity and receiver and the bistatic angle (β) is its opposing angle in the Tx-Tg-Rx triangle.

Table 1.1: Extensive list of full-polarimetric bistatic missions, platforms and experiments.
 Acronyms: *spaceb* = spaceborne, *airb* = airborne, *groundb* = ground-based, *acq.* = acquisition.

Bistatic config.	Ref.	Acq. Year	Tx System (Institution, Country)	Rx System (Institution, Country)	Acq. Band
<i>Geometries capable of large bistatic angles ($\beta > 10^\circ$):</i>					
spaceb-airb	[17, 18]	2011	TerraSAR-X (DLR, Germany)	F-SAR (DLR, Germany)	X
spaceb-groundb	[19, 20]	2009	TerraSAR-X (DLR, Germany)	Hitchhiker (University of Siegen, Germany)	X
	[21]	2019	ASTRA 1KR, DVB-Satellite(2) (SES Astra, Luxembourg)	SABBIA (Fraunhofer FHR, Germany)	Ku
airb-groundb	[22, 23]	2007 2017	Ingara (Australian Defence Science and Technology Organisation)	passive Rx (Australian DSTO)	X L
groundb-groundb	[24]	2010	TARA (Technical University of Delft)	PARSAX (TU Delft, Holland)	S
<i>Geometries with smaller bistatic angles ($\beta \leq 10^\circ$):</i>					
airb-airb	[25, 26, 27]	2018	BelSAR (MetaSensing, Belgium)	BelSAR (MetaSensing, Belgium)	L
<i>Quasi-monostatic:</i>					
spaceb-spaceb	[28]	2010 - ongoing	TerraSAR-X (DLR, Germany)	TanDEM-X (DLR, Germany)	X
	[29, 30, 31]	2022 - ongoing	LuTan-1A (Chinese Space Agency, China)	LuTan-1B (Chinese Space Agency, China)	L
airb-airb	[32, 33]	2017, 2021	N-SAR & N-SAR-SG (Nanjing Research Institute, China)	N-SAR & N-SAR-SG (Nanjing Research Institute, China)	L, P, X, Ku
groundb-groundb	[34]	2018	Tx unit (Tohokun University, China)	OEFS-Rx (Tohokun University, China)	C
	[35, 36, 37]	2020	KAPRI-Tx (GAMMA Remote Sensing, Switzerland)	KAPRI-Rx (GAMMA Remote Sensing, Switzerland)	Ku

1.2.3 Bistatic polarimetric diversity

Table 1.1 contains a list of bistatic full-polarimetric experiments extracted from literature. They are grouped by the location of transmitter and receiver and the bistatic angle (as specified directly in each resource or indirectly, by mentioning slant range and baseline). A threshold value of $\beta = 10^\circ$ for separating between classes with larger and smaller bistatic angles is considered. Nonetheless, there is no consensus in the literature regarding an exact threshold value for β .

The TerraSAR-X (TSX) / TanDEM-X (TDX) couple has played a pioneering role in the spaceborne area. It essentially features a quasi-monostatic implementation with bistatic angles smaller than 1° across an acquisition. The low separation between the two satellites has been imposed by the mission's main objective, as the couple forms a one-pass interferometer. Full-polarimetric bistatic acquisitions performed in a second phase of the missions have allowed a larger across-track baseline separation, of around 70 km (i.e., in the Pursuit Monostatic (PM) working mode) [38]. From early 2022, another similar quasi-monostatic PolInSAR mission has been launched by the Chinese Space Agency [39]. The LuTan-1 (LT-1) comprises two identical satellites carrying full-pol SAR instruments [31].

Three other spaceborne-spaceborne bistatic/multistatic SAR platforms are to be launched before 2030. While two of the projects will continue the legacy of quasi-monostatic implementations, one will provide observations from a truly bistatic configuration (with expected bistatic angles larger than 20°). The instruments will also include some type of polarimetric diversity: full-pol capabilities for the quasi-monostatic geometries and dual-pol for the bistatic mission. The main characteristics of the future bistatic missions are presented in Table 1.2. These examples indicate the current phase of technological advancements in microwave remote sensing. As so, it is now possible to combine bistatic and polarimetric diversities, even for spaceborne-spaceborne implementations. The thesis aims to aligns with modern interests in bistatic radar polarimetry.

Table 1.2: Future spaceborne-spaceborne missions to combine bistatic and polarimetric diversities.

Name	Ref.	Acq. Band	Inst.	Mission and system description
<i>Large bistatic angles:</i>				
Harmony	[40, 41]	C-Band	ESA	<ul style="list-style-type: none"> • one Sentinel-1 satellite as opportunistic Tx; • two passive payloads as bistatic Rxs (250 km along-track between Tx and each Rx); • dual-polarimetric diversity; • estimated launch: 2029.
<i>Quasi-monostatic:</i>				
Tandem-L	[42]	L-Band	DLR	<ul style="list-style-type: none"> • two SAR sensors with configurable formation flying; • tests new advancements in antenna and feeding design; • dual/full-polarimetric diversity; • estimated launch: 2025.
High Resolution Wide Swath (HRWS)	[43, 44]	X-Band	DLR	<ul style="list-style-type: none"> • follow-up mission of TanDEM-X. • one opportunistic monostatic Tx; • three passive transponder Rx companions (MirrorSAR concept [45]); • Rxs provide a single-pass multibaseline interferometric capability; • dual/full-polarimetric diversity; • estimated launch: 2027.

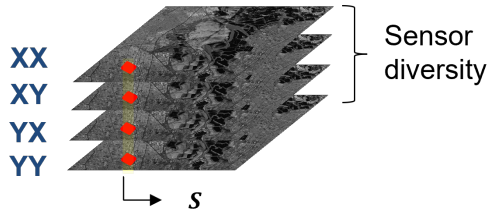
1.3 Scattering matrix

For any target illuminated inside the radar swath, a target is known to behave as a polarization state modifier [46]:

Assumptions Set - 1.2.

- I. The transformation of the incident electric field (E_i) into the scattered electric field (E_s) is a linear operation.

Given a generic (i.e., unspecified X-Y) set of polarization bases, the change between components of the incidence and scattering fields is performed through the scattering matrix, $S \in \mathbb{C}^{2 \times 2}$:



$$\begin{bmatrix} E_s^X \\ E_s^Y \end{bmatrix} = \begin{bmatrix} S_{xx} & S_{xy} \\ S_{yx} & S_{yy} \end{bmatrix} \begin{bmatrix} E_i^X \\ E_i^Y \end{bmatrix}. \quad (1.12)$$

Figure 1.6: Full-polarimetric radar observations.

For an element S_{xy} of the matrix, X represents the receiving polarization and Y is the transmitting one. When having a double index (S_{xx} or S_{yy}), the element is known as co-polar, while otherwise as cross-polar. The Tx and Rx instruments can be manufactured to use basis combinations different from linear (e.g., circular, hybrid), case in which the scattering matrix will be expressed accordingly. Nowadays, the complex elements of S represent the primary measurement output of a polarimetric system. The total power (or span) of a generic scattering matrix is ¹

$$\|S\|_F^2 = |S_{xx}|^2 + |S_{xy}|^2 + |S_{yx}|^2 + |S_{yy}|^2. \quad (1.13)$$

Targets are broadly described by having either a deterministic or a nondeterministic scattering response. A *deterministic target* has a polarization response stable in both space and time, which is completely characterized by a scattering matrix. It is equivalently called a single scatterer. Alternatively, the scattering response for a *nondeterministic target* does not remain stable and is modelled by using stochastic processes. The literature resources use the nomenclature of *partial/distributed target* (physically, the scatterer has dimensions which span multiple resolution cells), as well as that of *depolarizing target* ([47], Table 1 in [48]).

¹Frobenius norm: $\|A\|_F = \left(\sum_{i,j=1}^n |a_{ij}|^2 \right)^{1/2}$

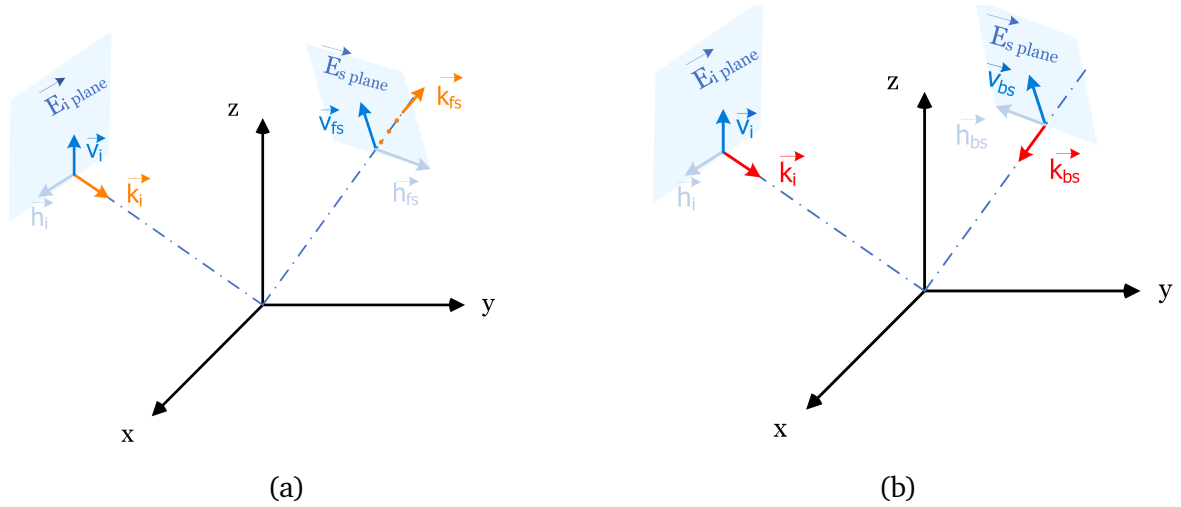


Figure 1.7: Scattering alignment conventions. (a) Forward Scattering Alignment. (b) Backscatter Alignment.

With fully polarimetric measurements, the complete 2×2 complex matrix is obtained at each pixel. With dual-pol acquisitions, the equipment can measure only one column or the diagonal elements of the matrix. As so, full-polarimetric data has a diversity order equal to 4, while this is equal to 2 for dual-pol diversity.

The study of transformations undergone by this matrix and its ability in distinguishing between different type of scattering processes is at the core of the current thesis.

1.3.1 Forward Scattering Alignment (FSA) and Backscattering (BSA)

Valid in all domains using wave polarization, (1.12) expresses the connection between the two Jones vectors of the incident and scattered waves, $\mathbf{E}_{\mathbb{J}_i}$ and $\mathbf{E}_{\mathbb{J}_s}$. For example, this is especially relevant for optical polarimetry or other domains for which the polarization is exclusively *wave-oriented* (i.e., it is a property of only the incoming electromagnetic signal, measured by a passive system). In this domain, the standard alignment of incident and scattered wave vectors with respect to a target located at the origin of an $x-y-z$ coordinate system is as shown in Fig. 1.7(a). It is known as the Forward Scattering Alignment (FSA). The scattering matrix is known as the Jones matrix.

However, in radar polarimetry the polarization is a property of both the incoming electromagnetic signal and of the active device which emits the radar signal and performs measurements. As suggested by the IEEE Antenna Standards, the polarization of an antennas is that of the wave it radiates, which implies that in the receiving case, the "coordinate systems used to describe the polarization of the antenna and the incoming wave are oriented in opposite directions" [2]. As so, there is a second convention in radar, known as the Backscatter Alignment (BSA) [4], referred to as the *antenna-oriented* convention. Fig. 1.7 compares the FSA and BSA geometric representations, with linear vertical (V) and horizontal (H) polarimetric bases. The

incident direction of the incoming plane wave is given by \hat{k}_i and the scattering directions are \hat{k}_{fs} or \hat{k}_{bs} for forward scattering and backscattering, respectively.

Versors \hat{v} and \hat{h} are the unit polarization vectors for the V and H components. When the BSA convention is used, the scattering matrix is called the Sinclair matrix. In the framework of this convention, compared to the optical one, the scattered versor is geometrically oriented as from the antenna to the target, i.e., a reversal of 180° from the general right-handed FSA convention. A simple mathematical connection has been established between the Jones and Sinclair matrices, but it was recently shown to be valid only under linear H-V polarization [49].

1.3.2 The monostatic simplification

Using the BSA antenna-oriented polarimetric base definition in both emission and reception conserves the symmetry of the measurement system.

In the monostatic case, the propagation LOS distance is the same between Tx and Rx. With the same polarimetric base definition in both emission and reception and under Assumption 1.2.I (which unless otherwise stated is implicitly considered in PolSAR), the two cross-polar components of the scattering matrix are equal (for example, $S_{vh} = S_{hv}$ in linear polarization). This is known as the PolSAR reciprocity theorem. The resulting 2×2 scattering matrix is mathematically complex symmetric, $S = S^T$. In this context, the preferred term in radar for 'symmetric' is 'reciprocal', in direct resemblance to the microwave's domain network theory. As a result, when referring to the scattering matrix, these two terms will be used interchangeably in the current thesis.

The reciprocity property provides important algebraic simplifications, which will be discussed through the manuscript. Because of this, the monostatic radar scattering matrix is exclusively described through the BSA geometric convention and the reciprocity is generally assumed. In order to avoid any exceptions from reciprocity, some monostatic applications perform as preprocessing step the symmetrization of the scattering matrix [50, 51, 52]. In other applications, obtaining the symmetric scattering matrices of elementary targets or natural media [53] from nonreciprocal, usually noise corrupted, measurements serves as a calibration procedure.

With data free of calibration errors, the monostatic reciprocity is still based on a set of assumptions, to be collectively met, regarding the: (a) geometry of the radar system (i.e., equality of propagation paths for the EM waves between Tx-Tg and Tg-Rx), (b) isotropic properties of propagation medium, (c) nature of target, (d) use of BSA convention. Under monostatic geometries, the scattering matrix may no longer verify reciprocity for example with:

- special ionospheric conditions which introduce noticeable Faraday rotations for satellite PolSAR acquisitions [54];
- targets of nonreciprocal materials (e.g., magnetized plasma, ferrite materials). This is however a rare case, different from that of most geophysical elements from inside a scene [53].
- use of FSA wave-oriented convention.

Finally, the reciprocity is no longer claimed for bistatic acquisitions. In this case, both BSA and FSA conventions can be used. One may claim that using the BSA in both monostatic and bistatic is the natural decision, providing this way a common reference framework for the radar domain. Difficulties arise however with respect to the mathematical apparatus needed for consimilarity transformations of non-reciprocal scattering matrices. This has been a topic so far not covered in PolSAR and to which the current thesis provides contribution. The algebraic framework presentation starts in Subsection 1.3.3. Chapter 2 will provide a close-up investigation into the matter.

Henceforth, $(\cdot)^T$, $(\cdot)^*$ and $(\cdot)^H$ are the transpose, complex-conjugate and complex-conjugate transpose operators.

1.3.3 Similarity and conjugate similarity transformations

Under the BSA convention of the radar domain, the scattered wave vector is represented in the coordinate system with an opposite orientation (i.e., from the receiving element to the target, Subsection 1.3.1) [4]. As the vector on the receiving path is reversed in direction, this will mathematically be modeled by a conjugation operation. Given a Jones vector propagating in the $\hat{\mathbf{k}}$ direction, the relation with the Jones vector of the wave having identical polarization and propagating in the opposite direction $-\hat{\mathbf{k}}$ is [9]:

$$\mathbf{E}_{\mathbb{J}_+} = \mathbf{E}_{\mathbb{J}_-}^* . \quad (1.14)$$

In this regard, the basis change relations of the two conventions (BSA vs. FSA) are quite different [55, 56]. This is generally presented as the contrasting example between Radar Polarimetry (under BSA) and Optical Polarimetry [48]. While the latter operates with similarity transformations performed on the Jones matrix, the former operates with conjugate similarity transformations performed on the Sinclair matrix.

Before moving further, a short description and comparison of the two mathematical operations is necessary.

Between three complex matrices $\mathbf{A}, \mathbf{B}, \mathbf{C} \in \mathbb{C}^{n \times n}$, two types of equivalent relations are possible, the *similarity* and *conjugate similarity*, as defined in Table 1.3. Matrices \mathbf{V} and $\mathbf{X} \in \mathbb{C}^{n \times n}$ are referred as the similarity and consimilarity transformation matrices. However, using a real matrix $\mathbf{X} \in \mathbb{R}^{n \times n}$ (e.g., an orthogonal rotation matrix), the consimilarity operation changes into a similarity one.

Table 1.3: General equations of similarity and consimilarity.

similarity	con(jugate) similarity
$\mathbf{A}\mathbf{V} = \mathbf{V}\mathbf{B}$	$\mathbf{A}\mathbf{X} = \mathbf{X}^*\mathbf{C}$

A proper choice of transformation matrices may allow for the diagonalization under similarity and conjugate similarity:

$$\mathbf{\Lambda} = \mathbf{V}^{-1}\mathbf{A}\mathbf{V} \quad (1.15) \quad \mathbf{\Gamma} = (\mathbf{X}^*)^{-1}\mathbf{A}\mathbf{X} \quad (1.16)$$

For \mathbf{V} unitary (i.e., $\mathbf{V}^H\mathbf{V} = \mathbf{V}\mathbf{V}^H = \mathbf{V}^{-1}\mathbf{V} = \mathbf{I}_{n \times n}$ and $\det(\mathbf{V}) = 1$) (1.15) is a *unitary*

similarity transformation: $\Lambda = \mathbf{V}^H \mathbf{A} \mathbf{V}$. If Λ is in diagonal form, matrix \mathbf{A} is said to be *normal*. This is well-known as an eigen-decomposition, with the elements on the diagonal of Λ as eigenvalues and the columns of \mathbf{V} as eigenvectors. Correspondingly, the diagonalization through consimilarity is used to obtain con(jugate)-eigenvalues and con(jugate)-eigenvectors.

Table 1.4: Eigenvalues/Eigenvectors and conjugate counterparts.

eigenvalue/eigenvector	coneigenvalue/coneigenvector
$\mathbf{A} \mathbf{v}_n = \lambda_n \mathbf{v}_n$	$\mathbf{A} \mathbf{x}_n = \xi_n \mathbf{x}_n^*$

Under the influence of Kennaugh's works, the methodology of basis change has been linked in radar polarimetry, for a long time, to that of finding the optimal polarization for a given scattering matrix (or, finding the states for which the radar receives minim/maximum power on certain directions) [57, 58]. Usually, the optimum condition refers to maximizing the power of the co-polar channels along making the cross-polar components zero, which is nonetheless the diagonalization of the scattering matrix through a consimilarity basis transformation operation. This is exploited, for example, by the Huynen-Euler multiplicative decomposition (Subsection 1.4.2).

With optical systems, i.e., under the FSA convention, the change of basis is performed using the standard similarity operation [59].

1.3.3.1 Conjugate similarity and unitary congruence

It is mathematically proven that for a complex symmetric matrix \mathbf{A} in (1.17), the transformation matrix \mathbf{X} is unitary [60]. Then, such *unitary consimilarity* is equivalent to a *unitary congruence* transformation:

$$\begin{aligned} \Gamma &= (\mathbf{X}^*)^{-1} \mathbf{A} \mathbf{X} = (\mathbf{X}^{-1})^* \mathbf{A} \mathbf{X} \\ &= (\mathbf{X}^H)^* \mathbf{A} \mathbf{X} = \mathbf{X}^T \mathbf{A} \mathbf{X}. \end{aligned} \quad (1.17)$$

Both the conjugate similarity transformation and the ability to claim the symmetry of the monostatic scattering matrix \mathbf{S} are by-products of imposing the BSA convention. The second weakens the first, so that monostatic scattering matrices verifying reciprocity are diagonalized under unitary congruence [61, 62, 63]. While this is distinct from the well-known unitary similarity diagonalization, the computation is always possible and the mathematical formalism is available in PolSAR from the early works of Graves [64]. As emphasized in the thesis, this is not the case for the general consimilarity operation.

The method used to determine the elements of the unitary congruence diagonalization (transformation and diagonal matrices) will follow after a short literature review.

1.3.3.2 Consimilarity in PolSAR

This subsection highlights some of the confusions surrounding the radar-oriented representation, with respect to: (a) naming inaccuracies and (b) interpretations of the physics of the scattering process described through the consimilarity operation.

- (a) In radar polarimetry, due to its many influences from antenna theory, microwave networks or signal processing domains, to name only a few, algebraic constructs are borrowed from these domains with exact or adapted terminology. Due to such branched inheritance the terminology may be confusing and not follow the one in standard mathematics.

The conjugate similarity equation is addressed in many ways throughout the literature, and unfortunately, sometimes in misleading or omissive terms. Moreover, the solutions proposed are usually applicable only under the reciprocity equivalence. In light of all such contradictions in the radar literature, Hubbert suggest to use only the optical convention, performing always the FSA-equivalent transformation and then solving any algebraic problem directly through similarity [55]. Nonetheless, the proposed framework is not general as it is based only on linear H-V measurements.

The earlier works of Graves (1958, [64]), Payne (1968, [65]) and Huynen (1970, [66]), have investigated to provide a diagonal form for the symmetric scattering matrix. While they offer the transformation equation in conjugate similarity/unitary congruence, they then refer to the decomposition using very common terms as "eigenvalue decomposition" and for the products those of "eigenvalue(s)" and "eigenvector(s)/eigenpolarization(s)". While former studies have in some cases adopted the same notation, others use terms as "Kennaugh eigen-values/vectors" [55], "pseudoeigen-values/vectors" [58, 67], or "Kennaugh pseudoeigen-values/vectors" [68] to provide a differentiation in nomenclature.

More recent works make another type of omission: they claim to compute the coneigenvalues/coneigenvectors via "conjugate similarity" or "conjugate diagonalization" even when the scattering matrix is explicitly symmetric [50].

- (b) On the other hand, it appears there is currently no consensus in the literature for the adequate formalism interpretation of the polarimetric radar consimilarity operation.

Lüneburg et al. start from the concept of directional polarization vectors, eq. (1.14), and interpret the conjugate similarity transformation as a time reversal operation, i.e., an operation described by an antilinear operator. The antilinear operator connects the conjugate propagation spaces for the transmitted and received electric fields, travelling in opposite directions. As part of this mathematical formalism, the Sinclair matrix becomes just the antimatrix or the matrix of the antilinear operator [69].

Bebbington et al. oppose such understanding and proposes instead the use of the spinorial formalism under the radar backscattering convention [70].

1.3.3.3 Solving unitary congruence diagonalization and connections to SVD factorization

The unitary congruence factorization (1.17) is sometimes referred to, as the Autonne-Takagi factorization. The terms from the decomposition are the Takagi (diagonal) values and the Takagi vectors. It is known that all complex symmetric matrices are Takagi-diagonalizable [71] and the Takagi factorization is applied only to symmetric complex matrices. This operation is also used, for example, in particle physics for the diagonalization of the complex symmetric mass matrix. Other domains in which the decomposition is relevant are mentioned in [72].

In PolSAR, Graves introduces the *polarization power scattering matrix*, also known as the Graves matrix, \mathbf{G} :

$$\begin{aligned} \mathbf{G} &= \mathbf{S}^H \mathbf{S} \\ &= \begin{bmatrix} |S_{xx}|^2 + |S_{yx}|^2 & S_{xx} \cdot S_{xy}^* + S_{yx} \cdot S_{yy}^* \\ S_{xy} \cdot S_{xx}^* + S_{yy} \cdot S_{yx}^* & |S_{yy}|^2 + |S_{xy}|^2 \end{bmatrix}. \end{aligned} \quad (1.18)$$

Graves argues that without a phase difference, decomposing this Hermitian matrix offers the same polarimetric information as the (monostatic) reciprocal scattering matrix [64]. He refers nonetheless to the possibility of obtaining the vectors and diagonal values of the unitary congruence transformation directly from matrix \mathbf{G} . With symmetric scattering matrices, $\mathbf{S} = \mathbf{S}^T$, the eigenvalues of $\mathbf{G} = \mathbf{S}^H \mathbf{S} = \mathbf{S}^{T*} \mathbf{S} = \mathbf{S}^* \mathbf{S}$ are the *squared absolute values of the coneigenvalues and its eigenvectors are equal to the coneigenvectors* [73]. However, according to [68, 71], in the degenerate case (equal eigenvalues of \mathbf{G}), the eigenvalue decomposition of the Hermitian \mathbf{G} matrix does no longer solve the Takagi factorization.

The unitary congruence of symmetric scattering matrices can also be interpreted as a special form of the Singular Value Decomposition (SVD), i.e., as a symmetric SVD (SSVD).

Every complex matrix $\mathbf{A}_1 \in \mathbb{C}^{n \times n}$ admits an SVD

$$\mathbf{A}_1 = \mathbf{V}_{1,1} \mathbf{\Sigma}_1 \mathbf{V}_{1,2}^H, \quad (1.19)$$

and every complex symmetric matrix $\mathbf{A}_2 \in \mathbb{C}^{n \times n}$ admits an SSVD [74]:

$$\mathbf{A}_2 = \mathbf{Q} \mathbf{\Sigma}_2 \mathbf{Q}^T, \quad (1.20)$$

where $\mathbf{Q}, \mathbf{V}_{1,1}, \mathbf{V}_{1,2} \in \mathbb{C}^{n \times m}$ are distinct unitary matrices with *singular vectors* as columns, while $\mathbf{\Sigma}_1, \mathbf{\Sigma}_2$ matrices are diagonal and contain real, non-negative elements, known as the *singular values*, $\mathbf{\Sigma} = \text{diag}(\sigma_1, \dots, \sigma_n)$. Singular values are usually sorted in ascending/descending order and the singular vectors are sorted accordingly.

From (1.17) and (1.20), the unitary congruence is indeed a SSVD (Fig. 1.8), given $\mathbf{Q} = \mathbf{X}^*$ and $\mathbf{\Sigma}_1 = \mathbf{\Gamma}$:

$$\mathbf{A} = (\mathbf{X}^T)^{-1} \mathbf{\Gamma} \mathbf{X}^{-1} = \left(\mathbf{X}^H \right)^T \mathbf{\Gamma} \mathbf{X}^H = \mathbf{X}^* \mathbf{\Gamma} (\mathbf{X}^*)^T. \quad (1.21)$$

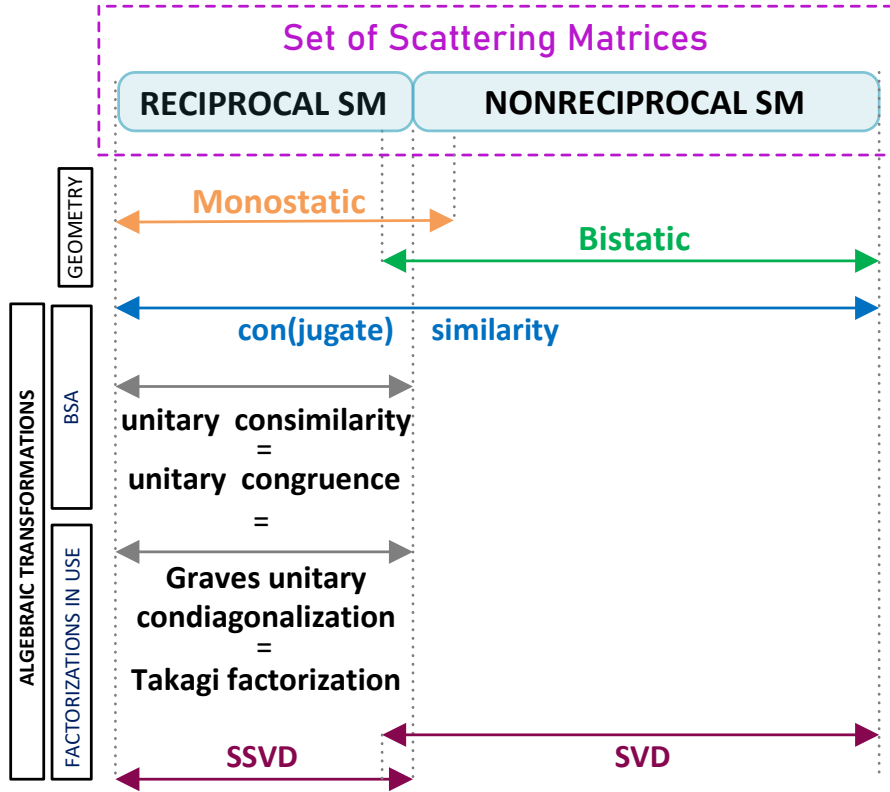


Figure 1.8: Conjugate similarity and SVD operations for reciprocal and nonreciprocal scattering matrices.

Combining the definition of the Graves matrix (1.18) with that of the SSVD (1.20):

$$G = (Q\Sigma_S Q^T)^* (Q\Sigma_S Q^T) = Q^* \Sigma_S^* \Sigma_S Q^T = Q^* G_{\Sigma_S} Q^T \quad (1.22)$$

$$= X G_{\Sigma_S} X^H = X G_{\Sigma_S} X^{-1} \quad (1.23)$$

Matrix G_{Σ_S} contains the eigenvalues of G , which are no others than the squared singular values. We conclude that for the case of symmetric scattering matrices, the singular values of S are equal to the absolute values of the coneigenvalues.

For general scattering matrices $S \neq S^T$, it remains true that a squared relation exists between the eigenvalues of the Graves matrix and the singular values of S (1.33). The eigenvectors are the left singular vectors, but there is no longer a connection with the general coneigenvalues and the general coneigenvectors.

$$G = V_2 \Sigma^H V_1^H V_1 \Sigma V_2^H = V_2 \Sigma^H \Sigma V_2^H = V_2 G_{\Sigma} V_2^{-1} \quad (1.24)$$

Changing a nonreciprocal scattering matrix (under BSA) into a new, distinct basis representation (diagonal or not) requires the use of two complex conjugate basis

transformations which solve the conjugate similarity operation (1.16). As seen, when the transformation matrix X remains unitary, the general conjugate similarity equation is a particular form of SVD, i.e., an SSVD. The transformation vectors are linearly independent and orthogonal. Nonetheless, the two transformations are no longer related when X is not unitary.

Until now, there has been little investigation in polarimetric radar of the general conjugate similarity transformation (i.e., for nonreciprocal scattering matrices). For the bistatic case, the SVD transformation is proposed in the literature. This allows the diagonal decomposition of the scattering matrix by means of two unitary transformations, one characterizing the Tx-Tg path and one the Tg-Rx path [75, 76]. Two sets of orthogonal basis vectors are used. With the consimilarity operation, a restriction of the model is that the two transformation matrices on each path are conjugate pairs.

However, transforming nonreciprocal matrices through the general conjugate similarity may be different in some regards, as there should be matrices nondiagonalizable but not by a unitary transformation (nonorthogonal set of basis vectors) and even matrices for which the consimilarity is verified, but not under a diagonal form. From a physical point of view, different properties of the target and propagation medium may not allow for preservation of the unitary property of transformation matrices associated to the monostatic/bistatic propagation paths. The investigation of the general conjugate similarity may contribute with new information in the analysis of scattering matrices.

1.4 Coherent decompositions

The information potentially contained in multi-polarization observations is exploited using decomposition techniques, which form a core theory in PolSAR. These techniques are used to separate the polarimetric signature captured by the radar instruments into a combination of simpler scattering responses, to which a physical significance can be associated. They are divided into coherent and incoherent methods. Distinctively, these decomposition methods are used with different types of scatterers, which then imposes different types of input variables. These are the scattering matrix (for single scatterers) and the second order statistics (i.e., coherency or covariance matrices - Section 1.5) of the scattering vector (for distributed targets).

Sections 1.4 and 1.5 will cover an elementary introduction of PolSAR coherent and incoherent decompositions, with the analysis deliberately restricted to methods which are relevant for the thesis.

The coherent methods are divided into two main classes, as they can decompose the scattering matrix via a summation or a multiplicative factorization [4]. The most well-known coherent decompositions are displayed in Fig. 1.9. We separate them considering on one side, their factorization type and on the other, their applicability to the decomposition of reciprocal and nonreciprocal scattering matrices. This is to say, we take into account the utility of these methods for both monostatic and bistatic scattering matrices.

The main developments proposed by the thesis are linked to the branch of coherent

decompositions. More precisely, the contributions rely on the use of multiplicative factorization methods adequate for both reciprocal and nonreciprocal scattering matrices (e.g., the polar decomposition).

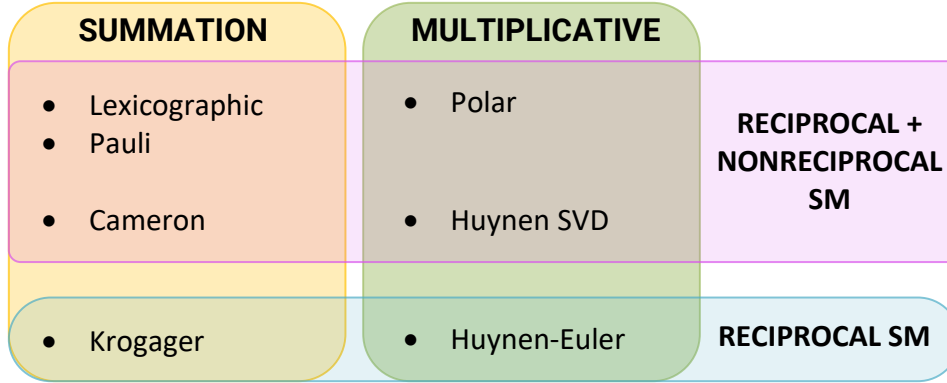


Figure 1.9: Classification of coherent decompositions.

Horizontal axis: factorization type (summation and multiplicative).

Vertical axis: applicability to reciprocal and nonreciprocal scattering matrices.

Acronyms: SVD: Singular Value Decomposition.

1.4.1 Summation decompositions

A summation decompositions uses a predefined alphabet basis of elementary matrices:

$$\mathbf{S} = \begin{bmatrix} S_{xx} & S_{xy} \\ S_{yx} & S_{yy} \end{bmatrix} = \sum_{i=1}^N k_{\mathcal{B},i} \Psi_{\mathcal{B},i}. \quad (1.25)$$

Set $\{\Psi_{\mathcal{B}}\}$ contains the algebraic bases and the corresponding coefficients are $k_{\mathcal{B},i}$, $i \in [1, N]$. The base matrices usually acquire the interpretation of elementary scattering responses.

The principal PolSAR summation decompositions are: lexicographic, Pauli [77], Krogager [78] and Cameron [79, 80]. The lexicographic and Pauli propose conventional basis representations, common to all scientific fields which use 2×2 (complex) matrices. While the first three methods can be used with both reciprocal and nonreciprocal scattering matrices, the Krogager model has been proposed only for reciprocal scattering matrices (Fig. 1.9).

In [81, 82], a three component scattering model is suggested for symmetric scattering matrices, which can be restricted to obtain both the Krogager and the Cameron decomposition.

The set of Pauli coefficients $\{k_{\mathcal{P},1}, k_{\mathcal{P},2}, k_{\mathcal{P},3}, k_{\mathcal{P},4}\}$ in Table 1.5 are generally complex numbers. The Pauli bases, σ_i , have a physical scattering interpretation, as follows: odd

Table 1.5: Target scattering vector models lexicographic and Pauli basis.

Lexicographic	$\{\Psi_{\mathcal{L}}\}$	$\left\{ \begin{bmatrix} 1 & 0 \\ 0 & 0 \end{bmatrix}, \begin{bmatrix} 0 & 1 \\ 0 & 0 \end{bmatrix}, \begin{bmatrix} 0 & 0 \\ 1 & 0 \end{bmatrix}, \begin{bmatrix} 0 & 0 \\ 0 & 1 \end{bmatrix} \right\}$
	$k_{\mathcal{L},i}, i \in [1,4]$	$S_{xx}, S_{xy}, S_{yx}, S_{yy}$
Pauli	$\{\Psi_{\mathcal{P}}\} = \{\sigma_i\}$	$\left\{ \begin{bmatrix} 1 & 0 \\ 0 & 1 \end{bmatrix}, \begin{bmatrix} 1 & 0 \\ 0 & -1 \end{bmatrix}, \begin{bmatrix} 0 & 1 \\ 1 & 0 \end{bmatrix}, \begin{bmatrix} 0 & -j \\ j & 0 \end{bmatrix} \right\}$
	$k_{\mathcal{P},i}, i \in [1,4]$	$\frac{1}{\sqrt{2}} \cdot \left(\frac{S_{xx}+S_{yy}}{\sqrt{2}}, \frac{S_{xx}-S_{yy}}{\sqrt{2}}, \frac{S_{xy}+S_{yx}}{\sqrt{2}}, \frac{j(S_{xy}-S_{yx})}{\sqrt{2}} \right)$

bounce, even bounce, diffused and asymmetric scattering mechanisms. Only the first three components are used in decomposing a reciprocal scattering matrix (i.e., $k_{\mathcal{P},3}$ associated to the asymmetric scattering equals zero).

1.4.2 Multiplicative decompositions

The second type of methods for the decomposition of the scattering matrix use a multiplicative factorization. They rely on elementary algebraic operations (e.g., diagonalization) to extract the decomposition factors. Subsequently, product matrices are expressed using parameters which can interpreted the scattering properties of targets.

■ Huynen

An important reference in PolSAR is the thesis and the early work of J.R. Huynen [66]. In search of an effective method to characterize the maximum polarization return from a coherent target, Huynen writes a model based on the unitary congruence transformation (Section 1.3.3.1) and proposes a factorization which is equivalent to a diagonalization operation for the case of symmetric matrices. The transformation matrix of unitary congruence is constructed via two matrices: one real rotation (\mathbf{R}) and one elliptical rotation (\mathbf{T}). Given that there exists a third matrix of complex phases, the transformation is also interpreted as the product of three elementary Euler rotation matrices and a diagonal matrix. As so, it is referred by different nomenclatures in the literature: directly Huynen or Huynen-Euler [83, 84] or Euler [85] and sometimes Kennaugh-Huynen [86]. Equation (1.20) transforms into (1.26):

$$\mathbf{S} = \mathbf{Q}\mathbf{S}_d\mathbf{Q}^T = \mathbf{R}(\phi_2)\mathbf{T}(\tau_2)\mathbf{S}_d\mathbf{T}(\tau_1)\mathbf{R}(-\phi_1) \quad (1.26)$$

$$\mathbf{S}_d = \begin{bmatrix} m \cdot e^{2j(\nu+\rho)} & 0 \\ 0 & m \cdot \tan^2\gamma \cdot e^{-2j(\nu-\rho)} \end{bmatrix} = \begin{bmatrix} \mu_1 & 0 \\ 0 & \mu_2 \end{bmatrix} \quad (1.27)$$

$$\mathbf{R}(\phi) = \begin{bmatrix} \cos\phi & -\sin\phi \\ \sin\phi & \cos\phi \end{bmatrix} \quad (1.28) \quad \mathbf{T}(\tau) = \begin{bmatrix} \cos\tau & -j\sin\tau \\ -j\sin\tau & \cos\tau \end{bmatrix} \quad (1.29)$$

For the monostatic case, $\phi_H = \phi_1 = \phi_2$ and $\tau_H = \tau_1 = \tau_2$. To obtain the Huynen parameters $(m, \gamma, \nu, \phi_H, \tau_H, \rho)$, one must solve the congruence unitary inversion.

This is usually done from Grave's eigendecomposition (Subsection 1.3.3.3). Dallman et al. propose to extract the parameters using a technique based on the Kennaugh matrix [87].

The extension of the Huynen method for the bistatic case (i.e., asymmetric scattering matrices) is inspired by the SVD factorization. However, it is important to emphasize that it is not the general complex SVD equation in (1.19) which is used by the proposed transformation in [75, 88, 89], but the particular real form:

$$\mathbf{S} = \mathbf{Q}_1 \Sigma_d \mathbf{Q}_2^\top. \quad (1.30)$$

An increased number of parameters is used by this decomposition as the rotation and ellipticity angles are now distinct for the transmission $\{\phi_1 = \phi_T, \tau_1 = \tau_T\}$ and reception $\{\phi_2 = \phi_R, \tau_2 = \tau_R\}$ paths.

■ Polar

Any complex square matrix $\mathbf{A} \in \mathbb{C}^{n \times n}$ can be decomposed using the polar decomposition as the product of two factors: one unitary and one Hermitian. There exist two different forms, with (1.31) being known as the right polar decomposition and (1.32) as the left polar decomposition:

$$\mathbf{A} = \mathbf{U}\mathbf{H} \quad (1.31) \quad \mathbf{A} = \mathbf{K}\mathbf{U}, \quad (1.32)$$

where $\mathbf{U} \in \mathbb{C}^{n \times n}$ verifies $\mathbf{U}\mathbf{U}^H = \mathbf{U}^H\mathbf{U} = \mathbf{I}$ and is the nearest unitary matrix to \mathbf{A} (in any unitarily invariant norm¹, as argued in [90, 91]). It is possible to write the Hermitian factors ($\mathbf{H}^H = \mathbf{H}$ and $\mathbf{K}^H = \mathbf{K}$) of the right/left forms as: $\mathbf{H} = \sqrt{\mathbf{A}^H \mathbf{A}}$ and $\mathbf{K} = \sqrt{\mathbf{A} \mathbf{A}^H}$. If \mathbf{A} is a normal matrix (i.e., it verifies $\mathbf{A}^H \mathbf{A} = \mathbf{A} \mathbf{A}^H$), it immediately follows that $\mathbf{H} = \mathbf{K}$. For all other \mathbf{A} matrices, $\mathbf{A}^H \mathbf{A}$ is similar to $\mathbf{A} \mathbf{A}^H$. This means that \mathbf{H} and \mathbf{K} are themselves similar (i.e., have the same eigenvalues and the same number of independent eigenvectors). By using the properties of the unitary \mathbf{U} factor, it is possible to transform from one expression to the other, as follows: $\mathbf{A} = \mathbf{U}\mathbf{H}\mathbf{U}^H\mathbf{U} = (\mathbf{U}\mathbf{H}\mathbf{U}^H)\mathbf{U} = \mathbf{K}\mathbf{U}$. As a result, $\mathbf{K} = \mathbf{U}\mathbf{H}\mathbf{U}^H = \mathbf{U}\mathbf{H}\mathbf{U}^{-1}$, which is the similarity equivalence.

Irrespective of choosing (1.31) or (1.32), the Hermitian term is always unique, while the unitary term is unique only if the decomposed matrix is non-singular.

The general interpretation of the two factors is as follows: the unitary factor performs a rotation, while the Hermitian factor acts as a stretching/deformation. From a mathematical perspective, the polar decomposition has a close connection to the SVD, from which it can be computed.

For the right polar decomposition, the Hermitian factor is the matrix square root of the Graves power matrix \mathbf{G} . In the case of a symmetric scattering matrix, given the eigendecomposition $\mathbf{H} = \mathbf{V}_{\mathcal{H}} \Lambda_{\mathcal{H}} \mathbf{V}_{\mathcal{H}}^H$, the eigenvalues $\text{diag}(\Lambda_{\mathcal{H}})$ of \mathbf{H} are none others than the Takagi factors/unitary coneigenvalues/singular values (Subsection 1.3.3.3). Equation (1.20) then becomes:

¹i.e., a norm satisfying $\|\mathbf{A}\| = \|\mathbf{U}\mathbf{A}\mathbf{V}^H\|$

$$\mathbf{S} = \mathbf{Q}\mathbf{\Sigma}\mathbf{Q}^\top = \mathbf{V}_{\mathcal{H}}^* (\mathbf{V}_{\mathcal{H}}^\top \mathbf{U} \mathbf{V}_{\mathcal{H}})^{1/2} \mathbf{\Lambda}_{\mathcal{H}} \left[(\mathbf{V}_{\mathcal{H}}^\top \mathbf{U} \mathbf{V}_{\mathcal{H}})^\top \right]^{1/2} \mathbf{V}_{\mathcal{H}}^{\mathbf{H}} \quad (1.33)$$

The unitary \mathbf{Q} transformation matrix of SSVD is a combination of the two unitary matrices from the polar decomposition: matrix \mathbf{U} and the eigenvector matrix of \mathbf{H} [92].

We further exploit the polar decomposition technique in Section 3.

1.4.3 Target scattering vector

S.R. Cloude has proposed the *target scattering vector* as a new and equivalent characterization of the scattering matrix, in his PhD thesis (1986) [77]. Some of the summation (e.g., Cameron [79]) and multiplicative (e.g., Huynen [89]) coherent decomposition methods have used equivalent vector forms to speed up algebraic computations.

The vectorization operation can be interpreted as a function, $\text{Vect}: \mathbb{C}^{2 \times 2} \rightarrow \mathbb{C}^{4 \times 1}$, which projects the scattering matrix \mathbf{S} into the set $\{\Psi\}$ of N basis functions.

$$\mathbf{k} = \text{Vect}(\mathbf{S}) = \frac{1}{2} \text{Tr}(\mathbf{S}\mathbf{\Psi}) \quad (1.34)$$

An important property of the target scattering vector is that it conserves the span (i.e., total power) of the original scattering matrix.

I. Full-polarimetric data

The two elementary representations of the target scattering vector are based on the lexicographic and Pauli summation decompositions.

- For bistatic observations, the target vectors $\mathbf{k}_{\mathcal{L}_4}$, $\mathbf{k}_{\mathcal{P}_4}$ are directly obtained by column concatenation of the decomposition coefficients when basis sets $\{\Psi_{\mathcal{L}}\}$ and $\{\Psi_{\mathcal{P}}\}$ are used (Table 1.5).
- For monostatic observations, only the first three coefficients in the Pauli decomposition are nonzero. Because of this, the (column) target vector has different dimensions, (3×1) vs. (4×1) , for the monostatic and bistatic cases, respectively. To comply with the power conservation property, the linear polarization monostatic lexicographic and Pauli target vectors are:

$$\mathbf{k}_{\mathcal{L}_3} = \left[S_{hh}, \sqrt{2}S_{hv}, S_{vv} \right]^\top \quad \mathbf{k}_{\mathcal{P}_3} = \frac{1}{2} \left[S_{hh} + S_{vv}, S_{hh} - S_{vv}, \sqrt{2}S_{hv} \right]^\top \quad (1.35)$$

In the rest of the chapter, the alphanumerical subscript of the target vector (\mathcal{L} or \mathcal{P}) and (3 or 4) is used to specify the algebraic basis and the number of elements in the vector.

Starting from the two elementary forms, the scattering vector has been expressed using PolSAR-relevant parameters. Such models distinguish themselves by combining elements of both summation and multiplicative coherent decompositions.

The vector's coefficients are obtained as from a summation model, but each of them is expressed using parameters derived from a multiplicative decomposition. The most well-known examples are indexed in Table 1.6.

The vectorization operation is sometimes expressed using the Kronecker product [93]. For example, the Huynen [89] and polar decomposition vectorizations (in lexicographic basis) are simply:

$$\mathbf{k}_{\text{Huynen}_{\mathcal{L}_4}} = (\mathbf{R}(\phi_2) \otimes \mathbf{R}(\phi_1))(\mathbf{T}(\tau_2) \otimes \mathbf{T}(\tau_1))\mathbf{k}_{\mathcal{L}_4}(\mathbf{S}_d), \quad (1.36)$$

$$\mathbf{k}_{\text{Polar}_{\mathcal{L}_4}} = (\mathbf{I}_2 \otimes \mathbf{U})(\mathbf{I}_2 \otimes \mathbf{H})\mathbf{k}_{\mathcal{L}_4}(\mathbf{I}_2). \quad (1.37)$$

Table 1.6: Other PolSAR full-polarimetric target scattering vector models.

Name	Ref.	SM bases		Parametrization model
		polarimetric	algebraic $\{\Psi\}$	
<i>Scattering matrix parametrization:</i>				
TSVM	[50]	linear	Pauli	Huynen-Euler
BiTSVM	[86]	linear	Pauli	Huynen SVD
<i>Unitary eigenvector matrix parametrization:</i>				
α/β	[94]	linear	Pauli or lexicographic	$\alpha-\beta-\gamma-\delta$
$\psi-\Omega-\Phi$ -LS	[95]	circular	lexicographic	$\alpha-\beta-\gamma-\delta$

II. Dual-polarimetric data

For dual-polarimetric measurements, irrespective of having a monostatic or bistatic geometry, the target scattering vector has uniquely a (2×1) dimension. However, because of the different number of degrees of liberty assumed by monostatic and bistatic measurements, the loss of polarimetric information may be different. General monostatic dual-pol cross-channel data will be more closely related to standard monostatic measurements [96].

General dual-polarimetric data contains either both the co-polarimetric channels or one of the two cross-polarimetric sets. In the case of linear polarization, there exist 3 possible dual-pol combinations: HH-VV, HH-VH and VV-HV.

Only the double co-pol HH-VV scattering vector can be represented in both lexicographic and Pauli basis [97]:

$$\mathbf{k}_{\mathcal{L}_2, \text{co-pol}} = [S_{hh}, S_{vv}]^T \quad \mathbf{k}_{\mathcal{P}_2, \text{co-pol}} = \frac{1}{2}[S_{hh} + S_{vv}, S_{hh} - S_{vv}]^T \quad (1.38)$$

1.5 Incoherent decompositions

The scattering response of partial targets is no longer relevant under pixel-level analysis. Moreover, there is common knowledge that radar images (even single-channel) are

affected by speckle. This phenomenon is modeled as a multiplicative noise and is the result of coherent summation from all elementary scattering responses in one resolution cell. The number of scatterers inside the resolution cell increases with coarser resolution and as the features/roughness of scatterers have dimensions comparable to the wavelength.

Under these circumstances, the multi-channel PolSAR data has a stochastic nature and pertinent analysis tools involve the computation of higher order moments. In what concerns the statistics of the target scattering vector, the subsequent assumptions are implied:

Assumptions Set - 1.3.

- I. The PolSAR multivariate target vector is modeled by a jointly Gaussian complex random vector, having zero mean and completely described as a second order stochastic process.

In the light of these assumptions, the most elementary statistical model used for the target scattering vector is that of zero-mean circular Gaussian [98]. The assumption of circularity completes 1.3.II, so that the second order statistics are entirely described by a covariance matrix [99]. Having two elementary models of the target vector (lexicographic and Pauli), incoherent PolSAR processing distinguishes between the Hermitian forms of covariance (\mathbf{C}) and coherency (\mathbf{T}) matrices:

$$\mathbf{C} = \mathbb{E}\{\mathbf{k}_{\mathcal{L}}\mathbf{k}_{\mathcal{L}}^{\text{H}}\} \quad (1.39)$$

$$\mathbf{T} = \mathbb{E}\{\mathbf{k}_{\mathcal{P}}\mathbf{k}_{\mathcal{P}}^{\text{H}}\} \quad (1.40)$$

Then, the probability density function (pdf) associated to the (lexicographic) target vector is [9]:

$$p(\mathbf{k}) = \frac{1}{\pi^m \det(\mathbf{C})} \exp\left(-\mathbf{k}^{\text{H}} \mathbf{C}^{-1} \mathbf{k}\right), \quad (1.41)$$

where $m = \{3,4\}$ is the vector dimension. Previously, $\mathbb{E}\{\cdot\}$ represents the expectation operator.

With real data, the covariance/coherency are obtained using a Maximum Likelihood (ML) estimator. Under the stationarity assumption, the expectation value can be computed by ensemble average in a local window having L total pixels.

$$\hat{\mathbf{C}} = \frac{1}{L} \sum_{i=1}^L \mathbf{k}_{\mathcal{L},i} \mathbf{k}_{\mathcal{L},i}^{\text{H}} \quad (1.42)$$

$$\hat{\mathbf{T}} = \frac{1}{L} \sum_{i=1}^L \mathbf{k}_{\mathcal{P},i} \mathbf{k}_{\mathcal{P},i}^{\text{H}} \quad (1.43)$$

It is assumed that $L > m$. Equations (1.42) and (1.43) are often referred as polarimetric complex multilooking operations.

The estimated complex covariance² matrix is assumed to follow a (scaled) complex

²or coherency. Henceforth, the covariance and coherency matrices are assumed to have the same statistical properties. This is implied whenever not addressed specifically in the text.

Wishart distribution, with probability density function:

$$p(\hat{\mathbf{C}}) = \frac{L^q (\det \hat{\mathbf{C}})^{L-q}}{(\det \boldsymbol{\Sigma})^L \Gamma_q(L)} \exp\left(-L \cdot \text{Tr}(\boldsymbol{\Sigma}^{-1} \hat{\mathbf{C}})\right), \quad (1.44)$$

where $\Gamma_q(L) = \pi^{\frac{q(q-1)}{2}} \prod_{i=0}^{q-1} \Gamma(L-i)$, $\Gamma(\cdot)$ represents the standard Euler gamma function, q is the covariance matrix order and $\boldsymbol{\Sigma} = \mathbb{E}\{\hat{\mathbf{C}}\}$. The model is valid as long as $L \geq q$. Finally, $\boldsymbol{\Sigma}$ may itself be estimated using a ML approach.

It is generally accepted that the Gaussian model for the target vector best describes PolSAR data from: a) homogeneous regions or b) for which a large number of elementary targets are present inside the resolution cells (under the applicability of the central limit theorem). This is often the case for medium and low resolution observations. For brevity in presentation, only the elementary models of multivariate normal and Wishart pdfs are introduced here.

For high and very high resolution PolSAR data, there are two viewpoints proposed by the literature:

(a) Non-Gaussian statistical modeling:

By far, this represents currently the common approach used in data analysis. As the highly heterogeneous PolSAR data deviates from the usual Gaussian model, the use of other probability distributions has proven necessary. A comprehensive presentation of such statistical models is provided in [1]. For example, a popular model for the target scattering vector of distributed targets, which allows to model heterogeneous clutter, is that of the Spherical Invariant Random Vector (SIRV) [100]. Previous work has shown that additional information can be retrieved for the non-Gaussian scattering vector by using, for example, blind source separation techniques which no longer impose orthogonality [101, 98].

(b) Dominance of single scattering mechanism:

As the actual number of physical targets decreases in high resolution acquisitions, the scattering behavior may begin to resemble, for more and more pixels in the PolSAR image, to that of single (i.e., coherent) scatterers. As a result, it becomes more and more suitable to exploit a data analysis approach involving coherent decompositions. This viewpoint is proposed, for example, in [95].

The work presented in the current thesis is based greatly on a coherent approach, which may be seen as the direct influence of the second viewpoint. However, from a practical implementation perspective, the direct use of coherent techniques is not proper for distributed targets, as well as for dealing with the speckle effect. While based on a coherent approach, the technique proposed in Chapter 3 incorporates a geometric averaging stage, which allows it to be applied for practical clustering

applications with real PolSAR data.

1.5.1 Entropy-alpha decomposition (monostatic/bistatic, quad-pol/dual-pol)

The entropy-average alpha angle method is based on an eigenvalue-eigenvector decomposition of the coherency matrix. The spectral theorem assures all Hermitian matrices are diagonalizable with real eigenvalues and the eigenvectors corresponding to distinct eigenvalues are orthogonal. Moreover, the eigenvectors form an orthogonal basis which spans the entire spectral space. In the followings, the possible dimensions of the scattering vector are $m = \{2,3,4\}$ for dual-pol, quad-pol monostatic and quad-pol bistatic observations, respectively. Then, the eigen-decomposition is:

$$\mathbf{T}_m = \mathbf{V} \mathbf{D}_m \mathbf{V}^H, \quad (1.45)$$

where $\mathbf{D}_m = \text{diag}(\lambda_1, \dots, \lambda_m)$ is a diagonal matrix with eigenvalues $\lambda_i, i = 1, \dots, m$ (in descending order). The sum of squared eigenvalues (or equivalently, the squared Frobenius norm of vector $[\lambda_1, \dots, \lambda_m]^T$) is equal to the span.

Matrix $\mathbf{V} = [\mathbf{v}_{m,1}, \dots, \mathbf{v}_{m,m}]$ is the unitary (i.e., $\mathbf{V}^H = \mathbf{V}^{-1}$), $m \times m, m \in \{2,3,4\}$ matrix of eigenvectors. Under the $\alpha - \beta - \gamma - \delta$ parametrization, the eigenvectors of \mathbf{V} are expressed using one of the forms in (1.46), depending on their dimension $m \in \{2,3,4\}$ [76]:

$$\left. \begin{array}{l} \cos \alpha_i e^{j \delta_{4,1}} \\ \sin \alpha_i \cos \beta_i e^{j \delta_{4,2}} \\ \sin \alpha_i \sin \beta_i \cos \gamma_i e^{j \delta_{4,3}} \\ \sin \alpha_i \sin \beta_i \sin \gamma_i e^{j \delta_{4,4}} \end{array} \right\} \mathbf{v}_4 \quad \left| \quad \left. \begin{array}{l} \cos \alpha_i e^{j \delta_{3,1}} \\ \sin \alpha_i \cos \beta_i e^{j \delta_{3,2}} \\ \sin \alpha_i \sin \beta_i e^{j \delta_{3,3}} \end{array} \right\} \mathbf{v}_3 \quad \left| \quad \left. \begin{array}{l} \cos \alpha_i e^{j \delta_{2,1}} \\ \sin \alpha_i e^{j \delta_{2,2}} \end{array} \right\} \mathbf{v}_2 \quad (1.46)$$

The α, β, γ are angular values of the model, while $\delta_{m,k}$ are random phase values. The eigen-decomposition allows the interpretation of coherency scatterer \mathbf{T}_m as the sum of m rank-1 matrices which occur with probability P_i (eq. 1.49).

1.5.1.1 Parameters definition and differences in plane partitioning

The Entropy-alpha classification scheme is, probably, the most well-known PolSAR incoherent decomposition [94]. The entropy (H) is a measure used to describe the randomness of a scattering target, while alpha (α) is the average of orientation angles ($\alpha_i, 1 \leq i \leq m$) from the eigenvectors's parametrization (eq. 1.46). These parameters are expressed as follows:

$$H = - \sum_{i=1}^m P_i \log_m P_i \quad 0 \leq H \leq 1 \quad (1.47) \quad \alpha = \sum_{i=1}^m P_i \alpha_i \quad 0^\circ \leq \alpha \leq 90^\circ \quad [deg.] \quad (1.48)$$

$$P_i = \frac{\lambda_i}{\sum_{j=1}^m \lambda_j} \quad 0 \leq P_i \leq 1; \quad 1 \leq i \leq m \quad (1.49)$$

With monostatic observations, the two parameters are known to be roll-invariant. According to the definition in [102], a parameter of such type does not incorporate the target's orientation angle (measured with respect to LOS) and its value remains constant even when such rotation of the physical object exists.

■ **Entropy:** $H \in [0,1], H \in \mathbb{R}$

A small value, close to zero, characterizes one dominant scattering mechanism in the resolution cell, while a larger value, close to one, is the mark for a mixture of m scattering mechanisms, all of similar power.

■ **Average alpha angle:** $\alpha \in [0^\circ, 90^\circ], \alpha \in \mathbb{R}$

i. *Quad-polarimetric*

The extreme values of the α parameter are assigned to single-bounce (i.e., $\alpha = 0^\circ$) and double-bounce (i.e., $\alpha = 90^\circ$) mechanisms. These correspond to surface and dihedral scattering, respectively. In between the two extremes, a value $\alpha = 45^\circ$ shows the dominance of an oriented dipole mechanism which corresponds in the physical world to volume scattering. However, the values of α are not discrete, and the change in scattering mechanism is gradual. As a result, [103] argues there exists up to a $\pm 10^\circ$ inherent statistical variability for real world scatterers (the larger the entropy, the larger the uncertainty).

ii. *Dual-polarimetric*

For interpretation of the dual-pol α parameter, the polarimetric basis combination (e.g., HH-VV, HH-HV, VH-VV) needs to be taken into account. Nonetheless, results in the PolSAR literature suggest that with dual-pol data, it is not always possible to extract the scattering mechanism from α and the parameter possesses no longer the roll-invariant property [102, 104]. We verify and confirm this observation in Subsection 1.5.2.1.

■ **$H - \alpha$ Plane Space:**

The values of the H and α parameters possess the advantage of offering a certain physical interpretation of the scattering mechanism. As so, the two parameters are combined to form a 2D Plane Space representation. The separation of scattering mechanisms inside the plane is better when a dominant average scattering mechanism exists inside the resolution cell [94] (i.e., discrimination more reliable towards lower entropies). For orthogonal scattering mechanism, there are bounds regarding the maximum and minimum alpha angles which can be obtained for a given entropy. This restricts the interpretation for the $H - \alpha$ plane space inside a feasible region [76, 98]. The curves separating between feasible and unfeasible regions correspond to a particular type of coherency matrices. But because the dimensions of the coherency matrix can change, different parametric limits exist and the surface occupied by the feasible region changes as well. This modification of boundaries of the $H - \alpha$ feasible space can be observed in Fig. 1.10.

i. *Quad-polarimetric*

Under this category, both monostatic and bistatic plane space representations are possible. The difference between the two increases at higher entropies. The feasible monostatic $H - \alpha$ plane space is divided by well-known limits (Table 1.7) into 8 zones. To the best of our knowledge, there are no specific limits proposed for the bistatic plane space.

ii. *Dual-polarimetric*

The $H\text{-}\alpha$ dual-pol plane space is symmetric with respect to the center of the alpha axis, $\alpha=45^\circ$. This new arrangement in the plane space produces an increase of the unfeasible area. In order to differentiate from the full-polarimetric eigen-decomposition, the method or plane space are also referred in the literature as $H2\alpha$ [105].

Multiple separations are proposed for the $H2\alpha$ plane space, with change even between different dual-pol combinations. Some methods choose to preserve the original segmentation of the plane into 9 classification zones (8 feasible + 1 unfeasible). Kegfeng et al. [96] propose only changes to partitioning limits, with different optimal boundaries for HH-VV, HV-VV, HH-VH modes. This is also the case for Ainsworth et al. [102], which proposes different limits for the HH-VH plane space. In contrast, for data obtained under a slant 45° dual-pol mode, Long et al. [106] divide the feasible plane space into 6 partitions, corresponding to a smaller number of elementary scattering mechanism.

1.5.2 Application: Dual-polarimetric bistatic and monostatic VV-HV H-alpha classification

The full-polarimetric bistatic diversity is of central focus in the current thesis. The state of technological developments certainly indicates the bistatic geometry is to become more and more common with future applications (Subsection 1.2.2). However, from an implementation perspective, the dual-polarimetric diversity may offer an appealing compromise, as it is the case with many of today's monostatic systems. As in the case of the Harmony mission [40], it is expected that the early and exploratory bistatic systems will not be equipped with quad-pol capabilities. Another example is with the TSX-TDX couple for which a full-polarimetric bistatic mode has been used in one of the scientific phases of the missions [107], but the regular operating modes have only single or dual-pol capabilities. At present moment, the available bistatic dual-pol analysis use real data from underlying quasi-monostatic acquisitions (as with TSX-TDX). We propose a short investigation, based on the $H\text{-}\alpha$ method and plane space representation, to analyze a set of truly bistatic (i.e., large bistatic angle) dual-pol acquisitions. The linear dual-pol VV-HV combination is available.

A synthetic example is discussed in Subsection 1.5.2.1 for illustrating, at first, some differences and changes in interpretation between $H\text{-}\alpha$ plane space of monostatic full-pol and restrained VV-HV dual-pol. Then, Subsection 1.5.2.2 focuses on the comparison between dual-pol simultaneous VV-HV monostatic and bistatic data. The former is acquired by a Sentinel-1 satellite and the latter by an opportunistic ground-based receiver, with the two forming a bistatic geometry similar to the one in Fig. 1.5.

1.5.2.1 Example 1: Monostatic quad-pol vs. monostatic VV-HV dual-pol

For the current application, the boundaries used inside the $H2\alpha$ plane are the ones proposed by K. Ji et al. [96] and shown in Table 1.7.

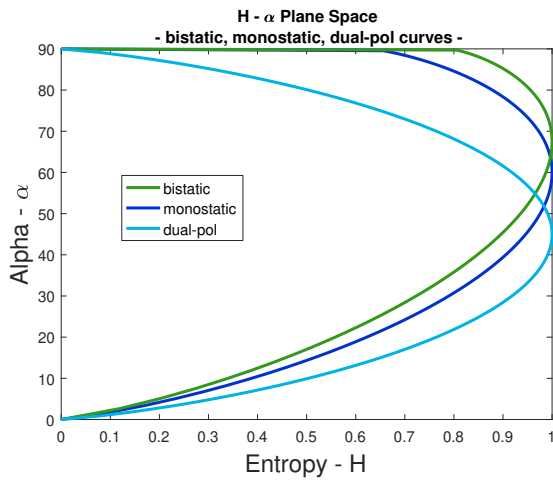


Figure 1.10: Shape of feature space (bistatic/monostatic/dual-pol) depending on dimensions of target vector.

Monostatic quad-pol [76]	
H:	[0,0.5,0.9,1]
L:	[42.5°,48°]
α :	C: [40°,50°]
	R: [40°,55°]
Dual-pol HV-VV [96]	
H:	[0,0.69,0.94,1]
L:	[26°,49°]
α :	C: [37.8°,53°]
	R: [53.8°]

Table 1.7: $H - \alpha$ Plane Space limits.

■ **Synthetic example nr. 1 / non-zero entropy:** 8 scatterers inside feasible zones of monostatic quad-pol plane space

This example examines the translation of a set of eight scatterers, originally represented in each of the eight feasible zones of the monostatic full-pol $H-\alpha$ plane space. The coherency matrices associated to each of these scatterers can be found in Annex B. The matrices are originally proposed for a different example in [108]. They are scatterers of non-zero entropy. The translation in positions inside the quad-pol and dual-pol plane spaces is shown in Fig. 1.11. For all eight scatterers, a change (i.e., a decrease) in the α angle parameter is observed. The targets having a high α angle are significantly affected. In terms of the entropy parameter, while the values indeed change, the scatterers of low and high entropy preserve their interpretation also in the dual-pol plane. For these scatterers, the newly associated entropy value is an underestimation of the monostatic quad-pol entropy. For scatterers of medium entropy, the translation inside the plane space is more significant and dependent also on the value of quad-pol α . Scatterers of medium entropy / low-medium α angles are reassigned towards the left-side of the plane space and change interpretation as low-entropy targets. In contrast, the green scatterer of quad-pol medium entropy / high α angle obtains a slight increase in entropy and is redistributed towards dual-pol medium entropy / medium α .

■ **Synthetic example nr. 2/ entropy free:** 5 unoriented/oriented elementary scatterers

A set of 5 elementary scatterers (sphere, dipole, diplane, quarter-wave, helix) are now considered. Their (normalized) monostatic scattering matrices are well-known references in the PolSAR literature. These S matrices can be found in Table B.1. For three of the elementary scatterers (i.e., dipole, dihedral and quarter-wave), distinct orientations are taken into account. For the dual-pol VV-HV case, only the second column of the scattering matrix is available. The coherency matrices are computed directly, without averaging.

Such elementary scatterers describe a single scattering mechanism and are of

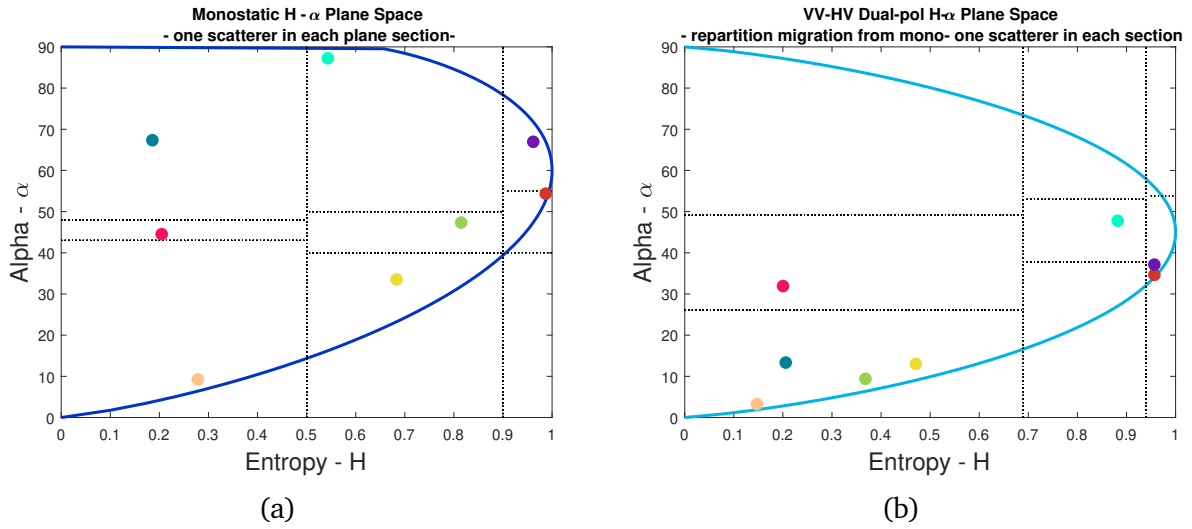


Figure 1.11: Monostatic quad-pol vs. VV-HV dual-pol. Translation in position [(a) to (b)] inside the $H - \alpha$ plane for 8 scatterer from each of the zones in the original monostatic Plane Space.

zero entropy. However, with full-polarimetric measurements they are mapped in different locations on the alpha axis. The average scattering alpha angle is computed, eq. (1.48), and we inspect the positioning on the alpha axis of both quad-pol and dual-pol results (Fig. 1.12). In the figures, the different sizes of the colored dots serve only a visual discrimination function.

For quad-pol, it is verified that the 9 scattering matrices map to unique points on the vertical axis (Fig. 1.12a-c-e). Only one confusion is observed: both dihedral (the notation used in the figures is "diplane") and helix are assigned an α value of 90° . Nevertheless, both rotation-free and oriented scatterers are represented by the same scattering mechanism. This demonstrates the well-known invariance of the α parameter (with respect to changes modeled as multiplicative product of the original scattering matrix with real rotations $\mathbf{R} \in \mathbb{R}^{2 \times 2}$). For the monostatic case, such an operation describes a rotation of the point target around the LOS axis.

On the other hand, this property is no longer preserved for the VV-HV dual-pol case. The position of different mechanisms changes and they are confused on the α axis, as observed in Fig. 1.12b-d-f.

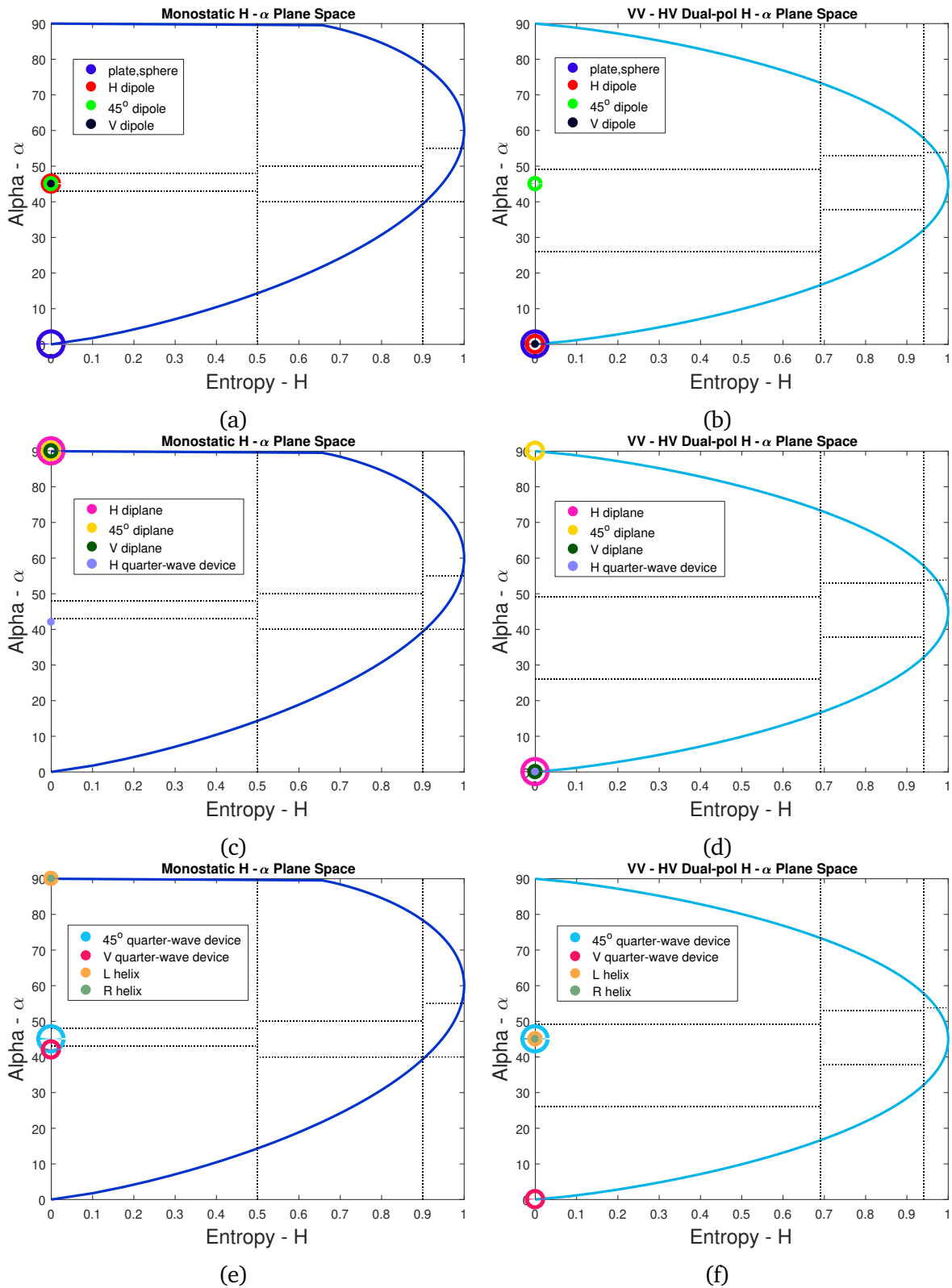


Figure 1.12: Monostatic quad-pol vs. VV-HV dual-pol. Changes in the α angle interpretation for the oriented and orientation-free, zero-entropy, elementary scatterer in Table B.1.

■ **Real data / monostatic / Brétigny dataset: quad-pol vs (artificially-restrained) dual-pol comparison**

We now extend the monostatic quad-pol/VV-HV dual-pol comparison to a real PolSAR dataset. The Brétigny full-polarimetric set, in detail described in Annex A.1.I, is used.

Two parallel runs are performed: one with the entire set of polarimetric channels (quad-pol processing) and another only with the VV-HV channel combination. The H/α parameters are computed via spatial averaging of target vectors having 3 and 2 elements, respectively. A moving window with 1 pixel displacement, size 5×5 is used. Results are divided into one of the 9 categories and the pixels distribution in the regions from the feature space is represented in the monostatic and dual-pol plane spaces (Figs. 1.13c and 1.13d). The color-coded representation of the pixels is given in Figs. 1.13a and 1.13b. This provides a first classification of the scattering mechanism inside the image, as identified through the two sets of parameters. All pixels from the image fall inside one of the feasible zones. For quad-pol, each zone is associated to a type of mechanism, as indicated by Fig. 1.13e. While the same colors have been used for similar positions in the dual-pol plane space, it is necessary to emphasize that the interpretation in terms of scattering mechanism is not nearly the same for these zones, due to the changes in the entropy and alpha parameters.

The quad-pol results in Fig. 1.13a indicate the image is mainly composed of points of moderately random entropy, with distinctive scatterers of low entropy being identified at the location of the four calibration targets, the parking space and the roofs of the two main buildings from the image. The same mechanism is recognized for one of the agricultural fields from lower left.

With dual-pol results, a major degradation is seen in attributing to class Z1 (Bragg scattering in monostatic) the great number of pixels in the image. This is consistent with the result from Fig. 1.11, indicating also the translation of scatterers of medium entropy towards low entropy in the dual-pol VV-HV plane space when their α angle is itself medium to low.

Xie and all. provide in [109] an analysis between quad-pol and (synthetic) HH-VV dual-pol data and present similar conclusions for the two dual-pol parameters: the α parameter has no longer a rotation invariant property and the entropy, while less impacted, has lower discrimination performances. The previous synthetic example nr. 1 has shown that the dual-pol entropy can be an underestimate/overestimate of the quad-pol entropy depending on the quad-pol alpha value.

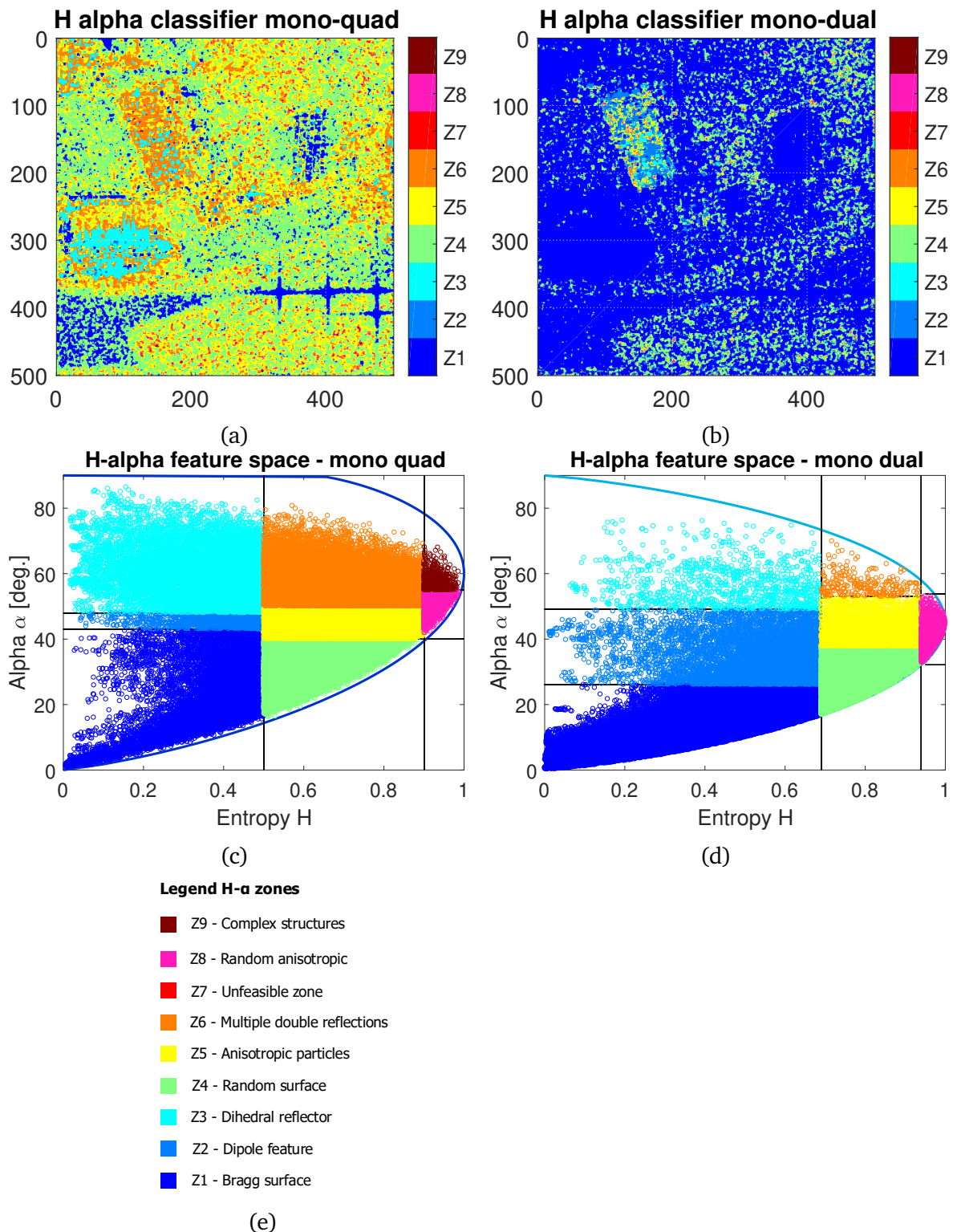


Figure 1.13: Brétigny monostatic dataset.

Simple $H-\alpha$ classifier: (a) Quad-polarimetric. (b) VV-HV Dual-polarimetric.

Plane space representations: (c) Quad-polarimetric. (d) VV-HV Dual-polarimetric. (e) Legend and zones description for the quad-pol $H-\alpha$ plane space.

1.5.2.2 Example 2: Monostatic vs. bistatic VV-HV dual-pol

Preceding examples have shown there is a high loss in interpretation with the α parameter for monostatic dual-polarimetric acquisitions. The current subsection focuses on a similar analysis between simultaneous monostatic and bistatic (VV-HV) dual-polarimetric data, an interpretation performed in the $H2\alpha$ plane space.

The Mill's Lake dual-pol dataset is used; its detailed description is available in Annex A.2. Because the bistatic images are acquired using a geometry with a very large Tx-Rx baseline (as in Fig. 1.5), the scattering response from the entire illuminated area covers a range of large bistatic angles. This is different from other dual-pol simultaneous monostatic-bistatic acquisitions, as for example with TSX/TDX and their (small bistatic angle) HH-VV acquisitions. To the best of our knowledge, there are no other studies addressing a polarimetric interpretation of dual-pol large-angle bistatic acquisitions.

RGB composites using the polarimetric channels are represented in Fig. A.5. For the plane space comparison, only a selection from the lower-right corner of the original images, of $2 \text{ km} \times 2 \text{ km}$ towards North-West is employed. The area under study is urban, combining high and low density apartment blocks, roads, construction sites, etc. From the more sparser bistatic image, only the pixels passing a certain intensity threshold [dB] are singled out for processing. The dual-pol $H-\alpha$ algorithm is applied to the same selection of pixels in the bistatic and monostatic images, which justifies the comparison between the two cases. Because range and azimuth focusing operations having the same settings have been applied to raw monostatic and bistatic data, there is a 1-to-1 correspondence between resolution cells from both images.

Figures 1.14a-b present the color-coded monostatic and bistatic dual-pol $H-\alpha$ classification result. Pixels which are not selected are represented in black. In both results, there is a dominance of scatterers with low entropy. However, the discrimination between multiple scattering mechanisms is not possible for the dual-pol monostatic case, where the majority of pixels are characterized by a combination of low entropy / low α angles (Fig. 1.14a). For the bistatic case, α takes a larger range of values, which makes it possible to discriminate between at least two low entropy scattering mechanisms (Fig. 1.14b). This is distinctively different from the previous monostatic dual-pol investigations in this section. All have show a decrease of α values for the dual-pol monostatic case.

We can take from the common monostatic/bistatic set of points, only those which are not affected by class transitions in the $H2\alpha$ plane space, i.e., they are represented in the same dual-pol scattering zones in both monostatic/bistatic classifications. Their distribution in the plane is seen in Fig. 1.14c. These pixels correspond to the diagonal of Table 1.8, in which the percentages of inter- and intra-class translation are represented. The sum of all rows and columns is 100%. Regarding inter-class migrations (from the monostatic to the bistatic dual-pol plane space), the largest displacements take place around small entropy. For example, more than 50% of scatterers from monostatic Z1 migrate to bistatic Z2 and Z3. These results indicate there are indeed some important differences in the analysis of low entropy targets in monostatic and bistatic dual-pol observations, possibly due to a change in the α interpretation with the large bistatic angle dual-pol observations. Further investigations will be necessary on the subject.

Nonetheless, this short example shows that even with partial polarimetric diversity, truly bistatic observations can increase discrimination capabilities.

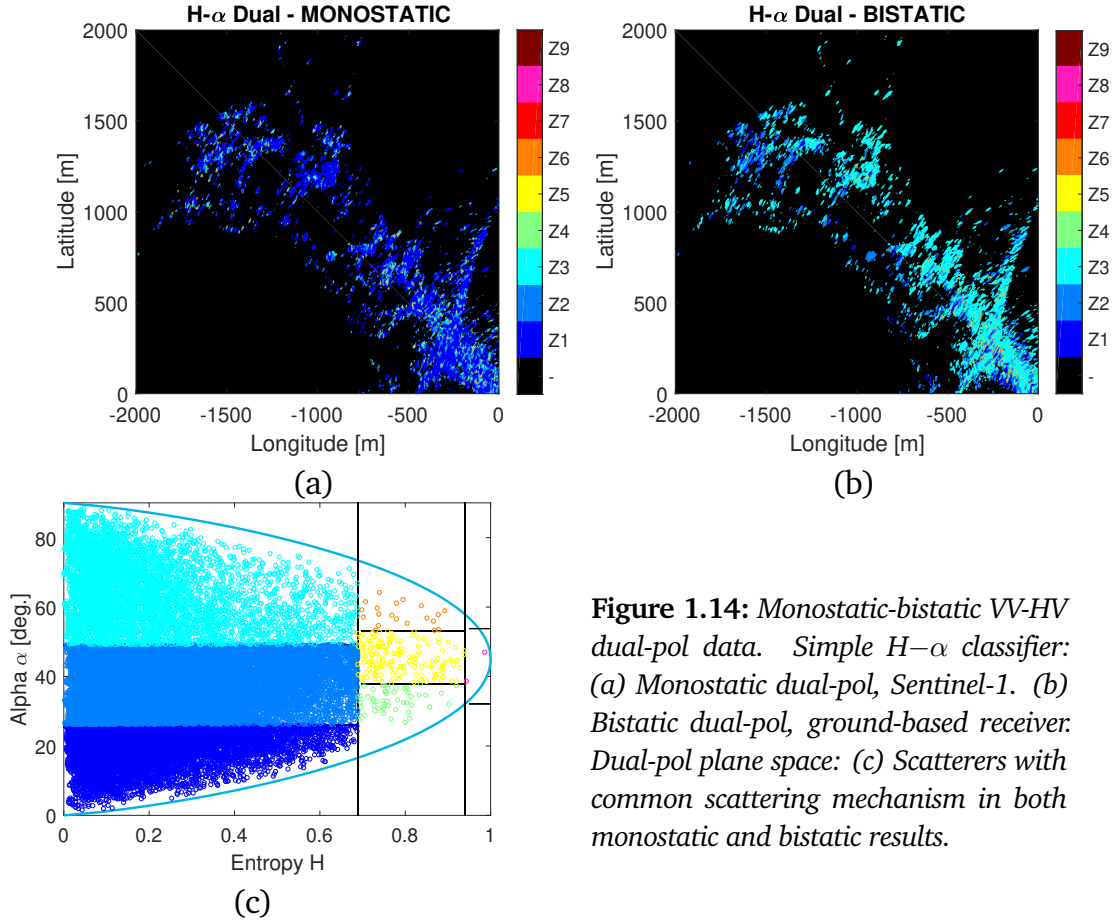


Figure 1.14: Monostatic-bistatic VV-HV dual-pol data. Simple $H-\alpha$ classifier: (a) Monostatic dual-pol, Sentinel-1. (b) Bistatic dual-pol, ground-based receiver. Dual-pol plane space: (c) Scatterers with common scattering mechanism in both monostatic and bistatic results.

Table 1.8: Transition percentages inside feasible zones of the plane space.

Monostatic classif. [%]	Bistatic classif. [%]							
	Z1	Z2	Z3	Z4	Z5	Z6	Z8	Z9
Z1	4.7218	18.5655	35.2691	0.3831	1.2642	0.5406	0.0726	0.0012
Z2	2.1910	8.3912	15.5611	0.1517	0.4482	0.2083	0.0230	0.0004
Z3	0.3690	1.1757	2.4196	0.0191	0.0601	0.0367	0.0047	0
Z4	0.2563	0.9877	1.7682	0.0234	0.0636	0.0226	0.0051	0
Z5	0.3152	1.0239	2.1212	0.0246	0.0714	0.0382	0.0043	0
Z6	0.0726	0.2376	0.5219	0.0016	0.0160	0.0090	0.0016	0
Z8	0.0511	0.1498	0.3085	0.0031	0.0133	0.0039	0.0012	0
Z9	0.0004	0.0020	0.0027	0	0.0004	0	0	0

1.6 Conclusions

This chapter has mapped out the theoretical foundation of the thesis. Elementary information of wave polarimetry, an anthology of bistatic full-polarimetric imaging radar instruments and the algebraic particularities of monostatic/bistatic data analysis with both coherent and incoherent methods have been covered. The last subsection integrates a comparative analysis on dual-pol monostatic and bistatic data.

While the rest of the thesis considers entirely a full-polarimetric analysis framework, the example from the last subsection serves as a remainder that the choice of multi-polarimetric (full- or dual-) diversity is often subject to compromises in real-world systems (i.e., technological development stages, data volume, power requirements, etc.). The case of many today's spaceborne SAR platforms is eloquent: even when equipped with full polarimetric capabilities, they are mostly operated in single or dual polarization (e.g., Sentinel-1A/B (C Band), TerraSAR-X (X Band), COSMO-SkyMed (X Band) or ALOS PALSAR 2 (L Band)). It is realistically to expect that for many of the future's bistatic missions, similar constraints may apply.

The next chapter will take a different approach on the subject of the conjugate similarity operation introduced in Section 1.3 and some of the current limitations will be addressed.

Real Representation Scattering Matrix (RRSM)

The shortest path between two truths in the real domain passes through the complex domain.

Jacques Hadamard

Contents

2.1	A state-of-art investigation on general conjugate similarity	46
2.1.1	On mathematical solutions for the consimilarity transformation	46
2.1.2	On properties of conjugate eigenvectors/eigenvalues	49
2.1.3	On homogeneous/inhomogeneous scattering matrices	49
2.1.4	Solution through the Real Representation Scattering Matrix	51
2.2	Properties of the Real Representation Scattering Matrix	53
2.2.1	Real canonical form and eigenvalues of RRSM	53
2.2.2	Real concanonical form and con-eigenvalues/eigenvectors	54
2.3	PolSAR monostatic data and the Real Representation	56
2.3.1	Graves method vs. RRSM method - Coneigenvalues comparison	57
2.3.2	On monostatic and bistatic SM nonreciprocity	60
2.4	Computational Electromagnetic simulations	64
2.4.1	Bistatic scattering - Coordinate system definition	64
2.4.2	Simulation software	65
2.4.3	Radar cross-section and monostatic evaluations	70
2.5	RRSM Eigen-classification with simulated data	78
2.5.1	Monostatic simulations	78
2.5.2	Bistatic simulations	79
2.6	Conclusions	85

Transforming a general scattering matrix through a con(jugate) similarity operation is a necessary mathematical procedure under the radar Backscatter Alignment. Generally, the interest is in recovering the factorization terms, which under diagonalization are known as conjugate eigenvalues and conjugate eigenvectors. These are the two pairs (ξ_k, \mathbf{x}_k) , $k = \{1, 2\}$ which verify:

$$\mathbf{S}\mathbf{x}_k = \xi_k \mathbf{x}_k^* \quad (2.1)$$

One of the aims of this chapter is to fill the gap in the understanding of the conjugate similarity transformation for general scattering matrices. As seen in Fig. 1.8, the known PolSAR techniques apply either the Graves/Takagi unitary congruence operation for (mathematically) symmetric matrices, or the SVD for non-symmetric ones. However, there is no PolSAR study ahead of this thesis to offer a general algebraic technique for the consimilarity factorization of non-symmetric scattering matrices. Sections 2.1 and 2.2 cover the conjugate similarity transformation and the proposed Real Representation method. In the end, it is not expected that the consimilarity transformation will become an ubiquitous substitute for the SVD analysis of nonreciprocal scattering matrices (currently "de facto") but serve as its complement. The results obtained from these two factorizations are not directly comparable, as they both render different information from the scattering process.

A different focus of this chapter is in the study of coneigenvalues, found by the proposed decomposition. This is covered in Sections 2.3 and 2.5 for both (real and simulated) monostatic and (simulated) bistatic full-polarimetric examples. The simulated data is obtained by a computational electromagnetic software, for which Section 2.4 provides more details.

2.1 A state-of-art investigation on general conjugate similarity

To the best of our knowledge, the methods available in the literature for solving a conjugate similarity transformation between two complex matrices are not direct. They are based on mappings to an equivalent space where the conjugate similarity can be evaluated as a similarity equation.

While the PolSAR mapping to the Hermitian power matrix is well-known, it is only particular to the unitary congruence case. This subchapter offers a general overview of the two different mappings which can be used to transform a general scattering matrix and then recover the conjugate similarity factorization of both monostatic and bistatic scattering matrices. References hereafter combine perspectives from both the mathematical literature and radar polarimetry to offer a cohesive outlook of these different techniques.

2.1.1 On mathematical solutions for the consimilarity transformation

With the objective of solving conjugate similarity transformations, two type of mappings have been identified for general complex matrices, as follows:

- *Complex (power) form:*

The earliest and most well-known equivalent mapping is through a complex matrix, obtained as the product of a square matrix and its conjugate. Consider the left multiplication of (2.1) via S^* :

$$\mathbf{S}^* \mathbf{S} \mathbf{x} = \xi \mathbf{S}^* \mathbf{x}^* = \xi (\mathbf{S} \mathbf{x})^* = \xi \xi^* \mathbf{x} = |\xi|^2 \mathbf{x}. \quad (2.2)$$

A similar equivalence can be obtained for the right multiplication $\mathbf{S} \mathbf{S}^*$.

The conjugate eigenvalues and the conjugate eigenvectors (ξ_k and \mathbf{x}_k , $k \in \{1, 2\}$) can be obtained from the eigen-decomposition of product $\mathbf{S}^* \mathbf{S}$ [60]. The left matrix product in (2.2) is equal to the polarimetric Graves power matrix equation only for the symmetric case, $\mathbf{S} = \mathbf{S}^T$, so that $\mathbf{G} = \mathbf{S}^H \mathbf{S} = \mathbf{S}^{T*} \mathbf{S} = \mathbf{S}^* \mathbf{S}$. Then, $\mathbf{S}^* \mathbf{S}$ is a Hermitian matrix, which is positive (semi-)definite, i.e., all eigenvalues are nonnegative and real, larger (or equal) to zero. Also, $\mathbf{S}^* \mathbf{S}$ preserves the trace of the Graves matrix (1.18), i.e., the squared span.

For a general non-symmetric scattering matrix, the monostatic Graves equality is no longer valid and using the Graves eigen-decomposition will not produce the conjugate vectors or the squared conjugate values (see Chapter 1, Subsection 1.3.3.3 for details). In addition, product $\mathbf{S}^* \mathbf{S}$ may no longer be Hermitian, but a general complex matrix. Its trace contains two possibly different inter-cross-channel sums.

Based on Hong et al. [110], two matrices \mathbf{A} and \mathbf{B} are consimilar if: $\mathbf{A} \mathbf{A}^*$ is similar to $\mathbf{B} \mathbf{B}^*$ and the product rank condition is satisfied: $\text{rank}[(\mathbf{A} \mathbf{A}^*)^k \mathbf{A}] = \text{rank}[(\mathbf{B} \mathbf{B}^*)^k \mathbf{B}]$, $(\forall) k \geq 1$. \mathbf{A} is con-diagonalizable if and only if $\mathbf{A} \mathbf{A}^*$ can be diagonalized with nonnegative eigenvalues and $\text{rank}(\mathbf{A}) = \text{rank}(\mathbf{A} \mathbf{A}^*)$.

Nonetheless, any complex matrix $\mathbf{S}^* \mathbf{S}$ is reducible, under similarity, to a Jordan canonical form, which is unique up to a permutation of its block summands. Hong and Horn show that while conjugate diagonalization is not guaranteed, every matrix is consimilar to some special matrices: its own conjugate, transpose, adjoint, to a real matrix and a Hermitian matrix [110]. The Jordan representation of the complex power matrix can then be reduced, by an inverse operation, to a so-called canonical form under consimilarity (i.e., a con-canonical form). The technique via the complex mapping will generally produce the Hermitian con-canonical form. Reference [111] comparatively catalogs proposed con-canonical form representations.

■ *Block forms:*

- (a) Having constituent blocks the original matrix and its complex conjugate:
To test for conjugate normal matrices, reference [112] introduces a block form composed of the original matrix and its conjugate. Properties of matrices under consimilarity are discussed using both the complex power form and this block form. Eventually, the block matrix serves a limited purpose in the reference as the computation of transformation factors under consimilarity returns to the use of the complex form.
- (b) Having constituent blocks the original matrix and its transpose:
An alternative expression for computing the eigenvalues of the Graves matrix based on a block representation is introduced in [113, 114, 75]. The scattering matrix and its transpose are block-stacked on the secondary diagonal of a 4×4 matrix. This initial form is derived from the set of two equations proposed in [113] as the "generalized Graves method" and which

¹ alternatively, under a change of notation, $\mathbf{S} \mathbf{S}^*$ can be used for the same purpose.

is used to determine the so-called optimal and reciprocal-optimal polarization vectors for the bistatic case. This proposed block matrix is then left multiplied by its Hermitian, with the result in the form of a new (block) matrix having $S^H S$ and $S^* S^T$ on the diagonal. This new block form is written in [113] as a set of two complex equations for the "generalized Kennaugh method", which proposes to determine the optimal polarization vectors in bistatic.

Using the 4×4 power matrix, the authors' aim is to determine the Graves eigenvalues. They show that the results converge only for non-degenerate cases, i.e., distinct eigenvalues. The technique is not extended for other eigenvalues cases. In this regard, it is not generally applicable for transformation of non-symmetric complex matrices under conjugate similarity.

- (c) Having constituent blocks the real and imaginary parts of the original matrix: In [68], Ling and Jiang propose the use of a real block form (containing the real and imaginary parts of the scattering matrix) as a matrix transformation which can offer an alternative solution for determining Kennaugh's "pseudo-eigenvalues". Some theoretical background for the real representation as an equivalent mapping under consimilarity is offered in [115, 116]. A closed-form solution is proposed for the factors in the consimilarity factorization. The technique allows to obtain the real Jordan canonical form of the real representation matrix and from it, the real concanonical form.

Combining references from both general mathematics and radar polarimetric literature, we have shortly looked into some of the equivalence mappings which could be used for the scattering matrix. The complex power and the block real forms emerge as possible solutions. While the Graves method has been popularized in PolSAR, according to the first technique presented, the consimilarity solution is possible through a Hermitian power matrix only for reciprocal scattering matrices.

Until recently, the RR remained unknown as a possible equivalent transformation. No examples of practical applications in PolSAR were provided in its mathematical introduction by article [68], but neither restrictions to the symmetry of the matrix were stated. Due to the real nature of the equivalent block matrix, the technique provides a more simpler solution than through the general complex form. And while the equivalent concanonical matrix is always real, this proves not as a limitation. While the classical Graves matrix analysis can obtain only real (coneigen)values, a complete description of the real representation eigenvalues contains complex-valued solutions. This allows to isolate those nonreciprocal scattering matrices characterized by complex (coneigen)values. The work in the current chapter offers a closer look to some of the properties of the Real Representation (RR) matrix [117, 118, 119]. The following subsections look into the applicability of the RR for the consimilarity equivalence of both monostatic and bistatic scattering matrices and explore the connections between the conjugate eigenvalues and the nonreciprocity degree of a scattering matrix.

2.1.2 On properties of conjugate eigenvectors/eigenvalues

From an algebraic perspective, there are distinct definitions on the existence and uniqueness of a coneigenvalue/coneigenvector pair (ξ, \mathbf{x}) , as proposed by Horn and Ikramov [120]. The two perspectives are compared below. In the manuscript, we adopt the definitions of the second, which are closely related to those of the more common eigenvalues/eigenvectors (i.e., eigen-pairs).

■ Existence

The first perspective claims a coneigen-pair (ξ, \mathbf{x}) associates to an eigen-pair of the complex-power form [116] only when the non-negative eigenvalues are distinct. Under this interpretation, the consimilarly diagonalizable matrices have necessarily positive and distinct coneigenvalues and only for them the sets (ξ_k, \mathbf{x}_k) , $k =$ matrix dimension, are recovered. Other matrices may have an incomplete coneigenvalue/coneigenvector set (ξ_k, \mathbf{x}_k) , $k <$ matrix dimension, or no con-eigen pair (ξ, \mathbf{x}) at all. This restricts the interpretation of results.

Ikramov eliminates the nonnegative constraint for the coneigenvalues, arguing that, alike simple eigenvalues, "any (square) matrix of order n should have exactly n coneigenvalues (counting multiplicity)" [120]. Under this interpretation, coneigenvalues may present solutions also over the complex domain.

For similarity solutions of square matrices, in the complex domain, at least one eigen-pair is always known to exist. With the second interpretation, this will also be the case with coneigenvalue/coneigenvector pairs.

■ Uniqueness

Starting from eq. (2.1), there is an equivalence of the coneigenvector \mathbf{x} up to multiplication by a complex phase, $e^{j\theta}$, $\theta \in [-\pi, \pi]$, as follows:

$$\mathbf{S}\mathbf{x}e^{j\theta} = \xi\mathbf{x}^*e^{-j\theta} \quad \rightarrow \quad \mathbf{S}\mathbf{x} = (\xi e^{-2j\theta})\mathbf{x}^* \quad (2.3)$$

Under this transformation, sources have argued that either there are infinitely many (ξ, \mathbf{x}) pairs [73], or that for a coneigenvector \mathbf{x} , there should be infinitely many coneigenvalues $\xi e^{-2j\theta}$ [121].

However, a similar claim has existed for the eigenvectors: it was argued that a nonzero scalar multiple of an eigenvector is also an eigenvector. Because of this, in numerical applications, the vectors are generally normalized to unit length.

With the proper normalization and conditioning, the discussion on the uniqueness of a coneigen-pair (ξ, \mathbf{x}) should be solved.

2.1.3 On homogeneous/inhomogeneous scattering matrices

In optics, the eigenvectors of a Jones matrix are the two polarizations which do not change upon propagation. Similarly, the coneigenvectors (as defined for the monostatic case) correspond to polarization vectors which do not change their polarization by radar backscattering.

Table 2.1: The homogeneous-inhomogeneous classification of Jones [123] / Sinclair [125] matrices under similarity/consimilarity.

Jones or Sinclair matrices	Operation: similarity or conjugate similarity Values: eigenvalues or coneigenvalues Vectors: eigenvectors or coneigenvectors
homogeneous	<ul style="list-style-type: none"> • matrix is diagonalizable; • values are distinct; • two orthogonal, linearly independent vectors.
inhomogeneous	<ul style="list-style-type: none"> • matrix may no longer be diagonalizable; • values may no longer be distinct; • vectors are linearly independent but not orthogonal.

Depending on the relationship between their eigen-pairs/coneigen-pairs the Jones/Sinclair matrices are separated into homogeneous and inhomogeneous (Table 2.1). The definitions are similar between the optical and the radar case.

For Jones matrices, Lu, Chipman [122] and Gutierrez [123] discriminate between: diagonalizable *homogeneous* (i.e., with orthogonal eigenvectors) and *inhomogeneous* matrices (i.e., have only independent eigenvectors, but which are no longer orthogonal). 2×2 Jones matrices which are referred to as *defective* have only one true polarization eigenstate (and a generalized eigenstate) [124]. They are a subset of the inhomogeneous case. While they are not diagonalizable, they can be reduced to an upper triangular Jordan canonical form.

For radar scattering matrices, Lüneburg et al. also separate between homogeneous and inhomogeneous [125, 73]. Their transformation of reference is unitary congruence (and not general consimilarity). The homogeneous Sinclair matrices are those which can be diagonalized by unitary consimilarity and thus have two orthogonal coneigenvectors. In such case, the two columns x_1 , x_2 of the transformation matrix X (1.17) geometrically span orthogonal subspaces and the reciprocity of the scattering matrix S is a sufficient condition to verify this. The inhomogeneous Sinclair scattering matrices are those for which their coneigenvectors are no longer orthogonal, but the eigendecomposition of the Graves matrix still returns real, non-negative values. However, due to the limitative case under which consimilarity is evaluated, this is only a particular degenerate case and does not cover for all inhomogeneous scattering matrices. While the percentage of matrices classified as inhomogeneous is negligible small for monostatic data, the separation is no longer sufficient in bistatic.

The SVD transformation - currently proposed for converting bistatic scattering matrices to a diagonal form - cannot be used to evaluate the homogeneous/inhomogeneous property. While all scattering matrices are diagonal under SVD, not all are homogeneous. For a general, nonreciprocal scattering matrix, a diagonal form under consimilarity may or may not be achieved and a complete characterization of inhomogeneous Sinclair matrices is then possible only under the use of general

consimilarity transformation techniques (Subsection 2.1.1).

The SVD and the consimilarity transformation of a scattering matrix are complementary and can be used to assess different type of properties. However, the second has been incompletely described in PolSAR, which is no longer sufficient for the analysis of bistatic data. An extensive understanding is thus necessary in order to properly exploit any possible new information.

2.1.4 Solution through the Real Representation Scattering Matrix

This subsection introduces a general framework for solving the consimilarity equivalence of reciprocal and nonreciprocal scattering matrices using the Real Representation of the polarimetric scattering matrix. Theoretical and practical aspects are discussed. The technique is able to provide for all scattering matrices a canonical form under consimilarity.

2.1.4.1 Real block representations of a complex matrix

Consider a generic square matrix having complex elements, $\mathbf{A} \in \mathbb{C}^{n \times n}$, $\mathbf{A} = \mathbf{A}_r + j\mathbf{A}_i$ and $\mathbf{A}_r = \mathcal{R}(\mathbf{A}) = \frac{\mathbf{A} + \mathbf{A}^*}{2}$, $\mathbf{A}_i = \mathcal{I}(\mathbf{A}) = \frac{\mathbf{A} - \mathbf{A}^*}{2j}$, $\mathbf{A}_r, \mathbf{A}_i \in \mathbb{R}^{n \times n}$ being the real and imaginary matrix components of \mathbf{A} . Generally, there are in literature two distinct definitions for the Real Representation (RR) of a complex matrix. As suggested by [126, 127], there is the so-called block-skew-circulant form (\mathbf{A}_{RR_1}) and the block-Hankel-skew-circulant form (\mathbf{A}_{RR_2}):

$$\mathbf{A}_{RR_1} = \begin{bmatrix} \mathbf{A}_r & -\mathbf{A}_i \\ \mathbf{A}_i & \mathbf{A}_r \end{bmatrix} \quad \mathbf{A}_{RR_2} = \begin{bmatrix} \mathbf{A}_r & \mathbf{A}_i \\ \mathbf{A}_i & -\mathbf{A}_r \end{bmatrix} \quad (2.4)$$

$$\mathbf{A}_{RR_1} = \begin{bmatrix} 1 & 0 \\ 0 & 1 \end{bmatrix} \otimes \mathbf{A}_r + \begin{bmatrix} 0 & -1 \\ 1 & 0 \end{bmatrix} \otimes \mathbf{A}_i \quad \mathbf{A}_{RR_2} = \begin{bmatrix} 1 & 0 \\ 0 & -1 \end{bmatrix} \otimes \mathbf{A}_r + \begin{bmatrix} 0 & 1 \\ 1 & 0 \end{bmatrix} \otimes \mathbf{A}_i \quad (2.5)$$

$$\mathbf{A}_{RR_1} = \sigma_1 \otimes \mathbf{A}_r + (\sigma_3 \sigma_2) \otimes \mathbf{A}_i \quad \mathbf{A}_{RR_2} = \sigma_2 \otimes \mathbf{A}_r + \sigma_3 \otimes \mathbf{A}_i \quad (2.6)$$

alternatively, some sources may use:

$$\mathbf{A}_{RR_3} = \mathbf{A}_{RR_1}^\top \quad (2.7)$$

$$\mathbf{A}_{RR_3} = \sigma_1 \otimes \mathbf{A}_r + (\sigma_2 \sigma_3) \otimes \mathbf{A}_i \quad (2.8)$$

For notation simplification, the sigma notation of Pauli matrices is considered, σ_i , $i \in [1,3]$, as introduced in Section 1.4.3. \otimes represents the Kronecker product.

The RRs $\mathbf{A}_{RR_1}, \mathbf{A}_{RR_2}, \mathbf{A}_{RR_3} \in \mathbb{R}^{2n \times 2n}$ are twice the dimension of the original matrix, $\mathbf{A} \in \mathbb{C}^{n \times n}$. Moreover, \mathbf{A}_{RR_1} and \mathbf{A}_{RR_3} are block-Toeplitz and \mathbf{A}_{RR_2} is block-Hankel. A transformation taking the form of \mathbf{A}_{RR_1} or \mathbf{A}_{RR_2} or \mathbf{A}_{RR_3} is verified to be injective homomorphic, i.e., a monomorphism. They provide a mapping from the complex domain $\mathbb{C}^{n \times n}$ to the real codomain $\mathbb{R}^{2n \times 2n}$.

Block composite real representations are used across broader literature domains, from signal processing to quantum computing, for applications usually involving a complex-to-real homomorphic mapping. For example, \mathbf{A}_{RR_1} alone is used in operations with complex random vectors involving: in [128] - the Independent Component Analysis (ICA) algorithm and in [129] - an orthogonalization precoding for Multiple Input Multiple Output (MIMO) signals. The SAR Tomography experiment in [130] uses \mathbf{A}_{RR_1} to transform into equivalent real form an approximate formula for the Compressive Sensing L-1 minimization, which is then implemented through a Recurrent Neural Network. In PolSAR, the same block form is used to write the sample covariance matrix (defined under the symmetric circularity assumption) of simulated data [131, 132].

In [133], a real canonical form for quaternion algebra under the block-Hankel expression \mathbf{A}_{RR_2} is proposed. Article [127] manipulates both \mathbf{A}_{RR_1} and \mathbf{A}_{RR_2} for a complete description of proper and improper complex signals. Finally, \mathbf{A}_{RR_3} is used in [134] for joint non-orthogonal complex diagonalization.

Due to its block symmetry, \mathbf{A}_{RR_2} is adopted in the thesis as the Real Representation mapping for the conjugate similarity transformations [115]. The reason for such a choice will become evident in subchapters to come.

2.1.4.2 Real representation Scattering Matrix (RRSM)

The Real Representation block symmetric form of a scattering matrix (i.e., the RRSM) is written as the linear monomorphism:

$$\begin{aligned} \mathbf{S}_{\text{RR}} &= \mathcal{R}(\mathbf{S}) + j\mathcal{I}(\mathbf{S}) \\ \mathbf{S}_{\text{RR}} &= \begin{bmatrix} \mathcal{R}(\mathbf{S}) & \mathcal{I}(\mathbf{S}) \\ \mathcal{I}(\mathbf{S}) & -\mathcal{R}(\mathbf{S}) \end{bmatrix} = \boldsymbol{\sigma}_2 \otimes \mathcal{R}(\mathbf{S}) + \boldsymbol{\sigma}_3 \otimes \mathcal{I}(\mathbf{S}) \end{aligned} \quad (2.9)$$

$$= \frac{1}{2}[\boldsymbol{\sigma}_2 \otimes (\mathbf{S} + \mathbf{S}^*) + \boldsymbol{\sigma}_3 \otimes (-j) \cdot (\mathbf{S} - \mathbf{S}^*)]. \quad (2.10)$$

Using the properties of the Kronecker product, this transforms into:

$$\mathbf{S}_{\text{RR}} = \frac{1}{2}[(\boldsymbol{\sigma}_2 - j\boldsymbol{\sigma}_3) \otimes \mathbf{S} + (\boldsymbol{\sigma}_2 + j\boldsymbol{\sigma}_3) \otimes \mathbf{S}^*]. \quad (2.11)$$

The mapping under the Real Representation is displayed in Fig. 2.1. For a scattering matrix in the complex domain $\mathbf{S} \in \mathbb{C}^{2 \times 2}$, the theorem of general consimilarity states that [115]: if \mathbf{S} is consimilar to a certain \mathbf{S}_{cst} , then their equivalent real representations \mathbf{S}_{RR} and $(\mathbf{S}_{\text{RR}})_{\text{st}}$ are similar; $\mathbf{S}, \mathbf{S}_{\text{cst}} \in \mathbb{C}^{2 \times 2}$ and $\mathbf{S}_{\text{RR}}, (\mathbf{S}_{\text{RR}})_{\text{st}} \in \mathbb{R}^{4 \times 4}$. We show that any \mathbf{S}_{RR} matrix has an equivalent form under similarity which is itself written as a RR. The equivalence transformation under consimilarity (in $\mathbb{C}^{2 \times 2}$ space) is \mathbf{X} , while the equivalence transformation under similarity is denoted \mathbf{Y} .

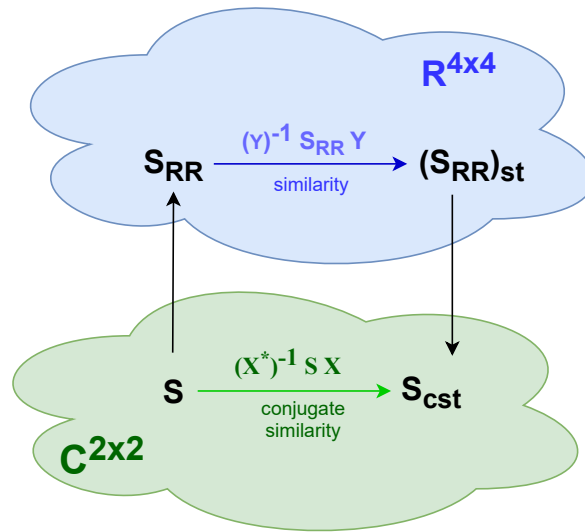


Figure 2.1: Mapping the consimilarity operation between two complex matrices (S, S_{cst}) to that of ordinary similarity between two real matrices $(S_{RR}, S_{RR_{st}})$.

2.2 Properties of the Real Representation Scattering Matrix

If two square matrices have the same distinct eigenvalues, they are similar to the same diagonal matrix. Then, there exists a family of matrices which are similar to one another and similar to the same diagonal form.

2.2.1 Real canonical form and eigenvalues of RRSM

The eigen-decomposition of a non-defective real representation scattering matrix $S_{RR} \in \mathbb{R}^{4 \times 4}$ is used directly to obtain its diagonal, equivalent form under similarity. The eigenvalues of S_{RR} are characterized by some unique properties, as follows:

- *Come in positive negative pairs:*

Firstly, the eigenvalues appear in positive-negative (\pm) pairs [115]. This means that for any eigenvalue $\lambda_i \in \{\mathbb{R}, \mathbb{C}\}$, $i \in \{1, 2\}$, then $-\lambda_i$ will necessary be an eigenvalue of the same algebraic/geometric multiplicity.

- *Have all the same algebraic type:*

For any real representation scattering matrix form, it is observed that all of its eigenvalues are of the same mathematical type. A well-known property states that for solutions in the complex domain, the eigenvalues of a real matrix are either real

or complex conjugate pairs. Combining this with the prior observation, 4×4 RRSM will have four eigenvalues of the same algebraic type. As a result, some matrices may have two real eigenvalue pairs (distinct or equal) while others may present a set of four (complex or purely imaginary) eigenvalues which are \pm complex conjugate. This is illustrated by the example in Annex D which considers the model of symmetric, skew-symmetric, Hermitian and skew-Hermitian scattering matrices.

Some problems may appear if having at least two equal eigenvalues, when it is not always possible to obtain a diagonal form for \mathbf{S}_{RR} . An almost diagonal form, the Jordan form can be used for this case. According to Jordan's theorem [60], every square matrix is similar to a matrix of the same dimensions having Jordan blocks on the diagonal. The two distinct real Jordan blocks $\mathbf{J}_p(\lambda)$, $\mathbf{J}_r(\lambda, \lambda^*)$ are introduced in detail in Annex C. In this way, it is possible to write every $(\mathbf{S}_{RR})_{st}$ into a real canonical form as a block real (R-Jordan) form:

$$(\mathbf{S}_{RR})_{\mathbf{J}} = (\mathbf{S}_{RR})_{st} = \left[\bigoplus_{k_1} \mathbf{J}_{p_{\mathcal{R}}}(\lambda_{k_1}) \right] \oplus \left[\bigoplus_{k_2} \mathbf{J}_{r_{\mathcal{I}}}(\lambda_{k_2}, \lambda_{k_2}^*) \right], \quad (2.12)$$

Summation variables k_1, k_2 depend on the size of the block, and can be:

$$\begin{array}{llll} k_1 \in \{1, \dots, 4\}, & k_2 = 0 & \text{and } p_{\mathcal{R}} = 1 & \text{(distinct or equal non-defective real eigvs.)} & \text{or} \\ k_1 \in \{1, 2\}, & k_2 = 0 & \text{and } p_{\mathcal{R}} = 2 & \text{(defective, real eigenvalues)} & \\ k_2 \in \{1, 2\}, & k_1 = 0 & \text{and } p_{\mathcal{I}} = 1 & \text{(complex-conjugate eigenvalues)} & \text{or} \\ k_2 = 1, & k_1 = 0 & \text{and } p_{\mathcal{I}} = 2 & \text{(imaginary-conjugate eigenvalues)} & \end{array}$$

where $p_{\mathcal{R}}, p_{\mathcal{I}} \in \{1, 2\}$ specifies the block dimension, which depends on the geometric multiplicity of each eigenvalue. The direct sum operator \oplus is used to connect the Jordan blocks in composed matrix form. For matrices which are not defective, i.e., they have a complete basis of eigenvectors, the Jordan form is no different from diagonal, i.e., $\bigoplus_{k=1, \dots, 4} \mathbf{J}_1(\lambda_k)$. Considering the \pm parity property of eigenvalues, this is equivalent to writing $\text{diag}\{\mathbf{J}_1(\lambda_1), \mathbf{J}_1(\lambda_2), \mathbf{J}_1(-\lambda_1), \mathbf{J}_1(-\lambda_2)\} = \text{diag}(\lambda_1, \lambda_2, -\lambda_1, -\lambda_2)$. It should be noted that the \pm parity property extends also to the Jordan blocks [115].

2.2.2 Real concanonical form and con-eigenvalues/eigenvectors

Due to the symmetry properties discussed above, the equivalent matrix under similarity of \mathbf{S}_{RR} will, for all cases, be written as a combination of \pm eigenvalues or \pm real Jordan blocks. Choosing as a convention to always have the positive and negatives values in the upper and lower parts of the direct summation, imposes that the canonical matrix form preserves itself the real representation (2.4). The positive half values will be arranged in descending order and their exact same order is mirrored in the negative lower part. The number of Jordan blocks is equal to the number of linearly independent RRSM eigenvectors spanning orthogonal subspaces. For our 4×4 matrices, when Jordan blocks start having dimensions of at least two, generalized eigenvectors need to be used. The set of eigenvectors and generalized eigenvectors will still be

linearly independent, but they no longer span orthogonal subspaces. The matrix composed of eigenvectors (and generalized eigenvectors, if any) is the transformation matrix under similarity (in the $\mathbb{R}^{4 \times 4}$ space), Y in Fig. 2.1. The similarity equivalence transforming the Real Representation Scattering Matrix to its R-Jordan canonical form is no different than eq. (1.15), which we re-write as:

$$S_{RR} = Y(S_{RR})_J Y^{-1} \quad (2.13)$$

Because of the parity property, the concanonical form S_{cst} can directly be computed by inverting the homomorphic transformation (2.9).

There is an almost one-to-one connections between the eigenvalues of S_{RR} and the coneigenvalues of S . Each \pm pair of eigenvalues from S_{RR} will correspond to a coneigenvalue (positive value is chosen). For example, any real pair of eigenvalues $(\lambda_k, -\lambda_k)$, $k \in \{1, 2\}$, has associated exactly one positive real coneigenvalue, $\xi_k = \lambda_k$, $\lambda_k > 0$. In a similar way, each \pm complex pair associates to a complex coneigenvalue. In the real concanonical form, the real block $J_{r_1}(\lambda, \lambda^*)$ is used instead of the equivalent complex block. Such choice is made to conserve the real-valued properties of the canonical form. However, even if the concanonical form is real, the conjugate eigenvalues obtained by the RRSM method are defined as both real and complex. The existence of complex eigenvalues allows for a complete characterization of the case of inhomogeneous Sinclair matrices under consimilarity (Subsection 2.1.3).

Table 2.2 briefly presents the connections and similarities between the eigenvalues/eigenvectors of the RRSM and the coneigenvalues/coneigenvectors of the scattering matrix SM . The SM coneigenvectors and RRSM eigenvectors share the same properties, which nonetheless are imposed by the latter. For complex eigenvalues of S_{RR} , the coneigenvectors of S will no longer be orthogonal. We obtain, one coneigenvector and one generalized coneigenvector. This can also happen for equal $S_{RR} \pm$ eigenvalue pairs.

While the coneigenvalues are taken directly as the half positive (real or complex) eigenvalues of RRSM, obtaining the coneigenvectors requires performing a different inversion operation. The transformation matrix X (Fig. 2.1) has the coneigenvectors aligned on its columns and can be derived through operations on the similarity transformation matrix Y . Annex E contains a closed-form algorithm for determining X . It relies on the above-introduced properties and takes its roots into an initial implementation suggested by [115, 68].

Table 2.2: Eigenvalues of RRSM and con-eigenvalues/eigenvectors of the SM.

	RRSM		SM
	eigenvalues	coneigenvalues	coneigenvectors
real	distinct pairs $\{\lambda_1, \lambda_2, -\lambda_1, -\lambda_2\}$	distinct real $\{\xi_1, \xi_2\}$	independent, orthogonal
	equal pairs $\{\lambda, \lambda, -\lambda, -\lambda\}$	equal real $\{\xi, \xi\}$	a. independent, orthogonal or b. independent, with one coneigenvector and one generalized coneigenvector
complex	conjugate pairs $\{\lambda, \lambda^*, -\lambda, -\lambda^*\}$	complex $\{\xi, \xi^*\}$	one coneigenvector and one generalized coneigenvector

2.3 PolSAR monostatic data and the Real Representation

Some pertinent questions now arise:

(Q1) *Why bother with the RR method, when the Graves method has served well, without noticeable complaints in the PolSAR community in computing the coneigenvalues?*

It is the author's hope that this question has been addressed by the previous sections. Indeed, the classical Graves may generally be enough when working only with monostatic PolSAR data (although restrictions apply if the symmetric scattering matrix is degenerate, as mentioned in Subsection 1.3.3.3). But with bistatic polarimetric diversity, this is no longer the case, as the framework of unitary congruence (under which the Graves method operates) is no longer applicable. The problem may also arise with monostatic data which is no longer reciprocal. The SVD decomposition has been employed by the PolSAR community for processing nonreciprocal scattering matrices. The justification of using this technique for bistatic scattering is that it offers the separation of incident and receiving trajectories, which then is used for the physical interpretation of the scattering process.

(Q2) *But, is the SVD the unique and complete method for the bistatic case? Or is it the proper choice for monostatic nonreciprocal data?*

As previously discussed, the similarity, consimilarity and SVD transformations are not alike from an algebraic perspective, although they may provide the same results for particular cases, as for example, in the monostatic reciprocal. The proper understanding of monostatic and bistatic scattering processes is possible only when incorporating a solid understanding of the advantages and limitations offered by the processing tools used for their study. And in coherent PolSAR, these three elementary algebraic operations are the ultimate decomposition tools from which parametric decomposition methods have originated.

The SVD is currently established as the unique method for all applications having nonreciprocal scattering matrices. From the algebraic perspective, one limitation seems

to apply. As previously argued, in Subsection 1.26, it is not the typical complex SVD proposed by parametrizations, as the bistatic Huynen-Euler, but the real SVD (eq. 1.30). Lüneburg reasons that this "careful choice of the polarization bases [...] leads to finer restricted equivalence classes with more detailed information and with more interesting polarization invariants" [75], but no further proofs are presented.

From a geometric perspective, the use of the SVD decomposition is justified in the bistatic case by the presence of two distinct traveling paths for the incidence/scattered wave. However, by the same principle, the argument should no longer be valid when considering nonreciprocal monostatic SM, for which the same factorization has been suggested.

The extensive contribution on conjugate similarity in this thesis is not on the basis of proposing a replacement to the SVD, which has indeed a solid understanding in bistatic, but in offering a complementary method and in filling some missing pieces of the algebraic understanding. Moreover, in agreement to both SM algebraic and scattering wave geometric arguments, the general conjugate similarity transformation seems more appropriate for when nonreciprocal (obtained even after any necessary compensations) SM are measured under the monostatic geometry.

(Q3) *Finally, how do the consimilarity techniques even compare? Are the coneigen-values/vectors obtained using the proposed RR and the Graves methods the same?*

For monostatic data, the comparison proposed by (Q3) is possible and will be addressed in the next subsection. Four monostatic polarimetric datasets are used: RAMSES Brétigny, CONVAIR Ice, CONVAIR Ottawa and EMISAR Foulum (Annex A).

2.3.1 Graves method vs. RRSN method - Coneigenvalues comparison

The first step of the evaluation is to compute the set $\{\lambda_1, \lambda_2, -\lambda_1, -\lambda_2\}$ of RRSN eigenvalues and separate them by their type: real versus complex.

As anticipated for monostatic data, where it is expected that scattering matrices are (almost) reciprocal, only a small percentage of RRSN eigenvalues are observed to fall into the complex case (yellow slice from pie-charts in Figs. 2.2b,d and Figs. 2.3b,d). This applies for datasets of different dimensions (details in Table A.1), acquired at three different frequency bands (X-Band: Brétigny, C-Band: both Convairs, L-Band: Foulum) and which nonetheless have different type of scatterers into the scene composition. While the values from the pie-charts are only qualitative, the complete characterization of RRSN eigenvalues type, for the four monostatic datasets, is available in Fig. E.3 of Annex E.

In a second step, the coneigenvalues are computed using the Graves method, which then allows for a comparison of values obtained using the two algorithms. For this, we compute the absolute difference ($\Delta d_i = |\xi_{i,RR} - \xi_{i,Graves}|, i \in \{1, 2\}$) only for pixel positions having real RRSN eigenvalues $\xi_{1,RR} = \lambda_1, \xi_{2,RR} = \lambda_2, \lambda_1, \lambda_2 \in \mathbb{R}$. No comparison with the Graves method is performed for positions which return complex eigenvalues.

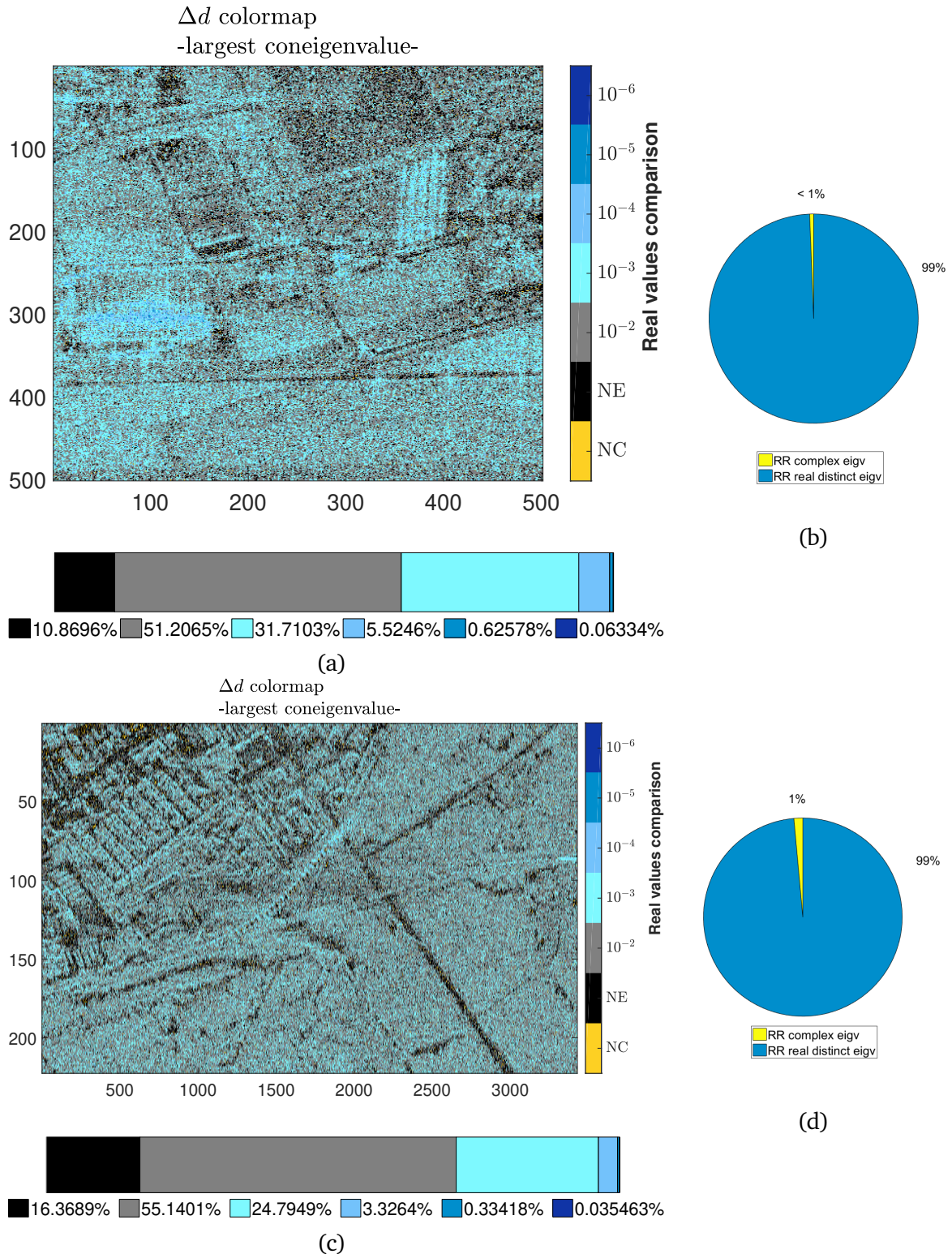


Figure 2.2: Comparison of absolute difference (Δd) between values obtained by the Graves method and values obtained using the RR method - Largest coneigenvalue (ξ_1).

Difference colormaps: (a) RAMSES Brétigny. (c) CONVAIR Ottawa.

Percentage of RRSM eigenvalues: real vs. complex: (b) Brétigny and (d) Ottawa PolSAR images.

Legend acronyms: NC (yellow) = Not Compared, NE (black) = Not Equal. Pixels are assigned in the following gray and blue classes if the values obtained by the two methods are equal under a tolerance δ_d ranging from 10^{-2} to 10^{-6} .

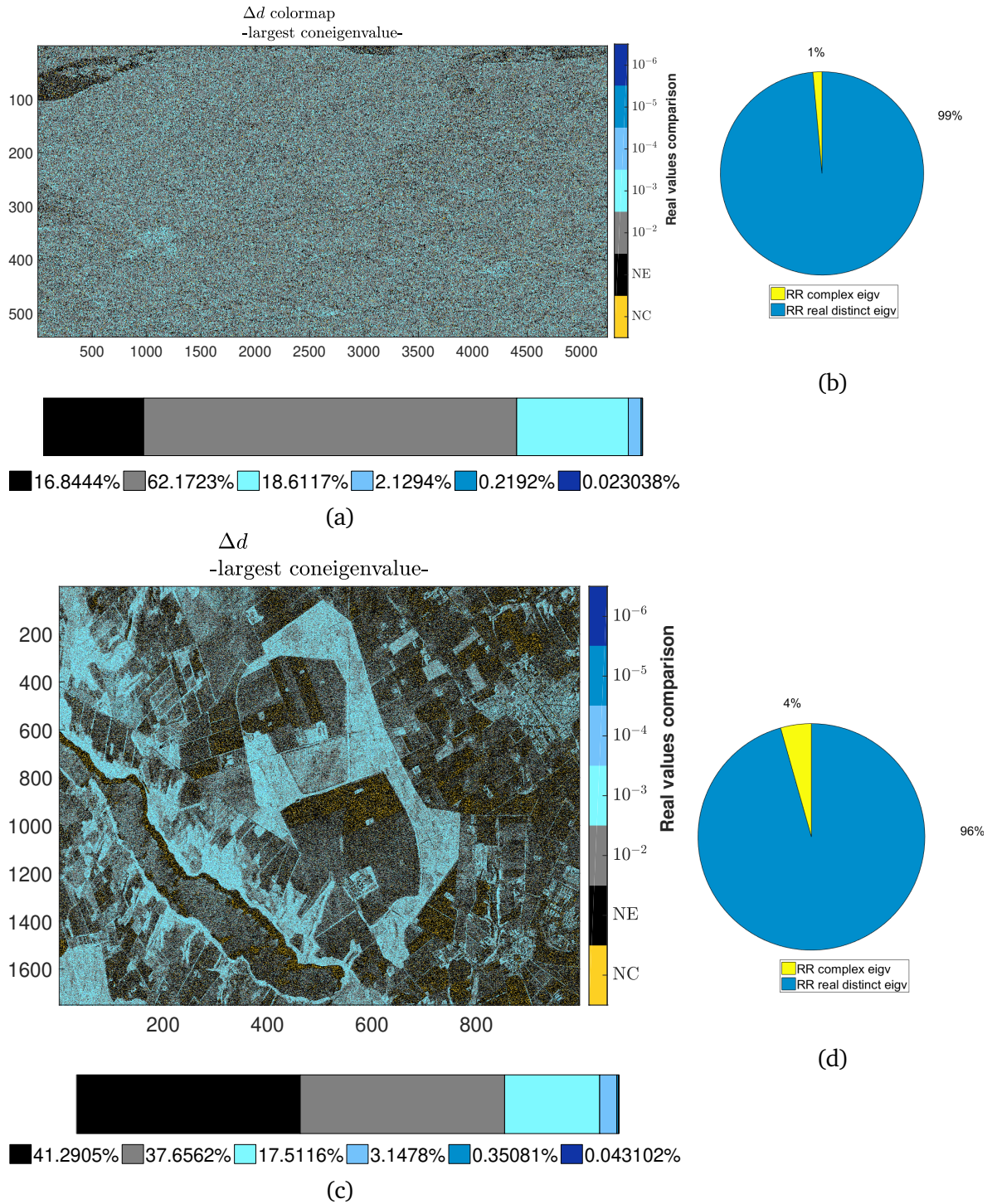


Figure 2.3: Comparison of absolute difference (Δd) between values obtained by the Graves method and values obtained using the RR method - Largest coneigenvalue (ξ_1). Difference colormaps: (a) CONVAIR Ice. (c) EMISAR Foulum. Percentage of RRSM eigenvalues: real vs. complex: (b) CV-Ice and (d) Foulum PolSAR images. Legend acronyms: NC (yellow) = Not Compared, NE (black) = Not Equal. Pixels are assigned in the following gray and blue classes if the values obtained by the two methods are equal under a tolerance δ_d ranging from 10^{-2} to 10^{-6} .

From a numerical perspective, the two values are considered equal if the absolute difference falls within a chosen tolerance, i.e., $\Delta d \leq 10^{-2}$. Within all datasets, the majority of pixels under evaluation have absolute differences smaller than this tolerance and this is valid irrespective if the difference is computed for the largest/smallest value, Δd_{ξ_1} or Δd_{ξ_2} .

For visual display, the result is represented using colormaps and multiple tolerance thresholds $\delta_d \in \{10^{-2}, 10^{-3}, 10^{-4}, 10^{-5}, 10^{-6}\}$ are used. This offers an enhanced separation in the visualization, as observed in Figs. 2.2a,c and Figs. 2.3a,c. Only the $\Delta d_{\xi_1, \xi_2} > \delta_d$ result of each dataset is represented. The colormap varies from gray to (shades of) blue as Δd differences fall under a smaller and smaller tolerance. The percentages corresponding to each tolerance interval are also shown. The black and yellow colors are reserved for two special cases. i.e., for pixels having $\Delta d > 10^{-2}$ (NE = Not Equal) and for pixels which have not been compared (NC = Not Compared), respectively.

The real coneigenvalues derived by the two methods are, for the most part, equivalent up to the second or third decimal. For coherent targets (e.g., see the known positions, south-east, where the trihedral reflectors are located in Fig. 2.2a), there is even a smaller tolerance observed. On the other hand, the black and yellow pixels tend to match those zones in the image with shadows (e.g., in urban area from Fig. 2.2c) or small backscattering intensities (roads in Fig. 2.2a and water surfaces in Figs. 2.3a,c). Nonetheless, the largest absolute errors are seen for the Foulum data, which has $\approx 45\%$ of its pixels mapped in the NE, NC categories. Such pixels are distributed within zones of agricultural fields and near the river's border.

The study in [135], which proposes a test hypotheses on heterogeneous covariance matrices, classifies the Foulum PolSAR dataset based on the properties of boxcar-estimated sample covariance matrices into 4 classes: matrices with no symmetry property or with reflection, rotation or azimuth symmetry. Comparing our result with the one proposed by the study, it is easy to spot that the zones which verify the covariance rotation and azimuth symmetries correspond to the areas for which the real coneigenvalues from the two methods are equal. The black and yellow zones in Fig. 2.3(c) fall within the areas which [135] identifies with either reflection symmetry or no reflection.

2.3.2 On monostatic and bistatic SM nonreciprocity

The previous subsection has demonstrated the equality between the monostatic real coneigenvalues using alternatively the RR and Graves methods. Because no interpretation was offered yet to the case of complex coneigenvalues, the remaining part of this chapter will be dedicated to such endeavor. The connection between nonreciprocal SMs (i.e., having different cross-polar components) and the presence of complex RRSMS eigenvalues is investigated. The main questions analyzed (from both theoretical and practical perspectives) are a) whether all nonreciprocal SMs have complex RRSMS eigenvalues and b) if such values can serve as descriptor(s) of scattering properties.

With monostatic systems, data calibration and preprocessing usually require a minimization of the difference between cross-channels (e.g., HV and VH). Usually, if

Table 2.3: *Non-exhaustive assessment of existing nonreciprocity parameters.*

Reference/year	Method Name: Parameter	Evaluated on
[79], 1990	Cameron: <i>Nonreciprocity angle</i>	S
[140], 2004	-: <i>Nonreciprocity factor</i>	S
[86], 2010	BiTSVM: <i>Difference helicity angle</i>	S
[141], 2010	-: <i>Nonreciprocity factor angle</i>	S
[142, 143], 2020	Nonreciprocity GLRT test statistics: -	C

there is an increased (absolute value) difference, a measurement error/data anomaly would be considered and methods for its mitigation employed.

With bistatic data, there is a great challenge for extracting the scattering information, as the nonreciprocity is the result of a coupled action: partly due to the target scattering itself and partly due to the asymmetry of the propagation paths [48]. Nonetheless, as fewer limitations are imposed to the bistatic scattering model, it is expected that extracting the information from nonreciprocal bistatic SMs has the potential to become an important PolSAR asset.

In [136], Trouvé et al. argue for three main geometrical effects which account for the bistatic scattering nonreciprocity: (a) the target orientation around LOS, (b) the pair of Tx and Rx linear polarimetric basis (i.e., basis convention) and (c) the antenna relative position (which corresponds to a unique bistatic angle). In the monostatic case, the two effects of (a) and (b) are coupled. Based on this, it is argued that a (real) rotation is sufficient for compensation, which is generally used in practical applications for minimizing the difference in the cross-channels.

In a similar manner, [136, 137] propose a change of basis convention in which the reference plane for the scattering process becomes the emitter-target-receiver plane. This is obtained applying two real (one left-side and one right-side) rotations on the scattering matrix. As a result, the matrix is said to transform to its emitter/transmitter principal polarizations [138, 139]. Mathematically, such operation takes the particular form of a real SVD and uses orthogonal transformations. Because the general SVD uses unitary transformations, even after applying this transformation, the resulting scattering matrix in the principal polarization basis may not necessarily be diagonal and contain the singular values in the co-polar positions.

2.3.2.1 Nonreciprocity parameters

The PolSAR "*nonreciprocity*" (sometimes, "*asymmetry*") is, primarily, understood as a property describing the scattering matrix. This is the meaning we intend for the term in this chapter. By extension, PolSAR datasets are reciprocal/nonreciprocal given the dominant SM properties. Distinctively, the term is sometimes used to describe a property of the physical object, i.e., the scattering target, or a common property of both target and retrodiffusion mechanism.

Table 2.3 offers an indexing of well-known parameters from literature which are used in assessing the nonreciprocity of the scattering matrix. Because in monostatic the loss of reciprocity was generally associated to an extra rotation of the (symmetric) scatterer or its reference system, many of the parameters have an angular interpretation, as: the Cameron nonreciprocity angle, $\theta_{rec} \in [0, \pi/2]$ [79], the helicity parameters difference from the extended bistatic Target Scattering Vector Model (BiTSVM, or TSVM-SVD), $\tau_2 = \tau_R - \tau_E \in [-\pi/2, \pi/2]$ [86], or the nonreciprocity factor angle [141], $\text{atan}(|\zeta|) \in [0, \pi/4]$. This last angular parameter is obtained from the nonreciprocity factor (NRF), which has complex values, in the range $[-1, 1]$ [140]. Quite recently, a noncoherent approach based on a Generalized Likelihood Ratio Test (GLRT) statistics has been proposed for assessing the (non)reciprocity of PolSAR data (under both homogeneous and heterogeneous statistical models [142, 143]).

In this manuscript, the nonreciprocity parameter NRF is used. Compared to all other angular parameters, it is a complex parameter with its dynamic range in $[0, 1]$. It evaluates the difference in cross-pol channels in relation to the SM span's square root:

$$\zeta = \frac{1}{\sqrt{2}} \frac{(S_{vh} - S_{hv})}{\|\mathbf{S}\|_F}. \quad (2.14)$$

While it may appear that the physical interpretation of the angular parameters is more straightforward (references in Table 2.3), the ζ amplitude ratio has its own meaning, on which we comment below. When expressed using the Pauli vector elements (Subsection 1.4.1):

$$\begin{aligned} \zeta &= \frac{1}{\sqrt{2}} \frac{(S_{vh} - S_{hv})}{\sqrt{|S_{hh}|^2 + |S_{hv}|^2 + |S_{vh}|^2 + |S_{vv}|^2}} \\ &= \frac{j \cdot k_{\mathcal{P},4}}{\sqrt{k_{\mathcal{P},1}^2 + k_{\mathcal{P},2}^2 + k_{\mathcal{P},3}^2 - k_{\mathcal{P},4}^2}}, \end{aligned} \quad (2.15)$$

ζ is understood as a ration between the Pauli asymmetric scattering descriptor and the difference between the symmetric-asymmetric powers in the SM, i.e., $(k_{\mathcal{P},1}^2 + k_{\mathcal{P},2}^2 + k_{\mathcal{P},3}^2)$ vs. $k_{\mathcal{P},4}^2$.

Figure 2.4 displays the absolute value and phase of the NRF ζ parameter for the monostatic datasets analyzed in Subsection 2.3.1. As shown by Subfigures (b)-(d)-(f)-(h), the phase values vary randomly in the definition interval $[-90^\circ, 90^\circ]$ with no evident visual information. The monostatic PolSAR images have generally small NRF absolute values, in Subfigures (a)-(c)-(e)-(g) less than 0.2. However, one of the most important observations from the modulus images is about the zones with higher values for $|\zeta|$, which we can see to generally superimpose with positions color-coded as NC (Not Compared, i.e., positions having RRSM complex eigenvalues) and NE (Not Equal, i.e., positions having different RRSM and Graves coneigenvalues results) in Figs. 2.2 and 2.3. This qualitative evaluation indicates a connection between the increase in the nonreciprocity of scattering matrices and the RRSM eigenvalues.

For an algebraic comparison, we consider the case of the four type of matrices (i.e., symmetric, skew-symmetric, Hermitian, skew-Hermitian and presented in detail

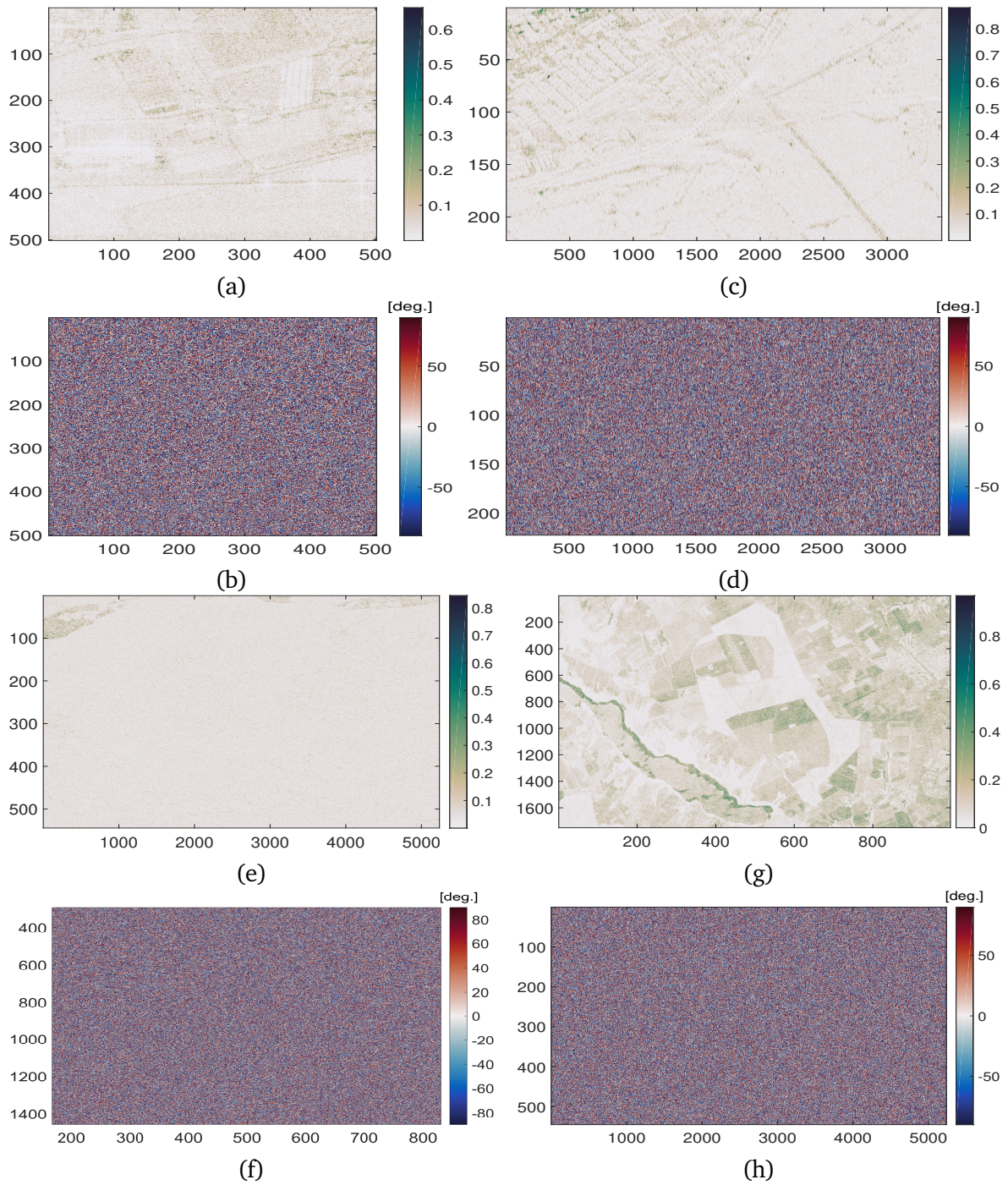


Figure 2.4: Absolute value and phase of nonreciprocity factor for monostatic datasets.

Absolute values: (a) RAMSES Brétigny. (c) CONVAIR Ottawa. (e) CONVAIR Ice. (g) EMISAR Foulum.

Phase values: (b) RAMSES Brétigny. (d) CONVAIR Ottawa. (f) CONVAIR Ice. (h) EMISAR Foulum.

Table 2.4: Four particular scattering matrices (Annex D): Expressions for Pauli vectors and the nonreciprocity factor. $a_1, a_2, b_a, b_2, c_1, c_2, d_1, d_2 \in \mathbb{R}$ as defined in (D.1).

	symmetric	skew-symmetric
$\mathbf{k}_{\mathcal{P}}$	$\frac{1}{\sqrt{2}} \begin{bmatrix} (a_1+b_1)+j(a_2+b_2) \\ (a_1-b_1)+j(a_2-b_2) \\ 2(c_1+jc_2) \\ 0 \end{bmatrix}$	$\frac{1}{\sqrt{2}} \begin{bmatrix} 0 \\ 0 \\ 0 \\ -2j(c_1+jc_2) \end{bmatrix}$
NRF	0	1
	Hermitian	skew-Hermitian
$\mathbf{k}_{\mathcal{P}}$	$\frac{1}{\sqrt{2}} \begin{bmatrix} (a_1+b_1) \\ (a_1-b_1) \\ 2c_1 \\ 2c_2 \end{bmatrix}$	$\frac{1}{\sqrt{2}} \begin{bmatrix} j(a_2+b_2) \\ j(a_2-b_2) \\ 2jc_2 \\ 2jc_1 \end{bmatrix}$
NRF	$\frac{j \cdot \sqrt{2} c_2}{\sqrt{(a_1)^2 + (b_1)^2 + 2(c_1^2 - c_2^2)}}$	$\frac{-\sqrt{2} c_1}{\sqrt{2c_1^2 - 2c_2^2 - a_2^2 - b_2^2}}$

in Annex D). The RRSM eigenvalues (and implicitly, the type of SM coneigenvalues) are always real or always imaginary if the SM are symmetric and skew-symmetric, respectively. As shown in Table 2.4, for these two type of matrices, the nonreciprocity parameter corresponds to values of: 0 (zero asymmetric component, $k_{\mathcal{P},4} = 0$) and 1 (zero symmetric components, $k_{\mathcal{P},i} = 0, i \in \{1, 2, 3\}$). Matrices of Hermitian and skew-Hermitian type can have either real or complex eigenvalues (Annex D). When evaluating the nonreciprocity value of example matrices SH_1 (Hermitian with real RRSM eigenvalues) and SH_2 (Hermitian with complex RRSM eigenvalues), the results are 0.0984 and 0.9569. But when evaluating the nonreciprocity value of example matrices SKH_1 (skew-Hermitian with real RRSM eigenvalues) and SKH_2 (skew-Hermitian with complex RRSM eigenvalues), the results are -0.6176 and 0.6031. In this case, by taking only the absolute value of the NRF, the matrices may be considered having similar properties, which we observe is no longer true.

We argue that an interpretation of the RRSM eigen-classification can be obtained from the obvious connection with the nonreciprocity parameter, which we continue to investigate in Subchapter 2.5.

2.4 Computational Electromagnetic simulations

2.4.1 Bistatic scattering - Coordinate system definition

The scattering geometry depicted in Fig. 2.5 is discussed further below. A point-like target is considered in the center of the spherical coordinate system. On the receiving path, we represent the scattering versors for the two possible conventions (Subsection

1.3.1): $\hat{\mathbf{k}}_{fs}$ (orange, for FSA) and $\hat{\mathbf{k}}_{bs}$ (red, for BSA). For the backscattering convention, the angular pairs (θ_i, φ_i) and (θ_s, φ_s) identify the incidence and scattering directions, with unit vectors $\hat{\mathbf{k}}_i$ and $\hat{\mathbf{k}}_{bs}$, respectively. The incident and scattered bistatic vectors determine the so-called bistatic plane of scattering [139, 137].

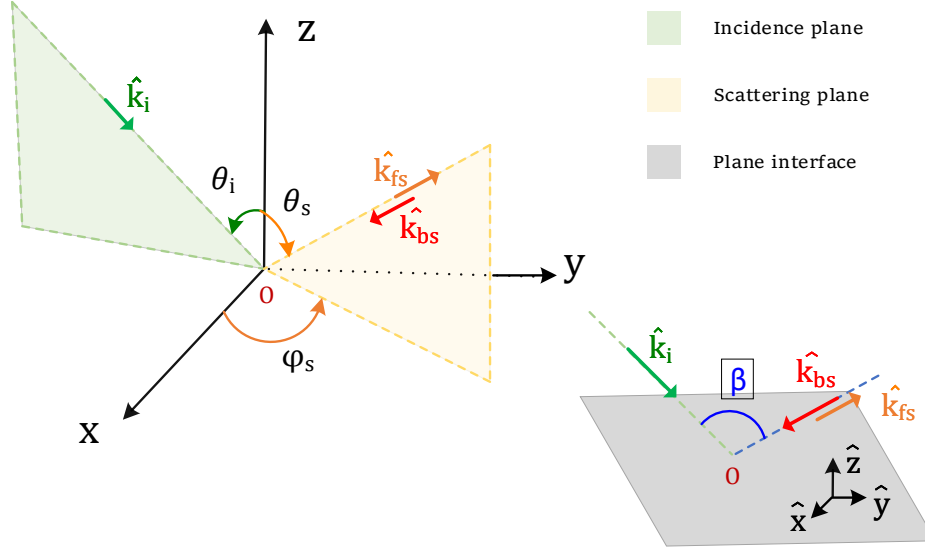


Figure 2.5: Bistatic scattering geometry (spherical coordinates)

In monostatic, the double equality of the angular parameters is obvious: $\theta_i = \theta_s$, $\varphi_i = \varphi_s$.

We consider the incidence versor: $\hat{\mathbf{k}}_i = [-\cos\varphi_i \sin\theta_i, -\sin\varphi_i \sin\theta_i, -\cos\theta_i]^\top$. Then, a backscattering configuration (i.e., BSA) will have $\hat{\mathbf{k}}_i = \hat{\mathbf{k}}_s$ [48].

In a bistatic geometry, when knowing the incidence and scattering directions, the bistatic angle can be obtained as follows:

$$\beta = \cos^{-1}(\hat{\mathbf{k}}_i \cdot \hat{\mathbf{k}}_s) \quad (2.16)$$

For a combination $\{(\theta_i, \varphi_i), (\theta_s, \varphi_s)\}$ in the scattering plane, the bistatic angle will change accordingly. Figure 2.6 displays two maps of bistatic angles covering the space of receiving positions $\varphi_s, \theta_s \in [-90^\circ, 90^\circ]$, when the incidence directions are: (a) $\theta_i = 0^\circ, \varphi_i = 50^\circ$ and (b) $\theta_i = 30^\circ, \varphi_i = 0^\circ$.

2.4.2 Simulation software

Resolution cells having a dominant response from an elementary mechanism are the ones associated to coherent scatterers. Computational electromagnetic simulations are here performed to obtain the monostatic and bistatic scattering response of elementary targets (i.e., dihedral and square plate). With each simulation evaluating only one

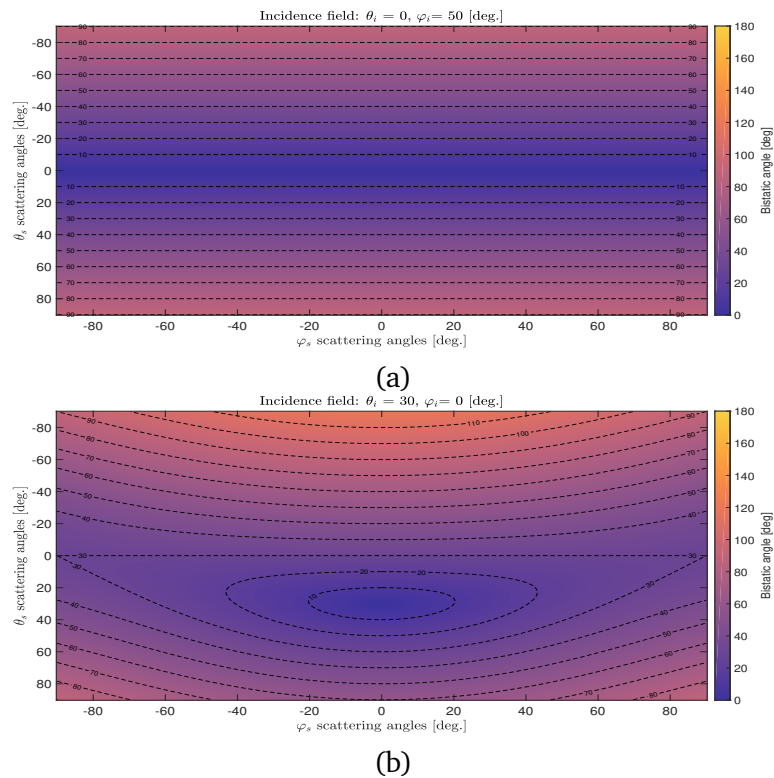


Figure 2.6: Distribution of bistatic angles in the entire scattering range having $\theta_s, \varphi_s \in [-90^\circ, 90^\circ]$ when incident direction is at: (a) $(\theta_i = 0^\circ, \varphi_i = 50^\circ)$. (b) $(\theta_i = 30^\circ, \varphi_i = 0^\circ)$.

target, the results will beyond doubt correspond to a coherent evaluation. The reason behind these simulations is threefold: (a) to obtain full-pol monostatic and bistatic scattering responses, the latter being scarcely available as real data, (b) under a wide range of evaluation angles and (c) with ample control of simulation geometry.

The evaluation frequency is chosen in the C-Band. From a polarimetric perspective, the plate and dihedral are associated to two elementary, distinct scattering mechanisms, i.e., single and double bounce.

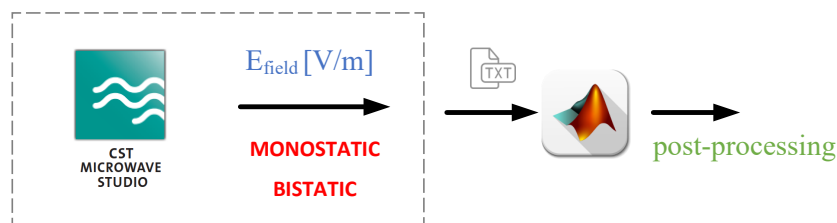


Figure 2.7: Processing workflow integrating the CEM software.

A computational electromagnetic (CEM) software (i.e., CST Microwave Studio -CST MWS) is used to obtain the scattering response. By this, we refer to estimated values of the electric field E_s scattered by each target (far field evaluation). Linear H and

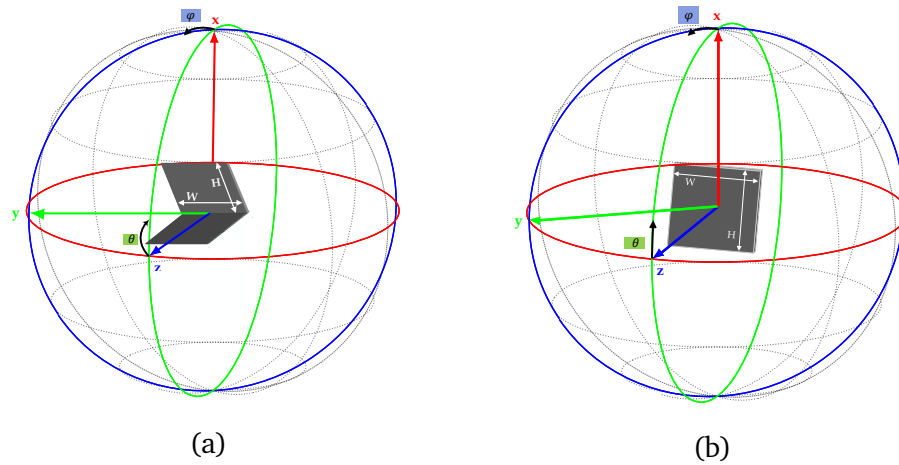


Figure 2.8: Scatterers in spherical coordinate system geometry: (a) 90° Dihedral. (b) Square plate.

V polarization bases are used. Under Assumption 1.2, the polarimetric scattering matrix models a linear dependence between the incident and scattered electric field vectors. As so, the elements of the matrix can be computed having known values of \mathbf{E}_s and \mathbf{E}_i . In each simulation, the V and H incidence components are set to 1 V/m. The general workflow for obtaining estimated components of scattering matrix elements appears in Fig. 2.7. The final objective is to use the RRSME eigenvalue evaluation technique on the simulated data, in the post-processing part. The bistatic SM estimates should no longer verify reciprocity. Results are discussed in Subsection 2.5.

The simulator environment uses a spherical coordinate system (Subsection 2.4.1). The (far-field) incidence/scattered Electric Field can be decomposed in two components:

$$\mathbf{E}_{i,s} = E_{i,s}^{\varphi} \cdot \hat{\varphi} + E_{i,s}^{\theta} \cdot \hat{\theta}, \quad (2.17)$$

where $\hat{\varphi}$ and $\hat{\theta}$ are the spherical versors along the azimuth and elevation directions, respectively.

The θ and φ angles of the spherical coordinate system are defined in the XZ and XY planes (e.g., in Fig. 2.5, Fig. 2.8) and can be expressed as:

$$\theta = \arccos\left(\frac{\hat{z}}{\hat{r}}\right), \quad (2.18) \quad \varphi = \arctan\left(\frac{\hat{y}}{\hat{x}}\right), \quad (2.19)$$

where \hat{r} is the spherical versor of the radial direction and $\hat{x}, \hat{y}, \hat{z}$ are versors of the Cartesian coordinate system. The incidence and scattered versors in the Cartesian system respect the BSA convention.

The geometrical alignment of the two targets, to be evaluated by simulation, is displayed in Fig. 2.8. The center of the coordinate system overlaps with the center of each target. For the dihedral (Fig. 2.8a), the Z axis matches the targets's bisector (and not aligned in the direction of the dihedral's lower plate, contrary to the first impression from Fig. 2.8a). The incidence waves will propagate towards the XOY plane (blue circle). Only the direction having $\theta = 0^\circ$ and $\varphi = 0^\circ$ is aligned along the

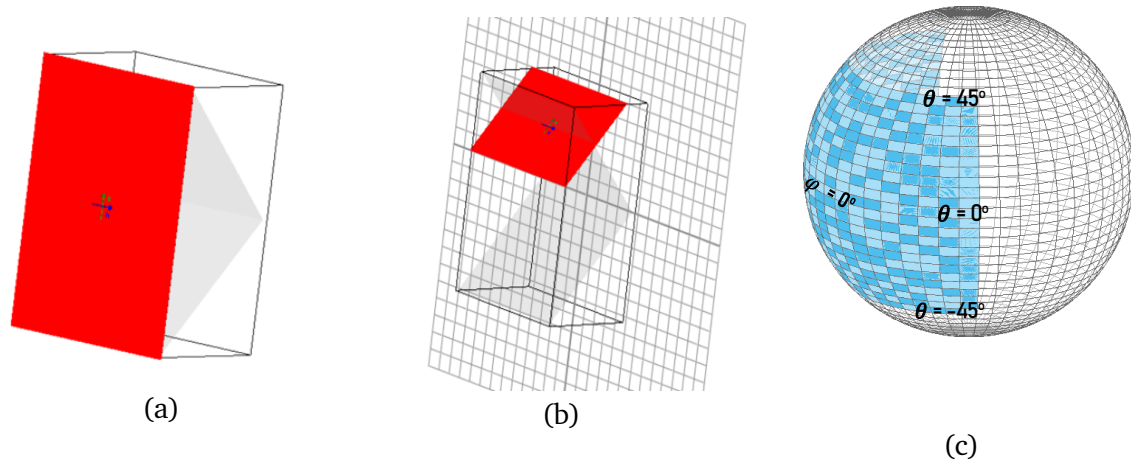


Figure 2.9: Incidence and scattering directions. (a) Plane wave incident from direction having: $\theta_i = 0^\circ, \varphi_i = 0^\circ$ (simulator view). (b) Plane wave incident from direction having: $\theta_i = 45^\circ, \varphi_i = 0^\circ$ (simulator view). (c) Range of incidence/scattering directions covering: $\theta \in [-45^\circ, 45^\circ], \varphi \in [-90^\circ, 90^\circ]$.

Table 2.5: Parameters used for monostatic and bistatic CST simulations.

Scatterer	CST Solver	CST Settings			
		Material	Dimensions	Accuracy setting	Meshing
Monostatic					
90° Dihedral	Integral Equation Solver	PEC	H=W=15λ	Medium	Surface Based (default)
Square Plate		PEC	H=W=15λ	High	High Frequency Mesh
Bistatic					
90° Dihedral	Transient Solver	PEC	H=W=16λ	-40 dB	Hexahedral (default)
Square Plate		PEC	H=W=20λ		High Frequency Mesh

Z axis. A plane wave propagating from this direction and incident on one of the targets will look as in Fig. 2.9(a). The wave propagates from positive to negative Z values. Fig. 2.9(b) displays the example from another incidence direction, i.e., $\theta = 45^\circ$ and $\varphi = 0^\circ$.

For each monostatic simulation, the estimation of received electric field is performed on the same direction to that of the incident plane wave excitation. In bistatic, the excitation plane wave direction is kept fixed, but the backscatter component is computed for a large range of directions having specified θ_s, φ_s values. The blue selection in Fig. 2.9(c) covers a spherical angular range $\theta \in [-45^\circ, 45^\circ], \varphi \in [-90^\circ, 90^\circ]$.

Table 2.5 summarizes the main characteristics of the electromagnetic (EM) simulations used for obtaining the scattering response of each target. A short discussion hereafter provides more details on the settings adopted and extends the information available in the table.

■ Material, Frequency, Dimensions

The simulated objects are large compared to the wavelength and modeled entirely

using an idealized material, a Perfect Electric Conductor (PEC). They have a width/height between $15-20\lambda$, so the objects are considered to operate in the "optical" scattering regime [144]. According to documentation specifications, both solvers used through the simulations can be used with objects from this dimension range.

Both dihedral and plate scatterers are 2D (i.e., objects of zero thickness with a height H and a width W). The monostatic analysis uses the same dimension of the square plates for both the individual scatterer and those composing the 90° dihedral.

The central frequency of the EM signals used in the simulations is $f_0 = 5.405$ GHz. A small-bandwidth (20 MHz around central frequency) is used. The central frequency is the same as the central frequency used by the Sentinel-1 satellites and the frequency at which, in the not-so-distant future, spaceborne large angle bistatic SAR images will be available through the Harmony mission.

■ Meshing and Accuracy

The simulator's front-end offers a graphical solid-modeling functionality for object drawing.

In each simulation, the geometric area of a target is divided into a certain number of meshing domains (or, meshing cells). The voltage/currents distribution inside each mesh cell and, from it, the electric/magnetic fields radiated are estimated using one of the selected numerical solvers. Separately, the program can compute other EM properties of the object, as for example, the Radar Cross Section (RCS).

The two solvers from our simulations (Table 2.5) use different meshing models. Each simulation has used its solver's default technique. The Integral Equation Solver (IES) divides the object's surface through a (curved) triangular and quadrilateral tessellation, while the Transient Solver (TDS) uses hexahedrals (i.e., variable size rectangular cuboids). The latter is a volume meshing element.

Generally, the meshing choice directly impacts the accuracy and time of the simulation (i.e., while a mesh of high density may provide more accurate results, it will take a longer time to evaluate it). In the employed simulator, the two are inter-related. Accuracy is an independent parameter to be specified by the user. If no manual mesh has been defined, one will be automatically generated based on the accuracy settings. The IES has three predefined accuracy levels (low, medium, high). At least the medium selection has been used with all simulations using this solver. Distinctively, the TDS allows the user to specify the value for a stop criterion. The solver stops the evaluation of a meshing cell and returns a result when the signal emitted has sufficiently decayed to zero (i.e., when the energy of the signal arriving at the evaluation port has decreased with $-X$ dB, compared to the maximum). The smaller the X value, the higher the accuracy. The default accuracy setting is of -30 dB and the extreme minimum limit is -80 dB.

■ Electromagnetic Solvers

The scattered E_s field is obtained via full wave electromagnetic analysis. Numerical full-wave solvers make rigorous use of the complete set of Maxwell equations and an important advantage of these field solvers is that they do not impose restrictions on an object's geometry or on the simulation frequency.

– *Integral Equation Solver*

This type of solver uses the integral form of the wave equations and represents the original problems using equivalent sources (current, in this case) placed at boundaries of planar surfaces or in finite volumes. Computations are performed in the frequency domain, which makes it especially powerful for high frequency simulations.

This solver of the CEM software uses the Multilevel Fast Multipole Method (MLFMM) [145, 146]. It is based on the Method of Moments (MoM). The latter is known to provide extremely accurate results with an increased time/memory computation consumption. The MoM uses the exact EM formulas everywhere in the analyzed domain; meanwhile, MLFMM separates between the near and far-field zones and applies a set of approximate formulas to cell areas found in the far field.

This solver has been used with dihedral and plate monostatic simulations (Table 2.5).

– *Transient Solver*

In this case, the solver operates in the time domain and searches for the result of the Maxwell equations through the Finite Integration Technique [147, 148]. Also full-wave, the method rewrites the set of integral equations in a discrete form. The reformulation is based on the summation/difference of electric or magnetic field and flux elements from the edges or faces of each discrete mesh element. It is a well studied method which has been applied, due to its flexibility, not only for CEM, but to wave problems in many domains [149]. In time domain, the simulation starts when a time domain signal, typically a Gaussian pulse, is emitted towards the structure under observation [145, 150].

This solver has been used for bistatic EM computations with the dihedral and plate targets (Table 2.5).

2.4.3 Radar cross-section and monostatic evaluations

2.4.3.1 RCS Definitions

From the IEEE Standards [2], the Scattering Cross Section (SCS) is an equivalent area of an object under observation and which depends on the frequency, polarization and direction of the plane wave incident on the object. The SCS (σ) multiplied by the incident power (P_i) produces by isotropic radiation the same amount of scattering power as the original object when measured on a fixed direction:

$$P_s = \frac{\sigma P_i}{4\pi r^2}. \quad (2.20)$$

Eq. (2.20) is representative for the monostatic case, with r representing the one-way distance between radar and target.

The Radar Cross Section (RCS) is the SCS measured at a given polarization. It is influenced by the geometrical and physical properties of the target. Nonetheless, the

RCS itself does not necessarily relate to the object's physical size and is independent on the distance between the object and the radar (i.e., definition imposed in the far field). The formal monostatic RCS formula is then [151, 4]:

$$\sigma_{xy} = \lim_{r \rightarrow \infty} 4\pi r^2 \frac{|\mathbf{E}_s^X|^2}{|\mathbf{E}_i^Y|^2}. \quad (2.21)$$

For distributed targets (e.g., ground, sea) the average RCS per unit area, also known as the normalized radar cross section (σ_0) is usually used.

Comparing (2.21) and (1.12), one can express the following connection between the elements of the scattering matrix and the RCS measured using a generic X-Y polarimetric basis combination [144]

$$\begin{bmatrix} \sigma_{xx} & \sigma_{xy} \\ \sigma_{yx} & \sigma_{yy} \end{bmatrix} = \lim_{r \rightarrow \infty} 4\pi r^2 \begin{bmatrix} |S_{xx}|^2 & |S_{xy}|^2 \\ |S_{yx}|^2 & |S_{yy}|^2 \end{bmatrix}. \quad (2.22)$$

Based on these relations, the intensity of SAR images is usually interpreted through the lenses of the RCS (for point targets). Nonetheless, it is essential to state that while this model is quite popular it represents only a simplified assumption. As argued by Döring et al. [13], the final radiometric intensity of SAR images may not be proportional to the RCS when considering the dependencies on aspect angle and frequency (both varying in an interval with real measurements) and the filtering of the original field measurements \mathbf{E}_s^X , \mathbf{E}_i^Y through the SAR complex point spread function.

These advanced effects are not considered when estimating the scattering matrix coefficients of the two elementary targets presented in the first part of this Section. It is important to emphasize that the estimation of scattering matrix coefficients is based exclusively on the simulated (amplitude and phase) electric field values and not on RCS.

Based on this, the following assumptions apply for the results:

Assumptions Set - 2.1.

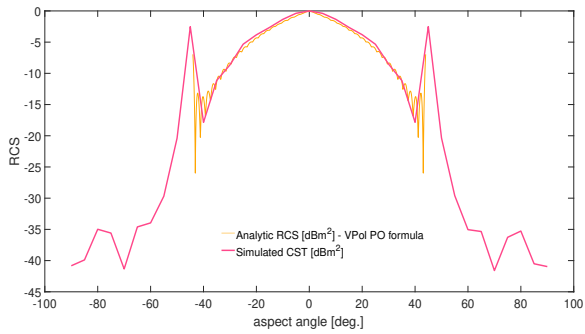
- I. The coefficients of the scattering matrix are proportional to the corresponding radar cross section square roots.
- II. The estimated coefficients of the scattering matrix are proportional to the ratio between the estimated scattered and incident electric fields.

2.4.3.2 Verification of monostatic simulations

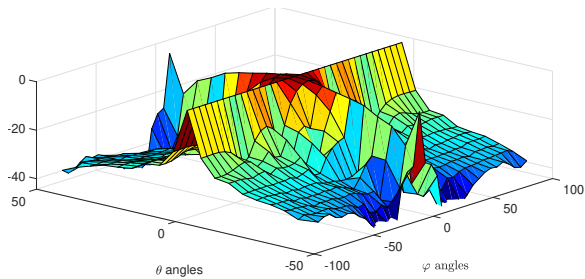
The estimated monostatic/bistatic scattering matrices cannot be directly verified apart from the monostatic estimates at coordinates $\{\theta = 0^\circ, \varphi = 0^\circ\}$, for which well-known

expressions exist (Table B.1). Two distinct testing strategies are proposed and assimilated as qualitative evaluations for the estimated results. The first evaluation is indirect, based on 1D RCS comparison between values obtained from simulation and values obtained through analytic formulas (and which are available, in the monostatic case, for both plate and dihedral targets). The second evaluation is also indirect, but uses the estimated scattering matrices. These are used to compute two roll-invariant, coherent, PolSAR parameters which have known values for the plate and dihedral (i.e., odd-bounce and even-bounce scattering mechanisms). The two testing strategies are applied only to the simulated monostatic data because, for them alone, compact and well-known analytic expressions (for the first evaluation strategy) and reliable parameter interpretations (for the second evaluation strategy) are available in the literature.

2.4.3.2.1 RCS verification



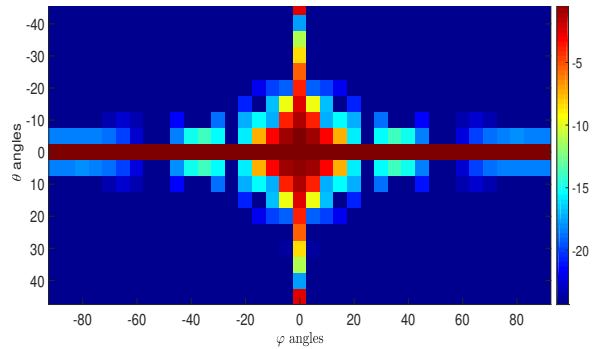
(a)



(b)

Figure 2.10: Monostatic Dihedral (V Polarization). (a) RCS comparison: CST simulated vs. analytic formula (1D, $[dBm^2]$).

CST Simulated: Absolute value for normalized Electric Field E_s $[dB(V/m)]$: (b) 3D. (c) 2D.



(c)

Modeling the RCS scattering of simple targets has been for a long time a subject of study in the electromagnetics scientific community. Nonetheless, the largest volume of work covers the monostatic case and the metallic plate and dihedral are two elementary models.

Physical Optics (PO) models are used, in general, for approximations at high frequencies (or when the ratio between a body's dimension and the wavelength is much greater than 1) and near-specular observations. The model is limited to some extent, as it does not consider more complex scattering phenomena, as: edge diffraction, multiple bounces, traveling or creeping waves, etc. Even so, it remains popular in radar as it proposes closed form approximations for the RCS of the elementary targets.

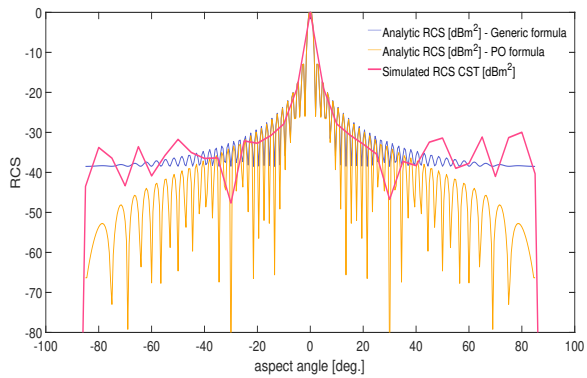
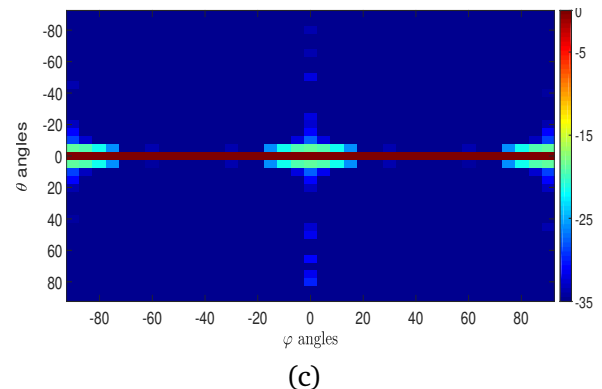
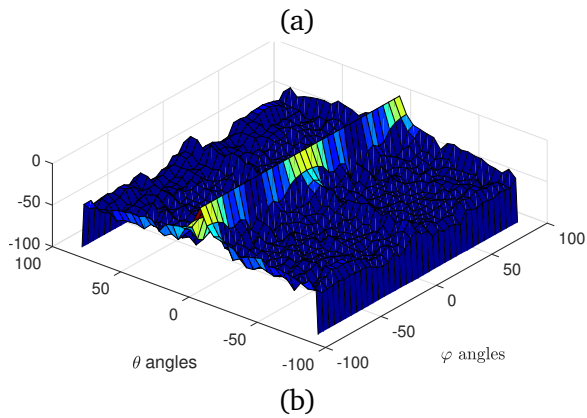


Figure 2.11: Monostatic Plate (V Polarization). (a) RCS comparison: CST simulated vs. 2 analytic formulas (1D, [dBm²]).

CST Simulated: Absolute value for normalized Electric Field E_s [dB(V/m)]: (b) 3D. (c) 2D.



With the CST simulator, the Integral Equation Solver is generally recommended for RCS computation [145]. This has been used for both (monostatic) dihedral and plate simulations and the RCS has been retrieved along with the estimated values of the electric field. With the availability of analytic RCS for the two objects, comparisons are displayed in Fig. 2.10(a) and Fig. 2.11(a).

■ Monostatic plate

Under the PO approximation and considering incident waves from angles (θ, φ) , the backscattering RCS of a perfectly conducting thin rectangular plate with edges of length $2a$ and $2b$ is:

$$\sigma_{plate,PO} = \frac{4\pi a^2 b^2}{\lambda^2} \left(\frac{\sin\left(\frac{2\pi a}{\lambda} \sin\theta \cos\varphi\right)}{\frac{2\pi a}{\lambda} \sin\theta \cos\varphi} \frac{\sin\left(\frac{2\pi b}{\lambda} \sin\theta \sin\varphi\right)}{\frac{2\pi b}{\lambda} \sin\theta \sin\varphi} \right)^2 (\cos\theta)^2 \quad (2.23)$$

According to [144], the expression is generally valid for (positive) aspect angles in $[0^\circ, 20^\circ]$. For values in a larger evaluation interval, an extended model for RCS is proposed otherwise. The set of equations for this RCS model is directly available in the reference. In Fig. 2.11(a), the results from the simple and extended analytic models (yellow and blue) is compared to the one obtained using the EM simulator (pink). The displayed results are for vertical polarization. The incidence is constant along one dimension ($\varphi = 0^\circ$) and the aspect angle varies between -90° and 90° . From values $|\theta| \leq 35^\circ$, the simulated RCS better

matches the power variation from the generic formula. All three curves show analogous angular positions for the local minimum and maximum extremas in their side-lobes. Nonetheless, the pink curve is coarser as the EM simulations are performed with a stepsize of 5° (in both azimuth and elevation), while the analytic model uses a finer step size. Figures 2.11(b) and (c) show the variation in both directions of the simulated electric field \mathbf{E}_s . The monostatic directions used for simulation cover the entire range $\theta, \varphi \in [-90^\circ, 90^\circ]$, i.e., from normal incidence on the metallic plate to reflection/refraction towards its edges. Strong specular reflections are observed near normal incidence on the plate's facet.

■ Monostatic dihedral

Under the most simple approximation, the right-angle dihedral is formed by the alignment at 90° of two plate objects, around one of their edges. We consider the two plates named A and B. For computing the monostatic RCS of the dihedral corner reflector, the PO approximation sums the contributions of: two double-bounce (from A to B and from B to A) and two single-bounce (one on each plate) scattering effects. The complete model can be found in [152, 151] and is valid for observation angles $\theta \in [-45^\circ, 45^\circ]$. The two side-lobes peaks at $\pm 45^\circ$ are considered to come from the single-bounce effects on the two plates [153]. When compared to the RCS obtained through the computational electromagnetic software (computed in a much larger observation interval, but with a step of 5°) there is a comparable decrease in power. The simulated monostatic electric field \mathbf{E}_s (V Polarization) scattered from the dihedral is shown (2D and 3D display) in Figs. 2.10(b)-(c). It is evaluated in angular intervals: $\theta \in [-45^\circ, 45^\circ]$ and $\varphi \in [-90^\circ, 90^\circ]$, so that all monostatic directions which can produce a scattering response from the interior of the dihedral are covered.

■ On bistatic RCS formulations

For the bistatic case, there are fewer analytic models available.

In many works, the quest for a bistatic RCS model has begun by an adaptation of the monostatic RCS analysis. Around 1965, Kell formulated a first Monostatic to Bistatic Equivalence Theorem (MBET) [154]. A review for some of the well-known MBET formulations is given in the introduction of [155]. The most generic MBET states that, for sufficiently smooth targets, the Bistatic Radar Cross Section (BiRCS) evaluated at one bistatic angle β is proportional to the Monostatic RCS measured on the bisector of the bistatic angle. An attempt for determining a threshold value for the compliance of the MBET is offered in [156], through simulations of 2D scatterers. The authors show that the MBET depends greatly on the so-called "smoothness" of a point target (understood as the property of a target to produce single or multipath propagation) so that the angular interval of MBET compliance decreases as the target's geometry produces multipath or shadowing effects. For experimental targets having a higher "smoothness", the study reports a maximum angle for which the MBET equivalence holds of $\approx 14^\circ$, while this angle decreases to $\approx 1.5^\circ$ with objects having very complex geometries and which are not "smooth".

No comparisons are performed for the bistatic RCS case in the thesis. At the same time, this verification can represent an extension for the work currently presented. Recent works as [157, 158, 159] have proposed some analytic models which approximate the bistatic scattering from plates and dihedrals.

2.4.3.2.2 SM verification through roll-invariant parameters

Table 2.6: Monostatic dihedral and plate results. Evaluation based on angular polarimetric descriptors. Percentage distribution of estimated values in 10° intervals between $[0^\circ, 90^\circ]$ (for all observation directions in the investigated range).

(a) Monostatic 90° Dihedral ($\theta \in [-45^\circ, 45^\circ]$, $\varphi \in [-90^\circ, 90^\circ]$)									
Angular intervals for values of polarimetric descriptor: [upper _{limit} , lower _{limit}] [deg.]									
	90–80	80 - 70	70 - 60	60 - 50	50 - 40	40 - 30	30 - 20	20 - 10	10 - 0
α_{Cloude}	28.7 %	18.2 %	12.8 %	9.8 %	15.1 %	8.53 %	4.03 %	1.42 %	1.42 %
α_{TSVM}	28.7 %	17.5 %	11.8 %	9.8 %	12.95 %	11.7 %	4.7 %	1.42 %	1.42 %

(b) Monostatic Plate ($\theta \in [-90^\circ, 90^\circ]$, $\varphi \in [-90^\circ, 90^\circ]$, but with multiple filtered directions)									
Angular intervals for values of polarimetric descriptor: [upper _{limit} , lower _{limit}] [deg.]									
	90 - 80	80 - 70	70 - 60	60 - 50	50 - 40	40 - 30	30 - 20	20 - 10	10–0
α_{Cloude}	2.32 %	3.48 %	6.72 %	13.0 %	18.8 %	9.28 %	8.12 %	16 %	22.27 %
α_{TSVM}	2.08 %	3.71 %	5.9 %	13.45 %	17.86 %	8.32 %	7.65 %	13.9 %	27.13 %

This subsection describes the second evaluation strategy of the simulated monostatic results. Two monostatic roll-invariant polarimetric descriptors are introduced for this task. The rotation invariance property (in short notation, *roll-invariance*) means that the values of such parameters are not affected by rotations of the target around LOS. The parameters to be used are:

(a) the coherent Cloude and Pottier α -angle (an equivalent form, compared to the one seen earlier in Chapter 1 and hereafter named as α -Cloude) [76, 136]:

$$\alpha_{Cloude} = \arccos\left(\frac{1}{\sqrt{2}} \frac{|S_{hh} + S_{vv}|}{\|\mathbf{S}\|_F}\right) \quad (2.24)$$

One can observe the similarity between (2.24) and the NRF definition in (2.14). Except for the \arccos inversion, only the denominator differs. While (2.24) analyses the total contribution of the co-pol channels, (2.14) uses the difference between the cross-pol ones.

(b) the α angle of the Touzi TSVM decomposition (α_{TSVM}) which appears in the parametrization of the symmetric target scattering vector [50]:

$$\mathbf{k}_{TSVM} = m \cdot e^{j\Phi_s} \begin{bmatrix} 1 & 0 & 0 \\ 0 & \cos 2\Psi & -\sin 2\Psi \\ 0 & \sin 2\Psi & \cos 2\Psi \end{bmatrix} \begin{bmatrix} \cos \alpha_{TSVM} \\ \sin \alpha_{TSVM} \cdot e^{j\Phi_{\alpha_{TSVM}}} \\ 0 \end{bmatrix}. \quad (2.25)$$

For symmetric (in the polarimetric sense) monostatic targets, the two parameters are expected to provide the same result [50]. Also, the two polarimetric descriptors have well-known values for the phenomenology of monostatic odd and even bounce, which characterize the response of the plate and dihedral, respectively.

The result of the indirect evaluation, through the two parameters, is presented hereafter.

■ Monostatic dihedral

The theoretical value which the two parameters attribute to monostatic dihedral scattering is of 90° . Article [103] reports an acceptable statistical variation of $\pm 10^\circ$ in the case of real quad-pol data. For all the monostatic directions investigated, Table 2.6(a) shows the percentage distribution of obtained values in each 10° interval in the $[0^\circ, 90^\circ]$ range.

Variations of at most $\pm 20^\circ$ in the θ direction (any φ value) seem to not produce significant changes of the scattering mechanism (Fig. 2.12(a),(b)). Moreover, for more than 45% of the analyzed monostatic directions, the values of the two polarimetric descriptors remain in the $[70^\circ, 90^\circ]$ range. For observation directions in the upper/lower parts of each dihedral's plate, near the edges, the estimated α values suggest a scattering mechanism similar to that of a dipole ($\alpha_{Cloude}, \alpha_{TSVM} \in [40^\circ, 50^\circ]$). Because of the edge's proximity this result is not surprising.

There are studies which propose that any elementary scattering matrix can be written as a coherent sum of oriented and unoriented dipole scatterers with fixed spatial separations [160, 161]. For example, the dihedral scattering matrix is modeled by two orthogonal dipoles (one H and one V) at a $\frac{\lambda}{4}$ separation, while the scattering matrix of (right and left) rotated dihedrals are written using dipoles with $\pm 45^\circ$ orientation angles. Based on this assumption, oriented dipoles can be used to decompose the phenomenology of randomly oriented dihedrals. And within our results, it is analogously possible to interpret that, depending on orientation, one of such dipole components becomes dominant, as shown for very skewed directions.

■ Monostatic plate

In case of the monostatic plate, there are directions for which the absolute values of the normalized simulated electric field are quite low (Fig. 2.11c). All for which a scattering response lower than -25 dB has been obtained are filtered from the analysis. This threshold is set after comparison with the dihedral's case, where almost all directions have a (normalized) scattering response larger than this limit (Fig. 2.10c). This allows for a consistent evaluation between scatterers. The directions filtered are shown in white for Figs. 2.13, 2.15 and they are not considered in any way for further computations. From an experimental setting, article [162] presents experimental evidence that oriented plates are expected to present a smaller backscattering response.

For the even-bounce scattering mechanism, the expected value of both α parameters is around 0° (\pm statistical fluctuations). Figs. 2.13(a),(b) indicate such values are dominant for directions having $\theta \in [-20^\circ, 20^\circ]$ and $\varphi \in [-35^\circ, 35^\circ]$. However, the sum of contributions having α around $[40^\circ, 50^\circ]$ or $[50^\circ, 60^\circ]$ is much greater than the contribution near smaller α values, as observed in Table 2.6(b). These α intervals are associated to a dipole scattering mechanism. The directions with such contribution appear around skewed incidence/scattering directions (Fig. 2.13).

In [160], the (unoriented) surface target has a SM obtained from two orthogonal H and V dipoles with a separation of $\frac{\lambda}{2}$. As so, in the oriented case, only one of these dipole components may become dominant, which is observed by our parametric evaluation. Nonetheless, this observation is only an assumption; further investigations would be necessary to prove it.

Fig. 2.13(c) analyzes the difference in α values between α_{Cloude} and α_{TSVM} . The color coding indicates predominantly small differences.

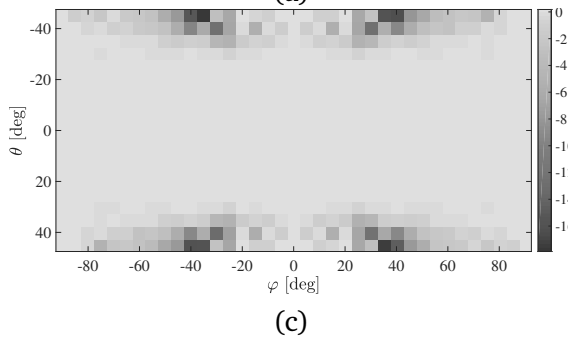
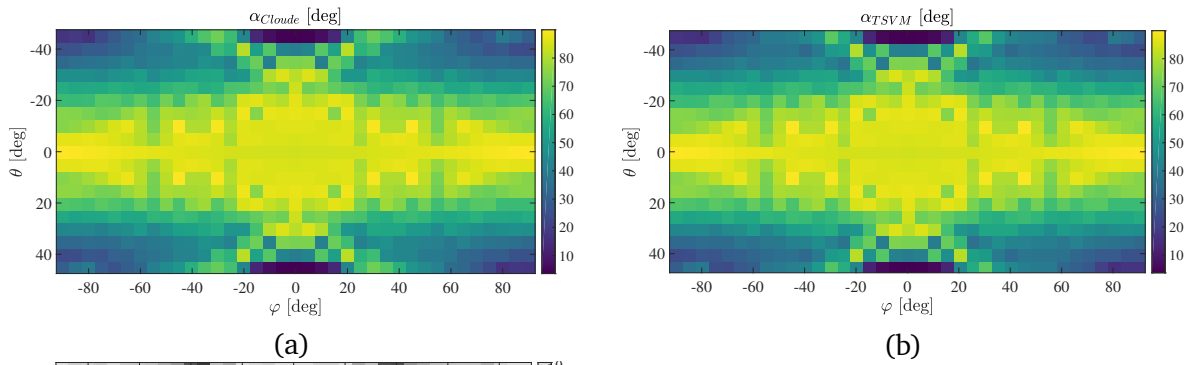


Figure 2.12: Monostatic 90° Dihedral. (a) Estimation of α_{Cloude} parameter for the dihedral's response for all observation directions. (b) Estimation of α_{TSVM} parameter for the dihedral's response for all observation directions. (c) Difference between results from (a) and (b).

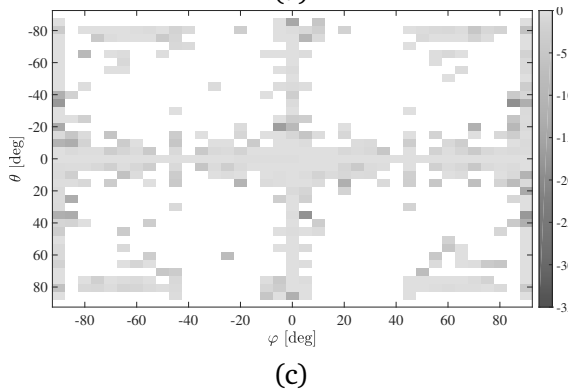
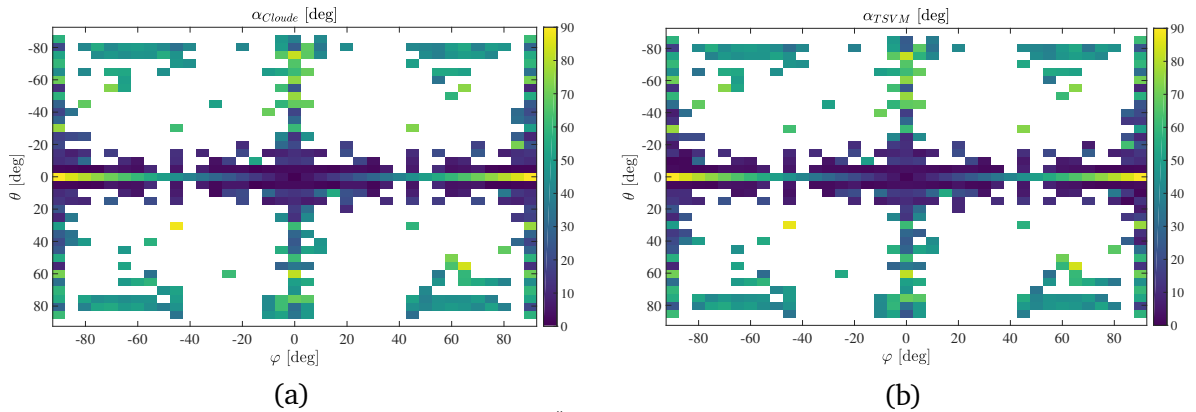


Figure 2.13: Monostatic Square Plate. (a) Estimation of α_{Cloude} parameter for the plate's response for a selection of observation directions. (b) Estimation of α_{TSVM} parameter for the plate's response for a selection of observation directions. (c) Difference between results from (a) and (b).

2.5 RRSM Eigen-classification with simulated data

This section continues the study of the relationship between the nonreciprocity parameter and the RRSM eigenvalues, started in Section 2.3. The simulated monostatic and bistatic data introduced in Section 2.4 is used.

2.5.1 Monostatic simulations

For the monostatic simulations, some information has already been presented in the two-folded verification of both RCS and estimated SM parameters. All results to follow are obtained using only the estimated SM.

- **Monostatic dihedral** Absolute NRF values (2.14) corresponding to the estimated scattering matrices in the simulation range ($\theta \in [-45^\circ, 45^\circ]$, $\varphi \in [-90^\circ, 90^\circ]$) are shown in Fig. 2.14(a). For almost all incidence/scattering positions, the estimated scattering matrices appear to verify reciprocity. However, around the $\theta=0^\circ$ region, $|\zeta|$ approaches 0.4–0.5 for $|\varphi| \geq 45^\circ$. Figure 2.14(b) displays a color-coded image separating between positions which have RRSM returning real (shades of blue) or complex (orange) eigenvalues. The classification is performed as presented in Annex E and Fig. E.1. The three categories have percentages as follows: 97.72% (real distinct eigenvalues pairs), 0.85% (real equal eigenvalues pairs), 1.42% (complex pairs).

Around the $\theta=0^\circ$ region the type of RR eigenvalues varies from real-distinct (near normal incidence) to real-equal and then complex. For all other directions in the monostatic dihedral results, the RRSM eigen-decomposition returns real values.

The scattering from oriented dihedrals is known to cause interpretation problems in monostatic PolSAR. Experimental results have confirmed that rotations around LOS determine an increase in the power from the cross-channel components and for a rotation angle equal to 45° the co-channel components S_{hh} and S_{vv} become zero. For example, an acknowledged effect of oriented dihedral in urban environments is its misinterpretation in incoherent, model-based decomposition techniques as volume scattering [163]. From our current result, the RRSM eigen-classification may offer through its complex eigenvalues a clear evidence of such an effect, independently or complementary to the NRF.

- **Monostatic plate**

As in the analysis from Fig. 2.13, only non-filtered directions are evaluated.

Compared to the results obtained for the dihedral, the plate scatterer appears to be more sensitive for variations of the φ angle at $\theta = 0^\circ$. The pattern can be observed by the rapidly increasing absolute values of the NRF parameter which becomes equal to 1 with $|\varphi| \geq 45^\circ$ (Fig. 2.15a). However, here the RRSM eigenvalues are of complex type even for values $|\zeta|$ lower than 0.5 (Fig. 2.15b). If the results from the α parameters evaluation (Figs. 2.13a,b) are considered, the change around $\theta=0^\circ$ produces the variation of the two angular parameters in their entire definition range.

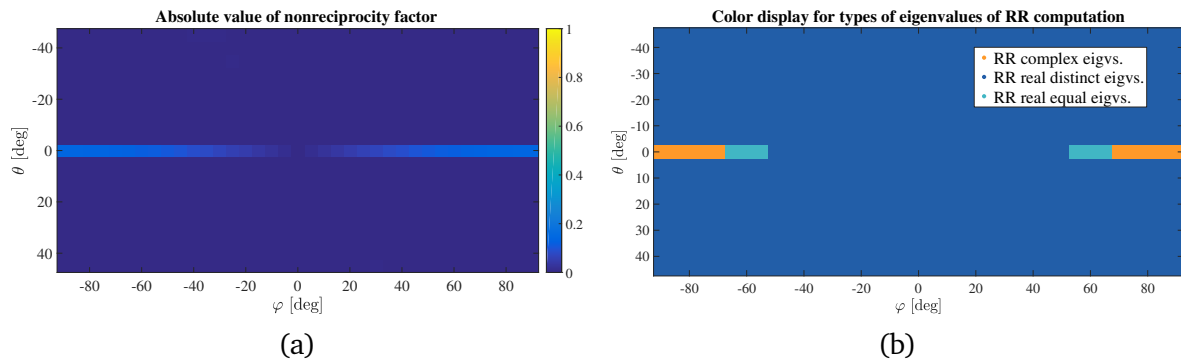


Figure 2.14: Monostatic Dihedral. (a) Absolute value of nonreciprocity factor. (b) RRSM eigen-classification color image.

Similar to the dihedral's case, for other directions characterized by non-zero θ and ϕ angles, there are no large changes for the NRF or the RRSM eigenvalues type.

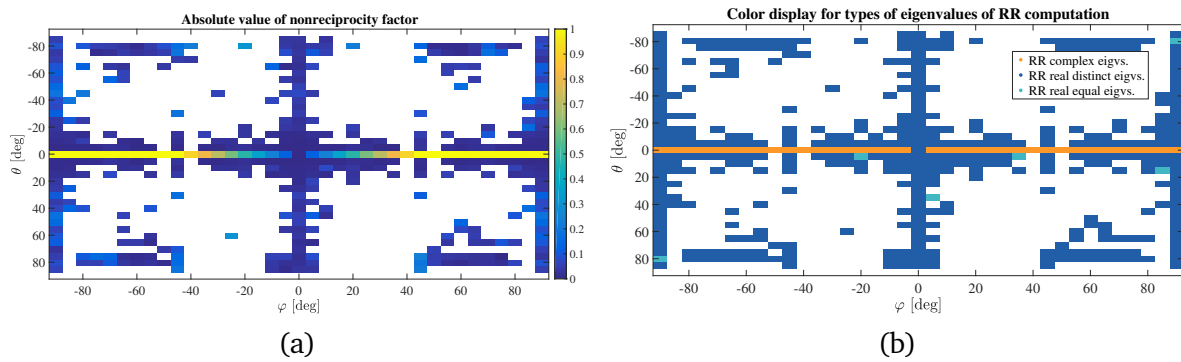


Figure 2.15: Monostatic Plate. (a) Absolute value of nonreciprocity factor. (b) RRSM eigen-classification color image.

2.5.2 Bistatic simulations

In the bistatic simulations, for each unique incidence/scattering angle combination $\{(\theta_i, \varphi_i), (\theta_s, \varphi_s)\}$, one estimation is obtained. For the results hereafter, the range of scattering directions covers $\theta_s, \varphi_s \in [-45^\circ, 45^\circ]$ (evaluation step of 0.5°).

Only a discrete selection of incidence directions is evaluated. Three values are considered for θ_i , i.e., 0° , 25° , 40° , while $\varphi_i = 0^\circ$ stays fixed. Each of these incidence directions are enough distinct and together cover a wide range in elevation, which allows for an extensive study of the bistatic scattering phenomena with each target. The two nonzero angles are quite close to the expected near- and far-range incidence angles of the future bistatic Harmony mission, of 20° and 44° [138], respectively. More, the central frequency of all simulations is equal to the central frequency used by the Sentinel-1 satellites. Choosing these parameters provides an immediate application context for the bistatic simulations.

Table 2.7: Bistatic dihedral/plate/sphere simulation results. RRSM eigen-classification percentage distribution.

Three incidence directions are considered: $(\theta_i, \varphi_i) \in \{(0^\circ, 0^\circ), (25^\circ, 0^\circ), (40^\circ, 0^\circ)\}$.

Incidence direction (θ_i, φ_i)	Real eigvs. pairs [%]		Complex eigvs. pairs [%]	Total [%]
	distinct	equal		
90° Dihedral				
$(0^\circ, 0^\circ)$	62.23	30.86	6.9	100
$(25^\circ, 0^\circ)$	73.17	7.17	19.65	100
$(40^\circ, 0^\circ)$	63.91	2.28	33.81	100
Square Plate				
$(0^\circ, 0^\circ)$	14.25	1.21	84.54	100
$(25^\circ, 0^\circ)$	21.95	1.81	76.24	100
$(40^\circ, 0^\circ)$	30.46	3.2	66.34	100

For each bistatic Rx direction, the simulated data is used to estimate scattering matrix elements. These are finally evaluated using the nonreciprocity factor and the RRSM eigenvalues classification. Additionally, the influence of the bistatic angle (Eq. 2.16) is now considered.

Results in Figs. 2.16, 2.17 are displayed using a common template in which:

- the first row displays the absolute value of the estimated electric field [dB].
- the second row shows the absolute value NRF obtained from estimated SM. The second and third rows are displayed with an overlay grid of iso-bistatic angle curves.
- the third row is a color-coded representation of the RRSM eigen-classification. Three main classes are used, as follows: orange - complex eigenvalues, dark blue - two real, distinct pairs of eigenvalues, cyan - two real, equal pairs of eigenvalues. The global percentage in each category can be consulted in Table 2.7.
- the fourth row shows the eigen-classification as a function of the bistatic angle. For bistatic intervals of 5° increment, the results have been transformed in an absolute percentage scale (100% for summation of all three categories). The complete values are directly available in Table 2.8. In a relative scale analysis, all percentages of one category from Table 2.8 should sum to the value in Table 2.7.

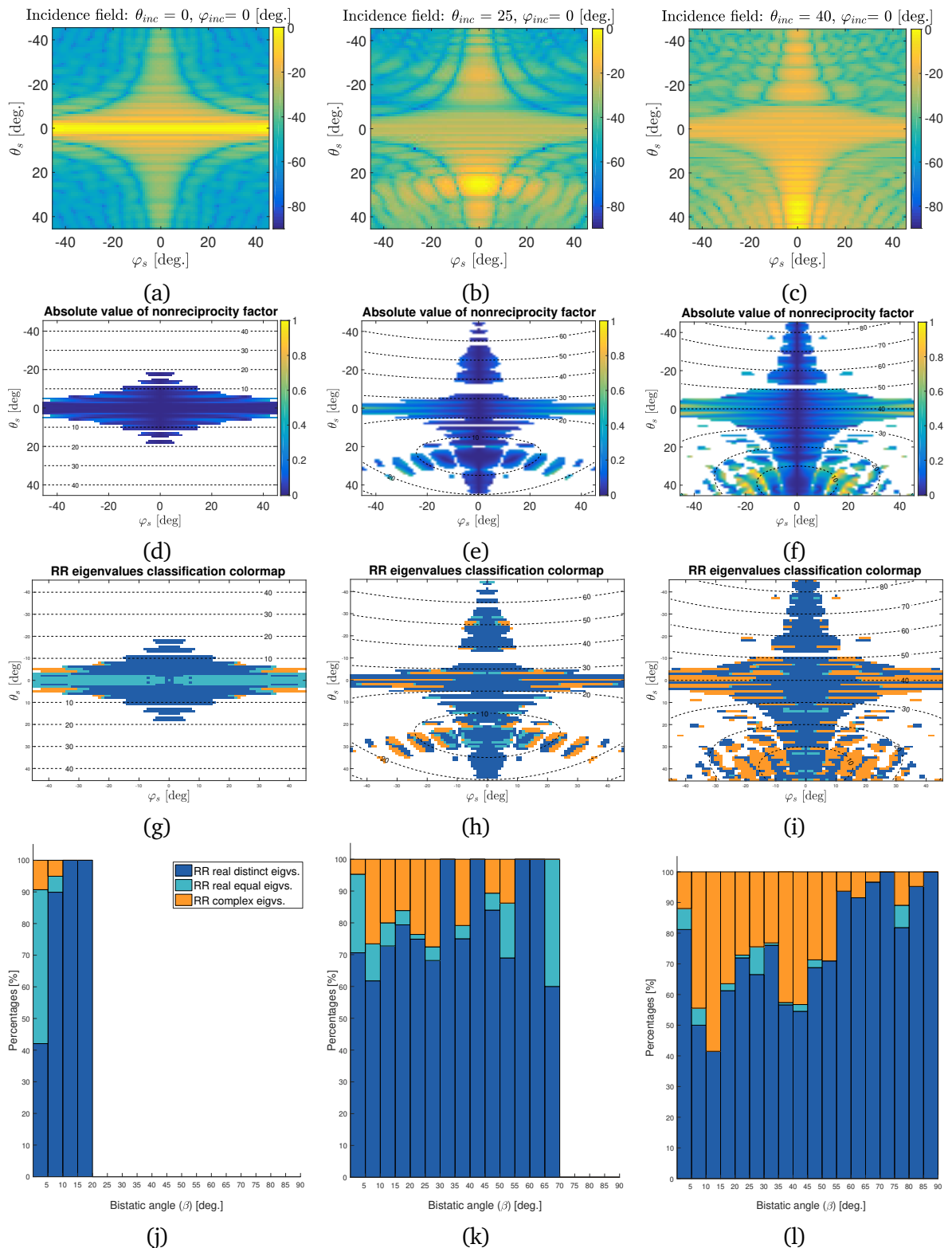


Figure 2.16: 90° Dihedral (Bistatic Results, Time Domain Solver).

Incidence directions at $\varphi_i = 0^\circ$ and $\theta_i = 0^\circ$ (first column), $\theta_i = 25^\circ$ (second column), $\theta_i = 40^\circ$ (third column) and scattering directions $\theta_s, \varphi_s \in [-45^\circ, 45^\circ]$.

(a)-(c) Normalized absolute value of bistatic E_s (in dB(V/m)), V Polarization). (Following results are after selecting scattering directions at which $|E_s| \geq -30$ dB)

(d)-(f) Absolute values of nonreciprocity factor

(g)-(i) RRSM eigen-classification type (color-coded image).

(j)-(l) RRSM eigen-classification as bargraphs for bistatic angle intervals between $[0^\circ, 90^\circ]$.

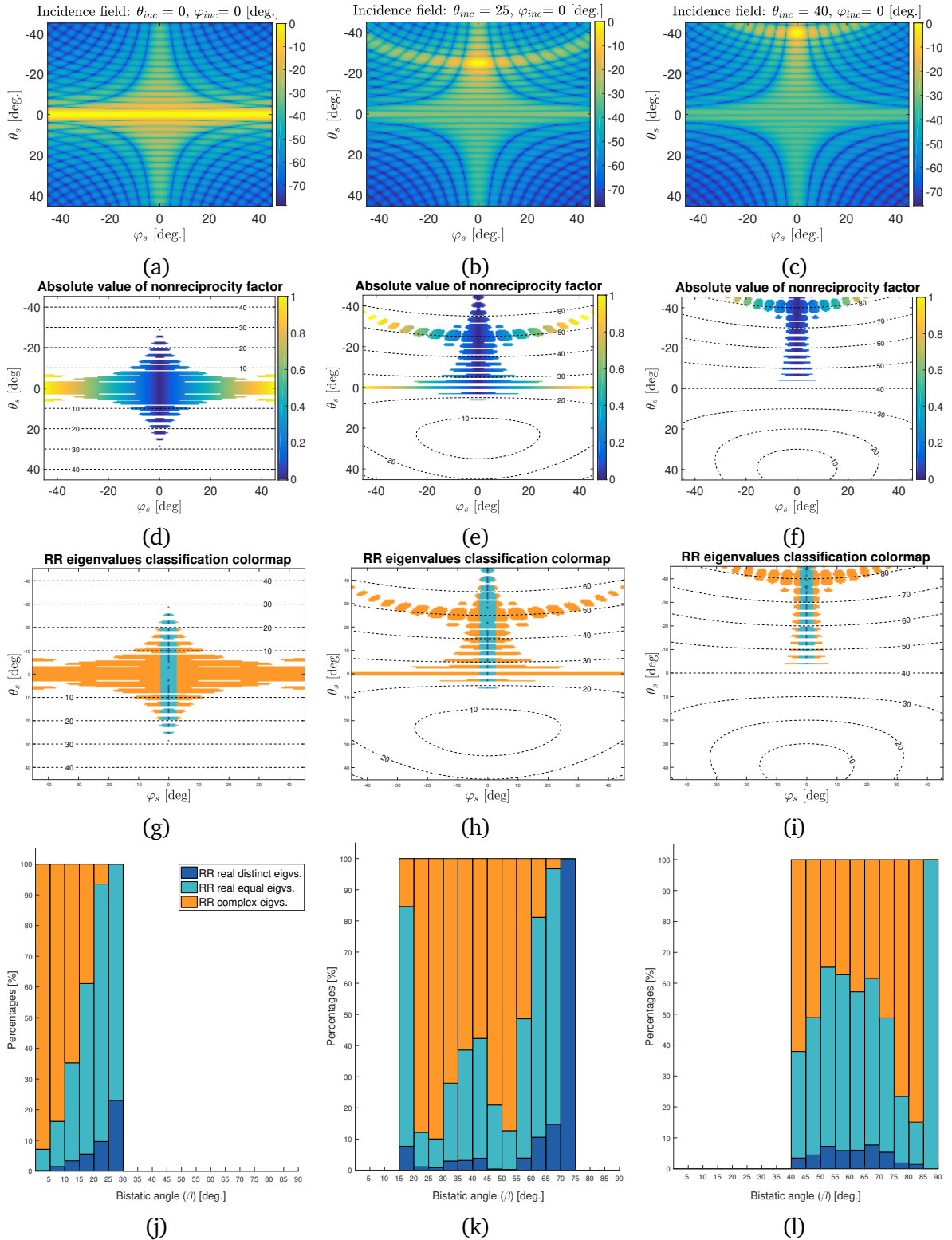


Figure 2.17: Square Plate (Bistatic Results, Time Domain Solver).

Incidence directions at $\varphi_i = 0^\circ$ and $\theta_i = 0^\circ$ (first column), $\theta_i = 25^\circ$ (second column), $\theta_i = 40^\circ$ (third column) and scattering directions $\theta_s, \varphi_s \in [-45^\circ, 45^\circ]$.

(a)-(c) Normalized absolute value of scattered bistatic E_{field} ([dB(V/m)], V Polarization). (Following results are after selecting scattering directions at which $|E_s| \geq -30$ dB).

(d)-(f) Absolute values of nonreciprocity factor

(g)-(i) RRSM eigen-classification type (color-coded image).

(j)-(l) RRSM eigen-classification type as bargraphs for bistatic angle intervals between $[0^\circ, 90^\circ]$.

Table 2.8: Bistatic dihedral and plate simulation results. RRSM eigen-classification vs. intervals of bistatic angles, $\beta \in [0^\circ, 90^\circ]$, with 5° increment. Three incidence directions are considered: $(\theta_i, \varphi_i) \in \{(0^\circ, 0^\circ), (25^\circ, 0^\circ), (40^\circ, 0^\circ)\}$.

		Bistatic angles (β) intervals [deg.]																	
		0 - 5	5 - 10	10 - 15	15 - 20	20 - 25	25 - 30	30 - 35	35 - 40	40 - 45	45 - 50	50 - 55	55 - 60	60 - 65	65 - 70	70 - 75	75 - 80	80 - 85	85 - 90
90° Dihedral																			
$(0^\circ, 0^\circ)$																			
RR real distinct eigvs. [%]	42.06	89.89	100	100	0	0	0	0	0	0	0	0	0	0	0	0	0	0	0
RR real equal eigvs. [%]	48.63	5.05	0	0	0	0	0	0	0	0	0	0	0	0	0	0	0	0	0
RR complex eigvs. [%]	9.3	5.05	0	0	0	0	0	0	0	0	0	0	0	0	0	0	0	0	0
$(25^\circ, 0^\circ)$																			
RR real distinct eigvs. [%]	70.59	61.77	72.73	79.37	74.87	68.23	100	75	100	84	68.96	100	100	60	0	0	0	0	0
RR real equal eigvs. [%]	24.71	11.63	7.27	4.48	1.47	4.27	0	4.16	0	5.3	17.24	0	0	40	0	0	0	0	0
RR complex eigvs. [%]	4.7	26.6	20	16.14	23.64	27.5	0	20.83	0	10.6	13.8	0	0	0	0	0	0	0	0
$(40^\circ, 0^\circ)$																			
RR real distinct eigvs. [%]	81.2	50.05	41.47	61.25	71.94	66.52	76.06	56.64	54.53	68.7	70.96	93.7	91.55	96.6	100	81.82	95.24	100	100
RR real equal eigvs. [%]	6.83	5.5	0	2.28	0.91	9.05	0.77	0.75	2.21	2.53	0	0	0	0	0	7.27	0	0	0
RR complex eigvs. [%]	11.96	44.44	58.52	36.46	27.15	24.43	23.16	42.61	43.26	28.76	29.1	6.3	8.45	3.3	0	10.91	4.76	0	0
Square Plate																			
$(0^\circ, 0^\circ)$																			
RR real distinct eigvs. [%]	0.18	1.48	3.36	5.57	9.67	23.1	0	0	0	0	0	0	0	0	0	0	0	0	0
RR real equal eigvs. [%]	6.91	14.76	31.93	55.55	83.87	76.9	0	0	0	0	0	0	0	0	0	0	0	0	0
RR complex eigvs. [%]	92.9	83.76	64.71	38.88	6.45	0	0	0	0	0	0	0	0	0	0	0	0	0	0
$(25^\circ, 0^\circ)$																			
RR real distinct eigvs. [%]	0	0	0	7.7	1.11	0.77	2.94	3.15	3.84	0.39	0.23	3.91	10.58	14.75	100	0	0	0	0
RR real equal eigvs. [%]	0	0	0	76.92	11.07	9.27	25	35.43	38.46	20.51	12.45	44.69	70.58	81.97	0	0	0	0	0
RR complex eigvs. [%]	0	0	0	15.38	87.82	89.95	72.06	61.42	57.69	79.1	87.31	51.39	18.84	3.28	0	0	0	0	0
$(40^\circ, 0^\circ)$																			
RR real distinct eigvs. [%]	0	0	0	0	0	0	0	0	3.45	4.44	7.25	5.88	5.98	7.69	5.36	1.86	1.38	0	0
RR real equal eigvs. [%]	0	0	0	0	0	0	0	0	34.48	44.44	57.97	56.86	51.28	53.84	43.45	21.54	13.69	100	100
RR complex eigvs. [%]	0	0	0	0	0	0	0	0	62.07	51.11	34.78	37.25	42.74	38.46	51.19	76.6	84.92	0	0

■ Bistatic dihedral

For the dihedral target, the range of scattering directions, i.e., $\theta_s, \varphi_s \in [-45^\circ, 45^\circ]$ ensures that responses come only from the two interior facets of the object. In the absence of a verification procedure for the estimated bistatic results, the electric field observations are limited to only those directions for which the normalized absolute value is larger than -30 dB. This will, at minimum, prevent too noisy results from being evaluated. The shape of our selection and the number of points fulfilling such constraint modifies with the change in incidence direction (i.e., from one column to the other in the results template).

At normal incidence (first column, $\theta_i = 0^\circ$, $\varphi_i = 0^\circ$), the absolute value of the nonreciprocity factor is quite low with values in the range $[0, 0.3]$ (Fig. 2.16d) and the RRSM eigen-classification shows a majority of real eigenvalues (Fig. 2.16g). So, even if the observations are bistatic and the bistatic angle varies up to 20° in the directions remaining after threshold selection, the scattering mechanism remains inherently symmetric.

At more skewed incidence directions ($\theta_i = 25^\circ$ or 40°), we observe an increase in the percentage of Rx directions returning complex RRSM eigenvalues. This appears for scattering directions distributed in the entire range of θ_s, φ_s values (Fig. 2.16h-i), but only if $|\varphi_s| > 5^\circ$. The RRSM eigen-classification remains dominated by real values (Fig. 2.16).

■ Bistatic plate

As in the monostatic case, the plate scatterer is square, i.e., it has a form factor (FF, i.e., ratio of height to width) equal to one. The main post-processing results are shown in Fig. 2.17(d)-(l).

The results indicate that, for the great majority of Rx directions, the RRSM eigenvalues are of complex type. In the spherical angular domain, this happens for φ_s outside $[-5^\circ, 5^\circ]$ and (\forall) θ_s . As a particular trend, local peaks of the RRSM complex eigenvalues percentages seem to appear at bistatic angles near integer multiples of θ_i .

The change in incidence directions produces for the plate a lower variation of the RRSM complex eigenvalues percentage by comparison to the dihedral's case (Table 2.7). Moreover, it indicates a slight decrease for the RRSM complex eigen-percentage even for more skewed θ_i .

In Fig. 2.18, only the RRSMs with complex values are considered for each target. They are evaluated in relation to the bistatic angle and both the NRF modulus and phase. Even with different numbers of scattering points and distinct ranges for the considered parameters, it is seen that the amplitude of the returned complex eigenvalues globally decreases when varying from incidence angle $\theta_i = 0^\circ$ (orange dots) to incidence angle $\theta_i = 40^\circ$.

The complex eigenvalues are not limited to a certain bistatic angle (the case with $\theta_i = 40^\circ$ is relevant, as such incidence allows for bistatic observations in the largest angular range). Moreover, the appearance of the complex values is not limited to a specific NRF phase angle and while a NRF modulus threshold seems to exist it is even

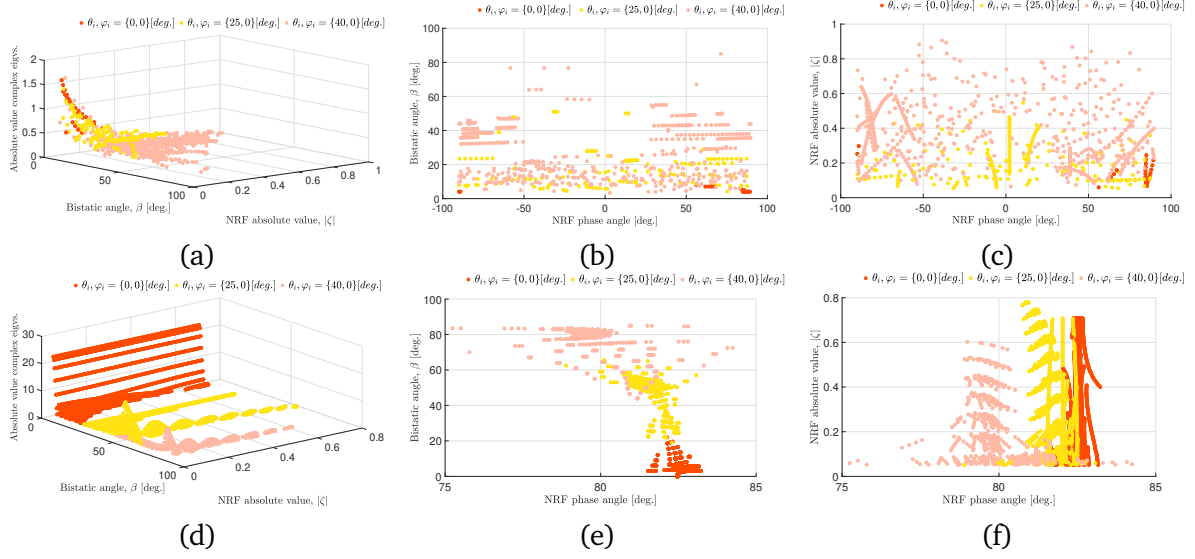


Figure 2.18: Bistatic targets. Combined representations with: the modulus of RRSM complex eigenvalues, the bistatic angle and the NRF parameter. (a-c) 90° Dihedral. (d-f) Plate.

lower than expected (i.e., as low as to $\approx [0.05, 0.1]$); nonetheless it is necessary to point out that this is very close to the auto-defined threshold value δ_{imag} , used inside the eigen-classification workflow, Annex E).

The main results from the bistatic analysis suggest that:

- (a) For low φ_s values in the scattering domain, the RRSM eigen-classification shows only real values.
- (b) Very skewed incidence/scattering bistatic combinations (for both θ and φ) may determine scattering effects characterized by RRSM complex eigenvalues.
- (c) The simulations are not conclusive in defining a threshold scattering direction (θ_s, φ_s) from which complex RRSM eigenvalues begin to appear. Moreover, there is no general result to suggest which is the minimum "skewness" with respect to the observation direction. With the plate scatterer, complex RRSM eigenvalues have appeared for φ_s values as low as 5° , or for observation directions having very low bistatic angles $\beta \in [0^\circ, 5^\circ]$.

2.6 Conclusions

This chapter has continued to explore the particularities of the conjugate similarity operation, has introduced the properties of coneigenvalues and coneigenvectors along with a state-of-art analysis of the known algebraic methods used to determine them. Within this context, the Real Representation and the homonym real block form of the scattering matrix are introduced and proposed. Compared to the known PolSAR method for consimilarity, i.e., the Graves method, it can be used with both reciprocal and nonreciprocal scattering matrices. The previously not considered case of conjugate (con)eigenvalues of inhomogeneous scattering matrices becomes available when using the Real Representation.

In order to consolidate not only an algebraic, but also a polarimetric understanding, experiments on full-pol data are performed in the chapter. Their main aim has been in uncovering relations or connections between the phenomena of complex (con)eigenvalues observed in the data and the scattering mechanisms in polarimetric monostatic and bistatic observations.

Monostatic (real and simulated) and bistatic (simulated) data has been used. The simulated data for individual, elementary targets (which applies as model of study to the specific case of coherent polarimetry) has been obtained using a Computational Electromagnetic Software.

It is to be stated that the PolSAR evaluation is incomplete in some regards. The representation itself and the eigen-decomposition of the Real Representation block matrix is applied only in a coherent manner, without statistical averaging. This type of evaluation is then, not appropriate to characterize distributed scatterers.

Moreover, the influence of coneigenvectors has been pursued only limited, which can be expanded by future work.

Generally, a congruent understanding of both values and vectors of a PolSAR decomposition has been acquired by having a parametric model which uses one (e.g., the Touzi model for the scattering vectors) or both (e.g., the $H-\alpha$ model for covariance matrices) of this information to provide interpretable parameters. From a practical perspective, the results presented in this part, position the Real Representation matrix more of a testing approach (e.g., with real monostatic data, of the compliance to the congruence assumption and the applicability of the Graves model). In this regard, efforts have been made for a factorization (based on SVD) of the Real Representation matrix, but the model selected has proven not unique in numerical implementation. Further research on the subject would be necessary.

Polar Decomposition Geometrical Clustering

Hard to find anything lovelier than a tree.

They grow at right angles to a tangent of the nominal sphere of the Earth.

Bill Nye

Contents

3.1	Unsupervised classification and clustering in PolSAR	88
3.1.1	Metrics, distances and similarity measures for PolSAR applications	88
3.1.2	PolSAR clustering	90
3.2	PolSAR polar factors	92
3.2.1	State of art on PolSAR Polar Decomposition	93
3.2.2	Algebraic and geometric properties of polar factors	94
3.3	Manifold of Hermitian/unitary factors	97
3.3.1	On manifolds and Riemannian geometry	97
3.3.2	Manifold embedding for Hermitian positive definite matrices	98
3.3.3	Manifold embedding for Unitary matrices	101
3.4	Geometric clustering with Hermitian factors	104
3.4.1	Evaluating the contribution of the unitary factor	104
3.4.2	Method description	106
3.5	Geometric clustering: Implementation and testing	108
3.5.1	Simulated datasets	108
3.5.2	Real datasets	111
3.6	Conclusions	113

This chapter describes a different algebraic operation (i.e., the polar factorization), which is applied to the scattering matrix for unsupervised classification. As introduced in Chapter 1, the general framework for data processing and information extraction in unsupervised PolSAR involves incoherent techniques and the use of the coherence/covariance matrix. This is a statistics-based processing and the informational space is 3×3 or 4×4 (depending on the column dimension of the monostatic/bistatic scattering vector; Section 1.5). The incoherent clustering technique introduced in this chapter proposes a different approach. The technique exploits the informational space of the scattering matrix (2×2), under the polar factorization. This is combined with a geometrical processing in the Riemannian manifold for the Hermitian scattering factors. The proposed analysis shows comparable and even improved results to the conventional

Wishart classifier, which performs covariance-based clustering. This proves the feasibility of the introduced framework, paving the way for possibly more advanced applications.

The chapter debuts with a short discussion on PolSAR metrics and the subdomain of unsupervised clustering applications, in Section 3.1. This is followed by a detailed examination of the polar decomposition (Section 3.2) and a discussion on the geometric properties of the two decomposition factors (Section 3.3). The presentation of the proposed approach and the evaluation of results on real and simulated data are covered in Sections 3.4 and 3.5. The main text is accompanied by Annexes F-H.

3.1 Unsupervised classification and clustering in PolSAR

3.1.1 Metrics, distances and similarity measures for PolSAR applications

The *metric* terminology is generally used for any quantifiable measure. From a mathematical perspective, a metric is a *distance* if it is a real-valued function, operating on a set of points $\{X\}$ and verifying the conditions of: (a) non-negativity, (b) symmetry, (c) triangular inequality, (d) identity ¹[164, 165].

Choosing an adequate metric is of particular importance in both simple and advanced data processing. Imposing a (dis)similarity measure on algebraic objects (i.e., vectors, matrices) generally requires to assign a metric function. However, a (dis)similarity measure is not necessarily a metric. Some of the PolSAR applications involving the use of metrics and similarity measures are in speckle filtering, change detection and unsupervised/supervised classification.

- i. *Speckle filtering*: Local and non-local filtering are two type of techniques used to reduce the effects of the granular speckle noise, which appears in the PolSAR coherent imaging systems. The speckle filtering methods can operate spatially or in a transformation domain.

Local approaches make use of a uniform, locally-defined window² to process the entire image. When similarity measures are necessary, they are applied point-wise. Differently, the non-local filters use a more global approach, usually patch-based [166, 167]. Pixels with resembling features are grouped together and processed in a consistent manner. If similarity measures are necessary, they are applied at the patch level.

- ii. *Change detection*: The automatic extraction of differences among (at least) two images acquired over a period of time for a common area is an important asset in remote sensing. The type of methods used in PolSAR change detection are diverse but most of them operate with distance/similarity measures [168, 169]. Case

¹Given $x, y, z \in X$

$$d(x, y) \geq 0 \quad (\text{a})$$

$$d(x, y) = d(y, x) \quad (\text{b})$$

$$d(x, z) \leq d(x, y) + d(y, z) \quad (\text{c}) \quad d(x, y) = 0 \text{ iff } x = y \quad (\text{d})$$

²known as kernel or convolutional filter, in computer science.

studies of PolSAR change detection have been reported in crop characterization [170], urban areas [168, 169] and so on.

Used as a stage in change detection strategies, or applied as a separate procedure, *edge detection* techniques may also use specific similarity measures [171].

iii. *Classification:*

Unsupervised classification techniques are pixel- or patch-based and split the PolSAR data depending on the scattering properties of targets, the probabilistic characteristics of the data, or a combination of the two. Otherwise, supervised approaches are based on the use of labeled data to train a classifier.

Apart from the more recent machine learning approaches, both supervised and unsupervised methods compare and split the data based on one or more metrics and similarity measures. In case of the former, the metric space can be automatically learned by the network.

The current chapter proposes a clustering-based unsupervised classification. This is presented in more detail in the sections to follow.

An introduction to the fundamental (distance) metrics and similarity measures used by PolSAR applications can be found in [164] and an in-depth review is available at [165]. The two primary types are the stochastic and the geometric. Stochastic metrics are used to evaluate probability distributions and quantify how alike two random variables (under a statistics a priori). With geometric metrics, the a priori is in the form of the geometric embedding considered for the variables. For example, the polarimetric covariances are complex Hermitian positive definite matrices, known to reside inside an open conic, smooth manifold.

■ **Stochastic Metrics**

Key words: Gaussian/Non-Gaussian, maximum/ratio likelihood, stochastic divergences.

Under the fully developed speckle condition, the multi-look covariance/coherence follow the (scaled) complex Wishart probability distribution function (pdf) [4]. When this is no longer the case, SIRV compound models have been assumed [100].

Under the most general case, the stochastic tests and measures have a distribution independent form.

The maximum likelihood (ML) metric based on the Wishart distribution (and having the homonym name) is one of the most popular Incoherent Target Decomposition (ICTD) metrics [172]. Log-likelihood and likelihood ratio testing are well-known approaches in testing probabilistic functions. For example, [173] proposes a likelihood ratio criterion under the Wishart distribution, while [174] derives the Bartlett and the revised-Wishart metrics under a relaxed Wishart distribution.

Alternatively, metrics or likelihood tests have been obtained considering the non-Gaussian (compound) distribution cases (e.g., K-Wishart metric) [165, 175].

The divergence-based stochastic metrics, with roots in information theory, have gained recognition also in PolSAR. Such metrics test the proximity/closeness

between two probability measures. Example of metrics (based on the $h - \phi$ divergence model) are: Kullback-Leibler, Battacharyya, Hellinger, Rényi of order β or Chi-squared. Frery et al. particularize these distances assuming the coherence matrices under the complex Wishart [131] and the relaxed scaled complex Wishart a priori [174], while Bouhlef and Méric [169] assume a non-Gaussian model under the \mathcal{G}_d^0 distribution.

The Chernoff [176], the Jeffries–Matusita [177] or the Jensen-Bregman Log divergence are other examples from the same category. Particularly, they can be viewed as special cases of some of the above-mentioned stochastic metrics [165].

In recent studies, another class of divergences have been introduced to PolSAR, i.e., the Hölder divergences and pseudo-divergences [178, 179]. They propose a different type of similarity metric, which measures the tightness of probabilistic inequalities.

■ Geometric Metrics

Key words: covariance matrix - manifold metric, Kennaugh matrix - spherical geodesic.

Such metrics are adapted to the geometric embedding of the data. Nonetheless, they have been used to a lesser extend than the stochastic ones.

For example, based on the property of real symmetric and Hermitian complex symmetric matrices of being enclosed in a Riemannian manifold (Section 3.3.2), several studies have proposed metrics adequate for this space (the affine invariant Riemannian metric (AIRM) or the log-Euclidean). In PolSAR, these have been applied for ICTD methods using complex covariances.

Given that Kennaugh matrices operate as transformations between polarization states on the Poincaré sphere (i.e., the transmitted and scattered Stokes vectors), Ratha and al. introduce a spherical geodesic distance for comparing such matrices [168, 180, 181]. The authors argue the same metric can be applied for covariance matrices. Hereafter, we refer to it as the angular geodesic metric.

3.1.2 PolSAR clustering

There are several types of clustering algorithms proposed in computer science for unsupervised classification: partitional, hierarchical, density, grid, model-based and others [182]. Many of them have been applied in PolSAR. Among the most popular are the partitional methods (e.g., k-mean, fuzzy c-means [183]). Other examples include the probabilistic model-based clustering (e.g., with the Expectation-Maximization method [183, 132]), the hierarchical clustering [176], the spectral clustering [184] and so on.

The introduction of the Wishart method has been a major milestone in PolSAR unsupervised classification [172]. Balancing the ability to provide results of good accuracy with implementation simplicity, the method has gained popularity with both novices and experienced members of the community. Its popularity has also consolidated the use of the coherency/covariance matrices as principal descriptors with ICTD.

The classifier is based on the k-means algorithms, with an iterative implementation in which the Wishart distance is adopted as metric. Equipped with this metric, the model was shown to represent an optimal Bayesian classifier, considering that the scattering vectors are modeled by zero mean complex circular Gaussian vectors, completely characterized by their covariance matrix [172].

The classical k-means algorithm is an iterative, partitioning clustering technique which separates the input data $X = \{x_i\}, i \in [1, N]$ into K subsets (i.e., classes) [185, 186]. Each sample x_i belongs to only one subset. The assignment to class K is made through the minimization of a least squares cost function, which computes the sum of squared errors with respect to each cluster centroid $C_k, k \in [1, K]$. A generic schema for centroid-based classification algorithms is displayed in Fig. 3.1.

The unsupervised centroid-based clustering approach has proven popular and versatile in PolSAR. Over the years, an important volume of publications have enriched the core model of Wishart clustering proposing changes to different stages in the original algorithm. A non-exhaustive selection, chosen to reflect the diversity of proposed modifications, is depicted by Table 3.1.

A common pattern is observed. The majority of these PolSAR clustering approaches seek to combine: a technique able to retrieve scattering mechanisms and a clustering procedure based on stochastic distances. The classical algorithm uses the $H - \alpha$ partitioning and in-class (Euclidean) averaging for computing the initial centroids. The number of classes is subsequently increased by introducing the $H - \alpha - \text{Anisotropy}$ 3D plane space for the scattering partitioning [187]. Lee et al. propose in [188] some updates in three areas: cluster initialization (by using the Freeman-Durden model-based decomposition), the number of initial classes and the merging criterion between iterations. This model became soon another popular choice, mostly with model-based initialization. For example, [189] changes this stage by using the scattering entropy power and the co-polarization ratio. Different initialization models using power factors have been introduced: Chunle et al. change to a non-negative eigenvalue decomposition of coherency matrices (to mitigate some of the limitations of the Freeman-Durden model) [190], while Ratha et al. use the comparison of the Kennaugh matrices by the angular geodesic distance [180]. The latter is modified by [175] to separate between homogeneous and inhomogeneous regions and then use either the Wishart or K-Wishart metric when performing the class assignment.

In [191, 192], Formont proposes changes of the classical algorithm in three essential parts: the estimation of the sample covariance matrix (Gaussian ML vs. Fixed Point model), the distance metric (Wishart vs. SIRV) and the centroid recomputation (classical mean vs. geometric (Riemannian) mean).

The combination of the k-means algorithm with a class assignment based on stochastic distances (i.e., Kullback-Leibler, Battacharyya, Hellinger, Rényi of order β and Chi-squared, all derived considering the Wishart distribution) is referred in [132] as stochastic clustering. While this implementation uses a random initialization, the same authors propose in [193] an initialization based on hierarchical clustering and the geometric mean of covariances (by considering their Riemannian manifold embedding).

In [194], the initialization uses the h/q decomposition (a proposed alternative to

$H - \alpha$), the inter-cluster classification is based on the Wishart metric, while the centroid is updated via the density clustering technique (DCT) based on the Log-Euclidean Riemannian metric.

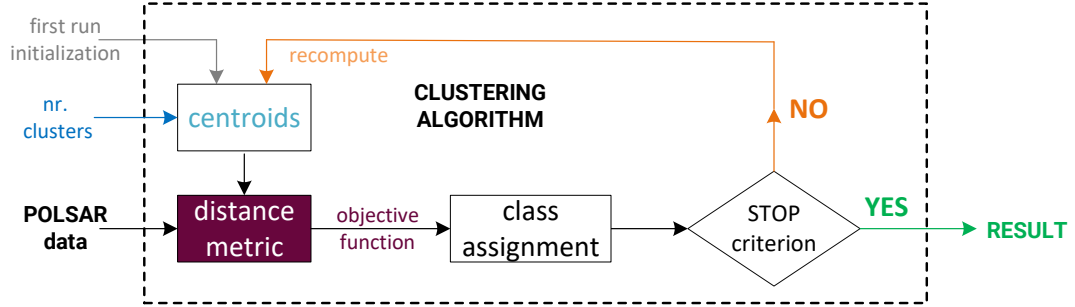


Figure 3.1: Generic scheme of a centroid-based clustering algorithm for PolSAR data.

Table 3.1: Partitional clustering PolSAR examples based on *k*-means.

Acronyms: SIRV: Spherical Invariant Random Vector. NNED: Non-negative Eigenvalue Decomposition. DCT: Density Clustering Technique. A: Anisotropy

Ref.	Parameters			
	nr.clusters	distance metric	C_k initialization	C_k update
classical Wishart, [172]	8*	Wishart	$H - \alpha$	in-class average (Euclidean)
[187], 2001	16*	Wishart	$H - \alpha - A$	
[188], 2004	15-16*	Wishart	Freeman-Durden	
[191], 2011	8*	Wishart and SIRV	$H - \alpha$	in-class average algebraic (Euclidean) and geometric (Riemannian)
[189], 2013	8*	Wishart	H -power and co-pol ratio	in-class average (Euclidean)
[190], 2014	16*	Wishart	NNED	
[180], 2018	15*	Wishart	w_a, w_b, w_{rs}	
[132], 2019	6 [§]	Wishart and stochastic divergences (Wishart distr.)	random	
[175], 2021	15-16*	Wishart and K-Wishart	w_a, w_b, w_{rs}	
[194], 2021	8*	Wishart	h/q	log-Euclidean DCT

* fixed by model. [§] from ground truth.

C_k = centroid, $1 \leq k \leq N$; N = nr. of clusters

3.2 PolSAR polar factors

While the polar decomposition has already been introduced in Section 1, the discussion here is more extensive. This technique has generally been used in PolSAR as a coherent method and for allowing feature extraction from the scattering matrix, $S \in \mathbb{C}^{2 \times 2}$. Since there are no constraints in applying the factorization, it can be used for both symmetric/asymmetric, or otherwise, monostatic/bistatic scattering matrices. The

decomposition can divide any scattering matrix into two terms, one unitary and one positive semi-definite (and therefore, also Hermitian). For brevity of notation they are further addressed as the \mathbf{U} and \mathbf{H} factors, respectively. Depending on the chosen ordering of the two terms, the factorization has two forms, the right and left polar decomposition, (1.31) and (1.32). The unitary factor, which is unique for invertible $\mathbf{S} \in \mathbb{C}^{2 \times 2}$, is the same in the two factorizations, while the Hermitian factors are unitary similar, i.e., they share the same eigenvalues.

The polar decomposition can be seen as the matrix equivalent of a more simpler expression, the polar form, which writes every non-zero complex number $s = s_1 + js_2$, $s \in \mathbb{C}$, as the product of a modulus and a phase element: $s = |s| \cdot e^{j\theta}$, $\theta \in [-\pi, \pi]$. With the matrix polar decomposition, the positive definite factor is the higher dimensional equivalent of positive numbers, while the unitary factor has a combined phase-rotation action.

Nonetheless, the polar decomposition is closely connected to the SVD, $\mathbf{S} = \mathbf{V}\mathbf{\Sigma}\mathbf{W}^H$, so that $\mathbf{S} = \mathbf{U}\mathbf{H} = (\mathbf{V}\mathbf{W}^H)(\mathbf{W}\mathbf{\Sigma}\mathbf{W}^H)$. The singular values of \mathbf{S} are the same as the diagonal values of $\mathbf{\Sigma}$.

From an algebraic perspective, the previous chapter has investigated into the use of the conjugate similarity in PolSAR, while the current chapter is oriented - through the polar decomposition - into the use of a similarity-type factorization.

3.2.1 State of art on PolSAR Polar Decomposition

The works of Carrea et al. are among the first to propose the polar factorization as a coherent PolSAR decomposition technique [195, 196]. The unitary and the positive definite factors are described as a rotation and as a boost matrix, respectively. Based on this model, several parameters (with a geometric meaning in the spherical Stokes space) are proposed for the decomposition of symmetric matrices [197].

Following works of Souyris et al. have express the scattering matrix's polar decomposition using the formalism of quaternions [198]. The quaternionic model proposes a new set of polarimetric features for data interpretation. By applying separate spatial averages (multi-looking) of scattering vectors obtained from the two factors, the model is extended to applications with incoherent targets [199, 200].

By exploiting the connection between the SVD and the polar decomposition, Cloude et al. propose a PolSAR algorithm for active calibrators which recovers the real rotation matrix from the unitary polar factor [201]. From it, the method then estimates the ionospheric Faraday rotation angle. As there is no reciprocity assumption implied, the algorithm can be applied for both monostatic and bistatic calibration.

In optical polarimetry, the polar factorization is among the most popular decomposition. It splits a complex 2×2 Jones matrix in a retarder (i.e., the unitary matrix) and a diattenuator (i.e., the Hermitian matrix). This is usually the case with a nondepolarizing Mueller matrix [202], while for a general Mueller matrix a model of three factor (retarder, diattenuator and depolarizer) is used. The same model is considered in

[203] for (pixel-by-pixel) classification of PolSAR data in Mueller matrix format.

3.2.2 Algebraic and geometric properties of polar factors

The polar decomposition of complex scattering matrices returns two distinct matrices: one unitary and one complex positive semi-definite. Here, we examine more closely some of their properties.

■ Complex positive definite factor:

A complex positive semi-definite matrix \mathbf{H} verifies $\mathbf{u}^H \mathbf{H} \mathbf{u} \geq 0 \forall \mathbf{u} \in \mathbb{C}^2$ and has non-negative eigenvalues. Such matrix is also necessarily Hermitian, $\mathbf{H}^H = \mathbf{H}$. The semi-definite restriction is covering the case when the matrix may present zero eigenvalues. The eigenvalues of the Hermitian factor are the same as the singular values of the scattering matrix. Moreover, the two matrices have the same rank. The question of semi-definiteness of \mathbf{H} is thus related to the 2×2 \mathbf{S} having full-rank (i.e., independent columns). Generally, this is indeed the case for the matrix of polarimetric measurements. Even in the rare occurrences of acquisitions having a low signal to noise ratio, the presence of additive thermal noise will guarantee in practice that the numerical singular values/eigenvalues of \mathbf{S} are different from zero. In the following, the discussion considers entirely the case of positive definite results with the polar decomposition.

Assumptions Set - 3.1.

- I. The \mathbf{H} polar factors obtained from the factorization of polarimetric data, in real world applications, have positive and non-zero eigenvalues.

i. Algebraic perspective:

The general form of Hermitian matrices, with elements above and below the main diagonal in complex conjugate symmetry, is well known. For the polar \mathbf{H} -factor, we then write:

$$\mathbf{H} = \begin{bmatrix} h_{1,1} & h_{1,2} \\ h_{2,1} & h_{2,2} \end{bmatrix} = \begin{bmatrix} h_{1,1} & h_{1,2} \\ h_{1,2}^* & h_{2,2} \end{bmatrix}. \quad (3.1)$$

It was shown that the \mathbf{H} matrices of the right/left factorization share the same eigenvalues (Section 1). As the two matrices are Hermitian, their eigenvalues are real numbers. And when the decomposed scattering matrix \mathbf{S} is (complex) symmetric (i.e., the general case of PolSAR monostatic), these eigenvalues share also a multi-facet interpretation: as Takagi factors and/or coneigenvalues and/or singular values.

ii. *Geometric perspective:*

The space of Hermitian positive definite matrices of fixed dimension $m \times m$ is a subspace of the Euclidean space $\mathbb{R}^{m(m+1)/2}$.

For the polar \mathbf{H} factor of the scattering matrix this means an embedding inside \mathbb{R}^3 . Nonetheless, from a geometrical perspective, this subspace takes the form of a smooth, open-conic manifold. A more in-depth overview on this subject and the geometric embedding for \mathbf{H} factors is covered in Section 3.3. Given the manifold's non-Euclidean geometry, the simple use of common (Euclidean) metrics is not the most adequate for conventional operations (distance, mean, other statistics) on the manifold.

The real Brétigny dataset and its polar \mathbf{H} and \mathbf{U} factors are considered for the examples in Figs. 3.2 and 3.3. An illustrative example for Hermitian matrices in (3.1) is considered by using function $\mathcal{F}(\cdot)$. The representation in (3.2) is inspired by [204], with a small change, to better fit the PolSAR framework. Although in a different order, the three coordinates in (3.2) are no other than the three Pauli coefficients $\{k_{\mathcal{P},1}, k_{\mathcal{P},2}, k_{\mathcal{P},3}\}$ (corresponding to the complete set of monostatic PolSAR basis):

$$\mathcal{F}(\mathbf{H}) = \frac{1}{\sqrt{2}} [h_{12} + h_{12}^*, \quad h_{11} - h_{22}, \quad h_{11} + h_{22}]. \quad (3.2)$$

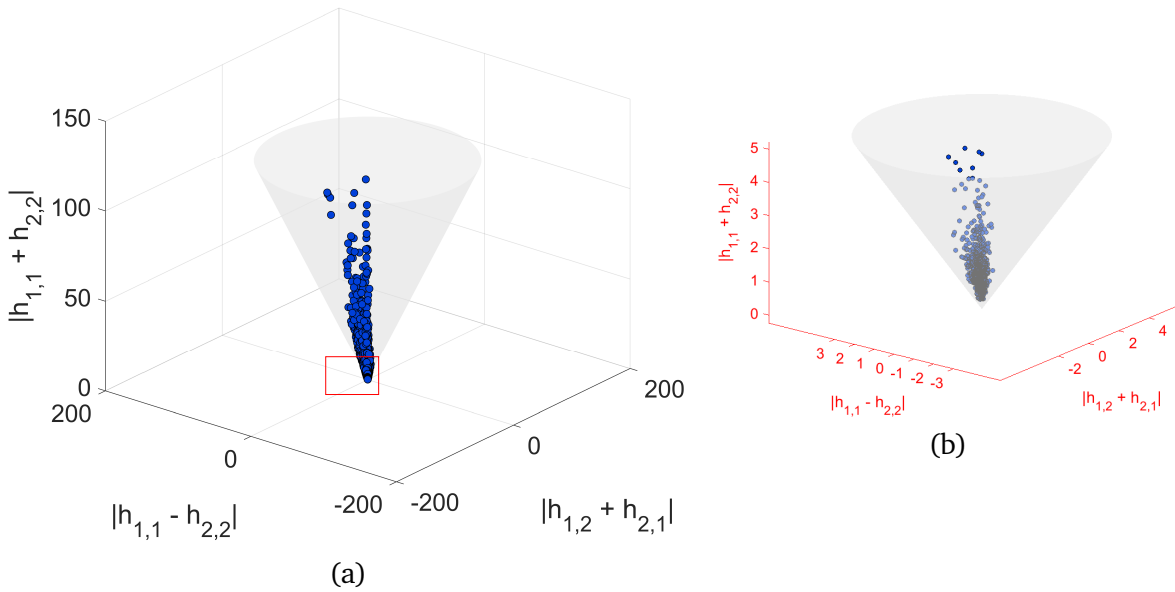


Figure 3.2: Brétigny Dataset. (a) Representation in \mathbb{R}^3 of $\mathcal{F}(\mathbf{H})$ coordinates for all \mathbf{H} factors in the dataset. (b) Zoomed view in red rectangle area from (a) and random selection of only 800 points.

■ **Unitary factor:**

For a unitary matrix, its Hermitian conjugate is equal to its inverse, so that:
 $\mathbf{U}\mathbf{U}^H = \mathbf{U}^H\mathbf{U} = \mathbf{I}$.

i. *Algebraic perspective:*

The unitary matrices are the complex counterparts of orthogonal matrices. Many distance functions are unitary-invariant so, as their real analogue, they are known to preserve lengths/amplitudes. The 2×2 group of unitary matrices is known as $U(2)$. Any member of this group can be expressed under a generic form

$$\mathbf{U} = \begin{bmatrix} u_{1,1} & u_{1,2} \\ u_{2,1} & u_{2,2} \end{bmatrix} = \begin{bmatrix} |u_{1,1}|e^{j\varphi_{1,1}} & |u_{1,2}|e^{j\varphi_{1,2}} \\ |u_{2,1}|e^{j\varphi_{2,1}} & |u_{2,2}|e^{j\varphi_{2,2}} \end{bmatrix} = \begin{bmatrix} a & b \\ -b^*e^{j\varphi} & a^*e^{j\varphi} \end{bmatrix} \quad (3.3)$$

where $a, b \in \mathbb{C}$, $|a|^2 + |b|^2 = 1$ and $0 \leq \varphi \leq 2\pi$.

The subgroup of unitary matrices having unit determinant belongs to the special unitary group, here $SU(2) = \{\mathbf{U} \in U(2) | \det(\mathbf{U}) = 1\}$.

A number of different factorizations have been proposed for unitary matrices [205, 206, 207] and they involve phase transformations and (real) rotations. For example, a 2×2 unitary matrix can be expressed as the product between a diagonal phase matrix and an $SU(2)$ matrix³, or equivalently, as the product of two phase matrices and one real rotation [205]. This can be expressed as

$$\mathbf{U} = e^{j\gamma} \begin{bmatrix} e^{j\varphi_1} & 0 \\ 0 & e^{-j\varphi_1} \end{bmatrix} \begin{bmatrix} \cos\theta & \sin\theta \\ -\sin\theta & \cos\theta \end{bmatrix} \begin{bmatrix} e^{j\varphi_2} & 0 \\ 0 & e^{-j\varphi_2} \end{bmatrix}. \quad (3.4)$$

That is, the combined action of a unitary matrix is that of both rotation and phase changes.

ii. *Geometric perspective:*

The $U(n)$ group of $n \times n$ unitary matrices forms a Lie group under matrix multiplication. It is an algebraic group that has the structure of a smooth manifold. From a topological perspective, the elements inside $SU(2)$ reside on a three-sphere, S^3 .

By using the same mapping for the \mathbf{H} factors (but taking the modulus $|\mathcal{F}(\mathbf{U})|$, as results are no longer real), the unitary \mathbf{U} factors seem to reside inside a spherical triangle region on the S^2 sphere (Fig. 3.3a). Taking the complex elements a and b from (3.3), a different mapping to \mathbb{R}^3 (which uses the model of the Stokes parameters), can be proposed:

$$\mathcal{L}(\mathbf{U}) = \begin{bmatrix} 2\mathcal{R}(a^*b), & 2\mathcal{I}(a^*b), & |a|^2 - |b|^2 \end{bmatrix}. \quad (3.5)$$

With the new mapping, the coordinates of the \mathbf{U} factors from the PolSAR Brétigny dataset appear in a conic hyperboloid inside the S^2 sphere (Fig. 3.3b).

³One particular form which $SU(2)$ matrices assume is: $\begin{bmatrix} a & b \\ -b^* & a^* \end{bmatrix}$ given $a, b \in \mathbb{C}$, $|a|^2 + |b|^2 = 1$.

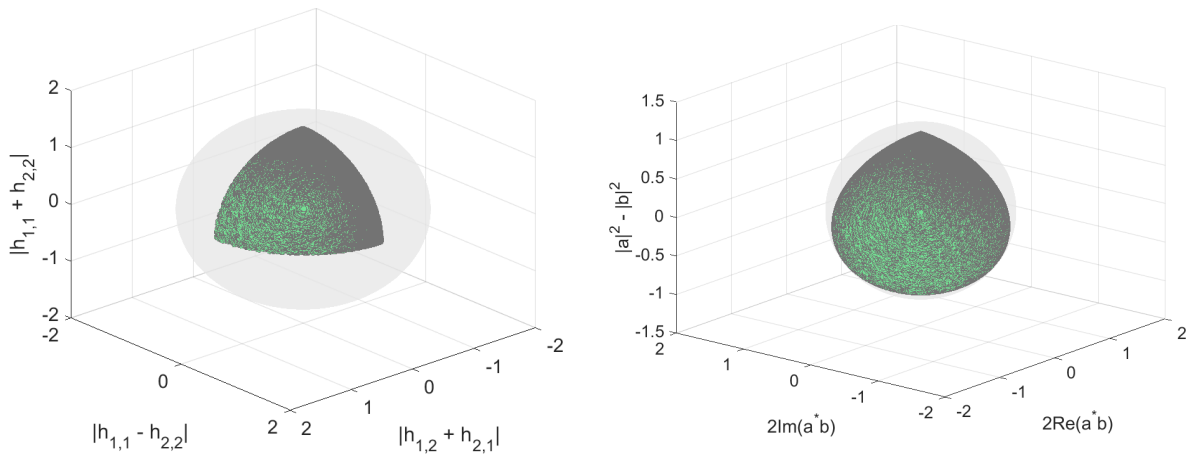


Figure 3.3: Brétigny Dataset. (a) Representation in \mathbb{R}^3 of $|\mathcal{F}(\mathbf{U})|$ for all \mathbf{U} factors in the dataset. (b) Representation in \mathbb{R}^3 based on $\mathcal{L}(\mathbf{U})$ for all \mathbf{U} factors in the dataset.

3.3 Manifold of Hermitian/unitary factors

3.3.1 On manifolds and Riemannian geometry

A *manifold* \mathbb{M} is a topological space, similar to an Euclidean space at each small vicinity. Real manifolds locally possess the properties of \mathbb{R}^n , while complex manifolds locally possess the properties of \mathbb{C}^n . At any point X in the manifold, the *tangent space* $T_X\mathbb{M}$ can be defined (Fig. 3.4). The reunion of all tangent spaces determines the tangent bundle. Each tangent space is a vector space and can be equipped with a bilinear, symmetric, positive-definite function as inner product, $\langle \cdot, \cdot \rangle_{T_X\mathbb{M}}$. The product induces a norm for vectors in $T_X\mathbb{M}$. So, a metric defined on the manifold is a choice of inner product for each $X \in \mathbb{M}$. When such inner product varies smoothly from point to point over the manifold, it is called a Riemannian metric. Finally, a manifold endowed with a Riemannian metric is a Riemannian manifold.

Because an n -dimensional manifold can be regarded also as an Euclidean subset, it is (naturally) equipped with the distance measures of this space, e.g., the Frobenius norm. But, in non-linear manifolds, using these metrics is no longer an adequate choice, as the topology of the space presents some form of curvature. One of the most simple examples of a nonlinear manifold is the S^{n-1} sphere contained in any \mathbb{R}^n .

For a clear separation, the metrics which can be imposed on a geometrical space can be intrinsic (i.e., compute the true length on the manifold) or extrinsic (i.e., possible to define, but not optimal in the space).

On non-linear manifolds, the intrinsic distance between two points is not a straight line, as in the Euclidean space, but a path which follows the curvature of the space. This is known as a *geodesic*. A comparison is displayed in Fig. 3.4. For coordinates \mathbf{A} and \mathbf{B} in the manifold, the geodesic function $\Gamma_{\mathbf{A}-\mathbf{B}} : [0,1] \rightarrow \mathbb{M}$ verifies equalities $\Gamma_{\mathbf{A}-\mathbf{B}}(0) = \mathbf{A}$ and $\Gamma_{\mathbf{A}-\mathbf{B}}(1) = \mathbf{B}$.

The geodesic is imposed by a Riemannian metric, which then represents the intrinsic way of measuring distances in the manifold.

The geometric center (hereafter, *barycenter*) of a set of m matrices $\{\mathbf{X}_1, \mathbf{X}_2, \dots, \mathbf{X}_m\} \in \mathbb{M}$, $m > 2$, can be mathematically expressed as the the minimizer of a sum of squared distances,

$$\operatorname{argmin}_{\mathbf{X}_0} \sum_{i=1}^m d(\mathbf{X}_0, \mathbf{X}_i)^2, \quad (3.6)$$

from the unknown barycenter \mathbf{X}_0 to each member \mathbf{X}_i of the set.

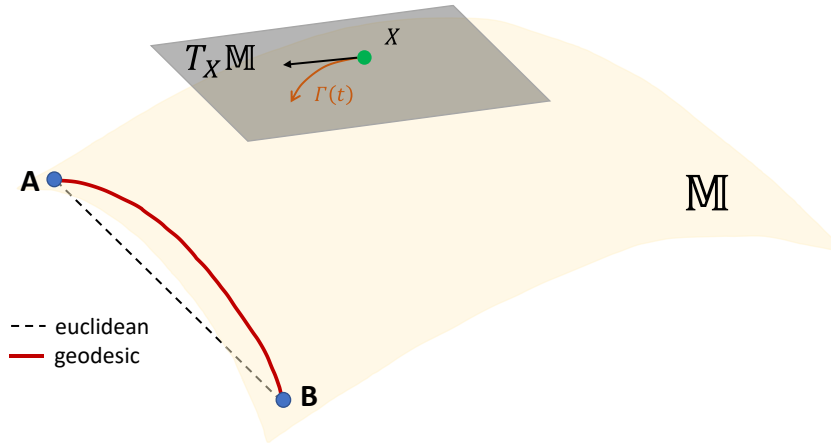


Figure 3.4: Example of a manifold (\mathbb{M}) and its tangent space at point X ($T_X \mathbb{M}$).

3.3.2 Manifold embedding for Hermitian positive definite matrices

The space of $n \times n$ symmetric positive definite (SPD) matrices when endowed with a Riemannian metric forms a Riemannian manifold. The same property can be extended to the space of Hermitian positive definite (HPD) matrices. There is a solid theoretical framework for SPD and HPD matrices in the scientific literature, as positive definite matrices appear in wide variety of domains (machine learning, computer vision, medical image analysis), often as covariance matrices.

The Riemannian manifold of positive-definite matrices is known to be non-linear, convex and smooth (i.e., infinitely differentiable). It takes the form of a convex, open half cone with negative curvature. For an n -dimensional space we refer to it as $\mathbb{P}(n)$.

For manifolds having a unique normal geodesic joining any two distinct points, the *convex property* is verified both globally and locally (i.e., for any two points X and Y from a subset of the manifold, the geodesic joining them in \mathbb{P} is also contained in the subset).

■ Riemannian geometry in PolSAR:

In PolSAR, it has been more than a decade since the Riemannian manifold embedding is used exclusively with coherency/covariance matrices. The main areas for practical applications are in unsupervised classification and segmentation [191, 208, 209, 210, 193], time-series change detection [211, 170], supervised classification [212, 213, 214] or speckle filtering [215, 216].

These techniques, generally share the common point of assuming a similarity metric which exploits the geometry of the manifold. The most commonly employed metrics in the Riemannian manifold of positive Hermitian matrices are the affine invariant Riemannian metric (AIRM) and the Log-Euclidean metric.

Nonetheless, there are some works which have taken a different geometric approach and instead of exploiting the Riemannian manifold of covariance matrices propose, for example, a higher dimensional embedding (e.g., into a Kernel Hilbert Space [217, 218, 219]). The distance metrics used in this case are not necessarily geodesics.

■ Affine Invariant Riemannian Metric:

Considering $\Gamma_{\mathbb{P}}(t) : [0,1] \rightarrow \mathbb{P}(n)$ with $\Gamma_{\mathbb{P}}(0) = \mathbf{A}$ to $\Gamma_{\mathbb{P}}(1) = \mathbf{B}$, a geodesic function in $\mathbb{P}(n)$, $\mathbf{A}, \mathbf{B} \in \mathbb{P}(n)$. The unique geodesic curve between any two positive definite matrices is given by [204]

$$\Gamma(t) = \mathbf{A}^{1/2} \left(\mathbf{A}^{-1/2} \mathbf{B} \mathbf{A}^{-1/2} \right)^t \mathbf{A}^{1/2}, \quad t \in [0,1] \quad (3.7)$$

The exact arc-length of the geodesic curve, i.e, the distance measure, between two manifold points is obtained by integration of the velocity (i.e., first derivative) along the geodesic, $t \in [0,1]$. Then, the minimum distance between \mathbf{A} and \mathbf{B} is obtained in the form of the affine invariant Riemannian metric (AIRM):

$$d_{\mathbb{P}(n)}(\mathbf{A}, \mathbf{B}) = \|\text{Log}(\mathbf{A}^{-1/2} \mathbf{B} \mathbf{A}^{-1/2})\|_F, \quad (3.8)$$

The AIRM geodesic distance complies to several invariance properties such as self-duality, congruence invariance, joint homogeneity and determinant identity, among others [220]. In particular, the congruence (or, affine) invariance implies that

$$d_{\mathbb{P}(n)}(\mathbf{J} \mathbf{A} \mathbf{J}^H, \mathbf{J} \mathbf{B} \mathbf{J}^H) = d_{\mathbb{P}(n)}(\mathbf{A}, \mathbf{B}), \quad (3.9)$$

for any non-singular matrix \mathbf{J} .

Table 3.2 contains a non-exhaustive list of applications from PolSAR, which employ AIRM as distance metric (in applications with the covariance/coherency matrices).

Table 3.2: Example of PolSAR applications using the AIRM metric.

	Applications	Method Type	Ref.
AIRM	supervised classif.	dictionary-based	[212, 213, 214]
	change detection	region-based	[211, 170]
	clustering	pixel-based	[191, 208]
		region-based	[210]
	cluster init.	pixel-based	[193]
AIRM-modif.	filtering	pixel-based	[171]
	segmentation	region-based	[209]

■ Barycenter:

The Riemannian barycenter (also known as the geometric / Fréchet / Karcher mean) is the minimizer of squared geodesic distances between the set of m positive definite matrices [221]. AIRM is the chosen geodesic distance for eq. (3.6).

While there is no closed-form solution for the minimization problem in (3.6) with $m \geq 3$, it was shown that the minimum always exists and is unique for Riemannian manifolds of negative curvatures [222]. This is exactly the case for the manifold of Hermitian positive definite matrices. When the dispersion of points on the manifold is not excessive, an estimate of the minimum can be attained with probability one by a simple gradient descent algorithm [223]. Implementations of the optimization by Newton algorithms is also possible.

A gradient descent method is used in the thesis to obtain an estimate of the Riemannian barycenter for a set of m Hermitian positive definite polar factors $\{\mathbf{H}_1, \mathbf{H}_2, \dots, \mathbf{H}_m\}$, $m > 2$. Its pseudocode and a short discussion can be found in Annex H. Unless otherwise stated, the right polar decomposition (1.31) will always be used to obtain the Hermitian factors. Under the usual stationarity condition, the barycenter minimization search is implemented using a local, boxcar moving window.

The Riemannian mean presents several invariant properties, as follows [204]:

- *permutation invariance*: This states that \mathbf{H}_0 is still the solution considering any rearrangement of the original set $\{\mathbf{H}_i\}$, $1 \leq i \leq m$.
- *congruence invariance*: Changing the matrix set to $\{\mathbf{V}\mathbf{H}_i\mathbf{V}^H\}$, $1 \leq i \leq m$, \mathbf{V} non-singular, the barycenter changes accordingly, becoming $\mathbf{V}\mathbf{H}_0\mathbf{V}^H$.
- *inversion invariance*: \mathbf{H}_0^{-1} is the corresponding barycenter for the set of inverse matrices $\{\mathbf{H}_i^{-1}\}$, $1 \leq i \leq m$.

Computing the barycenter estimate is, nonetheless, a type of averaging operation performed based on a geometric criterion. The usual averaging operation in PolSAR is the arithmetic mean. This is used, for example, in a window-based framework for the multi-look of complex polarimetric images, or the estimation of the sample covariance matrix.

A comparison between algebraic and geometric averaging (span results) for 2×2 polarimetric matrices of a real PolSAR dataset is displayed in Fig. 3.5. As the computation of both algebraic and geometric means requires a boxcar neighborhood, three window dimensions are chosen: 5×5 , 7×7 , 11×11 (pixels). For reference, different visualizations (Pauli: Fig. A.1(b), span: Fig. F.1(a)) of the single-look real Brétigny dataset are available in the manuscript's Annexes.

The left column of Fig. 3.5 displays the span of H barycenter estimates using the gradient solution. On the right column, the span from multi-look averaging of the S scattering matrices is displayed (analogous dimensions of the moving window). The spatial resolution of images on the same row is comparable and, overall, the span's dynamic range does not vary across the images. One can observe that, by using the conventional spatial averaging on S matrices, the image features and contours visually blend and become harder to discriminate. The coherent scatterers tend to become extended and blur into the background. For the left-column results (geometric manifold averaging), even with the decrease in resolution, the relative radiometric difference for distinct areas in the image is less affected. This improves discrimination between areas and better preserves contours.

Other comparisons of PolSAR algebraic and geometric averaging operations have been identified in the literature. For example, the bilateral, iterative filtering proposed in [171] is individually implemented using the Riemannian distance. The authors compare filtering results on both real and (Gaussian) simulated polarimetric data and conclude that the bilateral approach with the AIRM distance better preserves low entropy targets⁴ than the traditional boxcar filter. This is observed also throughout the comparison in Fig. 3.5.

In [224], the difference between scalar arithmetic and geometric averages of single channel amplitude values from multi-temporal SAR series is computed. Improved results in terms of speckle variation and signal to noise ratio are reported for the geometric mean computation, as long as the SAR images from the acquisitions stack remain similar, with no significant permanent changes.

As a result, the preference and motivation of this chapter is for manipulating the PolSAR H factors in the Riemannian manifold.

3.3.3 Manifold embedding for Unitary matrices

■ Metric:

On the manifold of unitary matrices, $\mathbb{U}(n)$, the geodesic distance considered between two matrices A and B is of the form [225]:

$$d_U(\mathbf{A}, \mathbf{B}) = \|\text{Log}(\mathbf{A}^H \mathbf{B})\|_F. \quad (3.10)$$

■ Barycenter:

⁴i.e., the ones which usually associate to coherent scatterers in PolSAR images,

The set of unitary matrices forms a compact and connected Lie group. While this group is again known to present the structure of a Riemannian manifold, it has been studied to a lesser extend.

Computing the barycenter of p unitary matrices $\{U_1, U_2, \dots, U_p\}$, requires again to solve the minimization operation given by (3.6). To the best of our knowledge, there is no closed-form solution neither for computing this center of mass [225]. The gradient update rule in eq. (H.6) is modified into:

$$U_{l+1} = U_l \cdot \text{Exp} \left[\epsilon \sum_{j=1}^p U_l^H \text{Log} (U_l^H U_j) \right]. \quad (3.11)$$

In practical implementation tests, some numerical problems have been observed, as the convergence is not attained for random positions across the entire image. Nonetheless, the unitary barycenters are not used for the final classification algorithm. With this in mind, while more sophisticated solutions for computing the geometric unitary may exist, they are not addressed here.

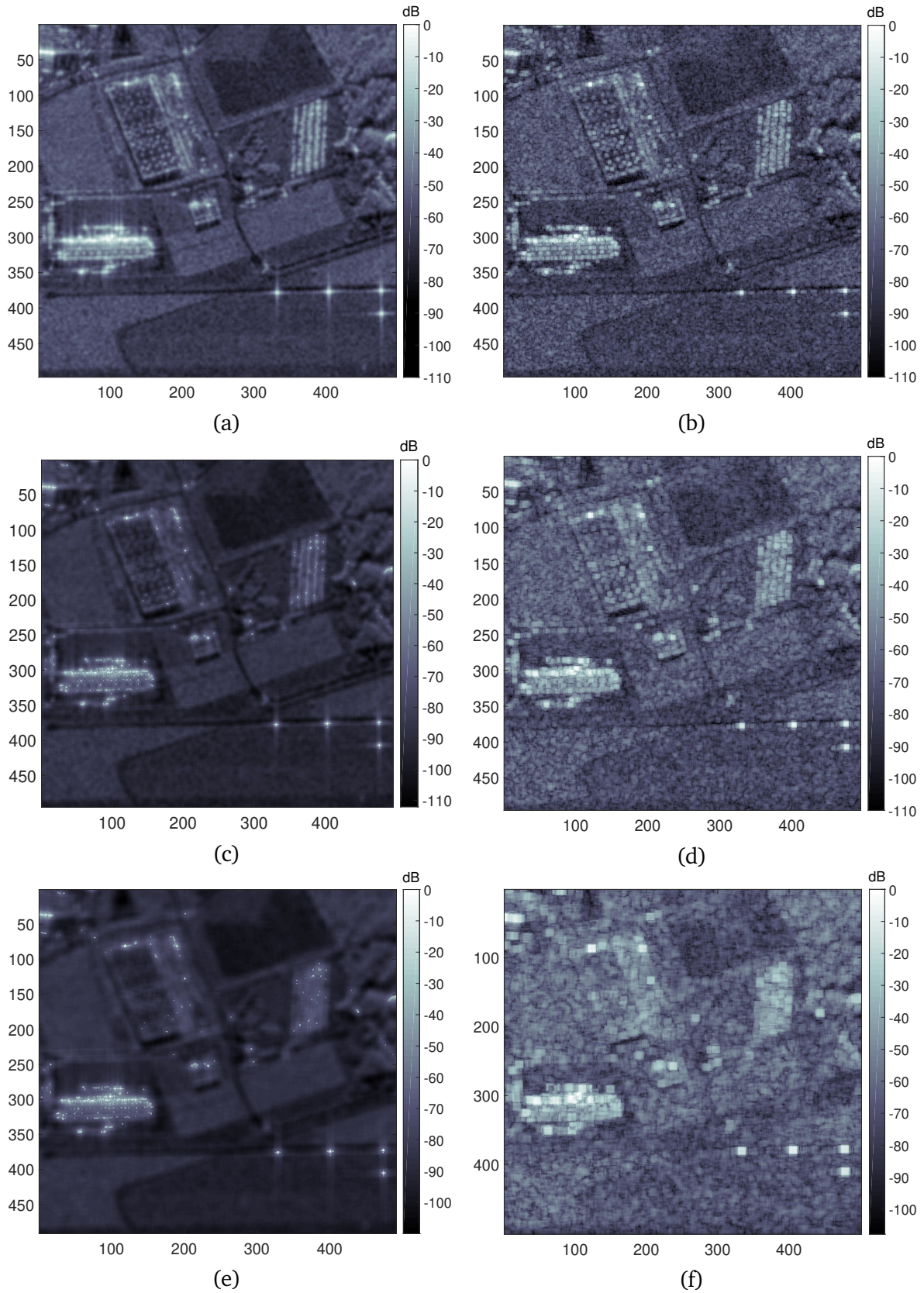


Figure 3.5: Brétigny Dataset.

left column- Geometric manifold average: Span of \mathbf{H} barycenters (boxcar estimation) [dB]

right column- Spatial average: Span of multilook \mathbf{S} data (boxcar estimation) [dB].

(a-b): 5×5 pixels. (c-d): 7×7 pixels. (e-f): 11×11 pixels.

The display uses Matlab's 'bone' colormap. The 1-look dataset span image [dB] is Fig. F.1(a).

3.4 Geometric clustering with Hermitian factors

3.4.1 Evaluating the contribution of the unitary factor

■ Rotation and phase component:

Checking the single-channel amplitude or the span images of the Hermitian and polar factors/estimated barycenters provides very different results. When evaluating the Hermitian matrices, they contain a rich spatial information as in the original PolSAR dataset (as observed in Fig. 3.5). By contrast, there is little visual information displayed by the span of the unitary matrices. However, this is expected. Apart from a normalization constant, the unitary factors are matrices with unit determinant. As discussed earlier, they are parametrized by one real rotation angle and several phase factors.

This subsection aims to assess if any type of pattern or particular information can be associated to the unitary component, by analyzing some phase and angular parameters. This evaluation is applied to the unitary barycenter estimates, which are derived using a similar iterative approach as with the Hermitian factor estimates, but with the appropriate distance (3.10) and updated rule from (3.11). It is important to mention that this implementation for the unitary case is not 100% convergent; the points for which unitary barycenters are not convergent are masked-out in white in any display to follow and not considered with computations.

The elementary form of a unitary matrix in (3.4) contains the contribution of one rotation and three phase factors. For decoupling the influence of the multiple phases, a normalization is proposed to the unitary matrices, as in [206]:

$$\begin{aligned} \mathbf{U}_{\text{ph-}} &= \mathbf{U} \begin{pmatrix} e^{-i\varphi_1} & 0 \\ 0 & e^{-i\varphi_4} \end{pmatrix} = \begin{pmatrix} |u_{11}| & |u_{12}| \cdot e^{i(\varphi_2 - \varphi_4)} \\ |u_{21}| \cdot e^{i(\varphi_3 - \varphi_1)} & |u_{22}| \end{pmatrix} \\ &= \begin{pmatrix} \cos\theta & -\sin\theta \cdot e^{-i\phi} \\ \sin\theta \cdot e^{i\phi} & \cos\theta \end{pmatrix} \end{aligned} \quad (3.12)$$

The normalized matrix $\mathbf{U}_{\text{ph-}}$ is in the form of a complex rotation with one angular θ and only one phase ϕ parameter. This is exemplified considering unitary barycenters estimated on the real Brétigny dataset. Results are shown in Fig. 3.6. With this dataset, about 25% of the image pixels do not attain unitary barycenter convergence (they are ignored for the statistical evaluation).

The rotation angle θ parameter takes values below 25° , while the absolute phase values $|\phi|$ are normally spread in the $[0^\circ, 180^\circ]$ interval, with a 90° mean and approximately 30° standard deviation (Fig. 3.6a-d). The only distinctive pattern is in the west-side area, marking the position of one building with multiple *coherent scatterers* (Fig. F.1a). There, the θ values approach zero degrees, while the ϕ presents also an extreme (i.e. $\pm 180^\circ$). This indicates that the phase normalized unitary matrices (3.12) are at those locations (almost) equal to identity. In turn, this can also imply that the original unitary polar factors, on which the optimization barycenter estimation is performed, are themselves close to identity. For such a case, the

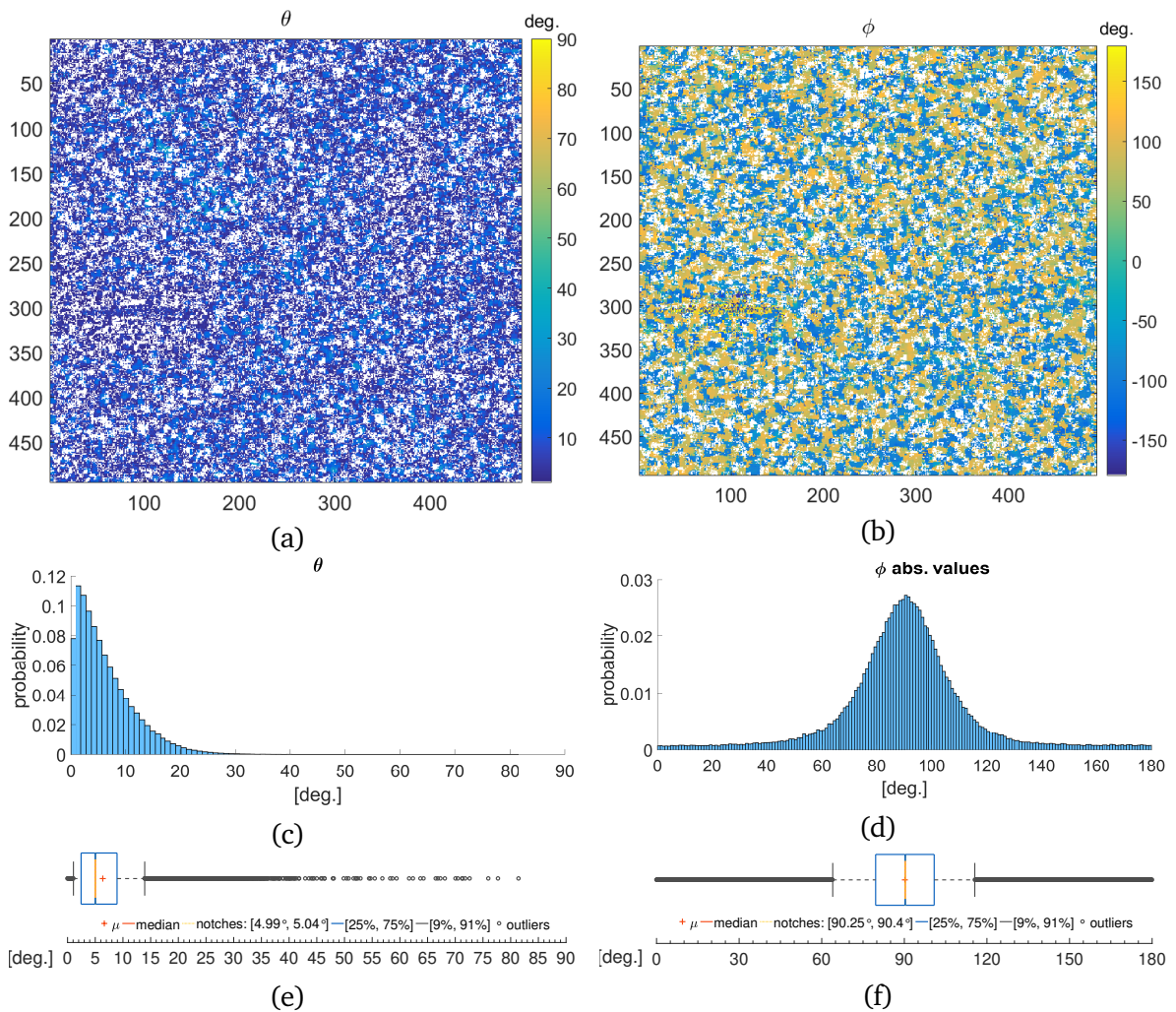


Figure 3.6: Brétigny Dataset. (a) Angles obtained from the normalized unitary barycenter matrices [deg.]. (b) Phase values obtained from the normalized unitary barycenter matrices [deg.]. Following statistics are computed excluding white-masked values: (c) Histogram of angles from (a). (d) Histogram of absolute phases from (b). (e) Notches boxplot with mean and median values for angular parameter in (a). (f) Notches boxplot with mean and median values for (absolute) phase parameter in (b).

Hermitian polar factors are completely descriptive and (almost) equal to the original scattering matrices. As a result, discarding the unitary polar factor in each of these locations has a minimal influence and the polarimetric information content is completely preserved. For other areas, having the angular parameter $\theta \in [0^\circ, 25^\circ]$ still assigns overall diagonal values close to one for (3.12), as $\min\{\cos\theta\} \approx 0.9$.

■ PolSAR roll-invariance and compensation:

As introduced in Chapter 1, rotation invariance is a desired property in PolSAR of both targets and descriptive parameters. In monostatic observations, a rotation of

the target around LOS has the same effect with an antenna turn around this axis. While the antenna is nonetheless kept fixed, a rotation of a target with azimuth symmetry has the final effect of a polarization rotation in the received signal.

For some descriptive parameters, their computation technique inherently eliminates rotations (e.g., the eigen-decomposition applied to the covariance matrix, which assures that the entropy and average alpha angles are invariant [4]), while for others, the orientation-compensation is applied as prerequisite. Such operation has been used in PolSAR with scattering matrices [226, 76], covariance/coherency matrices, Mueller/Kennaugh matrices [226, 181], alike.

For example, in model-based classification applications with uncompensated monostatic PolSAR data, the influence of rotations on targets is known to determine a shift of the perceived scattering mechanism (e.g., in case of rotated dihedrals, a change from double-bounce to volume scattering [163], as discussed in Section 2). Consequently, it is typical for PolSAR techniques to incorporate pre-processing to mitigate the effect of rotations. Huynen used to employ the term desying (i.e., "de Ψ ying", considering Ψ the rotation angle) for the angle removal procedure [66, 226]. Generally, real rotation matrices are employed for compensation, but several studies with covariances and SU(3) unitary matrices have shown an improved effect when both a real rotation and a phase compensation is performed [227, 228, 229]. For example, when compensating the scattering matrix, a real rotation will usually have the desired effect with symmetric (i.e., nonreciprocal) matrices. This is generally suitable for monostatic datasets and not necessarily when nonreciprocal effects are introduced (e.g., see the discussion in Chapters 1 and 2).

The introduction of a complex phase component has been associated in PolSAR to the action of a helix element, or the coherent summation of two different scattering mechanisms aligned along the LOS with a separation up to $\lambda/8$. In this context, Wentao et al. describe the effect of unitary compensation as the combination of a (normal) rotation and a helix angle compensation [230].

As a result, the use of the polar decomposition can prove highly beneficial. Because the unitary factor integrates both rotation and random phase components, the Hermitian factor becomes rotation invariant. As observed, in the previous example, man-made targets producing a strong radiometric reflection are not influenced by real or complex rotations, while for other scatterers the removal of unwanted rotations is envisioned as a prerequisite.

Given that contextual and spatial information is preserved by the Hermitian term across the PolSAR image and the matrices are endowed with the geometrically rich interpretation of the Riemannian cone, the Hermitian factor plays a key role in the proposed clustering method described hereafter.

3.4.2 Method description

A novel algorithm for unsupervised classification which performs geometrical clustering on the manifold of Hermitian polar factors is proposed here. The method integrates two fundamental concepts: the polar decomposition of scattering matrices and the

Riemannian geometry of its Hermitian factors. The method is applied in a cohesive manner for both coherent and incoherent scatterers. Three processing stages are identified, as follows:

Step 1: The scattering matrix is decomposed using the (right) polar decomposition (1.31). The \mathbf{H} factors can easily be obtained by computing the square root of $\mathbf{S}^H \mathbf{S}$.

Step 2: An identification of coherent scatterers based on the 98th percentile criterion proposed by Lee et al. [231] is performed, at first. As in the original algorithm, a 3×3 boxcar neighbourhood is used. The pixels fulfilling the criterion are considered to represent coherent targets. For them, no additional steps are needed and the Hermitian factors are used directly for clustering (Step 3). With all other pixels, barycenters are otherwise computed. This is the analogous of a N-look geometrical center of mass estimation in the manifold of Hermitian polar factors. The barycenters are obtained through an iterative method (Annex H) applied in local, square, sliding neighbourhoods of fixed size. Evaluating the Riemannian Hermitian barycenters may be designated henceforth using the acronym *PolBaRi* (*POLAR* decomposition *BA*rycenters estimation on the *RI*emannian manifold).

Step 3: A modified k-means⁵ algorithm is applied to the set of points containing estimated geometric means and coherent Hermitian factors. The computation is kept into the native Riemannian manifold of positive-definite matrices by choosing AIRM as an appropriate inter/intra-cluster separation metric. Given the schema in Fig. 3.1, the method proposes contributions in the data input format, the update of class centers and the metric used to evaluate the objective function.

In this implementation, the class centers are randomly initialized and the number of clusters is fixed and proposed as input parameter. Progressively, one of the K classes is assigned at each (barycenter) matrix location and the cluster centers are updated. The operation is repeated until the inter-class transfer is lower than a predefined threshold.

♠ Identical results have been obtained in practical tests with the monostatic datasets, when checking alternatively the right and left polar forms. As discussed, the two Hermitian factors $\left(\mathbf{H}_R = \left(\mathbf{S}^H \mathbf{S} \right)^{1/2} \text{ and } \mathbf{H}_L = \left(\mathbf{S} \mathbf{S}^H \right)^{1/2} \right)$ are similar, $\mathbf{H}_L = \mathbf{U} \mathbf{H}_R \mathbf{U}^H$, and have the same eigenvalues. Moreover, these values are exactly the real-valued singular values of \mathbf{S} . As pointed out in the previous chapters, for monostatic data verifying reciprocity, they are no other than the conjugate eigenvalues.

⁵From a computer science perspective, the better name to be used is k-medoids. It refers to a clustering technique, similar to k-means, apart from the centroid computation. While in k-means the class centroid may be different from the existing elements of a class (as the result of averaging), the metric criteria for k-medoids selects the center/centroid from the elements inside a class. Nonetheless, we stick to the more common name in PolSAR. The technique will be hereafter referred as Riemannian k-means.

3.5 Geometric clustering: Implementation and testing

This section presents the results obtained by evaluating the proposed clustering method on both real PolSAR and simulated polarimetric data. The analysis is exclusively applied to the monostatic case. Nonetheless, through the use of the polar decomposition, the method can be applied without changes to both monostatic and bistatic data. The choice of colormaps is arbitrary and a certain color does not imply a transferable meaning of scattering mechanisms between datasets.

3.5.1 Simulated datasets

The algorithm's assessment with simulated datasets is the main focus of this subsection. The phenomenology of dihedral and volumetric scattering is considered with the two simulations. The data does not deviate from the multivariate Gaussian case. Both qualitative and quantitative evaluation is addressed.

3.5.1.1 Simulated dataset based on monostatic CST results

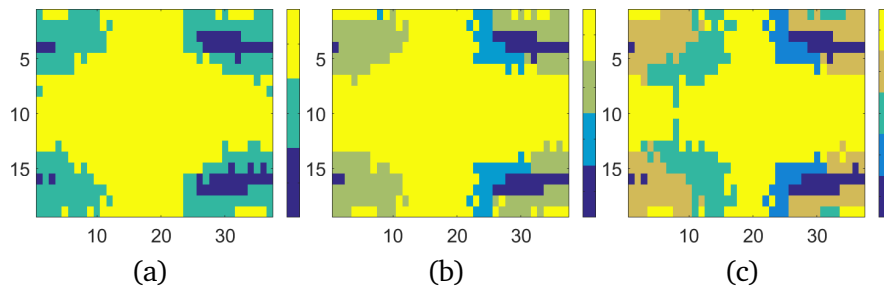


Figure 3.7: Simulated dataset 1. Geometric clustering using the proposed method with variable number of input classes: (a) 3, (b) 4, (c) 5.

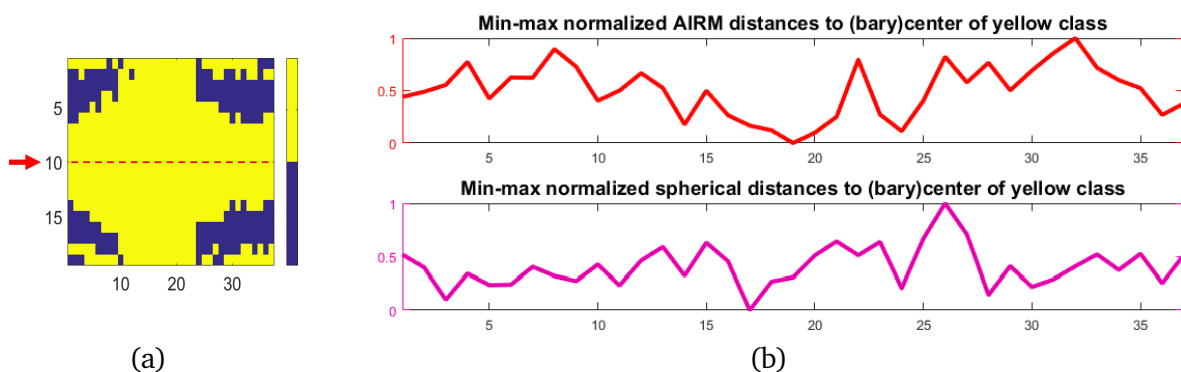


Figure 3.8: Simulated dataset 1. (a) Geometric clustering using the proposed method - Result with 2 classes. (b) Intra-class distance evaluation (centroid of yellow class to each \mathbf{H} barycenter from positions on the red line) by two geometric distances.

The data used in the first analysis is based on the monostatic simulations for the dihedral elementary object, from Chapter 2 - Section 2.5. The dimensions of the original simulation are slightly reduced, so that only the scattering interval $\theta, \varphi \in [-45^\circ, 45^\circ]$ is considered.

This dataset is not fed directly into the clustering algorithm. In order to account for noise variations and have a more reliable parameter estimation, pixel-wise covariance matrices are computed from the original simulated data and the Cholesky square root is multiplied by stochastic Gaussian vectors ($N = 50$ times repetition for each pixel), which generates a tensor with dimensions [orig. height \times orig. width $\times 4 \times 50$]. This is followed by the polar decomposition and the \mathbf{H} barycenter estimation, which reduces the data dimension to [orig. height \times orig. width $\times 4$]. The Riemannian clustering method is applied with varying number of classes and results are presented in Figs. 3.7 and 3.8(a). Even with the increase of the parametric input indicating the number of classes, the results steadily identify the two main classes at the same locations: the central cross-like shape (in yellow) and at the four corners. Inferring from the previous discussion of Fig. 2.12, in which the α_{Cloude} parameter is used to study the simulated scattering response, these zones correspond to the double bounce and single bounce mechanisms.

For the result obtained using only two parametric classes, the intra-class separation along a selected line (middle cut, with red in Fig. 3.8(a)) is compared in Fig. 3.8(b). Two geometric distances are considered: on one side, the affine invariant Riemannian metric used even in the computation of the results, and on the other, the angular geodesic distance [168, 181]:

$$d(\mathbf{H}_1, \mathbf{H}_2) = \frac{2}{\pi} \cos^{-1} \left[\frac{\text{Tr}(\mathbf{H}_1^H \mathbf{H}_2)}{\sqrt{\text{Tr}(\mathbf{H}_1^H \mathbf{H}_1)} \sqrt{\text{Tr}(\mathbf{H}_2^H \mathbf{H}_2)}} \right]. \quad (3.13)$$

Both results have been normalized. There is a similar outcome of the intraclass-to-centroid distance evaluation, when using the two metrics. This motivates to adapt the angular geodesic distance for testing with real PolSAR data.

3.5.1.2 Simulated dataset based on covariance matrix model

Evaluation on a different simulated dataset is proposed here. Compared with the previous, which has an important phenomenological component but no fixed ground-truth, the aim of this subsection is to test the algorithm on a benchmark dataset with known class separation. The dataset is simulated using the well-known model described in Annex F I-II, which has been used to model symmetric anisotropic media with Gaussian clutter. This is usually associated with volume scattering. Also, the choice of statistical model is best known for fitting homogeneous regions in real PolSAR images.

Fig. 3.9(a) displays the span of the simulated image, total size 300×300 (pixels), and in which four concentric regions are shown. The method from Annex F allows to

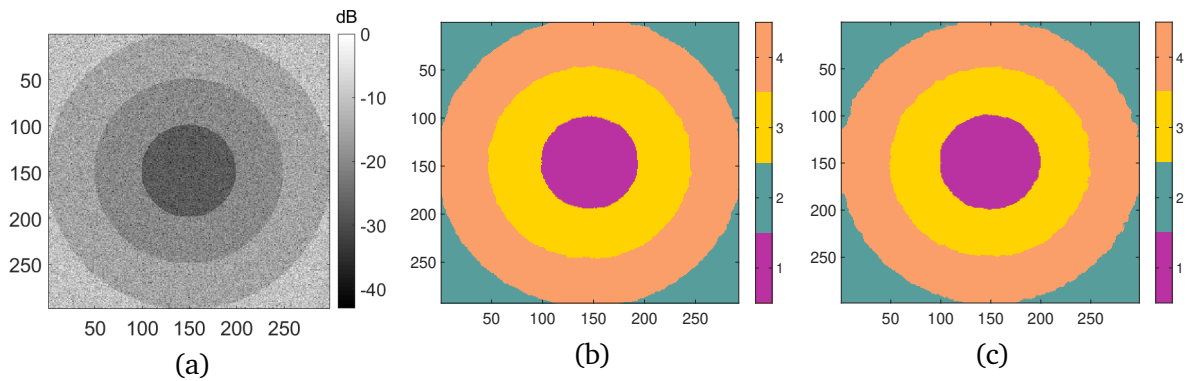


Figure 3.9: Simulated data - Example 2.

(a) 1-look Span [dB]. (b) Wishart Classifier. (c) Proposed method: PolBaRi+Riemannian k-means.

obtain synthetic responses of polarimetric channels with known statistics, i.e., having a known covariance/coherency matrix [232]. In the test image, the covariance is different for each region and the intensity is varied linearly from one region to another (i.e., the center area having the lowest intensity).

Results using the proposed method are compared to those obtained using the classical Wishart classifier [172]. With PolSAR multivariate data following the Gaussian model, the latter is known to provide an optimum solution. For both algorithms, the number of expected classes is an input parameter.

The clustering results are in Figs. 3.9(b) and (c), with the percentages of per-class accuracy, overall accuracy and Kappa index ⁶ in Tables 3.3 and 3.4. The evaluation shows similar results for both approaches with a slightly higher overall accuracy with the Riemannian k-means method.

Table 3.3: Per class accuracy [%].

Avg. class accuracy: 96.845 %.

Kappa index: 0.9736.

		Actual class			
		1	2	3	4
Wishart	1	91.45	0	8.55	0
	2	0	99.77	0	0.23
	3	0	0	99.46	1.54
	4	0	1.2	0.14	96.7

Table 3.4: Per class accuracy [%].

Avg. class accuracy: 99.017 %.

Kappa index: 0.9835.

		Actual class			
		1	2	3	4
Proposed	1	99.66	0	0.34	0
	2	0	98.81	0	1.19
	3	0.5	0	98.82	0.7
	4	0	0.57	0.65	98.78

⁶The kappa statistic provides a measure of agreement which reflects also the situation that the outcome is obtained solely based on chance. However, it does not give any indication where disagreement occurs. $k = \frac{p_o - p_e}{1 - p_e} \in [-1, 1]$, where p_o quantifies the overall accuracy and p_e measures prediction as if happened by chance. Finally, larger values are better, as $k=0$ denotes agreement purely by chance and $k=1$ is the perfect agreement.

3.5.2 Real datasets

This subsection continues the testing of the proposed geometric framework, with real monostatic PolSAR data. The Brétigny and Foulum datasets are used (Annex A). Apart from the Riemannian k-means method, the Wishart classifier and a covariance-based k-means using the angular geodesic distance are employed. The latter follows exactly the model of the Wishart method apart for the inter/inter-class distance, which is changed from statistical to geometric.

The initialization with the Wishart clustering is based on an initial $H - \alpha$ segmentation. The Riemannian k-means uses the same number of classes (i.e., 8) but considers a random initialization of class centroids (Fig. 3.1). Each algorithm uses a type of boxcar averaging: in the estimation of coherency matrices with the Wishart algorithm and in computing the geometric barycenters for the proposed method. The same size for the local sliding window (7×7 pixels) is considered. This dimension has been used with many previous covariance-based PolSAR publications as a good compromise between image resolution degradation, feature preservation (Fig. 3.5(d)) and accuracy of estimation. All clustering results have classes sorted in ascending order. Without the presence of actual ground-truth, the labeling of classes is not addressed and the comparison is overall visual.

3.5.2.1 Real dataset 1 - Brétigny

Clustering results for the Brétigny dataset are displayed in Fig. 3.10. The classes having the largest number of pixels (i.e., yellow, orange) are identified to cover mostly the same locations in the three images. However, the most striking difference between the three results is textural. The Wishart classifier (Wishart distance for inter/intra-class separation) obtains smooth, largely homogeneous areas. On the other hand, when having the angular geodesic as inter/intra-class metric, the results is quite the opposite, with an important heterogeneity. The Riemannian k-means implementation (Fig. 3.10(c)) is somewhere in between in terms of homogeneity. By far, it better conserves the largest number of details from the original image (Fig. F.1(a)). This can be observed, for example, with the bow-shaped field located North-Central, which is separated by the proposed method. A close-up from near one calibration target in the image (Fig. 3.10(d)) shows a partitioning which resembles the one in Subsection 3.5.1.1, for the simulated dihedral.

The result in Fig. 3.10(b), i.e., angular geodesic distance, suffers some important shortcomings: the calibration reflectors at known-location in the image (South-East) are not identified as expected and the oblique parking lot (Center-East) is confused with neighboring areas.

In the Wishart classification result (Fig. 3.10(a)), the roads and other areas of lower intensity blend with the background yellow class. With an improved segmentation, their contours (for comparison, see Fig. F.1(b)) are better distinguishable in the Riemannian k-means result.

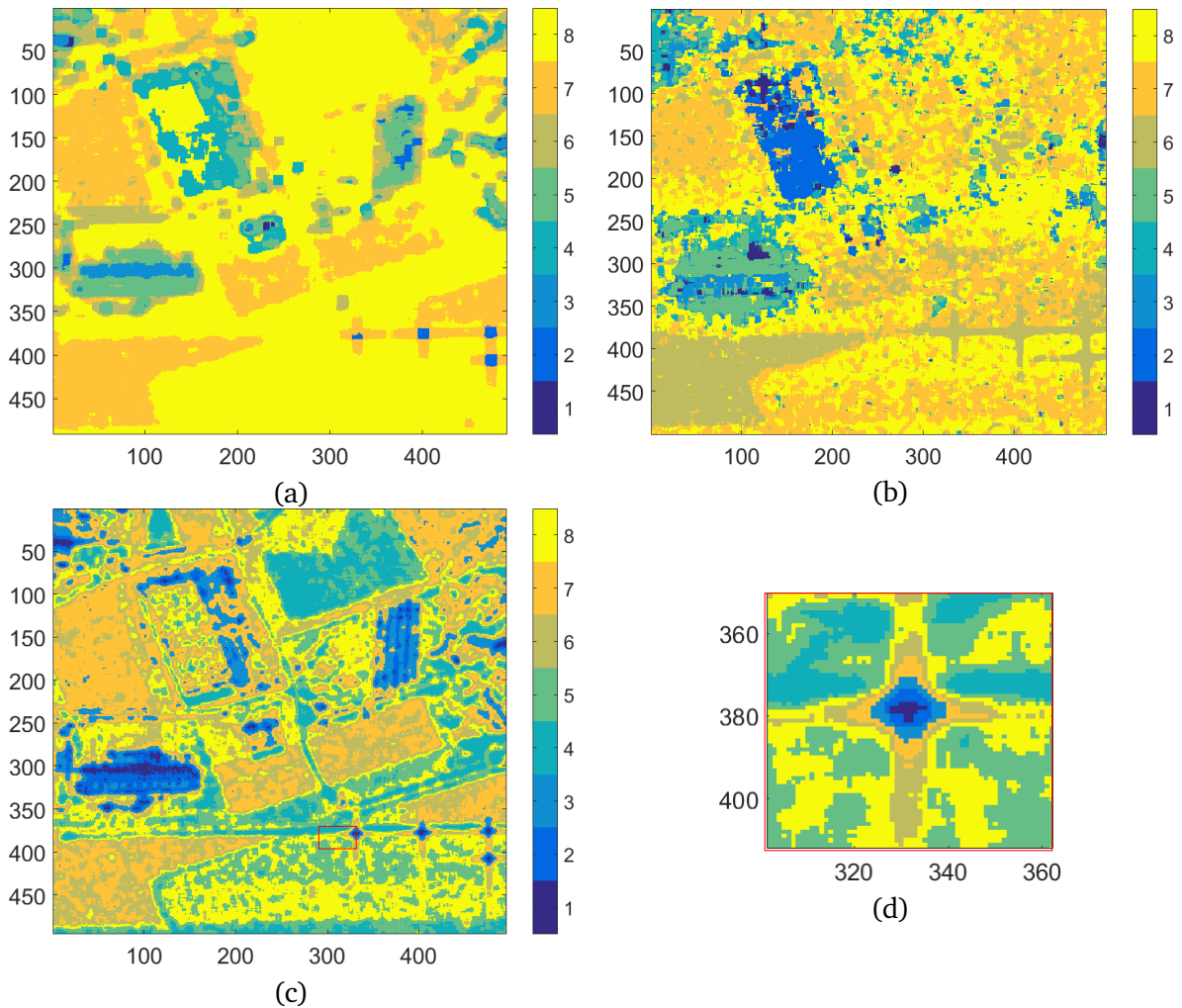


Figure 3.10: Real Dataset 1 - Brétigny. (a) Wishart. (b) Angular geodesic k -means. (c) PolBaRi+Riemannian k -means. (d) Close-up for red rectangle crop in (c).
 Note: The 1-look span image [dB] is Fig. F.1(a).

3.5.2.2 Real dataset 2 - Foulum

The three clustering methods are now applied to the Foulum dataset and results are presented in Fig. 3.11. Close-ups for a selection of five regions in the image are separately shown in Fig. 3.12(b)-(d). An incomplete ground-truth in Fig. A.3(c) is introduced for comparison.

Here, there is a more nuanced discussion which can be made. Inspecting the color-coding of Figs. 3.11(a) and (b), one observes that the clustering results with the classical Wishart and the geodesic k -means display similar results. Both have a clear delimitation of the lake (North-East), forest (Center and upper right corner) and of the two urban agglomerations (South). Although the fields have discernible contours, they overall belong to a single class, which is the same as the one assigned to the lake.

The Wishart classification for the forest is very similar to the one obtained with the Riemannian k-means. It can be observed from the optical image in Fig. A.3(a) that the area is not uniform (unlike the small forest in the upper right corner), but a mixture of essence and meadows/fields. Again, the model seems to better preserve the texture information of the original dataset. The strength of the Riemannian k-means results lies in the possibility to extract more classes in the agricultural regions. It is able to discriminate some crop fields which are not retrieved by the other two methods, exhibiting an improved accuracy with respect to the ground truth (lines 1-2-3 in Fig. 3.12). There remain certain areas where classes tend to blend (e.g., line 4) and in the lake's region (e.g., close-up line 5, Fig. 3.12), there is a large non-uniformity, as it combines multiple classes.

3.6 Conclusions

This chapter has focused on the polar decomposition and has introduced a geometric clustering technique which exploits the Riemannian manifold of the scattering matrices' Hermitian factors. The proposed technique is simple and effective in better preserving texture information in the end clustering result.

As drawbacks, the optimality of the clustering or the attribution of the scattering mechanism behind the thematic labeling are not currently investigated. Two soft spots of the proposed technique may be the algorithm initialization and the parametric number of clusters. It is known that both have an influence on the final outcome of k-means implementations. As a result, it can be expected that the combination of random initialization and fixed input parameter may not always provide the best outcome in practice. Immediate algorithmic improvements should: a) propose an optimum deterministic initialization and b) an adaptive selection of the number of classes for each unique dataset.

While there remain certain elements which can be addressed to improve the clustering estimation results, the implications of the proposed method are important. It shows that the informational space of the scattering matrix (only limited to the Hermitian factors) is able to provide comparable results to those obtained with conventional covariance techniques.

Recent experiments with complex neural networks using as input features only the complex Pauli elements (e.g., [233]) have shown to (slightly) outperform not only real neural networks implementations, but also complex ones using as input features the covariance matrix elements. This is quite similar to the conclusion obtained in this chapter. The proposed study and future developments may provide understandable insight on how these type of machine learning implementations finally converge to their outcome.

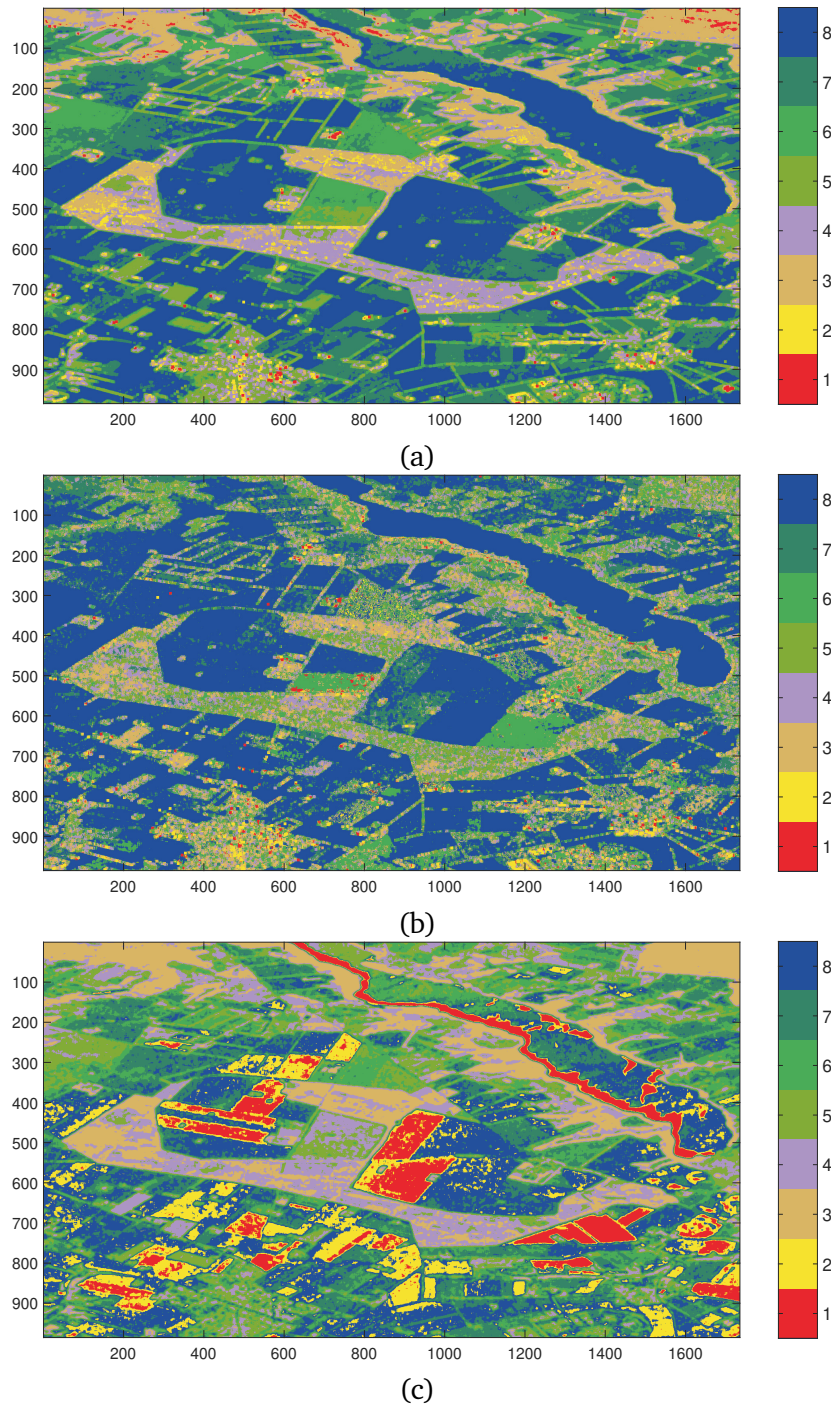


Figure 3.11: *Real Dataset 2 - Foulum.* (a) *Wishart.* (b) *Angular geodesic k-means.* (c) *PolBaRi+Riemannian k-means.*

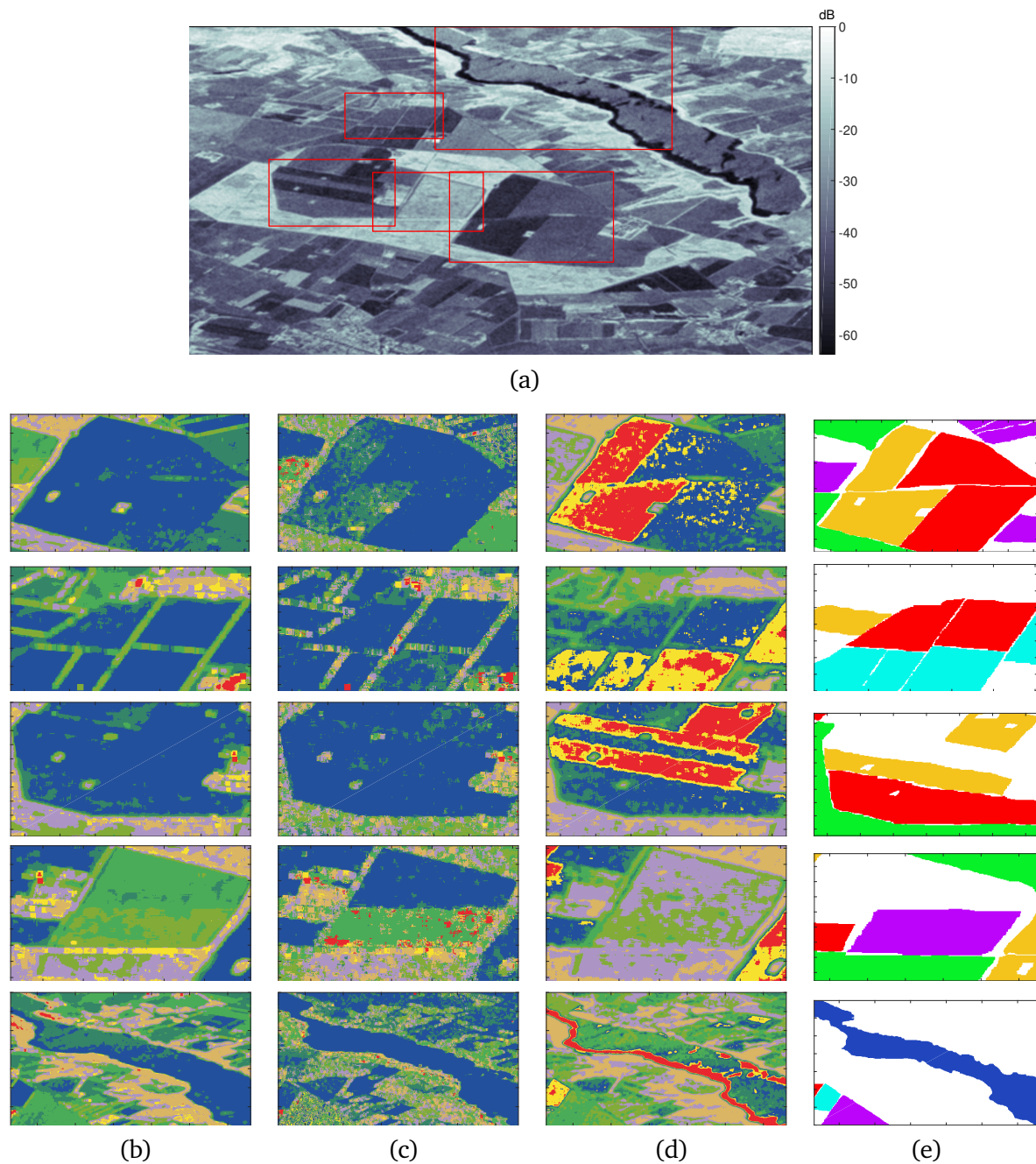


Figure 3.12: Real Dataset 2 - Foulum. (a) Span of estimated \mathbf{H} barycenters and red region selections. Close-ups of selected regions, considering the: (b) Wishart clustering. (c) Angular geodesic k -means. (d) Riemannian k -means. (e) incomplete ground-truth from Fig. A.3(c) [234]. There is no correspondence between the colormap of columns (b), (c), (d) (same as in Fig. 3.11) and the one of column (e).

Conclusion and perspectives

As always, this is the start of a conversation, not the end of one.

The purpose of this chapter is to summarize the contributions presented in the dissertation and introduce some perspectives of future research to complete and improve this work.

This thesis proposes contributions on the development of tools and methods for the processing of polarimetric radar images. The matrix formalism was adopted for data representation, which had a great influence on the final proposed methods. Motivated by recent technological achievements and the pursuit of future developments in bistatic and distributed systems, the context of bistatic polarimetric diversity serves as a backdrop. As so, there is an explicit or implicit questioning of the compatibility and generalization for the bistatic scenario for all proposed algorithms.

Summary

The thesis explores only a part of the multiple facets of polarimetric radar diversity and some of the topics which have been discussed and introduced throughout the manuscript can be found in Fig. 3.13.

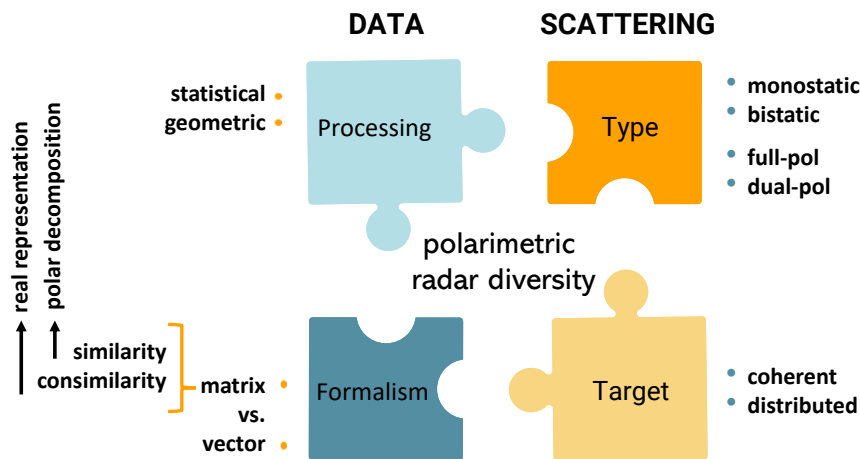


Figure 3.13: Key topics in radar polarimetry discussed throughout the thesis.

The data acquisition diversity is directly influenced by the properties of the sensor, i.e., the radar system. As an active instrument, the access to the complete or incomplete

(full- vs. dual-pol or compact) set of polarimetric parameters is conditioned by the type of wave diversity at emission. In the reception stage, the geometric setting has its own influence on the polarimetric diversity, which made us explore the monostatic vs. bistatic paradigm, in Chapters 1 and 2. Full-polarimetric diversity is generally assumed throughout the dissertation. However, a short example at the end of Chapter 1 explores the results of applying the dual-pol $H - \alpha$ on a test scene imaged simultaneously by dual-polarimetric monostatic and bistatic radar sensors. We firstly investigate the differences in parameter interpretation between dual-pol and quad-pol $H - \alpha$ and finally compare the dual-pol monostatic and bistatic results.

In other parts of the thesis, based on the full-polarimetric model, the data is assumed as single look complex and each pixel is described by a scattering matrix. Early PolSAR works, especially for basis change and the extraction of extreme polarimetric states (i.e., co-pol maximums, cross-pol minimums) have been the first to introduce the use of the matrix formalism. However, it is generally adopted only for scatterers under a deterministic model, while the vector formalism pertains for computations involving distributed scatters. The method proposed by Chapter 2 applies to a coherent target model, while the one in Chapter 3 is intended for real PolSAR data, where incoherent scatterers dominate. We summarize the main contributions of each of these chapters, as follows:

■ Chapter 2:

- *Method for complex conjugate-eigenvalues detection, based on the real representation*

This chapter provides a clear overview on consimilarity in PolSAR and proposes a representation based on the real representation scattering matrix RRSM. In truth, the consimilarity transformation appears as a distinct algebraic operation only in the case of nonreciprocal scattering matrices, while reducing to orthogonal congruence when the matrices are reciprocal (i.e., mathematically symmetric). However, with nonreciprocal scattering matrices, assumed only for the bistatic case, a different framework is considered by theory, which is the one of the singular value decomposition. The great simplifications of this model is that all monostatic PolSAR data needs to be reciprocal and the actual processing framework between reciprocal and nonreciprocal data is very different. Upon introducing the real representation, we present how it can be used with the conjugate similarity framework for both reciprocal and nonreciprocal scattering matrices. Reciprocal matrices will generally have a unique factorization. Experiments show that coneigenvalues results from reciprocal matrices compared under the Takagi factorization (i.e., on which the Graves method is based) and the RRSM eigen-decomposition are always equal (with at most a 10^{-2} tolerance) when the case reduces to orthogonal congruence (i.e., values are distinct). With non-reciprocal matrices, the factorization may provide solutions in the complex plane and at least one of the factors may not be unique.

- *Analysis of real (monostatic) and simulated (monostatic and bistatic) polarimetric data using the real representation detection*

In the second part of the chapter, polarimetric simulations based on a computational electromagnetic software have been obtained. They are generated

for two coherent targets (a square plate and a 90° dihedral), in monostatic and bistatic geometry and from a wide-range of observation angles. The detection method using the real representation eigen-decomposition has been applied to the simulated polarimetric datasets, as well as to real monostatic PolSAR data. Results have shown that complex coneigenvalues can be present in all cases. As expected, they appear with a very low probability (below 5%) with all tested monostatic data. The percentage is much higher under bistatic observations.

■ Chapter 3:

- *Analysis of the two factors in the polar decomposition*

In the first part of this chapter, the polar factorization is proposed for data representation. The unitary and positive definite polar factors are each explored through parametrizations and representations in \mathbb{R}^3 . Both algebraic and geometric properties are discussed and examples using real PolSAR data are provided.

- *Geometric clustering using the Hermitian factors* The embedding of polar H factors in the manifold of Hermitian positive definite (HPD) matrices is the main idea behind the proposed geometric clustering method. Preceding the actual clustering, the Hermitian polar factors from fixed spatial neighbourhoods have been "averaged" by a manifold-based method, which estimates a geometric center of mass for the set of matrices in the neighbourhood. This operation can be put in parallel to the estimation of the sample covariance matrices. The actual clustering, has been implemented as a centroid, partitional-based algorithm and having the AIRM Riemannian geodesic distance for intra/inter-cluster comparison. In light of this contribution, the method's performance has been tested using Hermitian factors from both real and simulated monostatic PolSAR data. Compared to the nonsupervised Wishart method, improved quantitative and qualitative results are obtained. With real polarimetric data, the final clustering result is observed to better preserve texture details.

Perspectives on future work

Extensions, as well as potential improvements, on each of the two main study axes of this thesis (i.e., the consimilarity & real representation and the polar decomposition & geometric clustering) are discussed in this subsection.

- *Bistatic data and complex coneigenvalues*

Our investigation using simulated data did not identify a link between descriptors of the bistatic geometry (e.g., the bistatic angle) and the complex coneigenvalues. This may suggest that, if existent, the connection is multivariate, with improved models and tests needed.

- *Conjugate similarity vectors with nonreciprocal data*

The work in Chapter 2 has been centered around the conjugate eigenvalues of non-reciprocal scattering matrices. An immediate extension is to consider the coneigenvectors (from the 2×2 scattering matrix, the 4×4 real representation matrix, or both). For uncovering some of their properties, a possible suggestion would be in identifying descriptive parameters or the proposal of a target vector model. For the time being, the model of conjugate similarity factorization is restricted to coherent applications. Introducing a unique target vector model would immediately allow its extension by a covariance-based incoherent decomposition technique.

On a different note, machine learning models could be employed using (a) consimilarity features, or (b) the proposed real representation. In the first scenario, networks based on complex parameters would be appropriate, whereas the second case could prove more simpler, requiring networks with real parameters. However, extra attention would be necessary with the latter, to fully account with the assumptions on the scattering coefficients, i.e., the real and imaginary parts must be uncorrelated.

Considering the second axis of the thesis, we identify two different types of improvements: possible updates (with more immediate results, as they are based on combining methods already known in the literature) and a number of possible advancements (with a higher degree of novelty):

- *Assessing focused changes of the geometric clustering method*

The algebraic median is known to be an estimate more robust to outliers. While keeping the core ideas of the geometric clustering method, a different test version may change the estimation process of the Riemannian mean to the estimation of the Riemannian median [221].

Differently, the AIRM metric can be changed and compared with other distance metrics, still adapted for the HPD manifold, as the log-Euclidean or the log-Cholesky distances [235]. And finally, the partition-based clustering algorithm may be changed to other clustering models (e.g., hierarchical).

- *New directions to explore*

A deterministic initialization of the clustering algorithm, ideally through a method reflecting scattering characteristics in the PolSAR data, would be envisioned.

A much broader comparison between classical ICTD methods and the one proposed in Chapter 3 would involve an understanding of the exact role carried by the Riemannian manifold dimension, as well as the exact difference in informational content. This could involve extending the geometric method to the computation of the geometric mean of PolSAR covariances or the Hermitian factor from the polar decomposition of the proposed real representation.

For a set of univariate data, approximations of the geometric mean are possible using the arithmetic mean and several central moments. An extension of this property to sets of covariance matrices would allow to also foster a connection between the geometric mean and the sample covariance (studied under different statistical assumptions, Gaussian and non-Gaussian).

Polarimetric datasets used in the thesis

A.1 Quad-pol Data

Table A.1: *Monostatic full-polarimetric datasets used in the paper.*

Dataset Name	Acquisition system (Institution)	System type	Band	Resolution (rg. \times az.) [m]	Size (rows \times columns)
I. Ramses Brétigny	RAMSES (ONERA)	airborne	X-Band	1.5 \times 1.5	501 \times 501
II. Emisar Foulum	EMISAR (TUD, Denmark)	airborne	L-Band	2 \times 2	1750 \times 1000
III. Convair Ice	CONVAIR (Environment Canada)	airborne	C-Band	4 \times 0.4	544 \times 5238
IV. Convair Ottawa	CONVAIR (Environment Canada)	airborne	C-Band	4 \times 0.4	222 \times 3429

A brief overview of the full-polarimetric PolSAR datasets used in the manuscript is offered in Table A.1. For each dataset, extended information is provided hereafter.

I. RAMSES Brétigny



Figure A.1: (a) Google Maps optical image, Brétigny (France), May 2004. (b) Pauli color composite Ramses Brétigny data.

The data has been acquired by the RAMSES (Radar Aéroporté Multi-spectral d'Etude des Signatures) radar airborne instrument of ONERA, the French

Aerospace Research Agency, over a test site near Brétigny-sur-Orge (France). Operated roughly between 1995-2010, RAMSES has served as a high modular experimental test bench for multi-frequency radar imaging [236]. For this full-polarimetric dataset, the instrument was operating in X-Band (9.5 GHz central frequency, 1.2 GHz bandwidth). The polarimetric images are characterized by a resolution of approximate 1.5 m, in both azimuth and range.

The crop image, acquired near an airport runway (Fig. A.1a) is rich in both natural and anthropomorphic targets. There are buildings, a parking lot, vegetation areas (crops, prairies, forest) as well as four calibration trihedrals (lower-right part). The acquisition campaign is recorder to have taken place in September 1999 [237]. The horizontal road at the bottom of the figure was parallel to the plane's flight path. The data is available in the form for four, linear polarization (HH, HV, VH, VV) channels. The Pauli color composite representation is provided in Fig. A.1b.

For comparison, an optical image from 2004 (closest in time available with © Google Earth) is shown in Fig. A.1(a). Nonetheless, there are not many differences apart from the presence of a new building in North-West. Although there isn't a real ground truth from the time of the acquisition, the different elements inside the scene can be easily distinguished from later data because there haven't been many changes. Based on information now available online (for example on Géoportail FR), a quite precise delineation of parcels can be achieved ¹.

Fig. A.2(a) presents a topographic map of the area and Fig. A.2(b) shows a cadastral map. Using the remaining figures, one can rapidly separate the agricultural fields (Fig. A.2e) from the prairies/pastures land (Fig. A.2c) in the south of the image or identify the corners of the water reservoir from north. The forest is a mixture of hardwood species (Fig. A.2d).

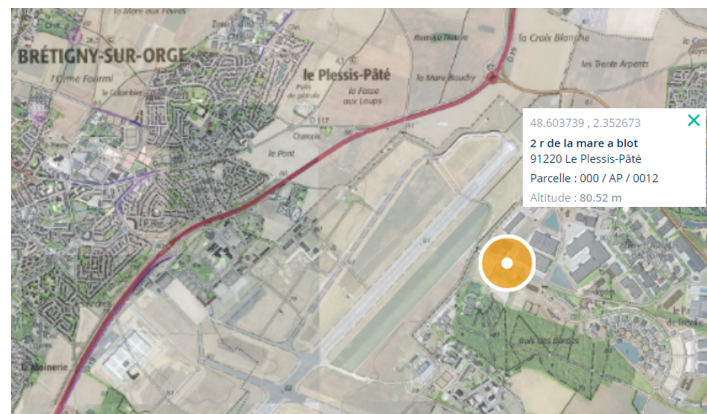
II. EMISAR Foulum

The ElectroMagnetic Institute Synthetic Aperture Radar (EMISAR) was a dual-frequency full-polarimetric SAR Danish airborne system developed for experimental purposes. It has been used for multi-pass interferometric and polarimetric experiments (full-polarimetric capability in C- and L-Bands) [238].

The sensor was used to acquire full-polarimetric data over ice and snow regions, as well as agricultural fields, during the European Multi-sensor Airborne Campaign (EMAC) in 1994–1999. The Foulum region (Central Jutland, Denmark) has served as a reference test site. The polarimetric dataset from this document was acquired in L-Band around April 1998 [142]. It shows a mixture of vegetation areas (different crop fields, forests), small urban areas and a lake/water reservoir (Pauli composite in Fig. A.3(b)).

The dataset is well-known in the PolSAR community; due to its richness of natural elements has been used for many publications. Some of them contain descriptions of the area's vegetation content, both perennial and annual, as in [173, 239]. Incomplete ground truth representations have been proposed in [240, 241, 234]. The example in [234] is reproduced in Fig. A.3(c).

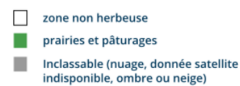
¹In the final stages of writing this manuscript, a ground-truth for the area has been proposed, with some insight data near the time of the Ramses acquisition [233]. However, this ground truth separates the small area considered in this work into three general classes, an a priori observed and used here by optical images inspection and/or cadastral maps.



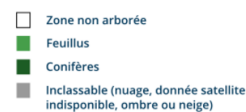
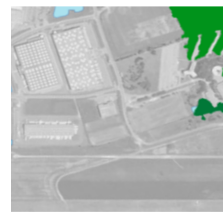
(a)



(b)



(c)



(d)



(e)

Figure A.2: Géoportail complementary information <https://www.geoportail.gouv.fr> (a) IGN Topographical map layer - Acquisition area view (2018). (b) IGN Topographical map - Close-up from (a) of the imaged zone. (c) CORINE Land Cover – Prairies (2015). (d) Forest (v.2, 2018) and Hydrologic (2021) Map Layers. (e) Example of Parcels Division (RPG) for 2007 (! NOT from the year of acquisition). For (c), (d), (e) an Aerial Photograph Layer (2000-2005) serves as basemap, similar to Fig. A.1a.

III. CONVAIR

The SAR-580 radar facility operated by the Environment Canada, Canadian Center for Remote Sensing, on-board a Convair-580 turbo airplane has served as experimental facility and precursor for a number of Canadian SAR missions, e.g., the RADARSAT family of satellites [242, 243]. The monostatic radar was dual-frequency, able to operate simultaneously in both C and X bands and, as in the case of EMISAR, was used for interferometric and polarimetric applications.

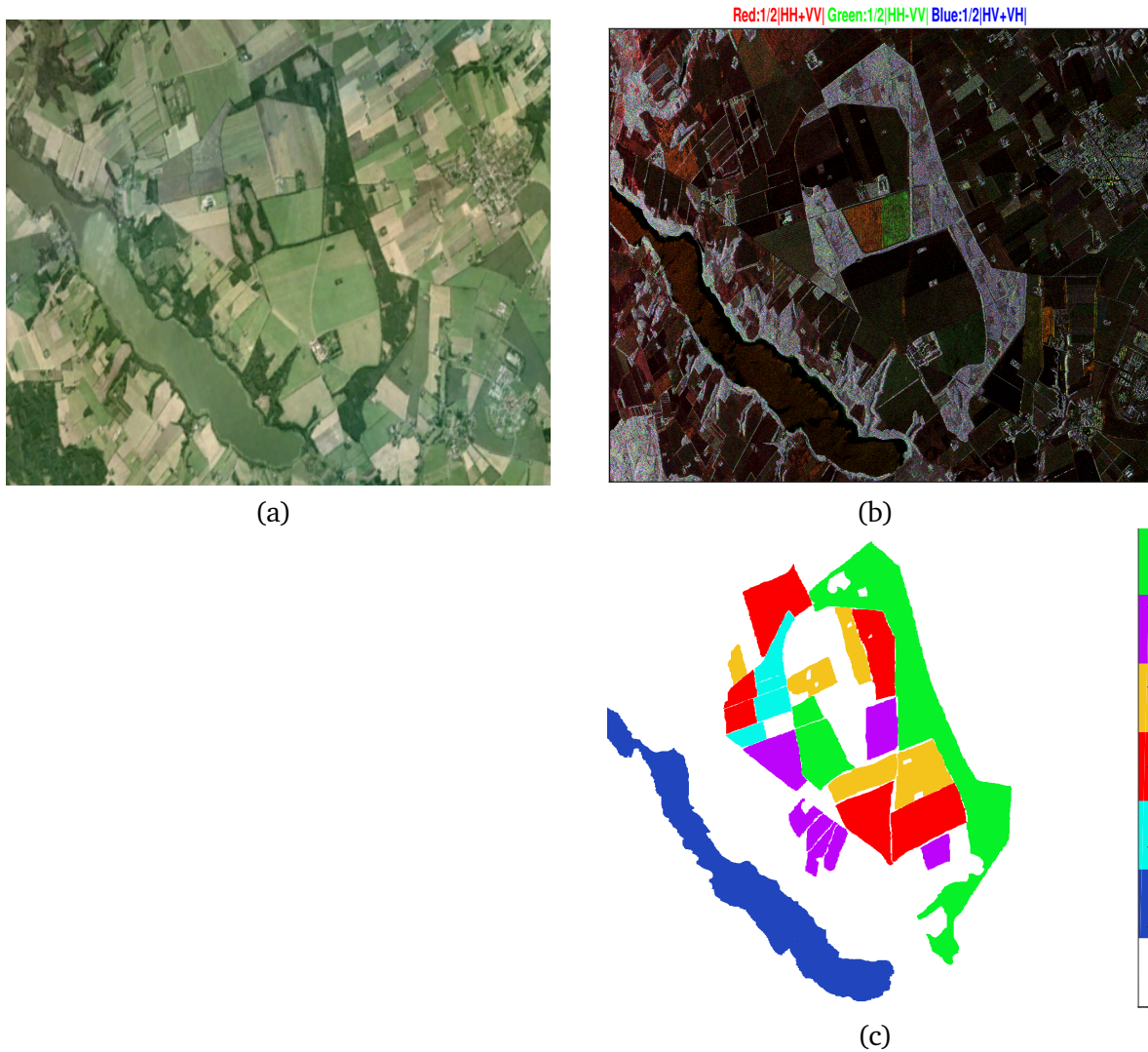


Figure A.3: (a) Google Maps optical image, Foulum (Denmark), July 2005. (b) Pauli color composite Emisar Foulum data. (c) Incomplete ground truth (Legend: blue - water; green - forest; cyan - peas; magenta - winter rape; red - winter wheat; yellow - beet, as in [234]).

Only the C-band system possessed full-polarimetric capability [244, 245].

Two different PolSAR datasets (Convair Ice and Convair Ottawa)¹ obtained by the C-Band monostatic radar system of Convair-580 on two different campaigns have been used in Subsection 2.3, Chapter 2. Both Convair Ice and Convair Ottawa datasets contain the complex Sinclair coefficients for each of the four PolSAR channel. The Pauli color representations are displayed in Fig. A.4. According to [142], the Ottawa (Ontario, Canada) dataset seems to have been acquired in June 2001.

According to their metadata, the Convair Ottawa and Ice datasets are complex

¹The two datasets, along with EMISAR Foulum have been obtained by the thesis's author from an old download of the ESA PolSARPro. The author acknowledges obtaining the data along with the software and is grateful to the developers and ESA for providing access.

multilooked (10-looks). A probable acquisition location for the Convair Ice data is in the Gulf of St. Lawrence, Canada [246, 247]. Unfortunately, no precise information are available to ensure a precise geographic positioning for the CONVAIR imaged areas.

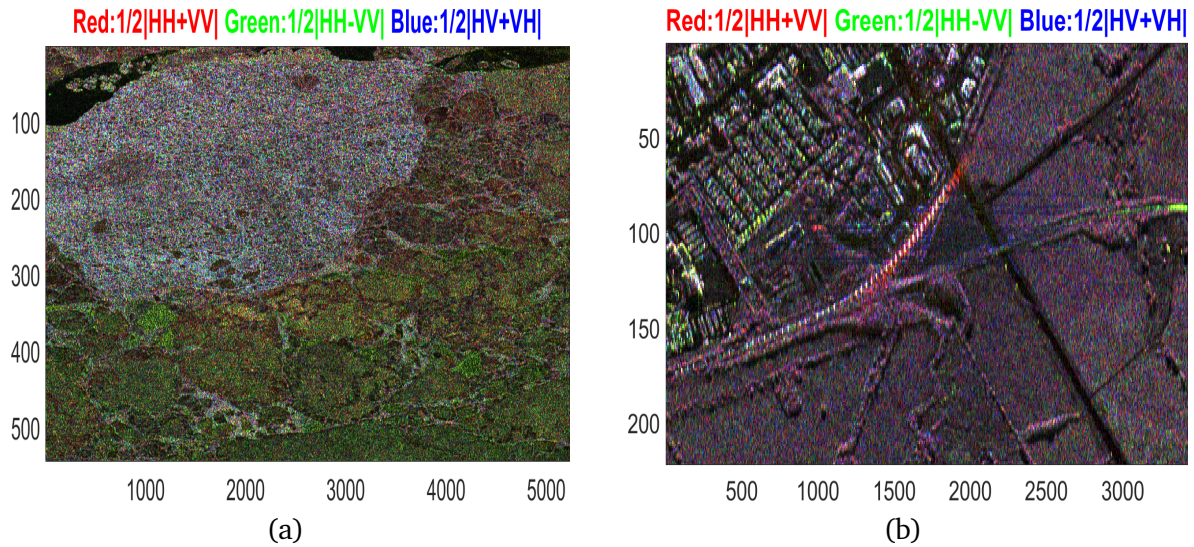


Figure A.4: (a) Pauli color composite Convair Ice data. (b) Pauli color composite Convair Ottawa data.

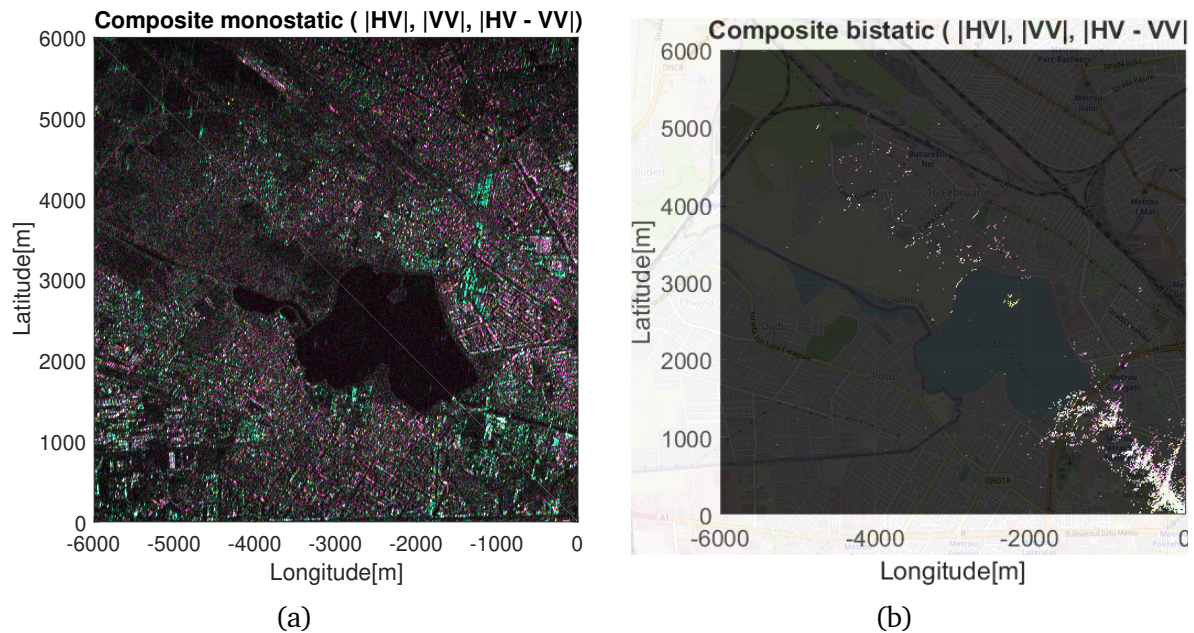


Figure A.5: RGB Color composite dual-pol VV-HV images. (a) Monostatic Sentinel-1. (b) Bistatic ground-based (superimposed on OpenStreetMap image of the area).

A.2 Monostatic-Bistatic VV-HV Dual-pol Data

The dual-polarimetric bistatic dataset used in Subsection 1.5.2 *Application: Dual-polarimetric bistatic and monostatic VV-HV H-alpha classification* has been obtained by a ground-based opportunistic receiver from the University Politehnica of Bucharest [248].

The receiver can be equipped to up to three receiver channels and can exploit the C-Band Sentinel-1 A/B SAR satellites as transmitters of opportunity. The bistatic acquisition geometry is similar to the one displayed in Fig. 1.5. For the specific latitude, the satellite operates in Interferometric Wide (IW) mode and transmits radio pulses in linear V polarization. Its central frequency is of 5.405 GHz. The bistatic acquisitions from the receiver are range and azimuth focused using a dedicated time-domain processor. The processor is compatible for performing the same operations also on the Sentinel-1 raw radar data (free to download from the Copernicus Hub, <https://scihub.copernicus.eu>).

For the dual-polarimetric acquisitions (17.09.2019), the receiver was equipped with two antennas able to measure the electromagnetic scattering signal in orthogonal Horizontal and Vertical bases. As so, the images were obtained in VV and HV polarimetric modes, for an area of Bucharest city, Romania. During acquisitions, the ground receiver was placed on top of the university building (at a GPS elevation of around 165 m)². At the time of acquisition, the two antennas had a height difference of almost 1 m (i.e., the simultaneous data channels have distinct phase centers).

The focusing grid is aligned with the local latitude and longitude, and has a 2×2 m pixel spacing. The position of the receiver is taken as origin for the image's latitude/longitude axes (e.g., lower right corner in Fig. A.5). The bistatic and monostatic data is directly co-registered at the output of the SAR processor, as the focusing operations are performed using a common grid.

Because the difference in altitude between the receiver and the observed scene is only in the order of several dozens of meters, the bistatic scene is more sparse than the monostatic one. In addition, a threshold selection is applied before displaying the bistatic RGB color composite representation in Fig. A.5b.

Because of the relative difference in position at the bistatic receiver, a phase imbalance is considered to exist between the two linear channels. However, it can be shown analytically that with respect to the eigenvalue decomposition of the coherency matrix, this relative phase difference has an impact only on the $\delta_{2,i}$ components of the \mathbf{u}_2 eigenvector parametrization (Eq. 1.46). The eigenvalues of Hermitian coherency matrices, used in computing the entropy parameter (Eq. 1.47) are real numbers. Also, for α (Eq. 1.48) no phase information is used. As a result, the phase imbalance should have no major effects for neither the entropy, nor the α parameters. Other possible sources of error are compensated or considered negligible for this acquisition. Precise synchronization between transmitter and receiver diminishes the geometric errors, while good channel isolation significantly reduces cross-talk at reception.

²The author of the thesis has not participated in the data acquisition campaign, but it is grateful for access to this unique monostatic-bistatic dual-pol dataset.

Scattering and Coherency matrices for elementary scatterers

I. Scattering matrices of 5 elementary scatterers

Table B.1: Elementary scatterers in HV basis.

H dipole	45° dipole	V dipole
$\begin{bmatrix} 1 & 0 \\ 0 & 0 \end{bmatrix}$	$\frac{1}{2} \cdot \begin{bmatrix} 1 & 1 \\ 1 & 1 \end{bmatrix}$	$\begin{bmatrix} 0 & 0 \\ 0 & 1 \end{bmatrix}$
H dihedral	45° dihedral	V dihedral
$\begin{bmatrix} 1 & 0 \\ 0 & -1 \end{bmatrix}$	$\begin{bmatrix} 0 & 1 \\ 1 & 0 \end{bmatrix}$	$\begin{bmatrix} -1 & 0 \\ 0 & 1 \end{bmatrix}$
H quarter-wave	45° quarter-wave	V quarter-wave
$\begin{bmatrix} 1 & 0 \\ 0 & j \end{bmatrix}$	$\frac{1-j}{2} \cdot \begin{bmatrix} 1 & 1 \\ 1 & 1 \end{bmatrix}$	$\begin{bmatrix} j & 0 \\ 0 & 1 \end{bmatrix}$
sphere/plate	left helix	right helix
$\begin{bmatrix} 1 & 0 \\ 0 & 1 \end{bmatrix}$	$\frac{1}{2} \cdot \begin{bmatrix} 1 & j \\ j & -1 \end{bmatrix}$	$\frac{1}{2} \cdot \begin{bmatrix} 1 & -j \\ -j & -1 \end{bmatrix}$

II. Coherency matrices for monostatic quad-pol to dual-pol example

Table B.2: Coherency matrices corresponding to distinct scatterers in the $H - \alpha$ plane space. From example in [108].

	T_{11}	T_{12}	T_{13}	T_{22}	T_{23}	T_{33}
T9	0.41	-0.006-j0.002	-0.004-j0.006	0.03	-0.003-j0.016	0.01
T8	0.97	0.52-j0.51	0.28-j0.34	0.69	0.39-j0.002	0.24
T6	0.23	0.44+j0.14	-0.06-j0.003	1.21	-0.16+j0.03	0.04
T5	0.41	-0.08-j0.06	-0.036-j0.02	0.11	0.01+j0.001	0.081
T4	0.38	-0.006+j0.006	0.03-j0.02	0.36	-0.01-j0.01	0.06
T3	0.009	-0.04+j0.03	-0.004+j0.02	0.65	0.05+j0.33	0.89
T2	0.18	0.008+j0.01	-0.001+j0.003	0.13	0.0001+j0.0001	0.18
T1	0.34	0.008+j0.05	-0.01+j0.007	0.6	-0.02+j0.08	0.59

III. Connection between elements of the monostatic 3×3 coherency matrix and the 2×2 VV-HV coherency

In this subsection, starting from the nine elements of a monostatic 3×3 coherency matrix, in linear H-V polarizations, we analytically deduce the correspondence with the four elements in the reduced VV-HV 2×2 coherency matrix. The equations to follow present these operations.

$$\mathbf{T}_3 = \begin{bmatrix} T_{3,11} & T_{3,21}^* & T_{3,31}^* \\ T_{3,21} & T_{3,22} & T_{3,32}^* \\ T_{3,31} & T_{3,32} & T_{3,33} \end{bmatrix} \quad (\text{B.1})$$

$$= \frac{1}{2} \mathbb{E} \left\{ \begin{bmatrix} (S_{hh} + S_{vv})(S_{hh} + S_{vv})^* & (S_{hh} + S_{vv})(S_{hh} - S_{vv})^* & 2(S_{hh} + S_{vv})S_{hv}^* \\ (S_{hh} - S_{vv})(S_{hh} + S_{vv})^* & (S_{hh} - S_{vv})(S_{hh} - S_{vv})^* & 2(S_{hh} - S_{vv})S_{hv}^* \\ 2S_{hv}(S_{hh} + S_{vv})^* & 2S_{hv}(S_{hh} - S_{vv})^* & 4S_{hv}S_{hv}^* \end{bmatrix} \right\}. \quad (\text{B.2})$$

Some of the monostatic \mathbf{T}_3 matrix parameters are expanded hereafter:

$$T_{3,11} = \frac{1}{2} \mathbb{E} \{ S_{hh}S_{hh}^* + S_{hh}S_{vv}^* + S_{vv}S_{hh}^* + S_{vv}S_{vv}^* \} \quad (\text{B.3})$$

$$T_{3,22} = \frac{1}{2} \mathbb{E} \{ S_{hh}S_{hh}^* - S_{hh}S_{vv}^* - S_{vv}S_{hh}^* + S_{vv}S_{vv}^* \} \quad (\text{B.4})$$

$$T_{3,12} = \frac{1}{2} \mathbb{E} \{ S_{hh}S_{hh}^* - S_{hh}S_{vv}^* + S_{vv}S_{hh}^* - S_{vv}S_{vv}^* \} \quad (\text{B.5})$$

$$T_{3,21} = \frac{1}{2} \mathbb{E} \{ S_{hh}S_{hh}^* + S_{hh}S_{vv}^* - S_{vv}S_{hh}^* - S_{vv}S_{vv}^* \} \quad (\text{B.6})$$

$$T_{3,31} = \mathbb{E} \{ S_{hv}S_{hh}^* + S_{hv}S_{vv}^* \} \quad (\text{B.7})$$

$$T_{3,32} = \mathbb{E} \{ S_{hv}S_{hh}^* - S_{hv}S_{vv}^* \}. \quad (\text{B.8})$$

From the property that the expected value of the sum of several random variables is equal to the sum of their expectations, the operator can be distributed to each term from B3-B9.

The only possible variation in the form of the dual-pol VV-HV scattering vector is in switching the position of its two elements. As so, a differentiation between a covariance and a coherency matrix is not actually possible. Nonetheless, we preserve the notation \mathbf{T}_2 of a coherency matrix for the desired second order statistics matrix.

$$\mathbf{T}_{2, \text{VV-HV}} = \mathbf{C}_{2, \text{VV-HV}} = \begin{bmatrix} T_{2,11} & T_{2,21}^* \\ T_{2,21} & T_{2,22} \end{bmatrix} = \mathbb{E} \left\{ \mathbf{k}_{\mathcal{L}_2} \cdot \mathbf{k}_{\mathcal{L}_2}^H \right\} \quad (\text{B.9})$$

$$= \mathbb{E} \left\{ \begin{bmatrix} S_{vv} \\ S_{hv} \end{bmatrix} [S_{vv} \quad S_{hv}]^* \right\} = \mathbb{E} \left\{ \begin{bmatrix} S_{vv}S_{vv}^* & S_{vv}S_{hv}^* \\ S_{hv}S_{vv}^* & S_{hv}S_{hv}^* \end{bmatrix} \right\} \quad (\text{B.10})$$

Deducing the four elements from the reduced coherency matrix is required the computation of four expectations from the dual-pol measurements. Further, relations B.12-B.15 are considered to offer an estimate of the elements of the VV-HV \mathbf{T}_2 matrix.

$$T_{2,11} = \frac{T_{3,11} + T_{3,22} - T_{3,12} - T_{3,21}}{2} \quad T_{2,21} = \frac{T_{3,31} - T_{3,32}}{2} \quad (\text{B.11})$$

$$T_{2,22} = \frac{T_{3,33}}{2}. \quad (\text{B.12})$$

Jordan canonical form

Every square matrix is similar to a Jordan canonical form, which is unique up to permutations of its constituent blocks [60]. A Jordan matrix \mathbf{J} is a direct sum (here, symbol \oplus) of Jordan blocks.

$$\mathbf{J} = \mathbf{J}_{p1} \oplus \mathbf{J}_{p2} \oplus \dots \quad (\text{C.1})$$

A Jordan block, $\mathbf{J}_p(\lambda_k)$, associated to an eigenvalue λ_k has dimensions $p \times p$. Every diagonal entry of a block is equal to λ_k and there are $p-1$ values of "1" on the first upper-diagonal (or first lower-diagonal, depending on the convention). The rest of the block's elements are equal to zero.

$$\mathbf{J}_p(\lambda_k) = \lambda_k \mathbf{I}_p + \mathbf{L}_p \quad (\text{C.2})$$

$$\mathbf{L}_p = \begin{bmatrix} 0 & 1 & \dots & \dots & 0 \\ 0 & 0 & \dots & \dots & \vdots \\ \vdots & \vdots & \dots & \dots & \vdots \\ 0 & \dots & \dots & 0 & 1 \\ 0 & \dots & \dots & 0 & 0 \end{bmatrix}$$

The Jordan blocks of sizes 1, 2, 3 (for a real-valued eigenvalue λ) are:

$$\mathbf{J}_1(\lambda) = \lambda \quad \mathbf{J}_2(\lambda) = \begin{bmatrix} \lambda & 1 \\ 0 & \lambda \end{bmatrix} \quad \mathbf{J}_3(\lambda) = \begin{bmatrix} \lambda & 1 & 0 \\ 0 & \lambda & 1 \\ 0 & 0 & \lambda \end{bmatrix}$$

Each Jordan block has associated one linear independent eigenvector. For blocks with dimensions larger or equal to 2, generalized eigenvectors must be chosen so to span the complete column space; i.e., each Jordan block of size p will have one eigenvector and $p-1$ generalized eigenvectors [249].

A real $n \times n$ matrix will have in general real and complex eigenvalues, the latter occurring in complex conjugate pairs.

The Real Jordan form (R-Jordan) offers a canonical form, of matrices under similarity, but with real entries. The general idea behind creating a real Jordan block representation is based on combining the information offered by the real and imaginary parts of two complex conjugate eigenvalues and their corresponding eigenvectors (generalized eigenvectors, if the case).

Given the isomorphic transformation:

$$\phi: \mathbb{C} \rightarrow \mathbb{R}^{2 \times 2}, \phi(x+jy) = \begin{bmatrix} x & y \\ -y & x \end{bmatrix} = x \cdot \begin{bmatrix} 1 & 0 \\ 0 & 1 \end{bmatrix} + y \cdot \begin{bmatrix} 0 & 1 \\ -1 & 0 \end{bmatrix} \quad (\text{C.3})$$

The second matrix may be considered an equivalent of the complex unit j , because it can be obtained from the square root of the identity matrix.

We now consider a complex non-degenerate eigenvalue $\lambda = a + i \cdot b$, $a, b \in \mathbb{R}$. For real matrices λ^* is also itself an eigenvalue. Because the complex conjugate pair (λ, λ^*) is completely specified by only one complex number, the pair will have associate a real square Jordan block, \mathbf{J}_{r_1} .

The real Jordan blocks of sizes 1, 2 are:

$$\mathbf{J}_{r_1}(\lambda, \lambda^*) = \begin{bmatrix} a & b \\ -b & a \end{bmatrix}$$

$$\mathbf{J}_{r_2}(\lambda, \lambda^*) = \begin{bmatrix} \mathbf{J}_{r_1}(\lambda, \lambda^*) & \mathbf{I}_2 \\ \mathbf{0} & \mathbf{J}_{r_1}(\lambda, \lambda^*) \end{bmatrix}$$

Some other resources may adopt to use the transpose of \mathbf{J}_{r_1} presented here, as constructive block of the R-Jordan form.

Real representation of 4 particular scattering matrices

Consider a general scattering matrix, \mathbf{S} :

$$\mathbf{S} = \begin{bmatrix} a_1 + ja_2 & c_1 + jc_2 \\ d_1 + jd_2 & b_1 + jb_2 \end{bmatrix} \quad (\text{D.1})$$

with $a_1, a_2, b_1, b_2, c_1, c_2, d_1, d_2 \in \mathbb{R}$. Starting from eq. (D.1) we model the RRS M^1 of four particular algebraic matrices (Table D.1), which the scattering matrix may plausibly take in the bistatic case. The type of eigenvalues attributed to each associated RRS M matrices is discussed below. These results and observations serve as model for the discussion involving the nonreciprocity factor from Chapter 2, Section 2.3.

The general forms considered hereafter are:

¹Real Representation Scattering Matrix

Table D.1: Four particular scattering matrices. General form (\mathbf{S}) and Real Representation (\mathbf{S}_{RR}).

Type	\mathbf{S}	\mathbf{S}_{RR}	\mathbf{S}_{RR} eigenvalues
complex symmetric	$\begin{bmatrix} a_1 + ja_2 & c_1 + jc_2 \\ c_1 + jc_2 & b_1 + jb_2 \end{bmatrix}$	$\begin{bmatrix} a_1 & c_1 & a_2 & c_2 \\ c_1 & b_1 & c_2 & b_2 \\ a_2 & c_2 & -a_1 & -c_1 \\ c_2 & b_2 & -c_1 & -b_1 \end{bmatrix}$	two real, equal/distinct \pm pairs
complex skew-symmetric	$\begin{bmatrix} 0 & -c_1 - jc_2 \\ c_1 + jc_2 & 0 \end{bmatrix}$	$\begin{bmatrix} 0 & -c_1 & 0 & -c_2 \\ c_1 & 0 & c_2 & 0 \\ 0 & -c_2 & 0 & c_1 \\ c_2 & 0 & -c_1 & 0 \end{bmatrix}$	two imaginary \pm complex-conjugate pairs
Hermitian	$\begin{bmatrix} a_1 & c_1 - jc_2 \\ c_1 + jc_2 & b_1 \end{bmatrix}$	$\begin{bmatrix} a_1 & c_1 & 0 & -c_2 \\ c_1 & b_1 & c_2 & 0 \\ 0 & -c_2 & -a_1 & -c_1 \\ c_2 & 0 & -c_1 & -b_1 \end{bmatrix}$	two real, equal/distinct \pm pairs or two complex \pm complex-conjugate pairs
skew-Hermitian	$\begin{bmatrix} ja_2 & c_1 + jc_2 \\ -c_1 + jc_2 & jb_2 \end{bmatrix}$	$\begin{bmatrix} 0 & c_1 & a_2 & c_2 \\ -c_1 & 0 & c_2 & b_2 \\ a_2 & c_2 & 0 & -c_1 \\ c_2 & b_2 & c_1 & 0 \end{bmatrix}$	two real, equal/distinct \pm pairs or two complex \pm complex-conjugate pairs

- (a) *complex symmetric*, $S = S^T$: It can be rapidly assessed that the RR of a reciprocal (i.e., symmetric) scattering matrix is itself symmetric, $S_{RR} = S_{RR}^T$ (Table D.1). Distinctively, the RRSM is a special form of a Hamiltonian matrix. This symmetric RRSM can be brought to a diagonal form through an eigen-decomposition and its four eigenvalues will all be real (in equal or distinct \pm pairs).
- (b) *complex skew-symmetric*, $S = -S^T$: Here, both S and S_{RR} are skew-symmetric. It is well known that for any skew-symmetric matrix with real entries, its eigenvalues are purely imaginary. For this reason, the eigenvalues of the RR will have the particular form of a double \pm imaginary pair.
- (c) *Hermitian*, $S = S^H$: The RR of a Hermitian scattering matrix can be decomposed into both a real symmetric ($S_{RR_{c1}}$) and a real skew-symmetric component ($S_{RR_{c2}}$):

$$S_{RR} = S_{RR_{c1}} + S_{RR_{c2}} = \underbrace{\begin{bmatrix} a_1 & c_1 & 0 & 0 \\ c_1 & b_1 & 0 & 0 \\ 0 & 0 & -a_1 & -c_1 \\ 0 & 0 & -c_1 & -b_1 \end{bmatrix}}_{S_{RR_{c1}}} + \underbrace{\begin{bmatrix} 0 & 0 & 0 & -c_2 \\ 0 & 0 & c_2 & 0 \\ 0 & -c_2 & 0 & 0 \\ c_2 & 0 & 0 & 0 \end{bmatrix}}_{S_{RR_{c2}}} \quad (D.2)$$

$$a_1, b_1, c_1, c_2 \neq 0.$$

The RRSM eigenvalues of the Hermitian matrix can appear both as \pm real or as \pm complex conjugate pairs. Matrices SH_1 and SH_2 are chosen for demonstrative purposes. They are both Hermitian, but while the eigen-analysis for the RR of SH_1 returns real and distinct \pm eigenvalues pairs, the RR of SH_2 has only complex eigenvalues.

$$SH_1 = \begin{bmatrix} 0.5431 & 0.498 - 0.0635j \\ 0.498 + 0.0635j & 0.1857 \end{bmatrix}, \quad SH_2 = \begin{bmatrix} 0.2673 & 0.1513 + 0.798j \\ 0.1513 - 0.798j & 0.0057 \end{bmatrix}$$

- (d) *skew-Hermitian*, $S = -S^H$:
Because the RR of the skew-Hermitian presents again both a symmetric and a skew-symmetric component (D.3), some matrices may have only real eigenvalues (\pm real pairs) and others only complex ones.

$$S_{RR} = S_{RR_{d1}} + S_{RR_{d2}} = \underbrace{\begin{bmatrix} 0 & 0 & a_2 & c_2 \\ 0 & 0 & c_2 & b_2 \\ a_2 & c_2 & 0 & 0 \\ c_2 & b_2 & 0 & 0 \end{bmatrix}}_{S_{RR_{d1}}} + \underbrace{\begin{bmatrix} 0 & c_1 & 0 & 0 \\ -c_1 & 0 & 0 & 0 \\ 0 & 0 & 0 & -c_1 \\ 0 & 0 & c_1 & 0 \end{bmatrix}}_{S_{RR_{d2}}} \quad (D.3)$$

$$a_2, b_2, c_1, c_2 \neq 0.$$

We take as examples matrices SKH_1 and SKH_2 , which return only real and only complex eigenvalues, respectively.

$$SKH_1 = \begin{bmatrix} 0.9963j & 0.6403 + 0.3043j \\ -0.6403 + 0.3043j & 0.39j \end{bmatrix}, \quad SKH_2 = \begin{bmatrix} 0.958j & -0.7621 + 0.7211j \\ 0.7621 + 0.7211j & 0.2723j \end{bmatrix}$$

Solving the conjugate similarity equivalence for SM via RR

I. **Algorithm I:** Solution to consimilarity transformation of the scattering matrix, $S\mathbf{X} = \mathbf{X}^*C$, via the RRSM.

INPUT: Scattering matrix (S)

OUTPUT: Consimilarity transformation matrix (X) and the equivalent matrix under consimilarity (C - diagonal or concanonical form).

- (a) Write scattering matrix S in RR form (eq. 2.9).
- (b) Extract eigenvalues $\{\lambda_k\}$ and eigenvectors $\{\mathbf{v}(\lambda_k)\}$ of S_{RR} . If eigenvalues are repeated or complex, use the Jordan algorithm for obtaining the transformation vectors.
- (c) Check if eigenvalues are real or complex:
 - (a) *only real eigenvalues:*
 - (i) For real, distinct eigenvalues:
 $C_{RR} = \text{diag}([\lambda_1, \lambda_2, -\lambda_1, -\lambda_2])$.
 For real, equal eigenvalues:
 Verify if C_{RR} remains diagonal, or is written using Jordan blocks of second order (Appendix C):
 $C_{RR} = J_2(\lambda) \oplus J_2(-\lambda)$.
 ♠ Obs: C_{RR} is the real representation form of matrix $C = J_2(\lambda)$.
 - (ii) Check that the order of transformation vectors matches the order of eigenvalues from C_{RR} :
 $T = [\mathbf{v}(\lambda_1), \mathbf{v}(\lambda_2), \mathbf{v}(-\lambda_1), \mathbf{v}(-\lambda_2)]$, $\lambda_1 \geq \lambda_2 \geq 0$.
 - (b) *only complex eigenvalues:*
 - (i) Write C_{RR} with the real Jordan blocks:
 $C_{RR} = J_{r1}(\lambda, \lambda^*) \oplus J_{r1}(-\lambda, -\lambda^*)$
 ♠ Obs: C_{RR} is the real representation form of matrix $C = J_{r1}(\lambda, \lambda^*)$.
 For purely imaginary eigenvalues, the canonical form may become:
 $C_{RR} = J_{r2}(\lambda, \lambda^*)$.
 - (ii) Build the real transformation matrix T by column-wise operations with real and imaginary parts of (eigen)vectors

$\mathbf{v}(\lambda), \mathbf{v}(\lambda^*), \mathbf{v}(-\lambda), \mathbf{v}(-\lambda^*)$:

$$\mathbf{T}(:,1) = \frac{1}{2}[\mathcal{R}(\mathbf{v}(\lambda)) + \mathcal{R}(\mathbf{v}(\lambda^*))];$$

$$\mathbf{T}(:,2) = \frac{1}{2}[\mathcal{I}(\mathbf{v}(\lambda)) - \mathcal{I}(\mathbf{v}(\lambda^*))];$$

$$\mathbf{T}(:,3) = -\frac{1}{2}[\mathcal{I}(\mathbf{v}(-\lambda)) - \mathcal{I}(\mathbf{v}(-\lambda^*))];$$

$$\mathbf{T}(:,4) = \frac{1}{2}[\mathcal{R}(\mathbf{v}(-\lambda)) + \mathcal{R}(\mathbf{v}(-\lambda^*))];$$

- (d) Compute consimilarity transformation matrix \mathbf{X} using [115]:

$$\mathbf{X} = \frac{1}{4}[\mathbf{I}_2, j\mathbf{I}_2](\mathbf{T} - \mathbf{Q}_4 \mathbf{T} \mathbf{Q}_4)[\mathbf{I}_2; j\mathbf{I}_2]$$

where \mathbf{I}_2 represents the 2×2 identity matrix and $\mathbf{Q}_4 = \begin{bmatrix} \mathbf{0} & -\mathbf{I}_2 \\ \mathbf{I}_2 & \mathbf{0} \end{bmatrix}$.

- (e) Verify compliance of consimilarity solution: $\mathbf{X}^{-1} \mathbf{S} \mathbf{X}^* = \mathbf{C}$.

II. Example: Coneigen-values/vectors of elementary scatterers:

Table E.1 displays the results obtained by the proposed algorithm for calculating the conjugate eigenvalues and conjugate eigenvectors of some of the elementary scattering matrices in Table B.1. For the same type of scatterer (i.e., dipole, dihedral), we observe the coneigenvalues to be invariant, as the same values are preserved even if the target has a rotation associated. However, this does not allow for a complete discrimination as multiple type of scatterers can present the same coneigenvalues (e.g., as with dihedrals and quarter-waves). Using both parameters, it becomes possible to discriminate between scatterers.

III. Tolerance parameters for separating between eigenvalues type:

For numerical implementation it is important to offer correct evaluation criteria when dealing with:

- (a) RR complex eigenvalues with small imaginary part (orders of magnitude lower than the real part);
- (b) RR real eigenvalues of near value (which can be considered equal under a given tolerance);

This is necessary considering that in many places the implementation requires a comparison between eigenvalues. We define two tolerance parameters to help in evaluating the classification of each set of four eigenvalues. These parameters are:

- (a) δ_{imag} : used for comparing the ratio between the real and imaginary parts of one complex eigenvalue, (λ) . The value determined by the product $\delta_{imag} \cdot \mathcal{R}(\lambda)$ is evaluated against $\mathcal{I}(\lambda)$. If the imaginary part is lower than the threshold, it is considered negligible small compared to the real part and will be ignored. Because the complex RRSME eigenvalues come in \pm conjugate

pairs, i.e., they have the same magnitude, when dropping the imaginary part, a duplicate set of real eigenvalues remains in place.

- (b) δ_{r_eq} : used only in testing the case of \pm real pairs, the parameter is useful for numerically evaluating if two values are equal (under a given tolerance). With the present implementation, two values λ_1 and λ_2 , $\lambda_1, \lambda_2 \geq 0$ are within tolerance if they verify the relation: $|\lambda_1 - \lambda_2| \leq \delta_{r_eq} \cdot \max(\lambda_1, \lambda_2)$.

Table E.1: Coneigenvalues and coneigenvectors of elementary scatterers in Table B.1, Annex B.

Scatterers	Coneigenvs. $[\xi_1, \xi_2]$	Coneigenvectors
sphere/plate	[1,1]	$\mathbf{x}_1 = [1,0]^T$ $\mathbf{x}_2 = [0,1]^T$
H dipole	[1,0]	$\mathbf{x}_1 = [1,0]^T$ $\mathbf{x}_2 = [0,1]^T$
45° dipole	[1,0]	$\mathbf{x}_1 = \left[\frac{1}{\sqrt{2}}, \frac{1}{\sqrt{2}}\right]^T$ $\mathbf{x}_2 = \left[\frac{1}{\sqrt{2}}, -\frac{1}{\sqrt{2}}\right]^T$
V dipole	[1,0]	$\mathbf{x}_1 = [0,1]^T$ $\mathbf{x}_2 = [0,0]^T$
H dihedral	[1,1]	$\mathbf{x}_1 = \frac{1}{2} \cdot [1, -j]^T$ $\mathbf{x}_2 = \mathbf{x}_1^*$
V dihedral	[1,1]	$\mathbf{x}_1 = [0,0]^T$ $\mathbf{x}_2 = [0,1]^T$
H quarter-wave	[1,1]	$\mathbf{x}_1 = \frac{1}{2} \cdot \left[-1, \frac{1}{\sqrt{2}} + j\frac{1}{\sqrt{2}}\right]^T$ $\mathbf{x}_2 = -\mathbf{x}_1^*$
V quarter-wave	[1,1]	$\mathbf{x}_1 = \frac{1}{2} \cdot \left[-\frac{1}{\sqrt{2}} - j\frac{1}{\sqrt{2}}, -1\right]^T$ $\mathbf{x}_2 = -\mathbf{x}_1^*$

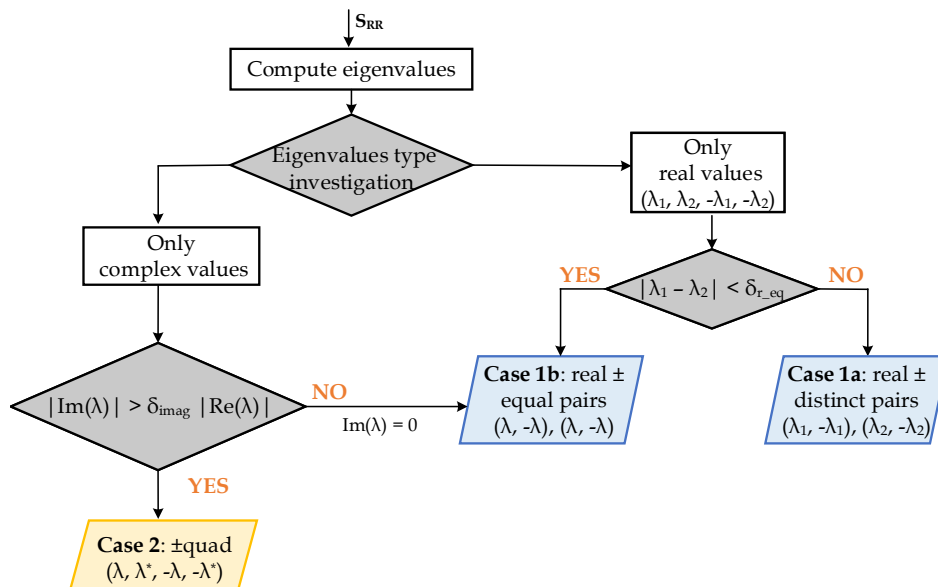


Figure E.1: Flowchart for RRSM eigenvalues testing, with tolerance parameters.

Fig. E.1 graphically summarizes how the two tolerance parameters δ_{r_eq} and δ_{imag} influence the eigenvalues evaluation.

- IV. **Selection of δ_{imag} parameter:** The value of tolerance parameter δ_{r_eq} is fixed to a numerical precision: $\delta_{r_eq} = 10^{-6}$. In the case of δ_{imag} , its influence on the eigenvalues classification type may be greater, which is why we perform a comparative analysis before its selection.

In Chapter 2 it was discussed and exemplified from a PolSAR algebraic perspective that truly reciprocal and monostatic data will not have RRSM complex eigenvalues. Moreover, these matrices will have a nonreciprocity ζ parameter equal to zero. By combining these two properties, we intend to check here the influence of three values $\delta_{imag} \in \{0.01\%, 1\%, 5\%\}$ on the distribution of RRSM having complex eigenvalues with respect to $|\zeta| \in [0, 1]$. The two monostatic Convair datasets are chosen for evaluation. It must be noted that no speckle filtering or reciprocity equalization ($S_{hv_{new}} = S_{vh_{new}} = \frac{S_{hv} + S_{vh}}{2}$) have been applied to the two scenes.

In Subsection 2.3.1, both datasets displayed smaller percentages of complex eigenvalues, $\approx 1\%$. In Table E.2 we see how by increasing the values of δ_{imag} to 0.05 and 0.1, the percentage of RRSM having complex eigenvalues slightly decreases, while the percentage of RRSM having real, equal eigenvalues increases by the same amount (i.e., complex eigenvalues pairs having very small imaginary components which no longer pass the threshold, lose their imaginary part and are reclassified as real, equal eigenvalues pairs). The percentages characterizing RRSM with real, distinct eigenvalues are not affected by variations of δ_{imag} .

Fig. E.2 evaluated the changes introduced δ_{imag} to the complex eigenvalues classification, given its dependence on the nonreciprocity parameter. The histograms in yellow/blue display the distribution of scattering matrices, with respect to the absolute NRF parameter values, when their RRSM eigenvalues pairs are of complex/real type. The first, second and third rows record changes of the distribution as $\delta_{imag} = \{0.01\%; 1\%; 5\%\}$, respectively. On the graphs, the red and magenta dotted lines mark values of $|\zeta| = \{0.05; 0.1\}$.

For $\delta_{imag} = 0.01\%$ and $\delta_{imag} = 1\%$, the yellow distributions reveal that a low number of scattering matrices classified to have RR complex eigenvalues appear for $|\zeta|$ values below 0.1 (i.e., nearly reciprocal matrices).

On the third line, evaluation with $\delta_{imag} = 5\%$, there remain very few scattering matrices having an absolute NRF lower than 0.1 and which still have RRSM complex eigenvalues. Nonetheless, due to the initial shape of the distribution, this determines the important overall decrease in the total number of scattering matrices classified as complex (as seen in Table E.2). With the blue histograms in Figs. E.2(g)-(h), we observe also that the majority of monostatic RRSM having real eigenvalues are characterized by a NRF below 0.1 for $\delta_{imag} = 5\%$.

The threshold value of δ_{imag} can play a role in removing scattering points affected by noise (or other errors) and correct for those scattering matrix with numerically very small imaginary parts. Hereafter we choose a level of significance, $\delta_{imag} = 5\%$.

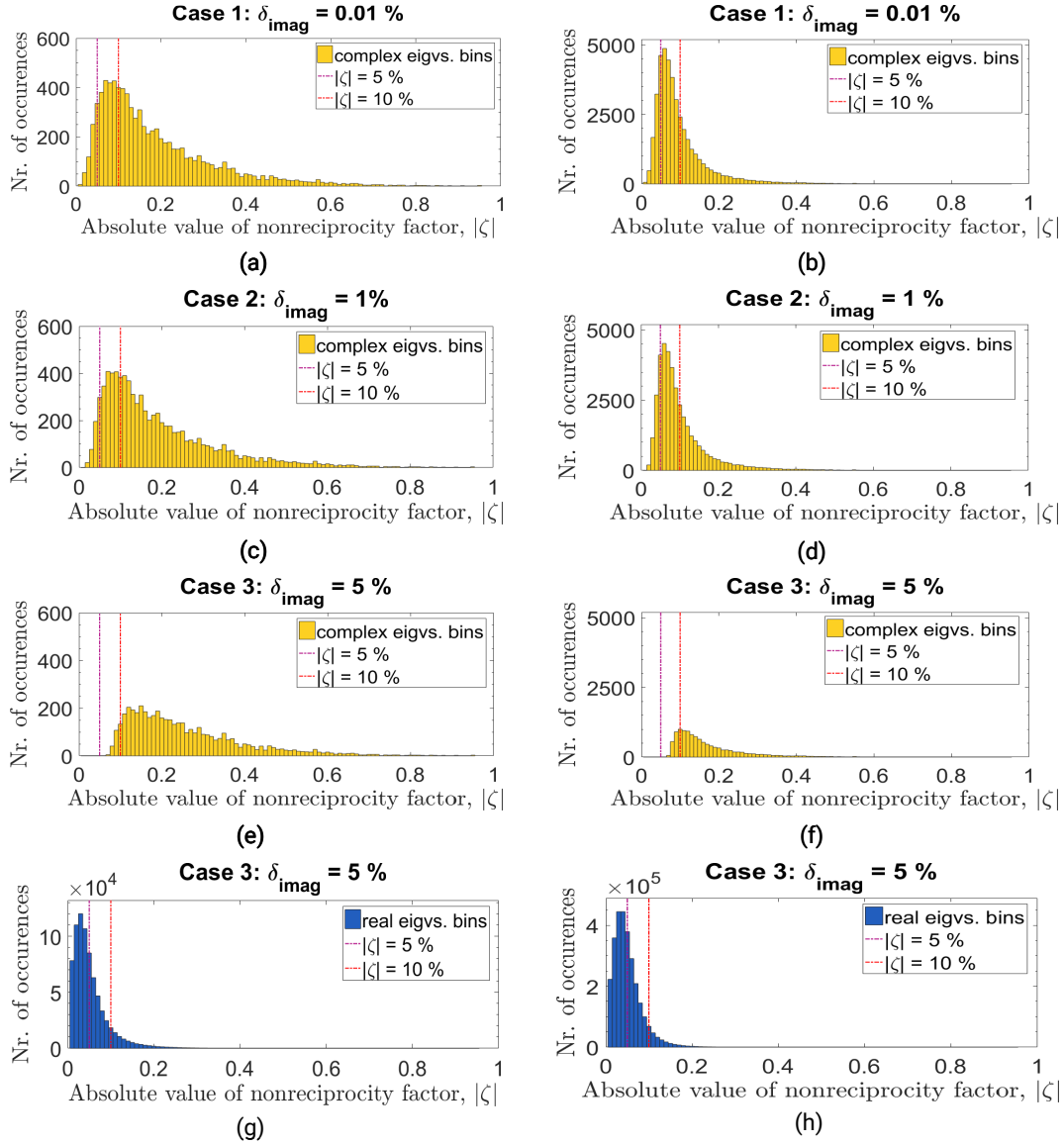


Figure E.2: *Convair Ottawa results (left); Convair Ice results (right); (a)(c)(e) Convair Ottawa dataset: Changes in the distribution of NRF absolute values for the RRSMs returning complex eigenvalues (yellow color), introduced by varying δ_{imag} . (b)(d)(f) Same as with (a)(c)(e), but for Convair Ice data. (g) Convair Ottawa dataset: Distribution of NRF absolute values for RRSMs returning real eigenvalues (blue color), when $\delta_{imag} = 5\%$. (h) Same as (g), for Convair Ice data.*

Table E.2: *Convair Ottawa and Convair Ice: Variations in the distribution of RRSM eigenvalues type for changes in tolerance parameter δ_{imag} .*

δ_{imag}	Real eigvs. pairs [%] distinct	Real eigvs. pairs [%] equal	Complex eigvs. pairs [%]	Total [%]
CONVAIR Ottawa				
0.01%	98.903	0.000	1.09	100
1%	98.903	0.045	1.05	100
5%	98.903	0.483	0.61	100
CONVAIR Ice				
0.01%	98.558	0.000	1.44	100
1%	98.558	0.104	1.34	100
5%	98.558	1.037	0.40	100

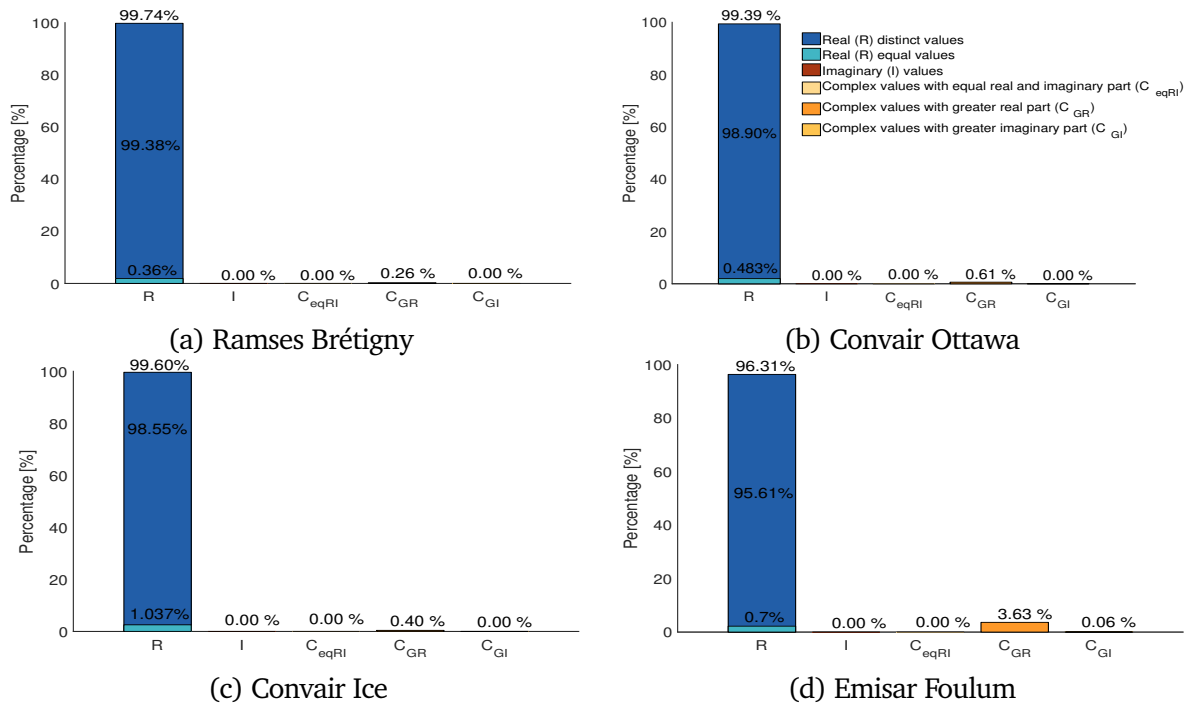


Figure E.3: Bargraphs for RRSM eigenvalues classification. (a) Ramses Brétigny. (b) Convair Ottawa. (c) Convair Ice. (d) Emisar Foulum.

V. Describing the complete RRSM classification of eigenvalues for real monostatic PolSAR data:

The two tolerance parameters are applied as in Fig. E.1 for any RRSM eigenvalues classification performed in the manuscript.

In Fig. E.3, we present the complete percentage description for the four monostatic datasets described in Annex A. There are 5 groups established for the classification, with the RR eigenvalues being divided based on the relationship between their real and imaginary parts: R , I , C_{eqRI} , C_{GR} , C_{GI} - if the values are real, purely imaginary, complex with equal real and imaginary parts, complex but with a larger real part and complex with a larger imaginary part, in the given order. For the case of real values, it is also inspected if the two \pm pairs are distinct or equal (blue and cyan color separation of the first bar).

The small percentage of eigenvalues observed in these PolSAR images as complex have all an imaginary part which is smaller than their real part.

PolSAR data simulation model and Sobel kernel gradient

Chapter 3 makes use of both real and simulated monostatic data. The simulated data, in the form of linear polarimetric channels (HH, HV, VH, VV), can be obtained from a well-known PolSAR technique which uses the Cholesky decomposition. This offers a unique factorization of Hermitian, positive-definite matrices into the product of a lower triangular matrix (L) and its conjugate transpose:

$$C = LL^H. \quad (F.1)$$

I. Model for PolSAR covariance

The product model *texture-speckle* is the most used to describe the PolSAR covariance matrix:

$$C = Z \cdot W, \quad (F.2)$$

where Z is a strictly positive and scalar variable which models the texture, while W is the speckle term. The latter is considered to follow a scaled complex Wishart distribution with probability density function as in (I.5). So, it models an equivalent Gaussian (homogeneous) area. The model followed by the scalar texture variable Z determines if the overall product C has a Gaussian or a non-Gaussian nature. For the examples below, we consider only the Gaussian case.

Several models with 2 or more layers having random (i.e., anisotropic) medium characteristics have been used to describe geophysical media with inhomogeneities (e.g., forest, snow, etc.) [250, 251]. Based on the 1st and 2nd order solutions to the Born approximation for the 2 layer model and assuming reflection symmetry ($\mathbb{E}\{S_{hh}S_{hv}^*\} \approx \mathbb{E}\{S_{vv}S_{hv}^*\} \approx 0$) of the anisotropic medium, the estimated (normalized) covariance matrix was shown to take the form:

$$C = \sigma_{hh} \begin{bmatrix} 1 & 0 & \rho\sqrt{\gamma} \\ 0 & \epsilon & 0 \\ \rho^*\sqrt{\gamma} & 0 & \gamma \end{bmatrix}, \quad (F.3)$$

where σ_{hh} , ρ , ϵ , γ elements inside matrix C are [252]:

$$\sigma_{hh} = \mathbb{E}\{|S_{hh}|^2\}, \quad (F.4) \quad \epsilon = \frac{\mathbb{E}\{|S_{hv}|^2\}}{\mathbb{E}\{|S_{hh}|^2\}}, \quad (F.5)$$

$$\epsilon = \frac{\mathbb{E}\{|S_{hh}S_{vv}^*|^2\}}{\mathbb{E}\{|S_{hh}|^2\}\mathbb{E}\{|S_{vv}|^2\}}, \quad (F.6) \quad \gamma = \frac{\mathbb{E}\{|S_{vv}|^2\}}{\mathbb{E}\{|S_{hh}|^2\}}. \quad (F.7)$$

We consider this model for the simulated data in each of the four regions in Fig. 3.9. From a physical point of view, this model of the covariance matrix has been adopted in cases which imply volume scattering, surface scattering and volume-surface interactions [135].

While two parameters are fixed: $\gamma_i = 1$ and $\epsilon_i = 0.1$, $1 \leq i \leq 4$, the other two change values for each zone (in the given order):

$$\rho = \{0, 0.25e^{j\pi}, -0.5, 0.75e^{-j\pi}\} \text{ and } \sigma_{hh} = \{1, 9, 25, 81\} \text{ [100, 232].}$$

II. Stochastic PolSAR data simulation from known covariance

From known covariance matrices, the estimated PolSAR channels of linear polarization can be computed using the procedure given below [253]. In the thesis, the covariance matrices for the test area in Subsection 3.5.1.2 follow the model described by (F.3).

Algorithm II: PolSAR data simulation using Cholesky factorization of model covariance.

INPUT: Model covariance (C_i) for each intended test region ($i = \text{nr. of regions}$). With covariance matrices of dimensions 3×3 only the monostatic PolSAR case is covered.

OUTPUT: Simulated scattering vector/matrix.

- (a) Decompose each scattering matrix C_i using (F.8), where $C_i^{1/2} = L_i$ is obtained via Cholesky decomposition (F.1).

$$C_i = C_i^{1/2} \left(C_i^{1/2} \right)^H \quad (\text{F.8})$$

- (b) For every k pixel in a test region:
- i. Simulate a complex, normal distributed vector w (zero mean and identity covariance I).
 - ii. Then, obtain the complex, single look v_k scattering vector via product:

$$u_{i,k} = \left(C_i^{1/2} \right)^H v_k \quad (\text{F.9})$$

- iii. Alternatively, reshape the vector into a stochastic scattering matrix, or generate a N -look PolSAR covariance/coherence [253].

III. Modified Sobel gradient with geodesic distance

■ The Sobel gradient

The classical Sobel operator [254, 255], known primarily for edge detection in digital image processing, proposes a simple computation of the first order derivative. It allows a simple gradient estimation based on finite differences. The method uses two 3×3 kernel filters (Tables F.1, F.2). Each of them, employed as a sliding window, is convoluted with a spatial neighbourhood of the same size to produce the vertical (G_V) and horizontal (G_H) gradient components. The gradient magnitude is simply:

$$G = \sqrt{G_H^2 + G_V^2}. \quad (\text{F.10})$$

Table F.1: Vertical Sobel kernel.

-1	0	1
-2	0	2
-1	0	1

Table F.2: Horizontal Sobel kernel.

-1	-2	-1
0	0	0
1	2	1

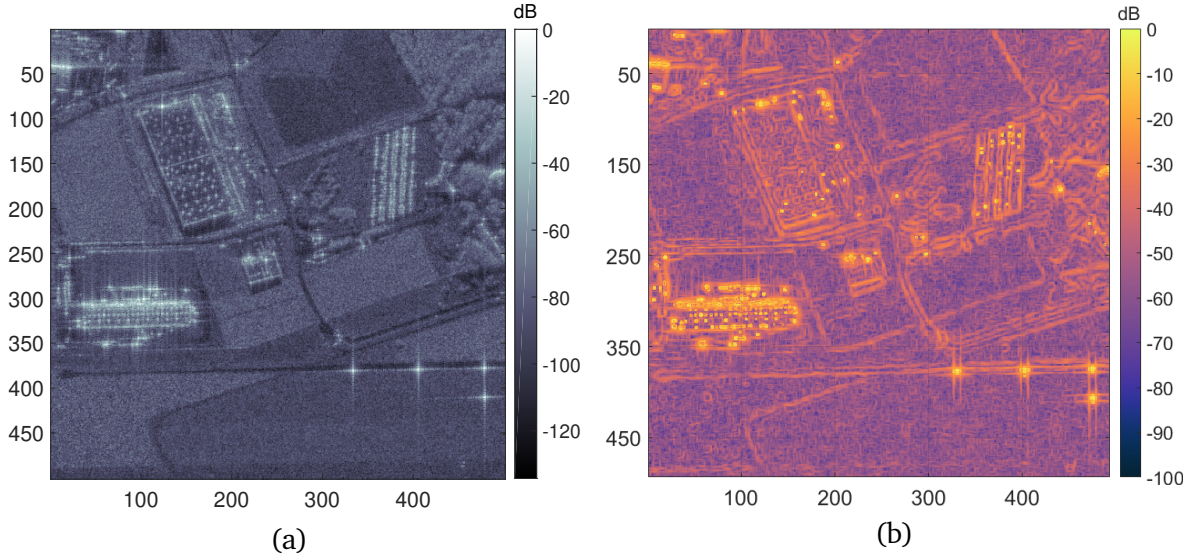


Figure F.1: *Brétigny Dataset* (a) Image 1-look span [dB]. (b) Magnitude of geodesic Sobel gradient [dB], \mathbf{G} , evaluated on the \mathbf{H} barycenters with the AIRM Riemannian metric.

■ Proposed model for manifold gradient

This subsection proposes to modify the gradient kernel evaluation by enriching it with a suitable geodesic metric. For this, a slight change is proposed in the last step of the classical kernel gradient method. The same filter weights in Tables F.1 are used and F.2 applied to 3×3 moving spatial neighbourhoods (i.e., classical convolution), while the final distance evaluation procedure between left/right or up/down components integrates the geodesic metric. Considering, at any evaluation moment, the center of the moving window $\mathbf{P}^{i,j}$ placed at position described by coordinates (row = i , column = j), the two gradient components are:

$$\mathbf{G}_V^{i,j} = d(\mathbf{P}_\uparrow^{i,j}, \mathbf{P}_\downarrow^{i,j}), \quad (\text{F.11}) \quad \mathbf{G}_H^{i,j} = d(\mathbf{P}_\rightarrow^{i,j}, \mathbf{P}_\leftarrow^{i,j}), \quad (\text{F.12})$$

where $d(\cdot)$ is either (3.8) or (3.10), depending which type of polar factors are used.

$$\mathbf{P}_\uparrow^{i,j} = \mathbf{P}^{i-1,j-1} + 2\mathbf{P}^{i-1,j} + \mathbf{P}^{i-1,j+1} \quad (\text{F.13})$$

$$\mathbf{P}_\downarrow^{i,j} = \mathbf{P}^{i+1,j-1} + 2\mathbf{P}^{i+1,j} + \mathbf{P}^{i+1,j+1} \quad (\text{F.14})$$

$$\mathbf{P}_\leftarrow^{i,j} = \mathbf{P}^{i-1,j-1} + 2\mathbf{P}^{i,j-1} + \mathbf{P}^{i+1,j-1} \quad (\text{F.15})$$

$$\mathbf{P}_\rightarrow^{i,j} = \mathbf{P}^{i-1,j+1} + 2\mathbf{P}^{i,j+1} + \mathbf{P}^{i+1,j+1}. \quad (\text{F.16})$$

The gradient filter enhances specific patterns (for Sobel, horizontal and vertical edges) in an image under evaluation. The proposed implementation allows to apply the kernel filter directly on the matrix space and not on only one of the amplitude channels, as usual. For the implementation, the space of the \mathbf{H} factors is of interest. Because the set of Hermitian matrices is closed under addition and real scalar multiplication (it is not closed under multiplication by complex numbers), performing the operations in (F.13 - F.16) will not modify the matrix space. In contrast, under the same operations, the set of unitary matrices is not a closed group. In this case, the summations may produce a result which is no longer unitary, making here the use of a unitary geodesic distance inappropriate.

Results from applying the proposed gradient on the Brétigny dataset are shown here. Fig. F.1(a) is obtained having as input the set of \mathbf{H} barycenter matrices (obtained based on the technique in Annex H). The shape of the three important structures from the image (horizontal West-Center, left-oblique North-West and right-oblique North-East) is easily distinguished, as well as some field contours. Moreover, bright pixels are clearly isolated. This validates the ability of the modified filter to perform the usual first order gradient estimation, but in a higher dimensional space, i.e that of 2×2 Hermitian matrices.

Matrix logarithm and matrix exponential

I. General matrix logarithm/exponential

Operator $\text{Exp}(\mathbf{X})$ denotes the *matrix exponential*:

$$\text{Exp}(\mathbf{X}) = \sum_{n=0}^{\infty} \frac{1}{n!} \mathbf{X}^n. \quad (\text{G.1})$$

For every nonsingular $\mathbf{Z} \in \text{GL}^1(n, \mathbb{C})$, there exists a solution to

$$\text{Exp}(\mathbf{X}) = \mathbf{Z},$$

which is

$$\mathbf{X} = \text{Log}(\mathbf{Z}).$$

This is called the *matrix logarithm* of \mathbf{Z} and is the inverse operation to the matrix exponential.

While property $\text{Exp}(\text{Log}(\mathbf{X})) = \mathbf{X}$ is always true, its complement does not hold for all nonsingular $\mathbf{X} \in \mathbb{C}^{n \times n}$, so we write $\text{Log}(\text{Exp}(\mathbf{X})) \neq \mathbf{X}$. This is because there are some \mathbf{X} matrices which have an infinite number of logarithms [91].

As a result, the notion of principal matrix logarithm is usually employed. For a matrix $\mathbf{X} \in \mathbb{C}^{n \times n}$ having positive, nonzero eigenvalues, the *principal matrix logarithm* is:

- 1) the unique solution $\mathbf{Y} \in \mathbb{C}^{n \times n}$ to $\text{Exp}(\mathbf{Y}) = \mathbf{X}$ and
- 2) has eigenvalues that verify $\{z \in \mathbb{C} \mid -\pi < \mathcal{I}(z) < \pi\}$. For a matrix $\mathbf{X} \in \mathbb{R}^{n \times n}$ having positive, nonzero eigenvalues, the principal matrix logarithm should be real.

II. Hermitian matrix logarithm//exponential

The properties of positive-definite matrices simplify the expression of the matrix logarithm and exponential operations, which can be computed using the eigenvalue decomposition of the matrix $\mathbf{X} = \mathbf{V}\mathbf{D}\mathbf{V}^H$, $\mathbf{D} = \text{diag}(\lambda_1, \lambda_2, \dots, \lambda_n)$ and the usual logarithm or exponential functions.

Given $\mathbf{D}_{exp} = \text{diag}[\exp(\lambda_1), \exp(\lambda_2), \dots, \exp(\lambda_n)]$

and $\mathbf{D}_{log} = \text{diag}[\log(\lambda_1), \log(\lambda_2), \dots, \log(\lambda_n)]$, then:

$$\text{Exp}(\mathbf{X}) = \mathbf{V} \cdot \mathbf{D}_{exp} \cdot \mathbf{V}^H, \quad (\text{G.2}) \quad \text{Log}(\mathbf{X}) = \mathbf{V} \cdot \mathbf{D}_{log} \cdot \mathbf{V}^H. \quad (\text{G.3})$$

¹GL(n) = General Linear group of invertible matrices of size $n \times n$.

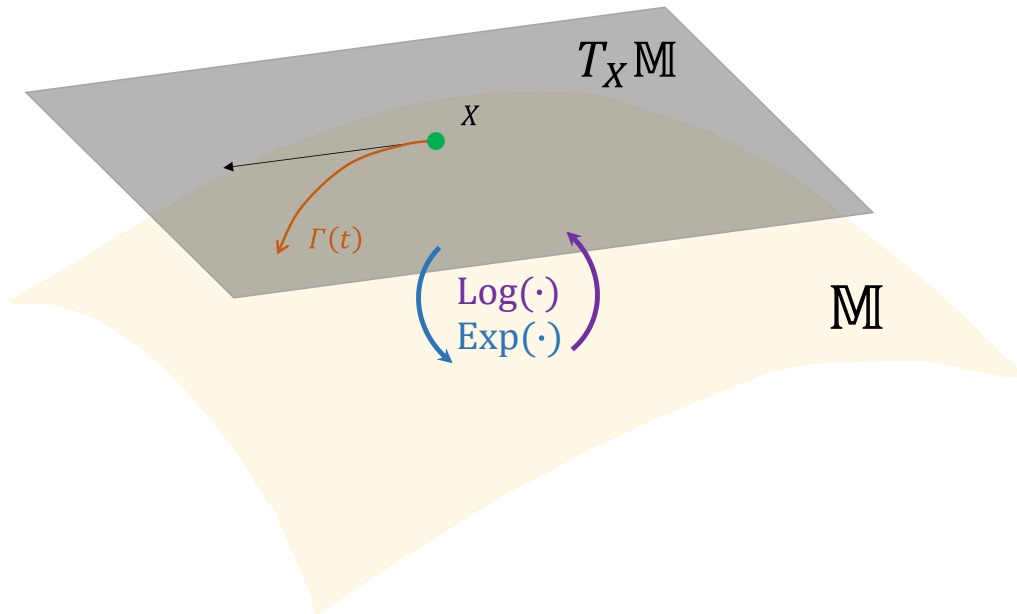


Figure G.1: Matrix logarithm and exponentiation as operations which allow to commute between the manifold (\mathbb{M}) and the tangent space ($T_X \mathbb{M}$) at point X , $\forall X \in \mathbb{M}$.

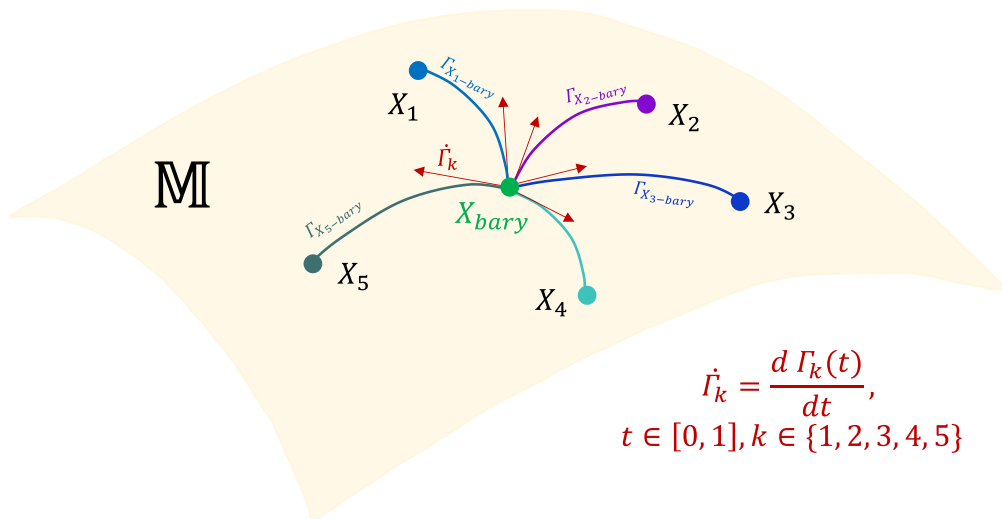


Figure G.2: Geodesics and tangent vectors passing through the set of points $\{X_i\}$, $1 \leq i \leq 5$, and their barycenter.

Riemannian barycenter computation

The Riemannian barycenter computation is obtained here by using an iterative gradient descent method. In the implementation proposed by Barbaresco (and which is considered in the manuscript), at each run, the update procedure searches to minimize the sum of tangent vectors of all geodesics passing through a point [256].

Considering the geodesic between two Hermitian positive definite matrices \mathbf{A} and \mathbf{B} on the Riemannian manifold as given in (3.8):

$$\Gamma(t) = \mathbf{A}^{1/2} \left(\mathbf{A}^{-1/2} \mathbf{B} \mathbf{A}^{-1/2} \right)^t \mathbf{A}^{1/2}, \quad t \in [0,1], \quad \Gamma(0) = \mathbf{A} \quad \text{and} \quad \Gamma(1) = \mathbf{B}.$$

Only the Riemannian geometric mean of two 2 such matrices has a closed-form expression. Given a set of matrices $\{\mathbf{B}_1, \mathbf{B}_2, \dots, \mathbf{B}_m\}$, $1 \leq k \leq m$, the set of geodesics connecting \mathbf{A} to each of them,

$$\Gamma_k(t) = \mathbf{A}^{1/2} \left(\mathbf{A}^{-1/2} \mathbf{B}_k \mathbf{A}^{-1/2} \right)^t \mathbf{A}^{1/2} \quad (\text{H.1})$$

$$= \mathbf{A}^{1/2} \text{Exp} \left[t \cdot \text{Log} \left(\mathbf{A}^{-1/2} \mathbf{B}_k \mathbf{A}^{-1/2} \right) \right] \mathbf{A}^{1/2}, \quad (\text{H.2})$$

and the tangent vectors passing through this point:

$$\left. \frac{d\Gamma_k(t)}{dt} \right|_{t=0} = \mathbf{A}^{1/2} \text{Log} \left(\mathbf{A}^{-1/2} \mathbf{B}_k \mathbf{A}^{-1/2} \right) \mathbf{A}^{1/2}. \quad (\text{H.3})$$

The true barycenter (or Karcher mean) of the $\{\mathbf{B}_m\}$ points is characterized by a zero vectorial sum of all tangent vectors (Fig. G.2):

$$\sum_{k=1}^m \left. \frac{d\Gamma_k(t)}{dt} \right|_{t=0} \rightarrow \sum_{k=1}^m \text{Log} \left(\mathbf{A}^{-1/2} \mathbf{B}_k \mathbf{A}^{-1/2} \right) = 0. \quad (\text{H.4})$$

The implemented gradient descent search uses the property in (H.4) to update the search of the geometric mean [256, 192].

Algorithm: Iterative gradient descent for geometric mean computation.

INPUT: Set of m Hermitian positive definite matrices.

OUTPUT: Riemannian mean.

1. Parameters definition, e.g., $\varepsilon = 0.1$ (start value for step-size), tolerance = 10^{-3} (fixed).
2. Initialization: Compute the Riemannian mean of the first two matrices from the set, $\mathbf{P}_{(0)} = \mathbf{H}_1 \left(\mathbf{H}_1^{-1} \mathbf{H}_2 \right)^{\frac{1}{2}}$ [204].
3. For $m \geq 3$, $\mathbf{P}_{(l)} = \mathbf{P}_{(0)}$

Repeat

$$\nabla \mathbf{P} = \sum_{k=1}^N \text{Log} \left(\mathbf{H}_k^{-\mathbf{H}/2} \mathbf{P}_{(l)}^{-1} \mathbf{H}_k^{-1/2} \right) \quad (\text{compute gradient}) \quad (\text{H.5})$$

$$\mathbf{P}_{(l+1)} = \mathbf{P}_{(l)}^{\mathbf{H}/2} \text{Exp} \left(-\frac{\varepsilon}{N} \nabla \mathbf{P} \right) \mathbf{P}_{(l)}^{1/2} \quad (\text{update estimate}) \quad (\text{H.6})$$

$$D_{(l+1)} = \left\| \left[\mathbf{P}_{(l)} - \mathbf{P}_{(l+1)} \right]^{-1} \mathbf{P}_{(l)} \right\|_F \quad (\text{evaluation by norm}) \quad (\text{H.7})$$

$$\varepsilon = \begin{cases} 0.5\varepsilon & \text{if } D_{(l+1)} > D_{(l)} \\ 1.2\varepsilon & \text{otherwise} \end{cases} \quad (\text{update step-size, for } l \geq 1) \quad (\text{H.8})$$

while $D \geq \text{tolerance}$.

The tangent space $T_X \mathbb{M}$ at a point X on the manifold \mathbb{M} is the one containing all possible geodesic tangent vectors. To perform the gradient evaluation on the manifold, a projection needs to be performed to the tangent space, where the descent direction is evaluated (Fig. G.1). The use of the matrix logarithm in (H.5) indicates this, after which the solution is again projected on the manifold by (H.6).

Publications and communications

Journal articles:

- **M. Ciuca**, G. Vasile, A. Anghel, M. Gay and S. Ciochina, "*Bistatic Analysis Using the Real Representation Scattering Matrix Eigen-Classification*," in IEEE Transactions on Geoscience and Remote Sensing, vol. 60, pp. 1-18, 2022, Art no. 5228318, doi: 10.1109/TGRS.2022.3175475.
This publication contains elements presented in Chapter 3.
- **M. Ciuca**, G. Vasile, A. Anghel, M. Gay and S. Ciochina, "*Real Representation of the Polarimetric Scattering Matrix for Monostatic Radar*" in Remote Sensing, 2023, 15, 1037, <https://doi.org/10.3390/rs15041037>.
This publication contains elements presented in Chapter 3.
- **M. Ciuca**, G. Vasile, M. Congedo and M. Gay, "*Riemannian Clustering of PolSAR Data using the Polar Decomposition*", under review with the IEEE Transactions on Geoscience and Remote Sensing.
Chapter 4 is adapted from this work.
- A. Anghel, R. Cacoveanu, **M. Ciuca**, B. Rommen and S. Ciochina, "Multi-channel Ground-based Bistatic SAR Receiver for Single-pass Opportunistic Tomography", in IEEE Transactions on Geoscience and Remote Sensing, 2023, doi: 10.1109/TGRS.2023.3294124.
Outside the main scope and not included in the thesis.

Conference proceedings:

- **M. Ciuca**, A. Anghel, R. Cacoveanu, G. Vasile, M. Gay and S. Ciochina, "*Spaceborne Transmitter - Stationary Receiver Bistatic SAR Polarimetry - Experimental Results*", IGARSS - 2020 IEEE International Geoscience and Remote Sensing Symposium, 2020, pp. 3869-3872 (pre-recorded video + online presentation).
This conference paper is a preliminary work, on which the experimental part from the end of Chapter 2 is based.
- **M. Ciuca**, G. Vasile, M. Gay, A. Anghel and S. Ciochina, "*Polarimetric Analysis Using the Algebraic Real Representation of the Scattering Matrix*", 2021 IEEE International Geoscience and Remote Sensing Symposium IGARSS, 2021, pp. 499-502, doi: 10.1109/IGARSS47720.2021.9554273 (pre-recorded video + online

presentation).

This conference paper is a preliminary work, which is extended in Chapter 3.

- **M. Ciuca**, G. Vasile, M. Gay, A. Anghel and S. Ciochina, "*Méthode générale de résolution de la similarité conjuguée en polarimétrie radar*" XXVIIIème Colloque Francophone de Traitement du Signal et des Images, Sep 2022, Nancy, France, (oral presentation).

The results from this conference paper have been presented in Chapter 3.

- **M. Ciuca**, G. Vasile, M. Congedo, "Geometric Clustering of PolSAR Data using the Polar Decomposition", accepted as oral presentation at IGARSS 2023.

This conference communication is based on Chapter 4.

- **M. Ciuca**, A. Anghel, R. Cacoveanu, B. Rommen and S. Ciochina, "*Single-Pass Spaceborne Transmitter-Stationary Receiver Bistatic SAR Tomography - Novel Solution with 3 Imaging Channels*", 2020 IEEE International Geoscience and Remote Sensing Symposium IGARSS, 2020, pp. 124-127. (pre-recorded video + online presentation).

Outside the main scope and not included in the thesis.

Virtual poster:

- **M. Ciuca**, A. Anghel, R. Cacoveanu, G. Vasile, M. Gay, S. Ciochina "*Spaceborne Transmitter – Stationary Receiver: A Monostatic and Bistatic Dual-Polarimetric Investigation*", Category - Sensors, Systems, Technology, ESA PhyWeek, 28 September – 2 October 2020, online event (recorded video available on Youtube: <https://www.youtube.com/watch?v=k5s9L3J5JEM>).

This work relates to the experimental part from the end of Chapter 2.

Résumé étendu

Introduction

La télédétection permet de détecter et de surveiller à distance les caractéristiques physiques d'un objet. La télédétection par micro-ondes est la branche qui utilise pour cette étude des signaux électromagnétiques appartenant au domaine des fréquences radar (≈ 300 MHz - 300 GHz). Ses sous-catégories sont la télédétection active et passive par micro-ondes.

La télédétection active, avec des instruments radar, est aujourd'hui une technologie conventionnelle dans d'observation de la Terre. Elle est considérée un complément à la technologie optique, notamment en raison de sa capacité d'imagerie avec moins de restrictions (d'utilisation possible dans la journée et dans la nuit, quelles que soient les conditions météorologiques). Le plus utilisé c'est le radar à synthèse d'ouverture (fr., RSO, eng., « Synthetic Aperture Radar », SAR¹), qui peut acquérir des images à haute résolution de la rétrodiffusion complexe d'une zone.

La dernière décennie a montré un intérêt croissant pour les systèmes radar multi-plateformes. Le lancement en 2010 du satellite jumeau de TerraSAR-X, TanDEM-X, ainsi que les études scientifiques préparatoires qu'il a nécessitées, ont constitué des étapes importantes dans cette direction. Ces efforts ont mis en évidence la maturité technologique et les avantages possibles de ce type de diversité (c'est-à-dire la possibilité d'effectuer plusieurs acquisitions dans un seul passage à partir de positions spatiales distinctes).

En combinant des ensembles d'observations de la même zone, le principal type de diversité pour toutes les applications de télédétection est multitemporelle. D'autres formes de diversité sont possibles en télédétection par micro-ondes : la fréquence, la polarisation et la géométrie multi-capteur peuvent être accessibles lorsque le radar est équipé d'instruments spécialisés.

En polarimétrie radar, l'instrument actif est celui qui fixe la polarisation à l'émission, qui sera généralement modifiée par l'interaction d'ondes électromagnétiques avec la surface des objets géophysiques, mesurée à une ou plusieurs fréquences. Un capteur SAR polarimétrique permet d'accéder à l'ensemble multidimensionnel du rayonnement rétrodiffusé. La surveillance des cultures, la classification de la couverture des sols, la détection des diffuseurs persistants en milieu urbain ou l'étude des glaciers figurent parmi les applications du « Polarimétrie SAR » (PolSAR).

Le travail présenté dans ce manuscrit se concentre sur l'étude de la diversité radar polarimétrique.

- Pendant près de vingt ans, les principales combinaisons PolSAR multi-diversité

¹l'acronyme anglais sera utilisé même dans cette section

étaient avec la multi-temporalité ou la multi-fréquence. Moins de recherches ont utilisé la technologie radar permettant de combiner la diversité polarimétrique et la diversité spatiale. Avec l'intérêt croissant pour des plateformes en géométrie bistatique et multistatique, ce type de diversité combinée sera un domaine d'intérêt important.

- L'augmentation constante, au fil des années, de la résolution spatiale a rendu les images radar plus performantes et plus attrayantes dans les applications pratiques. Cependant, les statistiques permettant de caractériser le vecteur cible sont devenues plus complexes et de nombreux modèles ont été proposés. La difficulté de choisir la solution optimale peut être résolue en introduisant des techniques qui ne dépendent pas de la distribution statistique des données.

Cette thèse vise à développer de nouveaux outils et méthodes pour la compréhension et l'analyse des images radar polarimétriques (polarisation linéaire). Les contributions abordent les défis identifiés.

Chapitre 1 fixe le cadre théorique. Il présente les descripteurs élémentaires de la polarisation des ondes, compare les conventions radar et optique (retrodiffusion contre diffusion) et les formalismes matriciels et vectoriels, qui sont au centre de la plupart des méthodes et décompositions cohérentes et incohérentes.

Chapitre 2 se développe autour de la question suivante : Quel traitement est disponible et adéquat si on utilise la convention radar (c'est-à-dire l'alignement par rétrodiffusion), adopte un calcul matriciel et gère des observations radar qui ne sont pas réciproques ? Le chapitre aborde la transformation de similarité conjuguée (ci-après, consimilarité) et propose une solution basée sur la représentation réelle (qui a révélé des solutions à valeurs complexes pour le cas de certaines matrices non-réciproques). Dans le cas réciproque, les résultats obtenus avec la représentation réelle correspondent généralement à ceux de la factorisation non-négative de la matrice de diffusion carrée. Ensuite, des applications sont explorées pour la représentation réelle, en particulier par le calcul de sa décomposition propre.

Chapitre 3 continue d'explorer les applications sous le formalisme matriciel, mais avec une opération basée sur la similarité, la décomposition polaire. La méthode proposée dans ce chapitre utilise le facteur H , défini positif Hermitien, de la décomposition polaire avec des opérations sur la variété Riemannien qui lui est associée. La moyenne géométrique intrinsèque des matrices Hermitiennes est implémentée, suivie d'un algorithme de regroupement avec une distance géodésique pour la répartition en clusters. Des tests qualitatifs et quantitatifs sont effectués sur des données monostatiques réelles et simulées. Malgré ce choix, la technique peut être appliquée avec des mesures en géométrie bistatique.

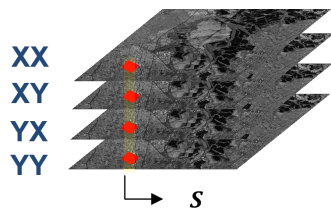
Le **dernier chapitre** présente une vue d'ensemble des contributions de la thèse et propose des perspectives de travail pour l'avenir. Pour que la synthèse de ce travail soit efficace, des éléments supplémentaires sont fournis, lorsque nécessaire, dans les **Annexes A-H**. Les contributions en publications et aux conférences pendant la durée de cette thèse sont énumérées dans **Annex I**.

Diversité radar polarimétrique

La polarisation d'une onde est définie par la direction d'oscillation des composantes du champ électrique dans le plan transversal de propagation. Elle est souvent assimilée à la figure "que dessinait l'extrémité du champ électromagnétique vectoriel en fonction du temps". Par ailleurs, la polarisation d'une antenne est "celle d'une onde plane qu'elle rayonne à grande distance dans une direction donnée" [3, 2].

L'imagerie radar conventionnelle suppose une géométrie *monostatique*, dans laquelle les unités d'émission et de réception sont situées au même endroit. Dans un système *bistatique*, l'émetteur et le récepteur sont situés à des endroits différents et présentent une séparation (« baseline ») considérable entre eux (plusieurs ordres plus grands que la longueur d'onde). Si l'émetteur et le récepteur ne sont que des équipements distincts, mais placés à proximité, la géométrie s'appelle *quasi-monostatique* (ou presque monostatique).

Une cible qui se trouve éclairée dans la scène radar est connue pour se comporter comme un modificateur de l'état de polarisation [46]. Pour un ensemble générique de bases de polarisation (X-Y), le changement entre les composantes des champs d'incidence et de rétrodiffusion s'effectue par la matrice de diffusion, $S \in \mathbb{C}^{2 \times 2}$:



$$\begin{bmatrix} E_s^X \\ E_s^Y \end{bmatrix} = \begin{bmatrix} S_{xx} & S_{xy} \\ S_{yx} & S_{yy} \end{bmatrix} \begin{bmatrix} E_i^X \\ E_i^Y \end{bmatrix}. \quad (\text{I.1})$$

Figure I.1: Observation radar polarimétrique.

Les cibles sont généralement décrites comme ayant une réponse de diffusion déterministe ou non déterministe. Une cible déterministe (ou diffuseur unique) a une réponse de polarisation stable dans le temps, qui est entièrement caractérisée par sa matrice de diffusion. En revanche, la réponse de diffusion d'une cible non déterministe ne reste pas stable et est modélisée à l'aide de processus stochastiques. Ce diffuseur est généralement partielle ou distribuée, avec des dimensions qui couvrent plusieurs cellules de résolution [47, 48].

Systèmes de coordonnées radar et optique

La polarisation est une propriété du signal électromagnétique reçu et aussi du dispositif radar qui transmet le signal et effectue les mesures. Comme le suggèrent les normes de l'IEEE, la polarisation d'une antenne est celle de l'onde qu'elle émet, ce qui implique que dans le cas réception, les systèmes de coordonnées utilisés pour décrire la polarisation de l'antenne et de l'onde entrante sont orientés dans des directions

opposées. Il existe un système de coordonnées spécifique utilisé dans le domaine de la polarimétrie radar, l'alignement de rétrodiffusion (« Backscattering Alignment », BSA). En revanche, en polarimétrie optique et dans d'autres domaines de la polarimétrie, le système de coordonnées conventionnel utilisé est l'alignement de la diffusion vers l'avant (« Forward Scattering Alignment », FSA). Selon la convention BSA, le vecteur de l'onde diffusée sur le trajet de réception est représenté avec une orientation inversée par rapport à FSA [4]. Cette différence d'orientation de 180° impose une opération mathématique de conjugaison. Dans ce contexte, les relations de changement de base des deux conventions sont très différentes: alors que FSA exploite les transformations de similarité effectuées sur la matrice de Jones, BSA exploite les transformations de similarité conjuguées effectuées sur la matrice de Sinclair [55, 56, 48].

Similarité et similarité conjuguée

La similarité et la similarité conjuguée sont deux relations d'équivalence des matrices complexes. À partir de trois matrices $A, B, C \in \mathbb{C}^{n \times n}$ on peut écrire :

Table I.1: Équations de similarité et de similarité conjuguée:

similarité	consimilarité
$AV = VB$	$AX = X^*C$

Les matrices V et $X \in \mathbb{C}^{n \times n}$ sont appelées matrices de transformation de base de la similarité et de la consimilarité. Mais en utilisant une matrice réelle $X \in \mathbb{R}^{n \times n}$, comme une matrice orthogonale de rotation, l'opération de consimilarité devient une opération de similarité. Si les matrices V et X sont unitaires ($V^H V = V V^H = I$ et $X^H X = X X^H = I$) les deux opérations sont assimilées à une décomposition en valeurs/vecteurs propres et à une décomposition en valeurs/vecteurs propres conjugués.

Table I.2: Valeurs/vecteurs propres et homologues conjugués.

valeur/vecteur propre	valeur/vecteur propre conjugué
$A v_n = \lambda_n v_n$	$A x_n = \xi_n x_n^*$

Pour une matrice complexe symétrique A , X est toujours unitaire et la similarité conjuguée est équivalente à une congruence unitaire :

$$\begin{aligned} \Gamma &= (X^*)^{-1} A X = (X^{-1})^* A X \\ &= (X^H)^* A X = X^\top A X. \end{aligned} \tag{I.2}$$

La possibilité de considérer la matrice S comme symétrique et l'introduction de l'opération de similarité conjuguée sont des conséquences directes de l'imposition de la convention BSA. La première affecte la seconde, de sorte que les matrices de diffusion monostatiques vérifiant la réciprocité sont toujours diagonalisées sous congruence

unitaire. Le formalisme mathématique pour la diagonalisation en congruence unitaire est disponible dans PolSAR depuis les premiers travaux de Graves [64] et est plus connu dans la littérature mathématique sous le nom de factorisation d'Autonne-Takagi [71]. Cette thèse s'intéresse à l'étude du cas où les matrices ne sont plus symétriques et cette factorisation ne peut plus être appliquée.

Avec des matrices de diffusion symétriques, $S = S^T$, les valeurs propres de la matrice de Graves, $G = S^H S = S^{T*} S = S^* S$, sont les valeurs absolues au carré des valeurs propres du consimilarité et ses vecteurs propres sont égaux aux vecteurs propres du consimilarité [73]. Néanmoins, si les valeurs propres de G sont égales, cette décomposition ne permet plus de résoudre la factorisation de Takagi [68, 71]. La congruence unitaire des matrices de diffusion symétriques peut également être assimilée à la forme symétrique de la décomposition en valeurs singulières (une SSVD). Pour le cas bistatique, la transformation SVD est directement proposée dans la littérature. Elle permet la décomposition de la matrice de diffusion par une matrice diagonale et deux transformations unitaires, l'une caractérisant le trajet émetteur-cible (Tx-Tg) et l'autre le trajet cible-récepteur (Tg-Rx) [76]. Dans le cas de la consimilarité, les deux matrices de transformation de chaque trajet sont des paires conjuguées. Ces connexions sont indiquées dans la Figure I.2.

La transformation générale de la similarité conjuguée pour des matrices de diffusion non réciproques n'a pas encore été suffisamment étudiée dans le domaine des radars polarimétriques. Elle peut apporter de nouvelles informations dans l'analyse des matrices de diffusion.

Décompositions PolSAR cohérentes et incohérentes

Les observations de multipolarisation sont exploitées à l'aide de techniques de décomposition qui constituent le fondement de la théorie PolSAR. Ces techniques sont utilisées pour séparer la signature polarimétrique capturée par les instruments radar dans une combinaison de diffusions plus simples, auxquelles une signification physique peut être associée. On distingue les méthodes cohérentes et incohérentes (Figure I.3).

■ Décompositions cohérentes

Les méthodes cohérentes sont divisées en deux classes principales. Elles peuvent décomposer la matrice de diffusion par sommation ou factorisation [4].

Une décomposition par addition utilise l'ensemble des matrices élémentaires qui forment une base. La décomposition de Pauli est le plus connu exemple pour matrices 2×2 . Les matrices de Pauli ont une interprétation physique, comme suit : écho impair, écho pair, mécanisme diffus et mécanisme asymétrique. Seuls les trois premiers composants sont non-zéro lors de la décomposition d'une matrice de dispersion réciproque.

Une décomposition multiplicative (par exemple, la diagonalisation) s'appuie sur des opérations algébriques pour extraire des facteurs élémentaires. La décomposition de Huynen [66] et la décomposition polaire [198] sont proposées

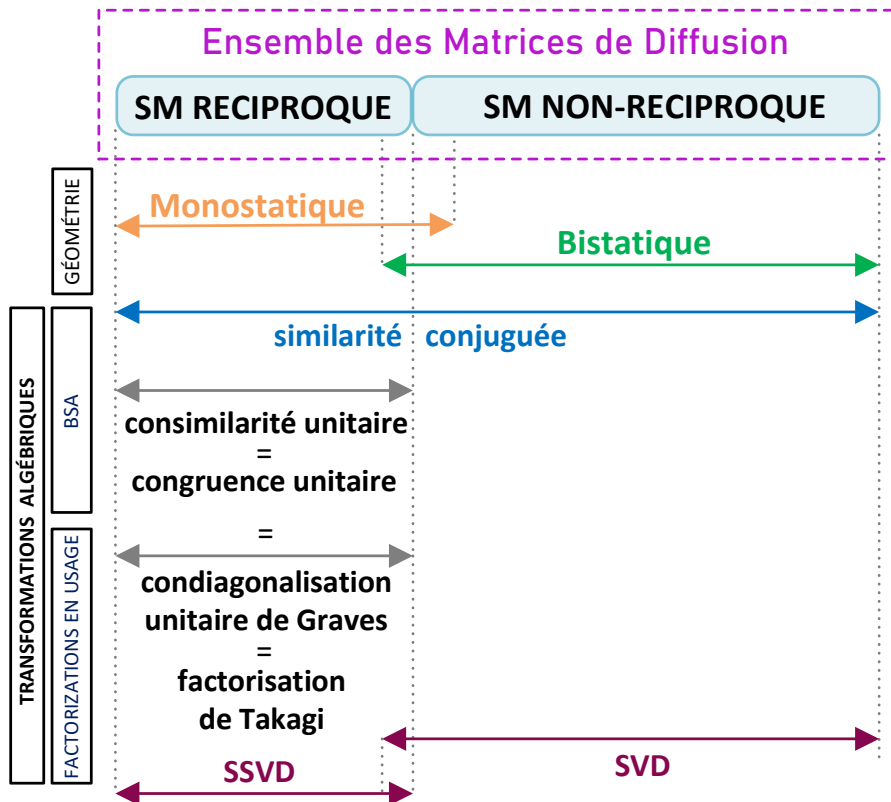


Figure I.2: Similarité conjuguée et opérations SVD pour les matrices de diffusion réciproques et non réciproques.

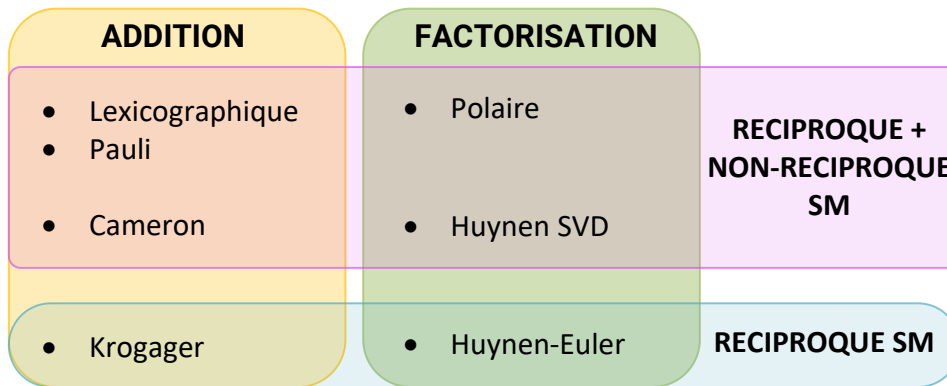


Figure I.3: Classification des décompositions cohérentes.

Axe horizontale: Type de factorisation. Axe verticale: Applicabilité aux matrices de diffusion réciproques et non réciproques. Acronyme : SVD : Singular Value Decomposition.

à titre d'exemple. Les principaux développements proposés par la thèse sont liés à la branche des décompositions cohérentes. Plus précisément, les contributions

reposent sur l'utilisation de méthodes de factorisation multiplicative adéquates pour les matrices de diffusion réciproques et non-réciproques.

■ Décompositions incohérentes

Le vecteur de diffusion de la cible propose une représentation équivalente de l'information polarimétrique [77, 76]. Sa connexion avec la matrice de diffusion peut être représentée par une projection dans l'ensemble des N éléments d'une base $\{\Psi\}$ (qui sont généralement la base lexicographique ou la base de Pauli):

$$\mathbf{k} = \text{Vect}(\mathbf{S}) = \frac{1}{2} \text{Tr}(\mathbf{S}\Psi) \quad (\text{I.3})$$

I. Données en polarimétrie complète

Les observations bistatiques utilisent généralement un ensemble complet de quatre matrices de base, alors que dans le cas monostatique (sous l'hypothèse de réciprocité), l'ensemble est réduit à seulement trois matrices.

II. Données en double polarimétrie

Pour les données en double polarimétrie, que la géométrie soit monostatique ou bistatique, le vecteur diffusion de la cible a la même dimension, uniquement 2×1 (c'est-à-dire un ensemble incomplet de deux matrices de base). Dans le cas d'une polarisation linéaire, il existe trois combinaisons double-polarimétriques possible : HH-VV, HH-VH et VV-HV.

Application: Classification H-alpha monostatique et bistatique pour double polarisation VV-HV

Une analyse au niveau du pixel n'est plus pertinente pour la réponse de diffusion des cibles partielles. Plus la surface au sol de la cellule de résolution radar est grande, plus le nombre d'objets réels imaginés augmente.

Les données PolSAR ont une nature stochastique dans ce cas et les outils pertinents d'analyse exigent le calcul de moments d'ordre supérieur. Le modèle statistique élémentaire utilisé pour le vecteur de diffusion de la cible est celui d'une distribution Gaussienne circulaire à moyenne nulle [98]. La fonction densité de probabilité de la vecteur cible s'exprime :

$$p(\mathbf{k}) = \frac{1}{\pi^m \det(\mathbf{C})} \exp\left(-\mathbf{k}^H \mathbf{C}^{-1} \mathbf{k}\right), \quad (\text{I.4})$$

$m \in \{3,4\}$ (en fonction de la dimension du \mathbf{k}), $\mathbf{C} = \mathbb{E}\left\{\mathbf{k}_{\mathcal{L}}\mathbf{k}_{\mathcal{L}}^H\right\}$ c'est la matrice de covariance et $\mathbb{E}\{\cdot\}$ c'est l'opérateur d'espérance mathématique. Il est généralement considéré que le modèle gaussien pour le vecteur cible décrit le mieux les données PolSAR provenant : a) de régions homogènes ou b) pour lesquelles un grand nombre de cibles élémentaires sont présentes à l'intérieur de la cellule de résolution (sous l'application du théorème de la limite centrale). C'est souvent le cas pour les

observations à moyenne et basse résolution. Comme les méthodes présentées dans la thèse ne fait pas directement référence à des modèles statistiques, le cas Gaussien est implicitement supposé (c'est-à-dire, le cas non-Gaussien pour les données à très haute résolution est ignoré). La covariance complexe, $\hat{\mathbf{C}}$, estimée généralement par la moyenne spatiale selon le critère du maximum de vraisemblance suit alors une distribution complexe de Wishart avec une fonction de densité de probabilité :

$$p(\hat{\mathbf{C}}) = \frac{L^q (\det \hat{\mathbf{C}})^{L-q}}{(\det \Sigma)^L \Gamma_q(L)} \exp\left(-L \cdot \text{Tr}(\Sigma^{-1} \hat{\mathbf{C}})\right), \quad (\text{I.5})$$

dans laquelle $\Gamma_q(L) = \pi^{\frac{q(q-1)}{2}} \prod_{i=0}^{q-1} \Gamma(L-i)$, $\Gamma(\cdot)$ représente la fonction gamma, q est l'ordre de la matrice de covariance estimée à partir de L échantillons et $\Sigma = \mathbb{E}\{\hat{\mathbf{C}}\}$.

La classification Entropy-alpha est probablement la décomposition PolSAR incohérente la plus connue. L'entropie (H) est une mesure des valeurs propres (λ_i) utilisée pour décrire le caractère aléatoire d'une cible diffusante et l'alpha (α) est la valeur moyenne des angles d'orientation (α_i) des vecteurs propres. Ces paramètres s'expriment comme suit :

$$H = -\sum_{i=1}^m P_i \log_m P_i \quad 0 \leq H \leq 1 \quad (\text{I.6}) \quad \alpha = \sum_{i=1}^m P_i \alpha_i \quad 0^\circ \leq \alpha \leq 90^\circ \quad [\text{deg.}] \quad (\text{I.7})$$

$$P_i = \frac{\lambda_i}{\sum_{j=1}^m \lambda_j} \quad 0 \leq P_i \leq 1; \quad 1 \leq i \leq m \quad (\text{I.8})$$

Si les mêmes définitions et formules pour H et α s'appliquent quelle que soit la dimension polarimétrique des données (complète ou double) [76], leur interprétation des propriétés de diffusion change, en particulier pour alpha qui perd la propriété d'invariance à la rotation pour la double polarimétrie [105, 102]. Il s'agit d'un résultat bien connu, étudié dans la littérature, pour le cas monostatique.

La partie applicative de ce chapitre présente de nouveaux résultats pour le cas de la double polarisation, en utilisant des images polarimétriques monostatiques et bistatiques simultanément enregistrées. Les résultats de l'expérience indiquent que les mécanismes de diffusion dual-pol impliqués dans la géométrie monostatique et bistatique sont suffisamment différents, de tel sorte qu'une augmentation de la valeur alpha en double polarimétrie est observée pour la plus grande partie des diffuseurs de l'image (Fig. I.4).

Le choix de la diversité multi-polarimétrique est souvent sujet à des concessions dans les systèmes réels, c'est pourquoi la double polarimétrie est souvent préférée. Le reste de la thèse portera entièrement sur un cadre d'analyse polarimétrique complet.

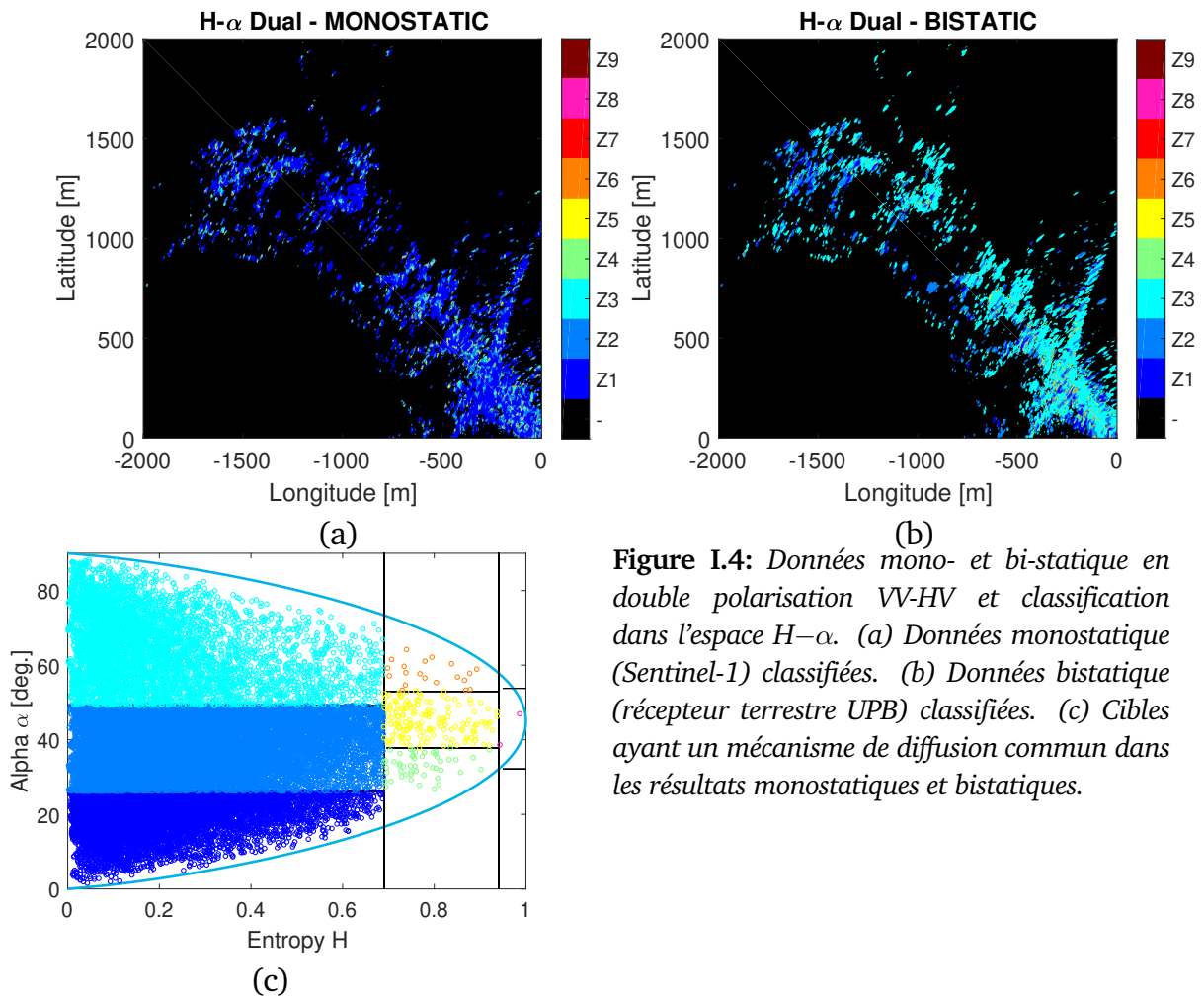


Figure I.4: Données mono- et bi-statique en double polarisation VV-HV et classification dans l'espace $H-\alpha$. (a) Données monostatique (Sentinel-1) classifiées. (b) Données bistatique (récepteur terrestre UPB) classifiées. (c) Cibles ayant un mécanisme de diffusion commun dans les résultats monostatiques et bistatiques.

Matrice de diffusion en représentation réelle

La transformation d'une matrice de diffusion générale par une opération de similarité conjuguée (consimilarité) est une procédure mathématique introduite dans le cadre de l'alignement de rétrodiffusion radar. En général, l'intérêt est de récupérer les termes de la factorisation qui, sous diagonalisation, sont appelés les valeurs propres conjuguées (ξ_k) et les vecteurs propres conjugués (\mathbf{x}_k), $k \in \{1,2\}$. On les appelle également convaleurs et convecteurs dans ce document :

$$\mathbf{S}\mathbf{x}_k = \xi_k \mathbf{x}_k^* \quad (\text{I.9})$$

Comme discuté dans le chapitre précédent, pour les matrices non réciproques, cette opération ne se réduit plus à celle de la congruence unitaire. L'un des objectifs de ce chapitre est de discuter des défis et des avantages de l'utilisation de la transformation de consimilarité dans ce cas. Les techniques PolSAR connues appliquent soit l'opération de congruence unitaire de Graves/Takagi pour les matrices réciproques, soit la

décomposition en valeurs singulières (SVD) pour les matrices non réciproques, en distinguant clairement que la première s'applique aux données monostatiques et la seconde aux données bistatiques. Le travail présenté dans cette partie offre un complément nécessaire, par exemple lorsque l'on dispose de données monostatiques non réciproques ou en tant qu'alternative à la méthode SVD pour bistatique.

La matrice de diffusion de la représentation réelle (RRSM)

Les méthodes disponibles dans la littérature pour résoudre une transformation de consimilarité ne sont pas directes, mais elles sont basées sur des « mappings » vers un espace équivalent où la similarité conjuguée peut être évaluée comme une équation de similarité. Cette transformation est un morphisme qui peut être basé sur le produit complexe entre la matrice de diffusion et son conjugué complexe [60], ou en utilisant une matrice par blocs [113, 115]. Dans cette contribution, nous utilisons la matrice de diffusion dans sa Représentation Réelle (RR) [116, 119]. Cette matrice est composée des blocs contenant les parties réelles, opérateur $Re(\cdot)$, et imaginaires, opérateur $Im(\cdot)$, de la matrice initiale : $S_{RR} \in \mathbb{R}^{4 \times 4}$ est appelé comme la représentation réelle de la matrice de diffusion (RRSM).

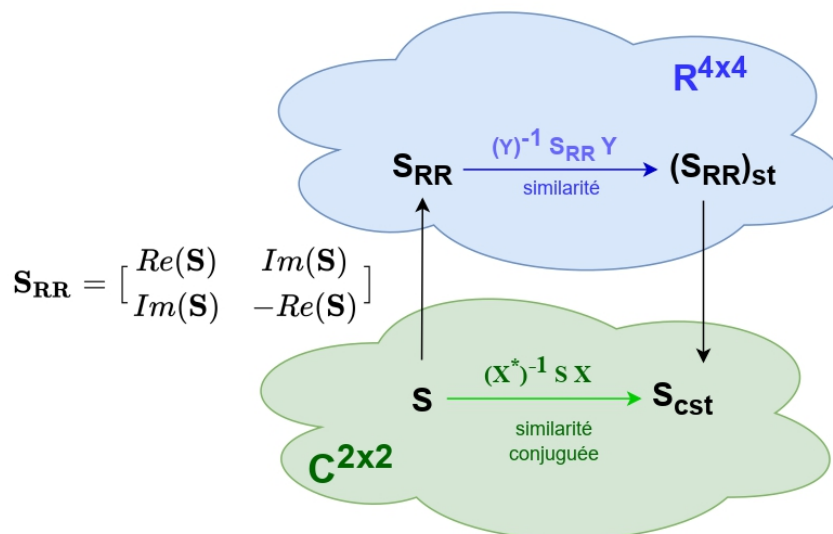


Figure I.5: Opération de similarité conjuguée entre deux matrices complexes (S , S_{cst}) et de similarité entre deux matrices réelles (S_{RR} , $S_{RR_{st}}$). La transformation d'équivalence par consimilarité est $X \in \mathbb{C}^{2 \times 2}$ et la transformation d'équivalence par similarité dans l'espace réel des matrices blocs est $Y \in \mathbb{R}^{4 \times 4}$.

RRSM forme canonique et propriétés

Les valeurs propres de la représentation réelle ont des propriétés intéressantes : a) elles se trouvent en paires positives-négatives qui b) ont le même type algébrique (Table I.3).

Table I.3: Valeurs propres de la RRSM et valeurs/vecteurs propres de la consimilarité pour SM.

	RRSM	SM	
	valeurs propres	convaleurs	convecteurs
réelles	paires distinctes $\{\lambda_1, \lambda_2, -\lambda_1, -\lambda_2\}$	réelles distinctes $\{\xi_1, \xi_2\}$	indépendants, orthogonaux
	paires égales $\{\lambda, \lambda, -\lambda, -\lambda\}$	réelles égales $\{\xi, \xi\}$	a. indépendants, orthogonaux ou b. indépendants, avec un con-vecteur et un con-vecteur généralisé
complexes	paires conjuguées $\{\lambda, \lambda^*, -\lambda, -\lambda^*\}$	complexes $\{\xi, \xi^*\}$	un con-vecteur et un con-vecteur généralisé

Lorsque au moins deux valeurs du \mathbf{S}_{RR} sont égales il peut ne pas être possible d'obtenir une forme diagonale pour la matrice $\mathbf{S}_{RR_{st}}$. La forme de Jordan, presque diagonale, peut être utilisée dans ce cas [60] :

$$(\mathbf{S}_{RR})_{\mathbf{J}} = (\mathbf{S}_{RR})_{st} = \left[\bigoplus_{k_1} \mathbf{J}_{p_{\mathcal{R}}}(\lambda_{k_1}) \right] \oplus \left[\bigoplus_{k_2} \mathbf{J}_{r_{p_{\mathcal{I}}}}(\lambda_{k_2}, \lambda_{k_2}^*) \right]. \quad (\text{I.10})$$

Chaque paire positive-négative de valeurs propres (à éléments réels ou complexes) de la forme canonique $(\mathbf{S}_{RR})_{\mathbf{J}}$ correspondra à une convaleur (la valeur positive de la paire est choisie). Par exemple, à une paire réelle de valeurs propres $(\lambda, -\lambda)$, correspond une convaleur réelle positive $\xi = \lambda$, $\lambda > 0$. Une paire complexe est associée à une convaleur complexe. L'existence de valeurs propres complexes permet une caractérisation complète du cas des matrices Sinclair inhomogènes (par rapport à la consimilarité). Pour des matrices de diffusion réciproques, la factorisation de Graves-Takagi est l'opération standard pour obtenir les convaleurs (Figure I.2).

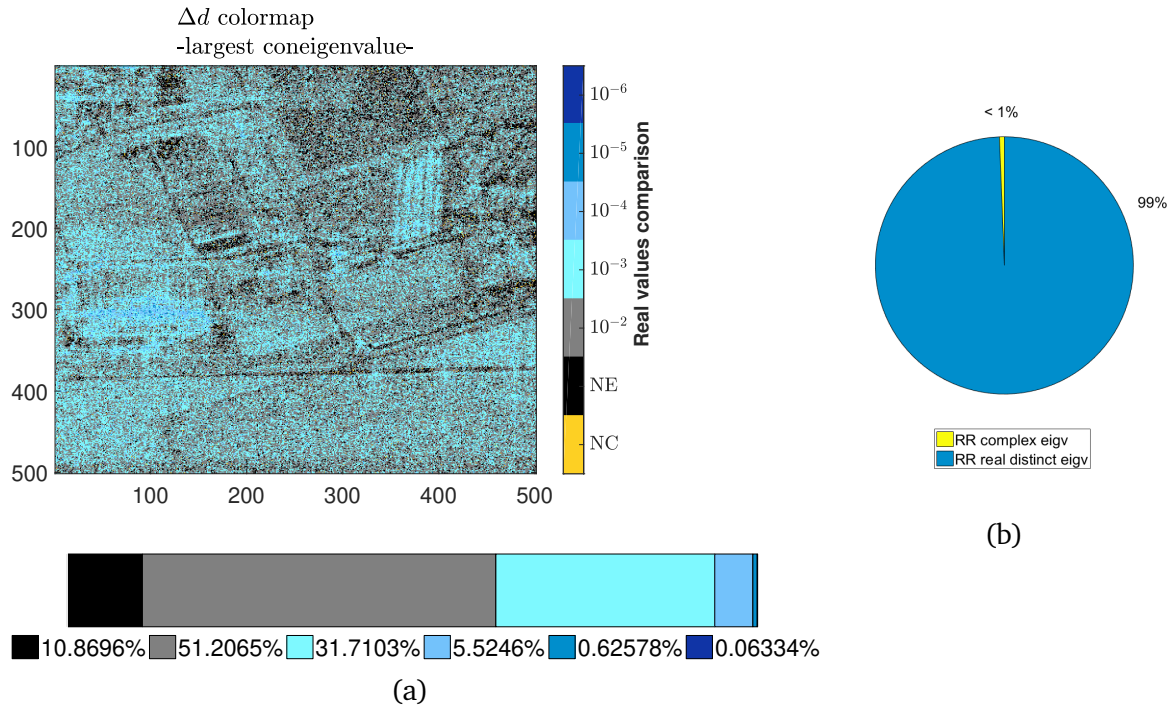


Figure I.6: Comparaison de la différence absolue (Δd) entre les valeurs obtenues par la méthode de Graves et les valeurs obtenues par la méthode RR - Plus grande convalueur (ξ_1). (a) En carte des couleurs. (b) Pourcentage des valeurs propres du RRSM réelles et complexes.

Légende des acronymes : NC (jaune) = Non comparée, NE (noir) = Inégales. Les pixels sont classés dans les classes de gris et de bleu si les valeurs obtenues par les deux méthodes sont égales sous une tolérance δ_d compris entre 10^{-2} et 10^{-6} .

Pour le cas monostatique, le nombre de matrices renvoyant des convalueurs complexes est généralement attendu faible. Les données (monostatiques, bande radar X) polarimétriques de Brétigny, considéré comme exemple, vérifiez cette hypothèse (Figure I.6b). Figure I.6 affiche la comparaison numérique entre les convalueurs estimés par les deux méthodes (Graves-Takagi et RR) dans le cas réciproque (qui présente uniquement des valeurs réelles). Pour la plupart, les valeurs obtenues sont équivalentes avec une tolérance $\delta_d \leq 10^{-2}$.

Le chapitre se poursuit ensuite par une analyse qui cherche la connexion entre le facteur de non-réciprocité [140] de la matrice de diffusion, $\zeta = \frac{1}{\sqrt{2}} \frac{(S_{vh} - S_{hv})}{\|S\|_F}$, et les convalueurs complexes. Notation $\|S\|_F = \left(\sum_{i,j \in \{x,y\}} |S_{ij}|^2 \right)^{1/2}$ c'est la norme de Frobenius.

La méthodologie est basée dans cette partie sur l'utilisation de données polarimétriques simulées (monostatiques et bistatiques, en bande radar C) de deux objets métalliques, considérés comme des cibles indépendantes dans la cellule de résolution : un dièdre et une plaque. D'un point de vue polarimétrique, le dièdre et la plaque sont associés à deux mécanismes élémentaires de diffusion distincts, l'écho pair et l'écho impair. Un logiciel de calcul électromagnétique est utilisé pour obtenir les réponses

du champ électrique diffusé à partir desquelles des matrices de diffusion sont estimées pour chaque objet dans un grand intervalle angulaire d'observation.

Dans la suite, l'exemple du dièdre est considéré. Les données simulées monostatiques sont vérifiées par deux méthodes différentes : la vérification de la section transversale radar (Figure I.7) et la vérification des matrices estimées à l'aide de paramètres polarimétriques dont la valeur est connue (Table I.4). Les mêmes ressources ne sont pas actuellement disponibles pour le cas bistatique, par conséquent les résultats de la simulation bistatique ne sont pas vérifiés au préalable. Enfin, les matrices de diffusion estimées par simulation sont mises sous la forme de la représentation réelle et les pourcentages des différents types de valeurs propres des RRSM sont calculés dans les deux cas, monostatique et bistatique.

■ Dièdre (cas monostatique)

I. Vérification de la surface équivalente radar simulée

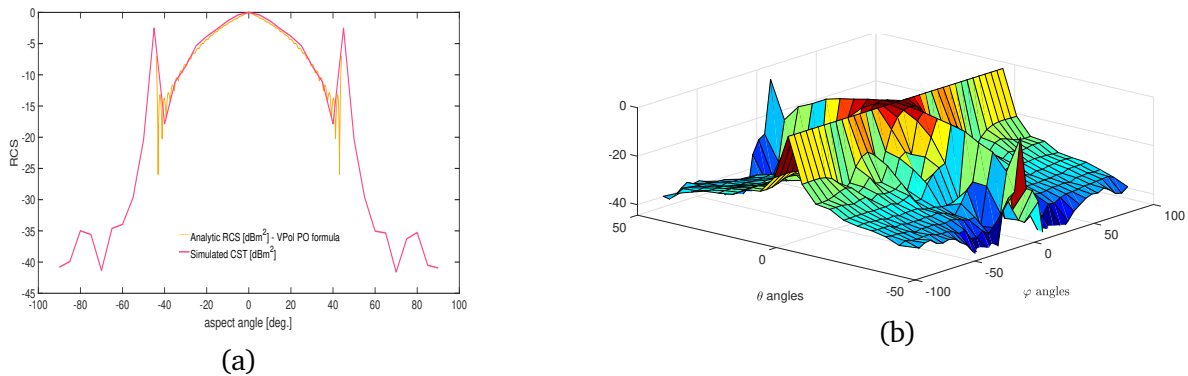


Figure I.7: Dièdre monostatique (V Polarisation). (a) Comparaison RCS : Valeurs simulées par logiciel et par formule analytique (1D, [dBm²]). (b) Valeurs absolues du champ électrique normalisé E_s (3D, [dB(V/m)]), simulées par logiciel.

II. Vérification des matrices de diffusion estimées par les paramètres polarimétriques

Table I.4: Dièdre monostatique. Évaluation basée sur des descripteurs polarimétriques angulaires (α_{Cloude} et α_{TSVM}). Pourcentage des valeurs estimées en intervalles de 10° entre [0°, 90°].

	90–80	80 - 70	70 - 60	60 - 50	50 - 40	40 - 30	30 - 20	20 - 10	10 - 0
α_{Cloude} [76]	28.7 %	18.2 %	12.8 %	9.8 %	15.1 %	8.53 %	4.03 %	1.42 %	1.42 %
α_{TSVM} [50]	28.7 %	17.5 %	11.8 %	9.8 %	12.95 %	11.7 %	4.7 %	1.42 %	1.42 %

Pour environ 45% des directions de diffusion, les valeurs des ces descripteurs polarimétriques (α_{Cloude} et α_{TSVM}) varient à moins de 20° degrés autour de la valeur théorique que les deux paramètres associent au mécanisme de diffusion représenté par le dièdre, 90°. Même si cela montre que le dièdre est généralement un diffuseur stable, il existe également des directions d'observation pour lesquelles d'autres mécanismes de diffusion sont observés. Les résultats sont similaires avec les deux paramètres.

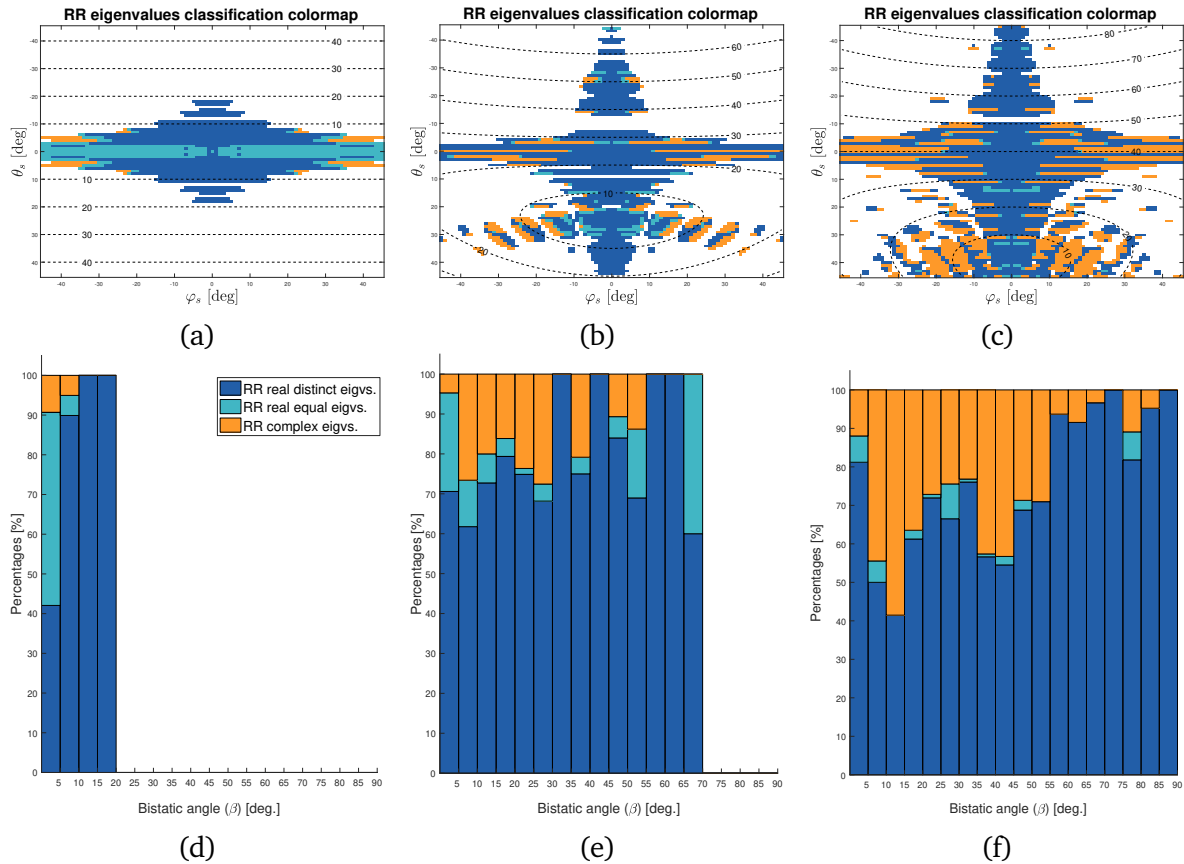


Figure I.8: Dièdre - Résultat bistatique

Directions de l'incidence : col. 1 : $\{\theta_i = 0^\circ, \varphi_i = 0^\circ\}$, col. 2 : $\{\theta_i = 25^\circ, \varphi_i = 0^\circ\}$, col. 3 : $\{\theta_i = 40^\circ, \varphi_i = 0^\circ\}$. (a)-(c) Classification des valeurs propres RRSM. (d)-(f) Classification des valeurs propres RRSM par rapport à l'angle bistatique, $\beta \in [0^\circ, 90^\circ]$.

■ Dièdre (cas bistatique)

Les résultats obtenus à partir des simulations bistatiques, pour trois angles d'incidence (et un intervalle angulaire de rétrodiffusion que dans le cas monostatique), sont illustrés dans la Figure I.8.

Le dièdre apparaît comme une cible plus stable (en comparaison avec la plaque), présentant des valeurs propres complexes dans certaines directions de diffusion, obliques par rapport à la bissectrice. Néanmoins, cette analyse n'est pas suffisante pour définir un critère d'angle bistatique imposant l'apparition de valeurs complexes.

Il convient de préciser que l'évaluation est incomplète sous certains aspects. La décomposition propre de la matrice bloc de la représentation réelle n'est appliquée que de manière cohérente, sans moyenne statistique. Ce type d'évaluation n'est donc pas approprié pour caractériser les diffuseurs distribués. En ce qui concerne l'influence des vecteurs propres, elle n'a pas été étudiée que de manière limitée et peut-être approfondie dans le cadre de travaux futurs.

Clustering géométrique avec facteurs Hermitiens

Ce chapitre propose un algorithme de traitement pour la classification non supervisée basée sur la décomposition polaire de la matrice de diffusion. Ceci est suivi d'un calcul géométrique du centroïde de la variété Riemannienne des facteurs de diffusion Hermitiens. L'analyse proposée montre des résultats comparables et même supérieurs à ceux du classificateur Wishart conventionnel, qui effectue un regroupement basé sur la covariance. Le schéma simplifié d'un algorithme de regroupement est présenté dans la Figure I.9.

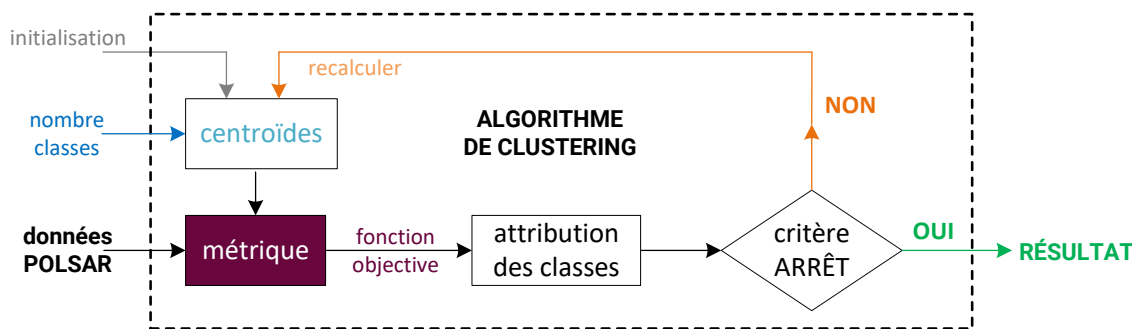


Figure I.9: Schéma générique d'un algorithme de clustering pour les données PolSAR.

Les facteurs de la décomposition polaire

La décomposition polaire est une opération de factorisation d'une matrice A comme le produit de deux facteurs : un facteur unitaire et un facteur complexe semi-défini positif (Hermitien). Il existe deux formes possibles, compte tenu de la permutation de l'emplacement des facteurs : (I.11) c'est la décomposition polaire droite et (I.12) c'est la décomposition polaire gauche.

$$A = UH \quad (\text{I.11})$$

$$A = KU, \quad (\text{I.12})$$

où $U \in \mathbb{C}^{n \times n}$ vérifiant $UU^H = U^H U = I$ est la matrice unitaire la plus proche de A (dans toute norme unitairement invariante [90, 91]). Les matrices H et K sont égales seulement si A est normale. Sans égard au choix, entre (I.11) ou (I.12), le terme Hermitien est toujours unique, tandis que le terme unitaire n'est pas encore unique si la matrice A est singulière. Les résultats expérimentaux de ce chapitre n'ont pas montré de différence importante dans l'utilisation de l'une ou l'autre des deux formes. La décomposition polaire droite de la matrice de diffusion polarimétrique S est considérée par convention dans tous les résultats qui suivent.

■ Facteur complexe défini positif :

La matrice complexe semi-définie positive H vérifie $\mathbf{u}^H H \mathbf{u} \geq 0 \forall \mathbf{u} \in \mathbb{C}^{2 \times 1}$ et a des valeurs propres réelles, non-négatives. Une telle matrice est également

Hermitienne, $\mathbf{H}^H = \mathbf{H}$. Dans le cas où la matrice de diffusion serait symétrique complexe (c'est-à-dire le cas supposé en monostatique), les valeurs propres du facteur Hermitien partagent une interprétation à plusieurs facettes : des convaleurs propres, des valeurs singulières ou des facteurs de la décomposition de Takagi.

D'un point de vue géométrique, l'espace des matrices Hermitiennes définies positives (« HPD ») prend la forme d'une variété conique ouverte. Compte tenu de la géométrie courbe de la variété, la simple utilisation de métriques Euclidiennes n'est pas optimale pour les opérations conventionnelles (distance, valeur moyenne, autres statistiques) sur la variété.

■ *Facteur unitaire :*

Les matrices unitaires sont les contreparties complexes des matrices orthogonales. De nombreuses fonctions de distance sont invariantes par rapport aux matrices unitaires, de sorte que, comme leur analogue réel, elles sont connues pour préserver les longueurs/amplitudes. Le groupe des matrices unitaires 2×2 est connu sous le nom de $U(2)$ et forme un groupe de Lie sous la multiplication des matrices. Ce dernier est un groupe algébrique qui a la structure d'un manifold lisse.

Des variétés et de la géométrie Riemannienne

Une variété (« a manifold ») \mathbb{M} est un espace topologique, similaire à un espace euclidien à chaque petit voisinage. En chaque point X de la variété, l'espace tangent $T_X \mathbb{M}$ pourra être défini (Figure I.10a).

Une métrique définie sur la variété est un choix de produit intérieur pour chaque $X \in \mathbb{M}$. Lorsqu'un tel produit intérieur varie de façon lisse d'un point à l'autre sur le manifold, on l'appelle une métrique Riemannienne. La mesure géodésique dans un espace Riemannien est imposée par cette métrique, qui suit la courbure de l'espace et représente alors la façon intrinsèque de mesurer les distances sur la variété. D'autres mesures extrinsèques peuvent être imposées, mais elles ne seront pas optimales (exemple de comparaison dans la Figure I.10a).

L'espace des matrices Hermitiennes forme un manifold Riemannien et lorsqu'il est endossé avec la métrique riemannienne invariante affine (« AIRM »), la distance minimale entre deux matrices \mathbf{A} et \mathbf{B} est :

$$d_{\mathbb{P}(n)}(\mathbf{A}, \mathbf{B}) = \|\text{Log}(\mathbf{A}^{-1/2} \mathbf{B} \mathbf{A}^{-1/2})\|_F \quad (\text{I.13})$$

et la géodésique entre ces deux est :

$$\Gamma(t) = \mathbf{A}^{1/2} \left(\mathbf{A}^{-1/2} \mathbf{B} \mathbf{A}^{-1/2} \right)^t \mathbf{A}^{1/2}, \quad t \in [0, 1], \quad \Gamma(0) = \mathbf{A} \quad \text{and} \quad \Gamma(1) = \mathbf{B}.$$

Le barycentre Riemannien est le minimiseur des distances géodésiques au carré entre un ensemble de matrices définies positives (Figure I.10b). Il n'existe pas de solution analytique quand plus de trois matrices sont impliquées, mais il a été démontré que le minimum existe et qu'il est unique quand l'estimation est réalisée par une méthode

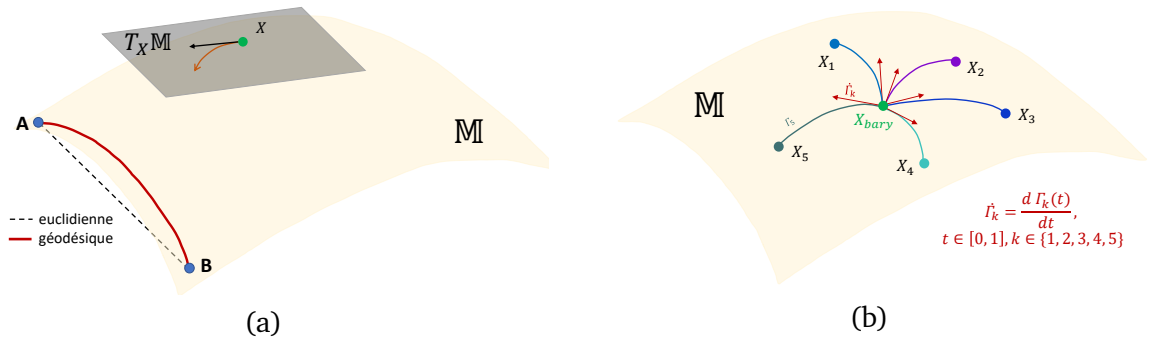


Figure I.10: Variété, espace tangent, géodésique. (a) Exemple d'une variété (M) et son espace tangent au point X ($T_X M$). (b) Géodésiques et vecteurs tangents passant par l'ensemble des points $\{X_i\}$, $1 \leq i \leq 5$ et leur barycentre.

d'optimisation [222]. La méthode de Karcher basée sur une implémentation de descente en gradient est utilisée dans cette thèse pour obtenir l'estimation du barycentre [223].

Clustering géométrique avec des facteurs Hermitiens

Il y a plus d'une décennie que des concepts liés à la variété Riemannienne des matrices Hermitiennes ont commencé à être appliqués dans PolSAR, mais en considérant exclusivement les matrices de covariance et de cohérence (aussi Hermitiennes). Les principaux domaines d'application sont liés à la classification et à la segmentation non supervisée [191, 210], la détection des changements [211, 170], la classification supervisée [212, 213] ou le filtrage du speckle [215, 216].

L'algorithme géométrique de regroupement (« clustering ») basé sur les k-means et proposé dans ce chapitre est construit sur deux aspects essentiels : 1) la décomposition polaire cohérente des données PolSAR et 2) un moyennage incohérent basé sur la géométrie Riemannienne. Ce cadre ne repose plus sur l'utilisation de matrices de covariance/cohérence. Au lieu de cela, nous exploitons directement la matrice de diffusion en appliquant la décomposition polaire. L'étude des propriétés des deux facteurs de décomposition a fait conclure que seul le facteur Hermitien constitue une entrée invariante à rotation pour la méthode de regroupement. Aucune vectorisation des données n'est effectuée (par rapport à la construction des vecteurs de diffusion) et l'algorithme est conçu pour exploiter la propriété géométrique des facteurs Hermitiens, qui sont intrinsèquement situés sur une variété Riemannienne. Plutôt que d'établir une moyenne statistique des vecteurs de diffusion (comme pour l'estimation de la matrice de covariance/cohérence), une moyenne locale (le barycentre) est calculée en utilisant la métrique géodésique de la variété. L'algorithme ne modifie pas la structure (algébrique/géométrique) des matrices de diffusion d'entrée. Aucun modèle statistique (homogène ou hétérogène) de clutter n'est supposé pour l'instant.

Des ensembles de données polarimétriques monostatiques (réelles - test qualitatif et simulées - test quantitatif) sont utilisés pour évaluer la méthode proposée. Des tests quantitatifs sur des données simulées suivant une distribution Gaussienne montrent

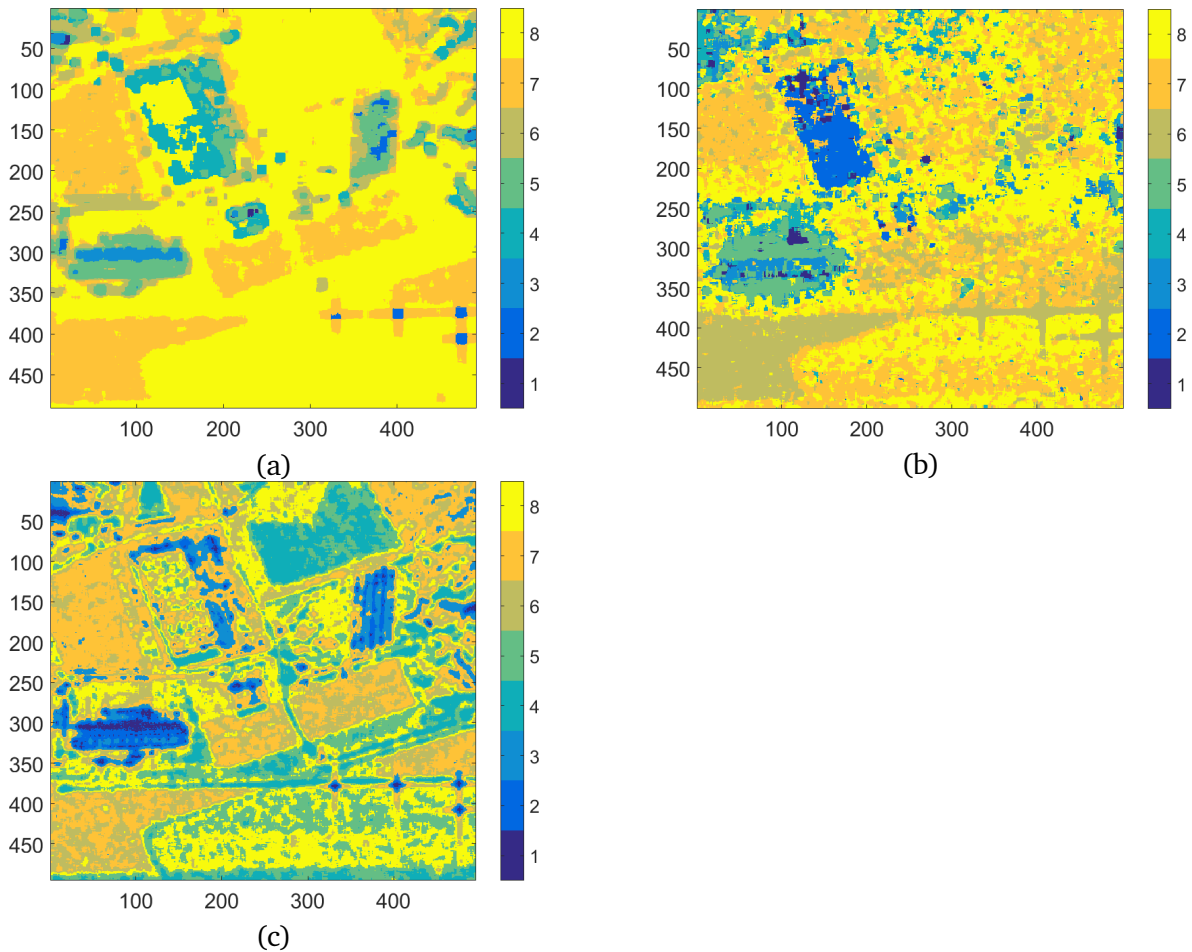


Figure I.11: Données réelles Brétigny. (a) Wishart. (b) *k*-means avec distance géodésique angulaire. (c) *k*-means avec distance géodésique Riemannienne.

des résultats comparables ou supérieurs à ceux de l'algorithme classique de Wishart.

Pour les données PolSAR réelles, la classification finale préserve mieux les informations de texture de l'image originale. Une amélioration de la séparation est observée parmi les zones voisines du faible intensité (comme observée par exemple sur certains champs de végétation avec les données Brétigny, Figure I.11).

Conclusions

Cette thèse propose des contributions sur le développement d'outils et de méthodes pour le traitement d'images radar polarimétriques (en polarisation linéaire). Le formalisme matriciel est adopté.

La géométrie du radar peut avoir sa propre influence sur la diversité polarimétrique, ce qui nous a amené à explorer les paradigmes monostatique et bistatique dans les

Chapitres 1 et 2. La diversité polarimétrique totale est généralement supposée tout au long de la thèse. Néanmoins, un court exemple à la fin du Chapitre 1 explore des résultats en double polarisation avec une scène test imagée simultanément par des capteurs radar monostatiques et bistatiques à double polarimétrie. Les différences d'interprétation des paramètres $H - \alpha$ entre la polarimétrie double et la polarimétrie complète sont étudiées et enfin, les résultats monostatiques et bistatiques en polarimétrie double sont comparés.

Dans les autres parties de la thèse, le modèle polarimétrique complet est utilisé, les données sont « single look complex » avec chaque pixel décrit par une matrice de diffusion, S . Cette méthode est généralement utilisée pour les diffuseurs déterministes, tandis que le formalisme vectoriel et la covariance s'appliquent aux calculs impliquant des diffuseurs distribués. La méthode proposée dans le Chapitre 2 s'applique à un modèle de cible cohérent et celle présentée dans le Chapitre 3 concerne surtout la classification des données PolSAR réelles, où les diffuseurs incohérents dominent.

■ Chapitre 2:

- *Méthode de détection des valeurs propres conjuguées complexes, basée sur la représentation réelle*

Ce chapitre commence par une discussion mathématique détaillée sur la transformation de similarité conjuguée : pourquoi elle apparaît dans PolSAR avec la convention BSA et quelles sont les méthodes connues pour effectuer la factorisation. Après avoir présenté la représentation réelle, nous expliquons comment elle peut être utilisée dans le cadre de la similarité conjuguée pour les matrices de diffusion réciproques et non réciproques. Les matrices réciproques ont une factorisation unique, cas dans lequel les expériences de ce chapitre démontrent que ces facteurs sont généralement les mêmes que ceux obtenus par une décomposition sur la matrice puissance $S^H S$. Pour les matrices non-réciproques, la factorisation peut fournir des solutions dans le plan complexe et au moins, un des facteurs peut ne pas être unique.

- *Analyse de données polarimétriques réelles (monostatiques) et simulées (monostatiques et bistatiques) à l'aide d'une détection avec la représentation réelle*

Dans la deuxième partie du chapitre, des simulations polarimétriques obtenues à l'aide d'un logiciel de calcul électromagnétique ont été présentées. Elles sont générées pour deux cibles cohérentes (plaque métallique carrée et dièdre à angle droit) dans des géométries monostatiques et bistatiques et à partir d'une large échelle d'angles d'observation. La méthode de détection utilisant la décomposition propre de la représentation réelle a été appliquée aux ensembles de données polarimétriques simulées, ainsi qu'aux données PolSAR monostatiques réelles. Les résultats ont montré que les valeurs propres de la similarité conjuguée peuvent être complexes dans tous les cas. Elles apparaissent avec une très faible probabilité (en dessous de 5%) pour toutes les données monostatiques testées. Le pourcentage est plus élevé dans le cas d'observations bistatiques.

■ Chapitre 3:

- *Analyse des facteurs de la décomposition polaire*
 Dans la première partie du chapitre, les propriétés algébriques et géométriques des deux facteurs obtenus par la décomposition polaire sont examinées en détail. Le facteur Hermitien, H , peut être assimilé à un résultat compensé en phase et en rotation de la matrice de diffusion originale.
- *Clustering géométrique de données à l'aide des facteurs Hermitiens*
 L'intégration des facteurs polaires Hermitiennes dans la variété des matrices à définition positive est l'idée principale qui sous-tend la méthode de regroupement géométrique proposée. En première étape, qui fait partie du pré-traitement, les facteurs Hermitiens provenant de voisinages spatiaux ont été utilisés pour calculer un centre de masse géométrique. Cette opération peut être mise en parallèle avec l'estimation de la matrice de covariance dans le voisinage. La deuxième étape est implémentée sur la base d'un algorithme par partitionnement k-means et d'une distance géodésique sur la variété HPD Riemannienne, utilisée pour la comparaison intra/inter-cluster.
 La performance de la méthode proposée a été testée sur des données monostatiques PolSAR réelles et simulées. Des résultats quantitatifs et qualitatifs améliorés ont été obtenus par rapport à la méthode de Wishart non supervisée. Avec des données polarimétriques réelles, on observe que le résultat final du regroupement préserve mieux les détails de la texture.

Perspectives

Des extensions, ainsi que des améliorations potentielles, sur chacun des deux principaux axes d'étude de cette thèse sont discutées dans cette section.

- L'étude utilisant des données simulées et la représentation réelle n'a pas permis d'identifier un lien entre les descripteurs de la géométrie bistatique (par exemple, l'angle bistatique) et les valeurs propres complexes de la similarité conjuguée. Cela peut suggérer que, s'il existe, le lien est multivarié, et qu'il est nécessaire d'améliorer les modèles et les tests.
- Une extension immédiate du travail effectué au Chapitre 2 consiste à considérer les vecteurs propres de la similarité conjuguée. Pour découvrir leurs propriétés, on pourrait suggérer d'identifier des paramètres descriptifs avec lesquels proposer un modèle vectoriel.
 Pour l'instant, le modèle de factorisation de la similarité conjuguée est limité aux applications cohérentes. L'introduction d'un modèle vecteur permettrait son extension par une technique de décomposition incohérente basée sur la covariance. Par ailleurs, des modèles d'apprentissage automatique pourraient être utilisés en s'appuyant sur des paramètres de la consimilarité ou de la représentation réelle.

Pour le deuxième axe de la thèse, les améliorations suivantes sont identifiées :

- La médiane algébrique est connue pour être une estimation plus robuste aux valeurs aberrantes. Tout en conservant les idées fondamentales de la méthode de regroupement géométrique, une version différente peut modifier le processus d'estimation de la moyenne Riemannienne en estimation de la médiane Riemannienne [221].
- D'autre manière, la métrique AIRM peut être modifiée et comparée à d'autres métriques, toujours adaptées à la variété HPD [235]. Une initialisation déterministe de l'algorithme de regroupement k-means, idéalement par une méthode reflétant les caractéristiques de rétrodiffusion PolSAR, serait aussi envisagée. De plus, d'autres types d'algorithmes de regroupement peuvent être proposés.
Encore, on peut étudier le rôle joué par la dimension de la variété Riemannienne en utilisant la covariance ou le facteur de la décomposition polaire de la représentation réelle (les deux étant des matrices Hermitiennes).

Bibliography

- [1] X. Deng, C. Lopez-Martinez, J. Chen, and P. Han, “Statistical Modeling of Polarimetric SAR Data: A Survey and Challenges,” *Remote Sensing*, vol. 9, no. 4, 2017 (cit. on pp. 2, 32).
- [2] “IEEE Standard for Definitions of Terms for Antennas,” *IEEE Std 145-2013 (Revision of IEEE Std 145-1993)*, pp. 1–50, 2014 (cit. on pp. 6–8, 18, 70, 151).
- [3] “IEEE Standard Definitions of Terms for Antennas,” *IEEE Std 145-1983*, pp. 1–31, 1983 (cit. on pp. 7, 151).
- [4] J.-S. Lee and E. Pottier, *Polarimetric Radar Imaging: From Basics to Applications*. CRC Press - Taylor and Francis Group, 2009 (cit. on pp. 7, 18, 20, 25, 71, 89, 106, 152, 153).
- [5] R. M. A. Azzam, “Three-Dimensional Polarization States of Monochromatic Light Fields,” *J. Opt. Soc. Am. A*, vol. 28, no. 11, pp. 2279–2283, 2011 (cit. on p. 8).
- [6] P. Réfrégier, J. Tervo, and A. Roueff, “A temporal-coherence anisotropy of unpolarized light,” *Optics Communications*, vol. 282, no. 6, pp. 1069–1073, 2009 (cit. on p. 8).
- [7] H. Mott, *Polarization in Antennas and Radar*. John Wiley and Sons, Inc., 1986 (cit. on p. 8).
- [8] M. John, “The Polarisation Ellipse and Associated Properties,” *The Mathematical Gazette*, vol. 94, no. 529, pp. 94–102, 2010 (cit. on p. 9).
- [9] I. Hajnsek and Y.-L. Desnos, *Polarimetric Synthetic Aperture Radar - Principles and Application*. Springer Cham, Open Access Book, 2020 (cit. on pp. 9, 10, 20, 31).
- [10] L. Zhang, G. Gao, C. Chen, S. Gao, and L. Yao, “Compact Polarimetric Synthetic Aperture Radar for Target Detection: A Review,” *IEEE Geoscience and Remote Sensing Magazine*, pp. 2–39, 2022 (cit. on p. 10).
- [11] A. Moreira, P. Prats-Iraola, M. Younis, G. Krieger, I. Hajnsek, *et al.*, “A Tutorial on Synthetic Aperture Radar,” *IEEE Geoscience and Remote Sensing Magazine*, vol. 1, no. 1, pp. 6–43, 2013 (cit. on pp. 11, 12).
- [12] D. Munson and R. Visentin, “A Signal Processing View of Strip-Mapping Synthetic Aperture Radar,” *IEEE Transactions on Acoustics, Speech, and Signal Processing*, vol. 37, no. 12, pp. 2131–2147, 1989 (cit. on pp. 11, 12).
- [13] B. J. Döring and M. Schwerdt, “The Radiometric Measurement Quantity for SAR Images,” *IEEE Transactions on Geoscience and Remote Sensing*, vol. 51, no. 12, pp. 5307–5314, 2013 (cit. on pp. 12, 71).
- [14] N. Willis and H. Griffiths, *Advances in Bistatic Radar*. SciTech Publishing, NC, 2007 (cit. on p. 13).
- [15] M. D’Errico, *Distributed Space Missions for Earth System Monitoring*. Springer Science+Business Media, New York, 2013 (cit. on p. 13).
- [16] P. Xiao, B. Liu, and W. Guo, “ConGaLSAR: A Constellation of Geostationary and Low Earth Orbit Synthetic Aperture Radar,” *IEEE Geoscience and Remote Sensing Letters*, vol. 17, no. 12, pp. 2085–2089, 2020 (cit. on p. 14).

- [17] M. Rodriguez-Cassola, P. Prats, U. Steinbrecher, R. Horn, A. Nottensteiner, *et al.*, “Bistatic SAR Experiments with the TanDEM-X Constellation,” in *Proc. IEEE Int. Geosci. Remote Sens. Symp. (IGARSS)*, 2012, pp. 1920–1923 (cit. on p. 15).
- [18] A. Reigber, R. Horn, A. Nottensteiner, P. Prats, R. Scheiber, *et al.*, “Current Status of DLR’s New F-SAR Sensor,” in *8th European Conference on Synthetic Aperture Radar*, 2010, pp. 1–4 (cit. on p. 15).
- [19] H. Nies, F. Behner, S. Reuter, O. Loffeld, and R. Wang, “Polarimetric and Interferometric Applications in a Bistatic Hybrid SAR Mode using TerraSAR-X,” in *Proc. IEEE Int. Geosci. Remote Sens. Symp. (IGARSS)*, 2010, pp. 110–113 (cit. on p. 15).
- [20] H. Nies, F. Behner, S. Reuter, O. Loffeld, and R. Wang, “SAR Experiments in a Bistatic Hybrid Configuration for Generating PolInSAR Data with TerraSAR-X Illumination,” in *8th European Conference on Synthetic Aperture Radar*, 2010, pp. 1–4 (cit. on p. 15).
- [21] I. Pisciotano, D. Cristallini, D. Pastina, and F. Santi, “Experimental Results of Polarimetric Passive ISAR Exploiting DVB-S2 Illumination,” in *IEEE International Radar Conference*, 2020, pp. 518–523 (cit. on p. 15).
- [22] A. S. Goh, M. Preiss, N. J. S. Stacy, and D. A. Gray, “The Ingara Bistatic SAR Upgrade: First Results,” in *International Conference on Radar*, 2008, pp. 329–334 (cit. on p. 15).
- [23] M. Preiss, A. S. Goh, and P. Pincus, “First Results from the Ingara L-Band SAR,” in *Proc. International Conference on Radar*, 2018, pp. 1–5 (cit. on p. 15).
- [24] O. A. Krasnov, Z. Wang, F. Van der Zwan, and A. Yarovoy, “A new Bistatic Radar System: PARSAX + TARA,” in *8th European Radar Conference*, 2011, pp. 146–149 (cit. on p. 15).
- [25] A. Orban, D. Defrere, and C. Barbier, “BelSAR : The First Belgian Airborne Campaign for L-band, Full-polarimetric Bistatic and Interferometric SAR Acquisitions over an Agricultural Site in Belgium,” in *13th European Conference on Synthetic Aperture Radar*, 2021, pp. 1–4 (cit. on p. 15).
- [26] K. A. De Macedo, G. Masalias, A. Coccia, and A. Meta, “Recent L-C- and X-band MetaSensing airborne sar campaigns for emerging applications,” in *17th European Radar Conference*, 2021, pp. 190–193 (cit. on p. 15).
- [27] J. Bouchat, E. Tronquo, H. Lievens, N. Verhoest, and P. Defourny, “Assessing the potential of fully-polarimetric simultaneous mono- and bistatic airborne sar acquisitions in l-band for applications in agriculture and hydrology,” in *2021 IEEE International Geoscience and Remote Sensing Symposium IGARSS*, 2021, pp. 2703–2706 (cit. on p. 15).
- [28] G. Krieger, A. Moreira, H. Fiedler, I. Hajnsek, M. Werner, *et al.*, “TanDEM-X: A Satellite Formation for High-Resolution SAR Interferometry,” *IEEE Transactions on Geoscience and Remote Sensing*, vol. 45, no. 11, pp. 3317–3341, 2007 (cit. on p. 15).
- [29] C. Li, H. Zhang, Y. Deng, R. Wang, K. Liu, *et al.*, “Focusing the L-Band Spaceborne Bistatic SAR Mission Data Using a Modified RD Algorithm,” *IEEE Transactions on Geoscience and Remote Sensing*, vol. 58, no. 1, pp. 294–306, 2020 (cit. on p. 15).
- [30] T. Li, X. Tang, X. Zhou, X. Zhang, S. Li, *et al.*, “Deformation Products Of Lutan-1(Lt-1) SAR Satellite Constellation for Geohazard Monitoring,” in *Proc. IEEE Int. Geosci. Remote Sens. Symp. (IGARSS 2022)*, 2022, pp. 7543–7546 (cit. on p. 15).

- [31] Y. Cai, R. Wang, W. Yu, D. Liang, K. Liu, *et al.*, “An Advanced Approach to Improve Synchronization Phase Accuracy with Compressive Sensing for LT-1 Bistatic Spaceborne SAR,” *Remote Sensing*, vol. 14, no. 18, 2022 (cit. on pp. 15, 16).
- [32] A. Liu, F. Wang, H. Xu, and L. Li, “N-SAR: A New Multichannel Multimode Polarimetric Airborne SAR,” *IEEE Journal of Selected Topics in Applied Earth Observations and Remote Sensing*, vol. 11, no. 9, pp. 3155–3166, 2018 (cit. on p. 15).
- [33] A. Liu, C. Zhou, H. Xu, X. Xia, and H. Zhao, “N-SAR-SG: The Second Generation Airborne SAR System in N-SAR Series with Multi-Band Capability,” in *Proc. IEEE Int. Geosci. Remote Sens. Symp. (IGARSS 2022)*, 2022, pp. 7464–7467 (cit. on p. 15).
- [34] S. Wang, W. Feng, K. Kikuta, G. Chernyak, and M. Sato, “Ground-Based Bistatic Polarimetric Interferometric Synthetic Aperture Radar System,” in *Proc. IEEE Int. Geosci. Remote Sens. Symp. (IGARSS)*, 2019, pp. 8558–8561 (cit. on p. 15).
- [35] M. Stefko, O. Frey, C. Werner, and I. Hajnsek, “KAPRI: A Bistatic Full-Polarimetric Interferometric Real-Aperture Radar System for Monitoring of Natural Environments,” in *Proc. IEEE Int. Geosci. Remote Sens. Symp. (IGARSS)*, 2021, pp. 1950–1953 (cit. on p. 15).
- [36] M. Stefko, O. Frey, and I. Hajnsek, “Snow Characterization at Ku-Band with a Bistatic Polarimetric Ground-Based Radar,” in *Proc. IEEE Int. Geosci. Remote Sens. Symp. (IGARSS 2022)*, 2022, pp. 4256–4259 (cit. on p. 15).
- [37] M. Stefko, S. Leinss, O. Frey, and I. Hajnsek, “Coherent Backscatter Enhancement in Bistatic Ku-/X-Band Radar Observations of Dry Snow,” *The Cryosphere Discussions [preprint]*, vol. 2021, pp. 1–32, 2021 (cit. on p. 15).
- [38] J.-L. Bueso-Bello, M. Martone, P. Prats-Iraola, C. González-Chamorro, T. Kraus, *et al.*, “Performance Analysis of TanDEM-X Quad-Polarization Products in Pursuit Monostatic Mode,” *IEEE Journal of Selected Topics in Applied Earth Observations and Remote Sensing*, vol. 10, no. 5, pp. 1853–1869, 2017 (cit. on p. 16).
- [39] J. Shi, D. Lü, Y. Wang, Y. Du, Y. Pang, *et al.*, “Recent Progress of Earth Science Satellite Missions in China,” *Chinese Journal of Space Science*, vol. 42, no. 4, pp. 712–723, 2022 (cit. on p. 16).
- [40] P. López-Dekker, H. Rott, P. Prats-Iraola, B. Chapron, K. Scipal, *et al.*, “Harmony: an Earth Explorer 10 Mission Candidate to Observe Land, Ice, and Ocean Surface Dynamics,” in *Proc. IEEE Int. Geosci. Remote Sens. Symp. (IGARSS)*, 2019, pp. 8381–8384 (cit. on pp. 16, 35).
- [41] J. Lopez Dekker, J. Biggs, B. Chapron, A. Hooper, A. Käab, *et al.*, “The Harmony Mission: Applications and Preliminary Performance,” in *6th Workshop on Advanced RF Sensors and Remote Sensing Instruments*, 2019 (cit. on p. 16).
- [42] S. Huber, F. Q. de Almeida, M. Villano, M. Younis, G. Krieger, *et al.*, “Tandem-L: A Technical Perspective on Future Spaceborne SAR Sensors for Earth Observation,” *IEEE Transactions on Geoscience and Remote Sensing*, vol. 56, no. 8, pp. 4792–4807, 2018 (cit. on p. 16).
- [43] M. Bartusch, A. E. N. Quiroz, S. Stettner, A. Moreira, and M. Zink, “German X-Band Spaceborne SAR Heritage and the Future HRWS Mission,” in *Proc. IEEE Int. Geosci. Remote Sens. Symp. (IGARSS 2021)*, 2021, pp. 804–807 (cit. on p. 16).

- [44] M. Bartusch, C. Bruens, A. E. Nuncio Quiroz, and S. Stettner, "HRWS: The upcoming German X-Band Spaceborne SAR Mission," in *EUSAR 2021; 13th European Conference on Synthetic Aperture Radar*, 2021, pp. 1–4 (cit. on p. 16).
- [45] J. Mittermayer, G. Krieger, A. Bojarski, M. Zonno, M. Villano, *et al.*, "MirrorSAR: An HRWS Add-On for Single-Pass Multi-Baseline SAR Interferometry," *IEEE Transactions on Geoscience and Remote Sensing*, vol. 60, pp. 1–18, 2022 (cit. on p. 16).
- [46] A.-L. Germond, "Theorie de la Polarimetrie Radar Bistatique," Ph.D. dissertation, Nantes University, 1999 (cit. on pp. 17, 151).
- [47] A. Marino, S. R. Cloude, and I. H. Woodhouse, "Detecting Depolarized Targets Using a New Geometrical Perturbation Filter," *IEEE Transactions on Geoscience and Remote Sensing*, vol. 50, no. 10, pp. 3787–3799, 2012 (cit. on pp. 17, 151).
- [48] N. Trouvé, "Comparaison des Outils Optique et Radar en Polarimétrie Bistatique," Ph.D. dissertation, 2011 (cit. on pp. 17, 20, 61, 65, 151, 152).
- [49] T Dallmann and D Heberling, "On the Connection Between Jones Matrix and Sinclair Matrix," in *PIERS Proceedings*, 2015, pp. 258–262 (cit. on p. 19).
- [50] R. Touzi, "Target Scattering Decomposition in Terms of Roll-Invariant Target Parameters," *IEEE Transactions on Geoscience and Remote Sensing*, vol. 45, no. 1, pp. 73–84, 2007 (cit. on pp. 19, 22, 30, 75, 161).
- [51] L. Liu, M. Xing, and Z. Bao, "Experimental Reaserch of Unsupervised Cameron/ML Classification Method for Fully Polarimetric SAR Data," in *1st Asian and Pacific Conference on Synthetic Aperture Radar*, 2007, pp. 797–800 (cit. on p. 19).
- [52] L. Li, Y. Zhang, Z. Dong, and D. Liang, "New Faraday Rotation Estimators Based on Polarimetric Covariance Matrix," *IEEE Geoscience and Remote Sensing Letters*, vol. 11, no. 1, pp. 133–137, 2014 (cit. on p. 19).
- [53] S. Yueh, S. Nghiem, and R. Kwok, "Symmetrization of Cross-Polarized Responses in Polarimetric Radar Images using Reciprocity," *IEEE Transactions on Geoscience and Remote Sensing*, vol. 31, no. 6, pp. 1180–1185, 1993 (cit. on p. 19).
- [54] E. Rignot, "Effect of Faraday Rotation on L-band Interferometric and Polarimetric Synthetic-Aperture Radar Data," *IEEE Transactions on Geoscience and Remote Sensing*, vol. 38, no. 1, pp. 383–390, 2000 (cit. on p. 19).
- [55] J. C. Hubbert, "A Comparison of Radar, Optic, and Specular Null Polarization Theories," *IEEE Transactions on Geoscience and Remote Sensing*, vol. 32, no. 3, pp. 658–671, 1994 (cit. on pp. 20, 22, 152).
- [56] E. Lüneburg, S. Cloude, and W.-M. Boerner, "On the Pproper Polarimetric Scattering Matrix Formulation of the Forward Propagation versus Backscattering Radar Systems Description," in *Proc. IEEE Int. Geosci. Remote Sens. Symp. (IGARSS 1997)*, vol. 4, 1997, 1591–1593 vol.4 (cit. on pp. 20, 152).
- [57] W.-M. Boerner, C. Liu, and X. Zhang, "Comparison of Optimization Procedures for 2x2 Sinclair, 2x2 Graves, 3x3 Covariance, and 4x4 Mueller (Symmetric) Matrices in Coherent Radar Polarimetry and its Application to Target Versus Background Discrimination in

- Microwave Remote Sensing and Imaging,” *EARSeL Advances in Remote Sensing*, vol. 2, no. 1, pp. 55–82, 1993 (cit. on p. 21).
- [58] A. Kostinski and W. Boerner, “On Foundations of Radar Polarimetry,” *IEEE Transactions on Antennas and Propagation*, vol. 34, no. 12, pp. 1395–1404, 1986 (cit. on pp. 21, 22).
- [59] W.-M. Boerner and J. J. Morisaki, “Critical Assessment of the Historical Development of Radar Polarization Technology Towards Radar Polarimetry Culminating in Fully Polarimetric-Interferometric SAR,” in *Proc. IEEE Int. Geosci. Remote Sens. Symp. (IGARSS 2012)*, 2012, pp. 119–122 (cit. on p. 21).
- [60] R. A. Horn and C. R. Johnson, *Matrix Analysis – Second Edition*. Cambridge University Press, 2013 (cit. on pp. 21, 47, 54, 129, 158, 159).
- [61] Y. Hong and R. A. Horn, “A Characterization of Unitary Congruence,” *Linear and Multilinear Algebra*, vol. 25, no. 2, pp. 105–119, 1989 (cit. on p. 21).
- [62] E. Lüneburg, J. Morisaki, and W.-M. Boerner, “On the Forward Scatter Alignment and the Backscatter Alignment Conventions of Bistatic Radar Polarimetry,” in *Proceedings of ISAP*, vol. 1, 2004, pp. 1273–1276 (cit. on p. 21).
- [63] K. D. Ikramov, “A Note on Complex Matrices that are Unitarily Congruent to Real Matrices,” *Linear Algebra and its Applications*, vol. 433, no. 4, pp. 838–842, 2010 (cit. on p. 21).
- [64] C. Graves, “Radar Polarization Power Scattering Matrix,” *Proceedings of the IRE*, vol. 44, no. 2, pp. 248–252, 1956 (cit. on pp. 21–23, 153).
- [65] W. T. Payne, “Analysis of the Polarization Scattering Matrix,” MITRE Corporation - Bedford - Massachusetts - Defence Advanced Research Projects Agency (DARPA) - United States Air Force, Technical Report - Project 8051, 1968 (cit. on p. 22).
- [66] J. R. Huynen, “Phenomenological Theory of Radar Targets,” Ph.D. dissertation, 1970 (cit. on pp. 22, 27, 106, 153).
- [67] Y. Li and Y.-Q. Jin, “Imaging and Structural Feature Decomposition of a Complex Target using Multi-aspect Polarimetric Scattering,” *Science China Information Sciences*, vol. 59, no. 8, pp. 1869–1919, 2016 (cit. on p. 22).
- [68] S. Ling and T. Jiang, “New Method for General Kennan’s Pseudoeigenvalue Equation in Radar Polarimetry,” *Front. Math. China*, vol. 7, no. 1, pp. 85–95, 2012 (cit. on pp. 22, 23, 48, 55, 153).
- [69] E. Lüneburg and S. R. Cloude, “Radar versus optical polarimetry,” in *Wideband Interferometric Sensing and Imaging Polarimetry*, International Society for Optics and Photonics, vol. 3120, 1997, pp. 361–372 (cit. on p. 22).
- [70] D. Bebbington and L. Carrea, “On Mathematical and Physical Principles of Transformations of the Coherent Radar Backscatter Matrix,” *IEEE Transactions on Geoscience and Remote Sensing*, vol. 50, no. 11, pp. 4657–4669, 2012 (cit. on p. 22).
- [71] H. E. Haber, “A Tale of Three Diagonalizations,” *International Journal of Modern Physics A*, vol. 36, no. 04, 2021 (cit. on pp. 23, 153).
- [72] X. Wang, M. Che, and Y. Wei, “Complex-Valued Neural Networks for the Takagi Vector of Complex Symmetric Matrices,” *Neurocomputing*, vol. 223, 2017 (cit. on p. 23).

- [73] E. Lüneburg and W.-M. Boerner, "Homogeneous and Inhomogeneous Sinclair and Jones Matrices," in *Wideband Interferometric Sensing and Imaging Polarimetry*, International Society for Optics and Photonics, vol. 3120, 1997, pp. 45–54 (cit. on pp. 23, 49, 50, 153).
- [74] A. Bunse-Gerstner and W. B. Gragg, "Singular Value Decompositions of Complex Symmetric Matrices," *Journal of Computational and Applied Mathematics*, vol. 21, no. 1, pp. 41–54, 1988 (cit. on p. 23).
- [75] E. Lüneburg and S. R. Cloude, "Bistatic Scattering," in *Wideband Interferometric Sensing and Imaging Polarimetry*, H. Mott and W.-M. Boerner, Eds., International Society for Optics and Photonics, vol. 3120, SPIE, 1997, pp. 56–68 (cit. on pp. 25, 28, 47, 57).
- [76] S. Cloude, *Polarisation: Applications in Remote Sensing*. Oxford University Press, 2009 (cit. on pp. 25, 33, 34, 36, 75, 106, 153, 155, 156, 161).
- [77] S. Cloude, "Polarimetry - The Characterization of Polarization Effects in EM Scattering," Ph.D. dissertation, Birmingham University, 1986 (cit. on pp. 26, 29, 155).
- [78] E. Krogager, W.-M. Boerner, and S. N. Madsen, "Feature-Motivated Sinclair Matrix (Sphere/Diplane/Helix) Decomposition and its Application to Target Sorting for Land Feature Classification," in *SPIE Proceedings [SPIE Optical Science, Engineering and Instrumentation - San Diego]*, 1997, 144–154 (cit. on p. 26).
- [79] W. Cameron and L. Leung, "Feature Motivated Polarization Scattering Matrix Decomposition," in *IEEE International Conference on Radar*, 1990, pp. 549–557 (cit. on pp. 26, 29, 61, 62).
- [80] W. L. Cameron and H. Rais, "Derivation of a Signed Cameron Decomposition Asymmetry Parameter and Relationship of Cameron to Huynen Decomposition Parameters," *IEEE Transactions on Geoscience and Remote Sensing*, vol. 49, no. 5, pp. 1677–1688, 2011 (cit. on p. 26).
- [81] H. Zhang, H. Li, C. Wang, and J. Chen, "The Equivalence Analysis for SDH Decomposition and Cameron Decomposition Based on a Unified Three-Component Scattering Model," in *2010 International Conference on Multimedia Technology*, 2010, pp. 1–4 (cit. on p. 26).
- [82] H. Li, C. Wang, H. Zhang, and L. Liu, "A Unified Three Component Scattering Model for Polarimetric Coherent Target Decomposition," *International Journal of Remote Sensing*, vol. 33, no. 9, 2868–2891, 2012 (cit. on p. 26).
- [83] T. Dallmann and D. Heberling, "On the Coneigenvalue Decomposition of Sinclair Matrices," in *PIERS Proceedings*, 2015, pp. 2714–2718 (cit. on p. 27).
- [84] L. Liang, Y. Zhang, and D. Li, "Fast Huynen–Euler Decomposition and its Application in Disaster Monitoring," *IEEE Journal of Selected Topics in Applied Earth Observations and Remote Sensing*, vol. 14, pp. 4231–4243, 2021 (cit. on p. 27).
- [85] Y. Dong and D. J. Crisp, "The Euler Decomposition and its Application to Sea Clutter Analysis," in *2008 International Conference on Radar*, 2008, pp. 133–138 (cit. on p. 27).
- [86] L. Bombrun, "Extension of the Target Scattering Vector Model to the Bistatic Case," in *Proc. IEEE Int. Geosci. Remote Sens. Symp. (IGARSS 2010)*, 2010, pp. 4047–4050 (cit. on pp. 27, 30, 61, 62).

- [87] T. Dallmann and D. Heberling, "Technique for Huynen-Euler Decomposition," *Electronics Letters*, vol. 53, no. 13, pp. 877–879, 2017 (cit. on p. 28).
- [88] C. Titin-Schnaider, "Extension of the Huynen Theory to Bistatic Coherent Mechanisms," in *Proc. 3rd Int. Workshop Sci. Appl. SAR Polarimetry Polarimetric Interferometry (PolInSAR)*, 2007, pp. 1–8 (cit. on p. 28).
- [89] C. Titin-Schnaider, "Characterization and Recognition of Bistatic Polarimetric Mechanisms," *IEEE Transactions on Geoscience and Remote Sensing*, vol. 51, no. 3, pp. 1755–1774, 2013 (cit. on pp. 28–30).
- [90] P. Neff, Y. Nakatsukasa, and A. Fischle, "A Logarithmic Minimization Property of the Unitary Polar Factor in the Spectral and Frobenius Norms," *SIAM Journal on Matrix Analysis and Applications*, vol. 35, no. 3, pp. 1132–1154, 2014. eprint: <https://doi.org/10.1137/130909949> (cit. on pp. 28, 163).
- [91] J. Lankeit, P. Neff, and Y. Nakatsukasa, "The Minimization of Matrix Logarithms: On a Fundamental Property of the Unitary Polar Factor," *Linear Algebra and its Applications*, vol. 449, pp. 28–42, 2014 (cit. on pp. 28, 143, 163).
- [92] A. M. Chebotarev and A. E. Teretenkov, "Singular Value Decomposition for the Takagi Factorization of Symmetric Matrices," *Applied Mathematics and Computation*, vol. 234, pp. 380–384, 2014 (cit. on p. 29).
- [93] R. Barakat, "Optical Matrix–Matrix Multiplier Based on Kronecker Product Decomposition," *Appl. Opt.*, vol. 26, no. 2, pp. 191–192, 1987 (cit. on p. 30).
- [94] S. Cloude and E. Pottier, "An Entropy Based Classification Scheme for Land Applications of Polarimetric SAR," *IEEE Transactions on Geoscience and Remote Sensing*, vol. 35, no. 1, pp. 68–78, 1997 (cit. on pp. 30, 33, 34).
- [95] R. Paladini, L. Ferro Famil, E. Pottier, M. Martorella, F. Berizzi, *et al.*, "Point Target Classification via Fast Lossless and Sufficient Ω – Ψ – Φ Invariant Decomposition of High-Resolution and Fully Polarimetric SAR/ISAR Data," *Proceedings of the IEEE*, vol. 101, no. 3, pp. 798–830, 2013 (cit. on pp. 30, 32).
- [96] K. Ji and Y. Wu, "Scattering Mechanism Extraction by a Modified Cloude-Pottier Decomposition for Dual Polarization SAR," *Remote Sensing*, vol. 7, no. 6, pp. 7447–7470, 2015 (cit. on pp. 30, 35, 36).
- [97] T. Ullmann, A. Schmitt, and T. Jagdhuber, "Two component decomposition of dual polarimetric hh-vv sar data: Case study for the tundra environment of the mackenzie delta region," *Remote Sensing*, vol. 8, no. 12, 2016 (cit. on p. 30).
- [98] L. Pralon, "Scene Analysis and Interpretation by ICA Based Polarimetric Incoherent Target Decomposition for Polarimetric SAR Data," Ph.D. dissertation, 2016 (cit. on pp. 31, 32, 34, 155).
- [99] B. Picinbono, "Second-Order Complex Random Vectors and Normal Distributions," *IEEE Transactions on Signal Processing*, vol. 44, no. 10, pp. 2637–2640, 1996 (cit. on p. 31).
- [100] G. Vasile, J.-P. Ovarlez, F. Pascal, and C. Tison, "Coherency Matrix Estimation of Heterogeneous Clutter in High-Resolution Polarimetric SAR Images," *IEEE Transactions on Geoscience and Remote Sensing*, vol. 48, no. 4, pp. 1809–1826, 2010 (cit. on pp. 32, 89, 140).

- [101] N. Basic, "Very High-resolution Polarimetric SAR Image Characterization Through Blind Sources Separation Techniques," Ph.D. dissertation, 2014 (cit. on p. 32).
- [102] T. L. Ainsworth, M. Preiss, N. Stacy, M. Nord, and J.-S. Lee, "Analysis of Compact Polarimetric SAR Imaging Modes," in *POLInSAR Workshop Proceedings*, 2007 (cit. on pp. 34, 35, 156).
- [103] M. Nord, T. Ainsworth, J.-S. Lee, and N. Stacy, "Comparison of Compact Polarimetric Synthetic Aperture Radar Modes," *IEEE Transactions on Geoscience and Remote Sensing*, vol. 47, no. 1, pp. 174–188, 2009 (cit. on pp. 34, 76).
- [104] S. Azadnezhad, Y. Maghsoudi, and D. Perissin, "Evaluation of Polarimetric Capabilities of Dual Polarized Sentinel-1 and TerraSAR-X Data to Improve the PSInSAR Algorithm using Amplitude Dispersion Index Optimization," *International Journal of Applied Earth Observation and Geoinformation*, vol. 84, 2020 (cit. on p. 34).
- [105] S. R. Cloude, "The Dual Polarization Entropy/Alpha Decomposition: A PALSAR Case Study," 2007 (cit. on pp. 35, 156).
- [106] T. Long, L. Zhang, Y. Li, and Y. Wang, "Geometrical Structure Classification of Target HRRP Scattering Centers Based on Dual Polarimetric H- α Features," *IEEE Access*, vol. 7, pp. 141 679–141 688, 2019 (cit. on p. 35).
- [107] J.-L. Bueso-Bello, P. Prats-Iraola, M. Martone, J. Reimann, U. Steinbrecher, *et al.*, "Performance Evaluation of TanDEM-X Quad-Polarization Products in Bistatic Mode," *IEEE Journal of Selected Topics in Applied Earth Observations and Remote Sensing*, vol. 11, no. 3, pp. 787–799, 2018 (cit. on p. 35).
- [108] M. Yahia, F. Khalfa, M. Chabir, and T. Aguilu, "Bias Compensation in H/A/alpha Polarimetric SAR Decomposition and its Implication for the Classification," *Progress In Electromagnetics Research B*, vol. 68, 105–121, 2016 (cit. on pp. 36, 127).
- [109] L. Xie, H. Zhanga, C. Wanga, and Z. Shana, "Similarity Analysis of Entropy/Alpha Decomposition between HH/VV Dual and Quad-polarization SAR data," *Remote Sensing Letters*, vol. 6, no. 3, pp. 228–237, 2015 (cit. on p. 39).
- [110] Y. Hong and R. A. Horn, "A Canonical Form for Matrices under Consimilarity," *Linear Algebra and its Applications*, vol. 102, pp. 143–168, 1988 (cit. on p. 47).
- [111] T. Starčič, "The Stabilizers for the Action of Orthogonal Similarity on Symmetric Matrices and Orthogonal *-Conjugacy on Hermitian Matrices," 2020 (cit. on p. 47).
- [112] M. G. K., "On Coneigenvalues of a Complex Square Matrix," *International Journal of Mathematical Modelling & Computations*, vol. 3, no. 3, pp. 253–258, 2013 (cit. on p. 47).
- [113] S. K. Cho and C. M. Chu, "Optimal Polarization in Bistatic Scattering," *SIAM Journal on Applied Mathematics*, vol. 49, no. 5, pp. 1473–1479, 1989 (cit. on pp. 47, 48, 158).
- [114] S. K. Cho, *Electromagnetic Scattering*. Springer Science & Business Media, 2012 (cit. on p. 47).
- [115] T. Jiang, X. Cheng, and L. Chen, "An Algebraic Relation Between Consimilarity and Similarity of Complex Matrices and its Applications," *Journal of Physics: Mathematical and General*, vol. 39, pp. 9215–9222, 2006 (cit. on pp. 48, 52–55, 134, 158).

- [116] T. Jiang and M. Wei, "On the Reduction of a Complex Matrix to Triangular or Diagonal by Consimilarity," *Numerical Mathematics-English Series*, vol. 15, no. 2, p. 107, 2006 (cit. on pp. 48, 49, 158).
- [117] M. Ciuca, G. Vasile, M. Gay, A. Anghel, and S. Ciochina, "Polarimetric Analysis using the Algebraic Real Representation of the Scattering Matrix," in *Proc. IEEE Int. Geosci. Remote Sens. Symp. (IGARSS)*, 2021, pp. 499–452 (cit. on p. 48).
- [118] M. Ciuca, G. Vasile, A. Anghel, M. Gay, and S. Ciochina, "Bistatic Analysis Using the Real Representation Scattering Matrix Eigen-Classification," *IEEE Transactions on Geoscience and Remote Sensing*, vol. 60, pp. 1–18, 2022 (cit. on p. 48).
- [119] M. Ciuca, G. Vasile, M. Gay, A. Anghel, and S. Ciochina, "Méthode Générale de Résolution de la Similarité Conjuguée en Polarimétrie Radar," in *GRETSI 2022 - XXVIIIème Colloque Francophone de Traitement du Signal et des Images*, 2022 (cit. on pp. 48, 158).
- [120] K. D. Ikramov, "On Condiagonalizable Matrices," *Linear Algebra and its Applications*, vol. 424, no. 2-3, pp. 456–465, 2007 (cit. on p. 49).
- [121] A.-G. Wu and Y. Zhang, *Complex Conjugate Matrix Equations for Systems and Control*. Springer, 2017 (cit. on p. 49).
- [122] S.-Y. Lu and R. A. Chipman, "Homogeneous and Inhomogeneous Jones Matrices," *J. Opt. Soc. Am. A*, vol. 11, no. 2, pp. 766–773, 1994 (cit. on p. 50).
- [123] J. C. Gutiérrez-Vega, "The Field of Values of Jones Matrices: Classification and Special Cases," *Proceedings of the Royal Society A*, vol. 476, no. 2242, 2020 (cit. on p. 50).
- [124] J. C. Gutiérrez-Vega, "Defective Jones Matrices: Geometric Phase and Passivity Condition," *J. Opt. Soc. Am. B*, vol. 37, no. 9, pp. 2586–2594, 2020 (cit. on p. 50).
- [125] E. Lüneburg and W.-M. Boerner, "Consimilarity Classification of General Radar Scattering Matrices," in *Proceedings of ISAP*, 1996, pp. 1041–1044 (cit. on p. 50).
- [126] C. Hellings and W. Utschick, "Block-Skew-Circulant Matrices in Complex-Valued Signal Processing," *IEEE Transactions on Signal Processing*, vol. 63, no. 8, pp. 2093–2107, 2015 (cit. on p. 51).
- [127] C. Hellings and W. Utschick, "Two Different Real Representations of Complex Matrices for Describing Widely Linear Systems," in *Proc. of the International Symposium on Wireless Communication Systems*, 2015, pp. 641–645 (cit. on pp. 51, 52).
- [128] J. Eriksson and V. Koivunen, "Complex Random Vectors and ICA Models: Identifiability, Uniqueness, and Separability," *IEEE Transactions on Information Theory*, vol. 52, no. 3, pp. 1017–1029, 2006 (cit. on p. 52).
- [129] H. Lee, S. Park, and I. Lee, "A New Two-step Precoding Strategy for Closed-loop MIMO Systems," *IEEE Transactions on Communications*, vol. 57, no. 3, pp. 861–870, 2009 (cit. on p. 52).
- [130] K. Qian, Y. Wang, Y. Shi, and X. X. Zhu, " γ -Net: Superresolving SAR Tomographic Inversion via Deep Learning," *IEEE Transactions on Geoscience and Remote Sensing*, vol. 60, pp. 1–16, 2022 (cit. on p. 52).

- [131] W. B. Silva, C. C. Freitas, S. J. S. Sant'Anna, and A. C. Frery, "Classification of Segments in PolSAR Imagery by Minimum Stochastic Distances Between Wishart Distributions," *IEEE Journal of Selected Topics in Applied Earth Observations and Remote Sensing*, vol. 6, no. 3, pp. 1263–1273, 2013 (cit. on pp. 52, 90).
- [132] N. C. R. L. Carvalho, L. Sant'Anna Bins, and S. J. Siqueira Sant'Anna, "Analysis of Stochastic Distances and Wishart Mixture Models Applied on PolSAR Images," *Remote Sensing*, vol. 11, no. 24, 2019 (cit. on pp. 52, 90–92).
- [133] Y. Tian, "Matrix Representations of Octonions and their Applications," *Advances in Applied Clifford Algebras*, vol. 10, no. 1, 2000 (cit. on p. 52).
- [134] A. Mesloub, K. Abed-Meraim, and A. Belouchrani, "A New Algorithm for Complex Non-Orthogonal Joint Diagonalization Based on Shear and Givens Rotations," *IEEE Transactions on Signal Processing*, vol. 62, no. 8, pp. 1913–1925, 2014 (cit. on p. 52).
- [135] L. Pallotta, A. De Maio, and D. Orlando, "A Robust Framework for Covariance Classification in Heterogeneous Polarimetric SAR Images and Its Application to L-Band Data," *IEEE Transactions on Geoscience and Remote Sensing*, vol. 57, no. 1, pp. 104–119, 2019 (cit. on pp. 60, 140).
- [136] N. Trouve, E. Colin-Koeniguer, P. Fargette, and A. De Martino, "Influence of Geometrical Configurations and Polarization Basis Definitions on the Analysis of Bistatic Polarimetric Measurements," *IEEE Transactions on Geoscience and Remote Sensing*, vol. 49, no. 6, pp. 2238–2250, 2011 (cit. on pp. 61, 75).
- [137] E. Kemptner and A. Osipov, "Plane-of-Scattering Bistatic Scattering Matrix of Simply Shaped Targets," in *European Conference on Antennas and Propagation (EuCAP)*, 2007, pp. 1–5 (cit. on pp. 61, 65).
- [138] L. Iannini, D. Comite, N. Pierdicca, and P. Lopez-Dekker, "Rough-Surface Polarimetry in Companion SAR Missions," *IEEE Transactions on Geoscience and Remote Sensing*, vol. 60, pp. 1–15, 2022 (cit. on pp. 61, 79).
- [139] L. Iannini, M. Kleinherenbrink, A. Theodosiou, and P. Lopez-Dekker, "Linear Principal Polarizations in Bistatic SAR Mission Companions," in *Proc. IEEE Int. Geosci. Remote Sens. Symp. (IGARSS)*, 2021, pp. 3073–3076 (cit. on pp. 61, 65).
- [140] V. Karnychev, V. Khlusov, L. Ligthart, and G. Sharygin, "Algorithms for Estimating the Complete Group of Polarization Invariants of the Scattering Matrix (SM) Based on Measuring all SM Elements," *IEEE Trans. Geosci. Remote Sens.*, vol. 42, no. 3, pp. 529–539, 2004 (cit. on pp. 61, 62, 160).
- [141] O. A. Krasnov and L. P. Ligthart, "Radar Polarimetry using Sounding Signals with Dual Orthogonality - PARSAX Approach," in *The 7th European Radar Conference*, 2010, pp. 121–124 (cit. on pp. 61, 62).
- [142] A. Aubry, V. Carotenuto, A. De Maio, and L. Pallotta, "Assessing Reciprocity in Polarimetric SAR Data," *IEEE Geosci. Remote Sens. Lett.*, vol. 17, no. 1, pp. 87–91, 2020 (cit. on pp. 61, 62, 122, 124).
- [143] L. Pallotta, "Reciprocity Evaluation in Heterogeneous Polarimetric SAR Images," *IEEE Geosci. Remote Sens. Lett.*, pp. 1–5, 2020 (cit. on pp. 61, 62).

- [144] B. R. Mahafza, *Radar Systems Analysis and Design using Matlab*. Taylor & Francis Group, 2013 (cit. on pp. 69, 71, 73).
- [145] “CST Studio - High Frequency Simulation: Workflow and Solver Overview,” CST Studio Suite, Dassault Systemes Deutschland GmbH, Technical Report, 2019 (cit. on pp. 70, 73).
- [146] K. Kalbasi and K. Demarest, “A Multilevel Formulation of the Method of Moments (EM Scattering),” *IEEE Transactions on Antennas and Propagation*, vol. 41, no. 5, pp. 589–599, 1993 (cit. on p. 70).
- [147] T. Weiland, “Time Domain Electromagnetic Field IELD Computation with Finite Difference Methods,” *International Journal of Numerical Modelling: Electronic Networks, Devices and Fields*, vol. 9, no. 4, pp. 295–319, 1996 (cit. on p. 70).
- [148] T. Weiland, M. Timm, and I. Munteanu, “A Practical Guide to 3-D Simulation,” *IEEE Microwave Magazine*, vol. 9, no. 6, pp. 62–75, 2008 (cit. on p. 70).
- [149] I. Munteanu and T. Weiland, “RF & Microwave Simulation with the Finite Integration Technique – From Component to System Design,” in *Scientific Computing in Electrical Engineering*, D. Ciuprina Gabriela and Ioan, Ed. Berlin, Heidelberg: Springer Berlin Heidelberg, 2007, pp. 247–260 (cit. on p. 70).
- [150] “Understanding Time Domain Meshing in CST Microwave Studio,” CST Studio Suite, Dassault Systemes Deutschland GmbH, Technical Report, 2010 (cit. on p. 70).
- [151] L. Andrade, E. Nohara, G. Peixoto, M. Rezende, and I. Martin, “Backscattering Analysis of Flat Plate and Dihedral Corner Reflectors using PO and Comparison with RCS Measurements in Anechoic Chamber,” in *Proceedings of the 2003 SBMO/IEEE MTT-S International Microwave and Optoelectronics Conference - IMOC 2003*, vol. 2, 2003, pp. 719–724 (cit. on pp. 71, 74).
- [152] E. Knott, “RCS Reduction of Dihedral Corners,” *IEEE Transactions on Antennas and Propagation*, vol. 25, no. 3, pp. 406–409, 1977 (cit. on p. 74).
- [153] A. Z. Tempelis, “Bistatic 3D Electromagnetic Scattering from a Right-Angle Dihedral at Arbitrary Orientation and Position,” Air Force Institute of Technology, Master Thesis, 2011 (cit. on p. 74).
- [154] R. Kell, “On the Derivation of Bistatic RCS from Monostatic Measurements,” *Proceedings of the IEEE*, vol. 53, no. 8, pp. 983–988, 1965 (cit. on p. 74).
- [155] C. J. Bradley, P. J. Collins, D. G. Falconer, J. Fortuny-Guasch, and A. J. Terzuoli, “Evaluation of a Near-Field Monostatic-to-Bistatic Equivalence Theorem,” *IEEE Geosci. Remote Sens. Lett.*, vol. 46, no. 2, pp. 449–457, 2008 (cit. on p. 74).
- [156] K. Wilson, “Method for predicting the maximum reliable angle to use in the monostatic-to-bistatic equivalence theorem,” *IEEE Antennas Propag. Mag.*, vol. 43, no. 3, pp. 108–111, 2001 (cit. on p. 74).
- [157] J. A. Jackson, B. D. Rigling, and R. L. Moses, “Parametric Scattering Models for Bistatic Synthetic Aperture Radar,” in *2008 IEEE Radar Conference*, 2008, pp. 1–5 (cit. on p. 74).
- [158] J. A. Jackson, B. D. Rigling, and R. L. Moses, “Canonical Scattering Feature Models for 3D and Bistatic SAR,” *IEEE Transactions on Aerospace and Electronic Systems*, vol. 46, no. 2, pp. 525–541, 2010 (cit. on p. 74).

- [159] D. Ao, Y. Li, C. Hu, and W. Tian, "Accurate Analysis of Target Characteristic in Bistatic SAR Images: A Dihedral Corner Reflectors Case," *Sensors*, vol. 18, no. 1, p. 24, 2017 (cit. on p. 74).
- [160] G. Singh and Y. Yamaguchi, "Model-Based Six-Component Scattering Matrix Power Decomposition," *IEEE Transactions on Geoscience and Remote Sensing*, vol. 56, no. 10, pp. 5687–5704, 2018 (cit. on p. 76).
- [161] Y. Wang, W. Yu, and W. Hou, "Five-Component Decomposition Methods of Polarimetric SAR and Polarimetric SAR Interferometry Using Coupling Scattering Mechanisms," *IEEE J STARS*, vol. 14, pp. 6662–6676, 2021 (cit. on p. 76).
- [162] I. Lahaie and D. Sengupta, "Scattering of Electromagnetic Waves by a Slowly Rotating Rectangular Metal Plate," *IEEE Journal of Antennas and Propagation*, vol. 27, no. 1, pp. 40–46, 1979 (cit. on p. 76).
- [163] J. M. D. Blasco, M. Fitrzyk, J. Patruno, A. M. Ruiz-Armenteros, and M. Marconcini, "Effects on the Double Bounce Detection in Urban Areas Based on SAR Polarimetric Characteristics," *Remote Sensing*, vol. 12, no. 7, pp. 1187–1209, 2020 (cit. on pp. 78, 106).
- [164] W. Yang, H. Song, G.-S. Xia, and C. López-Martínez, "Dissimilarity Measurements for Processing and Analyzing PolSAR Data: A Survey," in *IEEE International Geoscience and Remote Sensing Symposium (IGARSS)*, 2015, pp. 1562–1565 (cit. on pp. 88, 89).
- [165] X. Qin, Y. Zhang, Y. Li, Y. Cheng, W. Yu, *et al.*, "Distance Measures of Polarimetric SAR Image Data: A Survey," *Remote Sensing*, vol. 14, no. 22, 2022 (cit. on pp. 88–90).
- [166] C.-A. Deledalle, L. Denis, G. Poggi, F. Tupin, and L. Verdoliva, "Exploiting Patch Similarity for SAR Image Processing: The Nonlocal Paradigm," *IEEE Signal Processing Magazine*, vol. 31, no. 4, pp. 69–78, 2014 (cit. on p. 88).
- [167] L. Gomez, J. Wu, and A. C. Frery, "Non-Local Means Filters for Full Polarimetric Synthetic Aperture Radar Images with Stochastic Distances," *Image Processing On Line*, vol. 12, pp. 142–172, 2022, <https://doi.org/10.5201/ipol.2022.346> (cit. on p. 88).
- [168] D. Ratha, S. De, T. Celik, and A. Bhattacharya, "Change Detection in Polarimetric SAR Images Using a Geodesic Distance Between Scattering Mechanisms," *IEEE Geoscience and Remote Sensing Letters*, vol. 14, no. 7, pp. 1066–1070, 2017 (cit. on pp. 88–90, 109).
- [169] N. Bouhleb and S. Méric, "Multilook Polarimetric SAR Change Detection Using Stochastic Distances Between Matrix-Variate Gd0 Distributions," *IEEE Transactions on Geoscience and Remote Sensing*, vol. 58, no. 10, pp. 6823–6843, 2020 (cit. on pp. 88–90).
- [170] A. Alonso-González, C. López-Martínez, K. P. Papathanassiou, and I. Hajnsek, "Polarimetric SAR Time Series Change Analysis Over Agricultural Areas," *IEEE Transactions on Geoscience and Remote Sensing*, vol. 58, no. 10, pp. 7317–7330, 2020 (cit. on pp. 89, 99, 100, 165).
- [171] O. D'Hondt, S. Guillaso, and O. Hellwich, "Iterative bilateral filtering of polarimetric sar data," *IEEE Journal of Selected Topics in Applied Earth Observations and Remote Sensing*, vol. 6, no. 3, pp. 1628–1639, 2013 (cit. on pp. 89, 100, 101).
- [172] J.-S. Lee, M. Grunes, and R. Kwok, "Classification of Multi-look Polarimetric SAR Imagery based on Complex Wishart Distribution," *International Journal of Remote Sensing*, vol. 15,

- no. 11, pp. 2299–2311, 1994. eprint: <https://doi.org/10.1080/01431169408954244> (cit. on pp. 89–92, 110).
- [173] K. Conradsen, A. Nielsen, J. Schou, and H. Skriver, “A Test Statistic in the Complex Wishart Distribution and its Application to Change Detection in Polarimetric SAR Data,” *IEEE Transactions on Geoscience and Remote Sensing*, vol. 41, no. 1, pp. 4–19, 2003 (cit. on pp. 89, 122).
- [174] A. C. Frery, A. D. C. Nascimento, and R. J. Cintra, “Analytic Expressions for Stochastic Distances Between Relaxed Complex Wishart Distributions,” *IEEE Transactions on Geoscience and Remote Sensing*, vol. 52, no. 2, pp. 1213–1226, 2014 (cit. on pp. 89, 90).
- [175] J. Qu, X. Qiu, C. Ding, and B. Lei, “Unsupervised Classification of Polarimetric SAR Image Based on Geodesic Distance and Non-Gaussian Distribution Feature,” *Sensors*, vol. 21, no. 4, 2021 (cit. on pp. 89, 91, 92).
- [176] M. Dabboor, M. J. Collins, V. Karathanassi, and A. Braun, “An Unsupervised Classification Approach for Polarimetric SAR Data Based on the Chernoff Distance for Complex Wishart Distribution,” *IEEE Transactions on Geoscience and Remote Sensing*, vol. 51, no. 7, pp. 4200–4213, 2013 (cit. on p. 90).
- [177] M. Dabboor, S. Howell, M. Shokr, and J. Yackel, “The Jeffries–Matusita distance for the case of complex Wishart distribution as a separability criterion for fully polarimetric SAR data,” *International Journal of Remote Sensing*, vol. 35, no. 19, pp. 6859–6873, 2014 (cit. on p. 90).
- [178] F. Nielsen, K. Sun, and S. Marchand-Maillet, “On Hölder Projective Divergences,” *Entropy*, vol. 19, no. 3, 2017 (cit. on p. 90).
- [179] T. Pan, D. Peng, X. Yang, P. Huang, and W. Yang, “Classification for PolSAR Image Based on Hölder Divergences,” *The Journal of Engineering*, vol. 2019, no. 21, pp. 7593–7596, 2019 (cit. on p. 90).
- [180] D. Ratha, A. Bhattacharya, and A. C. Frery, “Unsupervised Classification of PolSAR Data Using a Scattering Similarity Measure Derived From a Geodesic Distance,” *IEEE Geoscience and Remote Sensing Letters*, vol. 15, no. 1, pp. 151–155, 2018 (cit. on pp. 90–92).
- [181] D. Ratha, E. Pottier, A. Bhattacharya, and A. C. Frery, “A PolSAR Scattering Power Factorization Framework and Novel Roll-Invariant Parameter-Based Unsupervised Classification Scheme Using a Geodesic Distance,” *IEEE Transactions on Geoscience and Remote Sensing*, vol. 58, no. 5, pp. 3509–3525, 2020 (cit. on pp. 90, 106, 109).
- [182] C. C. Aggarwal and C. K. Reddy, Eds., *Data Clustering: Algorithms and Applications*. CRC Press, 2014 (cit. on p. 90).
- [183] P. Kersten, J.-S. Lee, and T. Ainsworth, “Unsupervised Classification of Polarimetric Synthetic Aperture Radar Images using Fuzzy Clustering and EM Clustering,” *IEEE Transactions on Geoscience and Remote Sensing*, vol. 43, no. 3, pp. 519–527, 2005 (cit. on p. 90).
- [184] S. N. Anfinsen, R. Jenssen, and T. Eltoft, “Spectral Clustering of Polarimetric SAR Data with the Wishart-Derived Distance Measures,” in *Science and Applications of SAR Polarimetry and Polarimetric Interferometry*, H. Lacoste and L. Ouwehand, Eds., ser. ESA Special Publication, vol. 644, 2007 (cit. on p. 90).

- [185] A. K. Jain, "Data clustering: 50 years beyond k-means," *Pattern Recognition Letters*, vol. 31, no. 8, pp. 651–667, 2010, Award winning papers from the 19th International Conference on Pattern Recognition (ICPR) (cit. on p. 91).
- [186] S. Borra, R. Thanki, and N. Dey, *Satellite Image Analysis: Clustering and Classification*. Springer Nature, Singapore, 2019 (cit. on p. 91).
- [187] L. Ferro-Famil, E. Pottier, and J.-S. Lee, "Unsupervised Classification of Multifrequency and Fully Polarimetric SAR Images Based on the H/A/Alpha-Wishart Classifier," *IEEE Transactions on Geoscience and Remote Sensing*, vol. 39, no. 11, pp. 2332–2342, 2001 (cit. on pp. 91, 92).
- [188] J.-S. Lee, M. Grunes, E. Pottier, and L. Ferro-Famil, "Unsupervised Terrain Classification Preserving Polarimetric Scattering Characteristics," *IEEE Transactions on Geoscience and Remote Sensing*, vol. 42, no. 4, pp. 722–731, 2004 (cit. on pp. 91, 92).
- [189] S. Wang, K. Liu, J. Pei, M. Gong, and Y. Liu, "Unsupervised Classification of Fully Polarimetric SAR Images Based on Scattering Power Entropy and Copolarized Ratio," *IEEE Geoscience and Remote Sensing Letters*, vol. 10, no. 3, pp. 622–626, 2013 (cit. on pp. 91, 92).
- [190] C. Wang, W. Yu, R. Wang, Y. Deng, F. Zhao, *et al.*, "Unsupervised Classification Based on Non-negative Eigenvalue Decomposition and Wishart Classifier," *IET Radar, Sonar & Navigation*, vol. 8, no. 8, pp. 957–964, 2014 (cit. on pp. 91, 92).
- [191] P. Formont, J. Ovarlez, F. Pascal, G. Vasile, and L. Ferro-Famil, "On the Extension of the Product Model in POLSAR Processing for Unsupervised Classification using Information Geometry of Covariance Matrices," in *2011 IEEE International Geoscience and Remote Sensing Symposium*, 2011, pp. 1361–1364 (cit. on pp. 91, 92, 99, 100, 165).
- [192] P. Formont, "Outils Statistiques and Géométriques pour la Classification des Images SAR Polarimétriques Hautement Texturées," Ph.D. dissertation, 2013 (cit. on pp. 91, 145).
- [193] N. C. Carvalho, "Bisecting Stochastic Clustering: A New Algorithm for PolSAR Image Unsupervised Classification," Ph.D. dissertation, 2020 (cit. on pp. 91, 99, 100).
- [194] B. Han, P. Han, and Z. Cheng, "Block Classification of PolSAR Images based on Density Peak Clustering," in *2021 SAR in Big Data Era (BIGSAR DATA)*, 2021, pp. 1–4 (cit. on pp. 91, 92).
- [195] L. Carrea and G. Wanielik, "Polarimetric SAR Processing using the Polar Decomposition of the Scattering Matrix," in *Proc. IEEE Int. Geosci. Remote Sens. Symp. (IGARSS 2001)*, vol. 1, 2001, pp. 363–365 (cit. on p. 93).
- [196] L. Carrea, G. Wanielik, and L. Giubbolini, "The Polar Decomposition of the Scattering Matrix Applied to the Polarimetric Image of the Guard-rail," in *14th International Conference on Microwaves, Radar and Wireless Communications. MIKON - 2002. Conference Proceedings*, vol. 2, 2002, pp. 563–566 (cit. on p. 93).
- [197] L. Carrea, G. Wanielik, and M. Chandra, "Geometric Interpretation of the Characteristic Polarizations," in *15th International Conference on Microwaves, Radar and Wireless Communications (IEEE Cat. No.04EX824)*, vol. 3, 2004, 1083–1086 Vol.3 (cit. on p. 93).

- [198] J.-C. Souyris and C. Tison, "Polarimetric Analysis of Bistatic SAR Images From Polar Decomposition: A Quaternion Approach," *IEEE Transactions on Geoscience and Remote Sensing*, vol. 45, no. 9, pp. 2701–2714, 2007 (cit. on pp. 93, 153).
- [199] J.-C. Souyris and C. Tison, "Multi-look Polar Decomposition of Polarimetric SAR Images," in *Proc. IEEE Int. Geosci. Remote Sens. Symp. (IGARSS 2007)*, 2007, pp. 4144–4147 (cit. on p. 93).
- [200] P.-L. Frison, C. Lardeux, J.-C. Souyris, C. Tison, B. Stoll, *et al.*, "Radar Polar Decomposition for Natural Surfaces Cartography," in *IGARSS 2008 - 2008 IEEE International Geoscience and Remote Sensing Symposium*, vol. 4, 2008, pp. 363–366 (cit. on p. 93).
- [201] S. R. Cloude, R. Ossikovski, and E. Garcia-Caurel, "Bright Singularities: Polarimetric Calibration of Spaceborne PolSAR Systems," *IEEE Geoscience and Remote Sensing Letters*, vol. 18, no. 3, pp. 476–479, 2021 (cit. on p. 93).
- [202] S.-Y. Lu and R. A. Chipman, "Interpretation of Mueller Matrices based on Polar Decomposition," *J. Opt. Soc. Am. A*, vol. 13, no. 5, pp. 1106–1113, 1996 (cit. on p. 93).
- [203] H. Wang, Z. Zhou, J. Turnbull, Q. Song, and F. Qi, "PolSAR Classification Based on Generalized Polar Decomposition of Mueller Matrix," *IEEE Geoscience and Remote Sensing Letters*, vol. 13, no. 4, pp. 565–569, 2016 (cit. on p. 94).
- [204] M. Moakher, "A Differential Geometric Approach to the Geometric Mean of Symmetric Positive-Definite Matrices," *SIAM Journal on Matrix Analysis and Applications*, vol. 26, no. 3, pp. 735–747, 2005. eprint: <https://doi.org/10.1137/S0895479803436937> (cit. on pp. 95, 99, 100, 146).
- [205] P. Dita, "Factorization of Unitary Matrices," *Journal of Physics A: Mathematical and General*, vol. 36, no. 11, p. 2781, 2003 (cit. on p. 96).
- [206] J. Polcari, "Butterfly decomposition of arbitrary unitary matrices," Working Paper, 2014 (cit. on pp. 96, 104).
- [207] A. Rasin, "Diagonalization of Quark Mass Matrices and the Cabibbo-Kobayashi-Maskawa Matrix," Aug. 1997. arXiv: hep-ph/9708216 (cit. on p. 96).
- [208] Y. Wang, C. Han, and F. Tupin, "PolSAR Data Segmentation by Combining Tensor Space Cluster Analysis and Markovian Framework," *IEEE Geoscience and Remote Sensing Letters*, vol. 7, no. 1, pp. 210–214, 2010 (cit. on pp. 99, 100).
- [209] P. Salembier and S. Foucher, "Optimum Graph Cuts for Pruning Binary Partition Trees of Polarimetric SAR Images," *IEEE Transactions on Geoscience and Remote Sensing*, vol. 54, no. 9, pp. 5493–5502, 2016 (cit. on pp. 99, 100).
- [210] N. Zhong, W. Yang, A. Cherian, X. Yang, G.-S. Xia, *et al.*, "Unsupervised Classification of Polarimetric SAR Images via Riemannian Sparse Coding," *IEEE Transactions on Geoscience and Remote Sensing*, vol. 55, no. 9, pp. 5381–5390, 2017 (cit. on pp. 99, 100, 165).
- [211] A. Alonso-González, C. López-Martínez, and P. Salembier, "PolSAR Time Series Processing With Binary Partition Trees," *IEEE Transactions on Geoscience and Remote Sensing*, vol. 52, no. 6, pp. 3553–3567, 2014 (cit. on pp. 99, 100, 165).

- [212] N. Zhong, T. Yan, W. Yang, and G.-S. Xia, "A Supervised Classification Approach for PolSAR Images Based on Covariance Matrix Sparse Coding," in *2016 IEEE 13th International Conference on Signal Processing (ICSP)*, 2016, pp. 213–216 (cit. on pp. 99, 100, 165).
- [213] Y. Zhang, X. Lai, Y. Xie, Y. Qu, and C. Li, "Geometry-Aware Discriminative Dictionary Learning for PolSAR Image Classification," *Remote Sensing*, vol. 13, no. 6, 2021 (cit. on pp. 99, 100, 165).
- [214] J. Shi and H. Jin, "Riemannian Nearest-Regularized Subspace Classification for Polarimetric SAR Images," *IEEE Geoscience and Remote Sensing Letters*, vol. 19, pp. 1–5, 2022 (cit. on pp. 99, 100).
- [215] B. Pang, S.-q. Xing, Y.-z. Li, and X.-s. Wang, "Speckle Filtering Algorithm for Polarimetric SAR Based on Mean Shift," in *2012 IEEE International Geoscience and Remote Sensing Symposium*, 2012, pp. 5892–5895 (cit. on pp. 99, 165).
- [216] B. Pang, S. Xing, Y. Li, and X. Wang, "Novel Polarimetric SAR Speckle Filtering Algorithm Based on Mean Shift," *Journal of Systems Engineering and Electronics*, vol. 24, no. 2, pp. 222–223, 2013 (cit. on pp. 99, 165).
- [217] F. Yang, W. Gao, B. Xu, and J. Yang, "Multi-Frequency Polarimetric SAR Classification Based on Riemannian Manifold and Simultaneous Sparse Representation," *Remote Sensing*, vol. 7, no. 7, pp. 8469–8488, 2015 (cit. on p. 99).
- [218] H. Song, W. Yang, N. Zhong, and X. Xu, "Unsupervised Classification of PolSAR Imagery via Kernel Sparse Subspace Clustering," *IEEE Geoscience and Remote Sensing Letters*, vol. 13, no. 10, pp. 1487–1491, 2016 (cit. on p. 99).
- [219] X. Yang, W. Yang, H. Song, and P. Huang, "Polarimetric SAR Image Classification Using Geodesic Distances and Composite Kernels," *IEEE Journal of Selected Topics in Applied Earth Observations and Remote Sensing*, vol. 11, no. 5, pp. 1606–1614, 2018 (cit. on p. 99).
- [220] M. Congedo, B. Afsari, A. Barachant, and M. Moakher, "Approximate Joint Diagonalization and Geometric Mean of Symmetric Positive Definite Matrices," *PLOS ONE*, vol. 10, no. 4, pp. 1–25, Apr. 2015 (cit. on p. 99).
- [221] R. Bhatia, "The Riemannian Mean of Positive Matrices," in *Matrix Information Geometry*, F. Nielsen and R. Bhatia, Eds. Berlin, Heidelberg: Springer Berlin Heidelberg, 2013, pp. 35–51 (cit. on pp. 100, 120, 169).
- [222] A. Barachant, S. Bonnet, M. Congedo, and C. Jutten, "Multiclass Brain–Computer Interface Classification by Riemannian Geometry," *IEEE Transactions on Biomedical Engineering*, vol. 59, no. 4, pp. 920–928, 2012 (cit. on pp. 100, 165).
- [223] P. Formont, J.-P. Ovarlez, and P. Frédéric, *On the Use of Matrix Information Geometry for Polarimetric SAR Image Classification*, F. Nielsen and R. Bhatia, Eds. Berlin, Heidelberg: Springer Berlin Heidelberg, 2013, pp. 257–276 (cit. on pp. 100, 165).
- [224] N. Gasnier, L. Denis, and F. Tupin, "On the Use and Denoising of the Temporal Geometric Mean for SAR Time Series," *IEEE Geoscience and Remote Sensing Letters*, vol. 19, pp. 1–5, 2022 (cit. on p. 101).

- [225] S. Fiori and T. Tanaka, "An Algorithm to Compute Averages on Matrix Lie Groups," *IEEE Transactions on Signal Processing*, vol. 57, no. 12, pp. 4734–4743, 2009 (cit. on pp. 101, 102).
- [226] J. R. Huynen, "Physical Reality of Radar Targets," in *Radar Polarimetry*, H. Mott and W.-M. Boerner, Eds., International Society for Optics and Photonics, SPIE, 1993, pp. 86–96 (cit. on p. 106).
- [227] G. Singh, Y. Yamaguchi, and S.-E. Park, "General Four-Component Scattering Power Decomposition With Unitary Transformation of Coherency Matrix," *IEEE Transactions on Geoscience and Remote Sensing*, vol. 51, no. 5, pp. 3014–3022, 2013 (cit. on p. 106).
- [228] A. Bhattacharya, G. Singh, S. Manickam, and Y. Yamaguchi, "An Adaptive General Four-Component Scattering Power Decomposition With Unitary Transformation of Coherency Matrix (AG4U)," *IEEE Geoscience and Remote Sensing Letters*, vol. 12, no. 10, pp. 2110–2114, 2015 (cit. on p. 106).
- [229] D. Li, Y. Zhang, and L. Liang, "A mathematical extension to the general four-component scattering power decomposition with unitary transformation of coherency matrix," *IEEE Transactions on Geoscience and Remote Sensing*, vol. 58, no. 11, pp. 7772–7789, 2020 (cit. on p. 106).
- [230] W. An, M. Lin, and J. Zou, "A Study on Physical Meanings of a Unitary Transformation Used in Polarimetric Decomposition," in *IGARSS 2018 - IEEE International Geoscience and Remote Sensing Symposium*, 2018, pp. 5863–5866 (cit. on p. 106).
- [231] J.-S. Lee, T. L. Ainsworth, Y. Wang, and K.-S. Chen, "Polarimetric SAR Speckle Filtering and the Extended Sigma Filter," *IEEE Transactions on Geoscience and Remote Sensing*, vol. 53, no. 3, pp. 1150–1160, 2015 (cit. on p. 107).
- [232] A. Alonso-Gonzalez, C. Lopez-Martinez, and P. Salembier, "Filtering and Segmentation of Polarimetric SAR Data Based on Binary Partition Trees," *IEEE Transactions on Geoscience and Remote Sensing*, vol. 50, no. 2, pp. 593–605, 2012 (cit. on pp. 110, 140).
- [233] J. A. Barrachina, "Complex-Valued Neural Networks for Radar Applications," Ph.D. dissertation, 2022 (cit. on pp. 113, 122).
- [234] H. Dong, L. Zhang, and B. Zou, "PolSAR Image Classification with Lightweight 3D Convolutional Networks," *Remote Sensing*, vol. 12, no. 3, 2020 (cit. on pp. 115, 122, 124).
- [235] Z. Lin, "Riemannian Geometry of Symmetric Positive Definite Matrices via Cholesky Decomposition," *SIAM Journal on Matrix Analysis and Applications*, vol. 40, no. 4, pp. 1353–1370, 2019 (cit. on pp. 120, 169).
- [236] P. Dubois Fernandez, O. du Plessis, D. le Coz, J. Dupas, B. Vaizan, *et al.*, "The ONERA RAMSES SAR System," in *Proc. IEEE Int. Geosci. Remote Sens. Symp. (IGARSS)*, vol. 3, 2002, pp. 1723–1725 (cit. on p. 122).
- [237] I. Hajnsek, A. Moreira, and M. Davidson, "Airborne Campaigns for PolInSAR Applications Development," in *International Workshop on Applications of Polarimetry and Polarimetric Interferometry PolInSAR*, 2007 (cit. on p. 122).

- [238] N. Skou, J. Granholm, K. Woelders, J. Rohde, J. Dall, *et al.*, “A High Resolution Polarimetric L-band SAR-Design and First Results,” in *International Geoscience and Remote Sensing Symposium, IGARSS '95*, vol. 3, 1995, 1779–1782 vol.3 (cit. on p. 122).
- [239] H. Skriver, J. Dall, L. Ferro-Famil, T. Toan, P. Lumsdon, *et al.*, “Agriculture classification using POLSAR Data,” in *POLINSAR 2005*, Italy, 2005, pp. 32–37 (cit. on p. 122).
- [240] Y. Ji, J. T. S. Sumantyo, M. Y. Chua, and M. M. Waqar, “Unsupervised PolSAR Image Classification based on Sparse Representation,” *International Journal of Remote Sensing*, vol. 40, no. 16, pp. 6224–6248, 2019. eprint: <https://doi.org/10.1080/01431161.2019.1587209> (cit. on p. 122).
- [241] X. Zhang, J. Xia, X. Tan, X. Zhou, and T. Wang, “PolSAR Image Classification via Learned Superpixels and QCNN Integrating Color Features,” *Remote Sensing*, vol. 11, no. 15, 2019 (cit. on p. 122).
- [242] C. Livingstone, A. Gray, R. Hawkins, and R. Olsen, “CCRS C/X-Airborne Synthetic Aperture Radar: An R&D Tool for the ERS-1 Time Frame,” *IEEE Aerospace and Electronic Systems Magazine*, vol. 3, no. 10, pp. 11–20, 1988 (cit. on p. 123).
- [243] R. Hawkins, C. Brown, K. Murnaghan, J. Gibson, A. Alexander, *et al.*, “The SAR-580 Facility - System Update,” in *Proc. IEEE Int. Geosci. Remote Sens. Symp. (IGARSS 2002)*, vol. 3, 2002, 1705–1707 vol.3 (cit. on p. 123).
- [244] C. Livingstone, A. Gray, R. Hawkins, P. Vachon, T. Lukowski, *et al.*, “The CCRS Airborne SAR Systems: Radar for Remote Sensing Research,” *Canadian Journal of Remote Sensing*, vol. 21, no. 4, pp. 468–491, 1995. eprint: <https://doi.org/10.1080/07038992.1995.10855169> (cit. on p. 124).
- [245] C. Livingstone, A. Gray, P. Vachon, M. Lalonde, R. Hawkins, *et al.*, “The Canadian Airborne R&D SAR Facility: The CCRS C/X SAR,” in *Proc. IEEE Int. Geosci. Remote Sens. Symp. (IGARSS 1996)*, vol. 3, 1996, 1621–1623 vol.3 (cit. on p. 124).
- [246] R. Bruce, F. Dean, A. Henrik Steen, G. Rashpal, N. Son, *et al.*, “Preparation for the Operational use of RADARSAT-2 for Ice Monitoring,” *Canadian Journal of Remote Sensing*, vol. 30, no. 3, pp. 415–423, 2004. eprint: <https://doi.org/10.5589/m03-076> (cit. on p. 125).
- [247] “Applications Potential of RADARSAT-2: Supplement One,” Defence, Research and Development Canada, Canada Space Agency, Technical Report, 2004 (cit. on p. 125).
- [248] A. Anghel, R. Cacoveanu, A.-S. Moldovan, B. Rommen, and M. Datcu, “COBIS: Opportunistic C-Band Bistatic SAR Differential Interferometry,” *IEEE Journal of Selected Topics in Applied Earth Observations and Remote Sensing*, vol. 12, no. 10, pp. 3980–3998, 2019 (cit. on p. 126).
- [249] G. J. Tee, “Eigenvectors of Block Circulant and Alternating Circulant Matrices,” *New Zealand Journal of Mathematics*, vol. 36, no. 8, pp. 195–211, 2007 (cit. on p. 129).
- [250] S. V. Nghiem, M. Borgeaud, J. A. Kong, and R. T. Shin, “Polarimetric Remote Sensing of Geophysical Media with Layer Random Medium Model,” *Progress In Electromagnetics Research*, 1990 (cit. on p. 139).

-
- [251] M. Borgeaud, R. Shin, and J. Kong, "Theoretical models for polarimetric radar clutter," *Journal of Electromagnetic Waves and Applications*, vol. 1, no. 1, pp. 73–89, 1987 (cit. on p. 139).
- [252] L. Novak and M. Burl, "Optimal Speckle Reduction in Polarimetric SAR Imagery," *IEEE Transactions on Aerospace and Electronic Systems*, vol. 26, no. 2, pp. 293–305, 1990 (cit. on p. 139).
- [253] J.-S. Lee, T. L. Ainsworth, J. Kelly, and C. Lopez-Martinez, "Statistical Evaluation and Bias Removal of Multi-Look Effect on Entropy/Alpha/Anisotropy in Polarimetric Target Decomposition," in *7th European Conference on Synthetic Aperture Radar*, 2008, pp. 1–4 (cit. on p. 140).
- [254] C. C. Lee, "Elimination of Redundant Operations for a Fast Sobel Operator," *IEEE Transactions on Systems, Man, and Cybernetics*, vol. SMC-13, no. 2, pp. 242–245, 1983 (cit. on p. 140).
- [255] P. Mather and M. Koch, *Computer Processing of Remotely-Sensed Images: An Introduction, Fourth Edition*. John Wiley and Sons Ltd, UK, 2011 (cit. on p. 140).
- [256] F. Barbaresco, "Interactions between Symmetric Cone and Information Geometries: Bruhat-Tits and Siegel Spaces Models for High Resolution Autoregressive Doppler Imagery," in *Emerging Trends in Visual Computing*, 2009 (cit. on p. 145).